MODELING AND SIMULATION OF CONTACT AND IMPACT DYNAMICS IN MULTIBODY SYSTEMS

by

ABHISHEK CHATTERJEE

Presented to the Faculty of the Graduate School of
The University of Texas at Arlington in Partial Fulfillment
of the Requirements
for the Degree of

DOCTOR OF PHILOSOPHY IN MECHANICAL ENGINEERING

THE UNIVERSITY OF TEXAS AT ARLINGTON
August 2019

To my parents, Alokananda and Asoke Chatterjee, whose guidance and support made me who I am.

ACKNOWLEDGEMENTS

I would like to thank my adviser Dr. Alan Bowling for being such a great mentor and always motivating and supporting me through the thick and thin of my graduate study; I couldn't have hoped for a better advisor in grad-school. I wish to thank Dr. Kamesh Subbarao, Dr. Narges Shayesteh, Dr. Endel Iarve, and Dr. Mahdi Haghshenas-Jaryani for their interest in my research and for taking time to serve in my dissertation committee. I would also like to extend my gratitude to Dr. Daejong Kim, Dr. Kent Lawrence and Dr. Ashfaq Adnan, who have served in my dissertation committee in the past. I also want to thank Dr. Pranesh Aswath, who graciously offered me a research assistant position at the Office of the Provost, in my final year of the PhD program; I couldn't have completed my PhD without this job. I also wish to thank all of my colleagues at the Office of the Provost, who were all very kind to me.

I would like to thank all my current and past friends and colleagues from The Robotics, Biomechanics and Dynamic Systems Lab, Dr. Adrian Rodriguez, Dr. Mahdi Haghshenas-Jaryani, Dr. Ashley Guy, Manoochehr Rabiei, Vatsal Joshi, Eric Havenhill, Gurashish Singh, Yatish Nagraj, Rohit Katti, Pranav Parikh and Nachiket Kansara for all their support and valuable feedback regarding my work and also for being good companions in the lab. I would like thank all undergraduate students in our lab, especially Rashi Jain and Regan Kubicek, whom I have worked with on projects.

I would like to express my deepest gratitude to my mother, Alokananda Chatterjee and father Asoke Chatterjee, without whose support and sacrifices, it would have been impossible for me to pursue graduate school and chase my dream of becoming a robotics researcher. I would also like thank my grandparents, Rama and Krishna Bhattacharya, my aunts, Bratati Chatterjee and Adrija Bhattacharya, my uncles, Somnath Bhattacharya and Suman Chatterjee, and my cousins Sarbani, Sohini, Sanjeev, and Samridhi, who all made a lot of difference with their support and love. I would also like to thank all my friends from various points of my life, who directly or indirectly motivated me to pursue greater goals: Sajjad Bhai and Prashanti Bhabi, Tarebi (John T.), Niluk, Michael, Gary, Peter, Robert, Chris, Vishal, Sourav, Anup, Pranata, Hemjit, and many others.

I would also like to thank all my undergraduate professors, especially Dr. Salim Azzouz who mentored me during my undergraduate research and Dr. Dale McDonald who sparked in me the interest for Dynamics and Controls. Finally, I wish to thank some of my best friends since joining UTA, Danny John, Jaganmohan Chandrasekaran and his wife Ankita Patel, all of whom helped in making my journey through grad school very enjoyable and less stressful.

August 01, 2019

ABSTRACT

MODELING AND SIMULATION OF CONTACT AND IMPACT DYNAMICS IN MULTIBODY SYSTEMS

ABHISHEK CHATTERJEE, Ph.D.

The University of Texas at Arlington, 2019

Supervising Professor: Alan P. Bowling

Contact and impact analyses are an essential part of multibody dynamic simulations. Modeling of contact and impact problems have applications in a wide variety of areas including robotics, earthquake engineering, computer graphics, and manufacturing. Collisions between objects typically take place over surfaces that are represented by a set of points in the operation space, thereby requiring multi-point contact and impact analysis. Analysis of multi-point contact and impact may lead to indeterminate (underdetermined) problems with more number of unknowns (contact forces) than equations.

This work pertains to the problem of resolving multi-point contact and impact problems in multibody systems consisting of hard objects, that can be assumed to be rigid. In the first part of this work, a rigidity based modeling and simulation technique is developed for multi-point impacts between hard objects. In this proposed framework impacts are treated as discrete events during which the velocities of the system evolve in the impulse-domain, based on an impulse-momentum theory called *Darboux-Keller* shock. Constraints derived based on the rigid body assumption are used to resolve indeterminacy associated with multi-point analysis. An energetic terminal constraint is also proposed based on *Stronge's Hypothesis*, that guarantees the treatment of impact to be energetically consistent. This approach is used to derive both planar and three-dimensional models of multi-point indeterminate impacts.

The rigid impact model based on impulse-momentum theory, developed in the first part of this work, loses some information like force and deformation histories during impacts. This lost information, however can be useful in certain types of application. Hence, to retain this information, the second part of this work proposes a method of augmenting the rigid-impact model with a contact force model from the contact mechanics literature to simultaneously determine the force and deformation histories during an impact event. The contact force model used here is a viscoelastoplastic model of contact that considers the effects of permanent (plastic) deformation in the material. A relationship is developed between the permanent deformations of the material and the energetic terminal constraint proposed in the first part of this work to characterize the force histories during collisions.

The accumulation of discrete impact events during the time-domain simulation may lead to chattering or zeno phenomenon, causing the adaptive step-size integration to halt or fail. This work resolves this problem by transitioning to contact when the normal components of the post-impact velocities become very small. During contact, the forces between the participating rigid bodies satisfy the: 1) non-penetrability condition and 2) frictional force constraints based on Coulomb Friction. The non-penetrability condition enforces normal velocity and acceleration constraints on the equations of motion, whereas the Coulomb friction constrains the tangential forces at the contact points. These constraints placed on the equations of motion, lead to a reduction in the number of degrees of freedom (DOF) of the system. This work uses an online constraint embedding technique to enforce contact constraints.

TABLE OF CONTENTS

Appendix

LIST OF ILLUSTRATIONS

CHAPTER 1

INTRODUCTION

The motivation for this research is to develop modeling and simulation techniques for rigid contacts and impacts in multibody dynamic systems. Modeling of hard contact and impact problems have a wide variety of applications in areas such as robotic manipulation, earthquake engineering, vehicle dynamics, computer graphics and manufacturing. An important class of multibody contact and impact problems deals with the analysis of multi-point collisions with friction, which are very useful in modeling impacts between rigid surfaces. A very crucial requirement in such analyses is that of maintaining energy-consistency in solutions to such problems. This work develops methods for solving such multi-point frictional collision problem, that guarantees an energetically consistent solution. The solution methods proposed in this work utilized certain constraints based on the assumption of rigidity to resolve multi-point collision problems. This approach is used to solve both planar (2D) and spatial (3D) multi-point impact problems. This work also addresses certain problems related *stick-slip transition* and *slip-reversal* in frictional impacts. Rigid bodies typically tend to rebound instantaneously at collisions, which coincide with abrupt changes in the system's velocities. Hence, an event-based simulation approach is often needed to model collisions, where the time-domain integration of the equations of motion of the system is stopped upon collision-detection and then restarted with a new set of initial-conditions based on the evaluated post-impact states. However, this approach always causes the numerical integration to *chatter* or exhibit what is known as *zeno phenomenon*, as the rebound velocities get very small, resulting in the time-domain numerical integration to halt. Hence, a method of transitioning to contact is also proposed in this work. The rigid collision model proposed in the first part of this work treats collisions to be instantaneous and perfectly rigid. However, in reality collisions between rigid object do take place over tiny measurable periods of time, and exhibit minute deformations. Although the rigid collision model presented in the first part of this work is very convenient and useful for a lot of applications, it loses some information like the force histories, deformation histories, and time of impact. These information can be very useful for certain types of applications such as, biomedical/orthopedic applications or tribological applications. Hence, the last part of this work is dedicated to the problem of retaining/recovering the force, deformation and elapsed-time information while using the rigidity based collision model developed in the first part.

The various collision modeling methods presented in the literature can be generally subdivided into two groups: *rigid collision models* [1–4] and *deformable collision models* [5–11]. The *rigid collision models* are based on the assumption that bodies undergoing collision would experience no or negligible amounts of deformation. This method of impact modeling are typically applicable for objects composed of materials of very high stiffness that require very large forces to induce very small amounts of deformation. Rigid collisions also typically assume the time-duration of an impact to be very small. These assumptions lead to a considerable simplification of the impact problem, such that each collision essentially translate to an instantaneous change of velocities of the system, and in effect ignoring the very small of deformations and very large force quantities. The *deformable collision models*, on the other hand, rigorously model the dependence of deformations on the contact forces, based on the foundations of *solid mechanics* [12–17]. The deformable collision models are suitable for objects that undergo significant deformations during collision. However, their usage is somewhat impractical if the colliding bodies experience very small amounts deformation, since they require integration of very high forces at very small time scales. Rigid collision models are more appropriate for collisions with small deformation, since these models are usually based on the integration of impulses, which are “well-behaved" physical quantities, obtained by scaling the very large contact forces with the very small time of impact. However, a significant drawback of using a rigid collision model is that this analysis loses certain information during a collision viz. contact force history, deformations, and elapsed time of impact. The main objective of this work is to develop a framework for modeling rigid impacts, while including certain aspects of deformable collision models to retain the time-dependent force and deformation histories during an impact.

One of the key features of rigid collision models is that they result in nonsmooth jumps in the system velocities, and therefore they represent a type of hybrid dynamical system. The changes in the velocities of the system at collisions is governed by one of three different classes of restitution laws: 1) *Kinematic*, 2) *Impulsive* and 3) *Energetic*. *Kinetic restitution laws* are the simplest form of restitution law, that are applied directly to the pre-impact velocities to determine a set of post-impact velocities that are characterized by a kinematic *coefficient of restitution* parameter. An example of kinematic coefficients of restitution is Newton’s COR [3, 11]. A major drawback kinematic restitution laws is that they have been known to produce energetically inconsistent results, under certain conditions [18, 19]. The *impulsive* and *energetic* restitution laws, on the other hand, are based on what is known as *Darboux-Keller Shock Dynamics* [1, 20, 21]. In this description of rigid body impact dynamics the equations of motion of the system are integrated over a small time-period to be redefined as velocity-impulse relationships. Also, the tangential forces (differential impulses) are resolved in terms of Coulomb friction Law [4, 21, 22]. Hence, in this approach the velocities of the system during an impact is evolved in terms of the normal components of the impulses at various contact points. In the case of single point three-dimensional impacts, the Coulomb friction law yields a set of coupled ordinary differential equations that may be resolved separately for the conditions of sticking, slipping and slip-reversal [4, 22]. The Coulomb friction law defines these states in terms of the *stick-slip transition*. The transition to or from the slip state is associated with a discontinuous change in velocity. The Coulomb friction law models an idealized version of this behavior and is commonly used to establish a set of complementarity conditions for modeling the stick-slip phenomenon [23–27]. An *impulsive* restitution law characterizes the net impulses imparted to the contact points throughout the impact event in terms of the Poisson's COR [11,28]. Once the net impulses are known, the post-impact velocities can be determined based on the Darboux-Keller model. Poisson's COR has been known to always yields energetically consistent solutions. Nevertheless, it is worth noting that impulsive restitution law is a purely mathematical treatment of restitution law, and doesn't provide much insight on mechanism of the impact process [29]. Similar to the impulsive restitution law, the *energetic* restitution laws can also be formulated in terms of the Darboux-Keller model. An energetic restitution law was first proposed by Boulanger [30], and Routh [31], was later rediscovered by Stronge [2,22,26,32,33] and also applied it in the context of rigid impacts by using the Darboux-Keller model. A great advantage of energetic restitution law is that the post-impact velocities are constrained directly in terms of an energetic coefficient of restitution parameter, which grantees energy consistency during collision.

Previous works dealing with rigid body collision have also considered the problem of analyzing multi-point impacts [5, 6, 34–42]. An important feature of most multi-point impact problems is that the number of contact forces on the system exceed the number of degrees of freedom (DOF) of the system. This type of impact problems are also known as *indeterminate* impacts, since solving for the contact forces in such impacts yield an underdetermined problem. In the literature, one can find a number of different approaches for addressing this indeterminacy problem. One group of work resolves these indeterminate multi-point impact analysis problems using optimization based approaches [15, 43]. The optimization methods often pose multi-point impact as a linear complementarity problem

(LCP), where the contact forces are represented by Lagrange multipliers [16, 17, 44–46]. Posing contact and impact problems as LCPs, allows the use of a discrete numerical integration scheme, known as time-stepping [46–51]. An alternative approach to this is to use additional constraints on the contact forces to resolve the indeterminacy problem. The constraints applied on the contact forces of the system can be of two types: *compliance based* [5,6,34,35] or *rigidity based* [36–42]. The compliance based constraints allow some deformations at all contact points such that the forces on the system can be constrained in terms of some stiffness model. The force distribution obtained using compliance based approach depends upon the very small deformations at all contact point. This can sometimes make the resulting differential equations harder to integrate. In contrast, the rigidity based constraints doesn't allow any deformations at the contact points, such that the resulting force distribution only depends upon the positions and orientations of the impacting bodies [38, 42]. Constraints based on the rigid body assumption, also allows for all of the contact forces at various points on the body to be defined in terms of a single normal force (differential impulse) parameter. This in turn facilitates the characterization of the total normal work (energy dissipation due to the normal contact forces) in terms of a *global coefficient of restitution* parameter [36–42]. Hence, the idea of the energy based restitution law, proposed by Stronge for single-point impact [22, 32], can be generalized to characterize energy loss throughout the system, involving multi-point impacts. This work uses a *global* version of the ECOR to model the system level energy dissipation in multi-point impact problems, similar to [52], as opposed to defining a local ECOR for each impact point as in [28, 53, 54].

A vast amount of literature addresses the topic of COR estimation based on the material properties of the impacting bodies [55–57]. Yet, it is well-known that the COR can depend on more than the material properties. The global ECOR used herein depends on mass properties, initial velocities, the system configuration prior to collision, friction, and more. It is difficult to determine the global ECOR as a function of all of these properties. However, determining the global ECORs by matching experimental results provides interesting insights into the process of energy loss during a collision. After examining several cases of impact, it may be possible to develop some general guidelines for choosing the value of a global ECOR based on the particulars of the collision, but for now, the key use of the proposed analysis is to investigate energy losses.

The Darboux-Keller [1, 20, 21] based impact models scale the forces during impact with the time of impact, transforming the equations of motions into a velocity-impulse relationship. This converts the impact problem to a first-order dynamics problem with respect to the impulses, where the forces, displacement and time evolution during an impact is disregarded. This scheme is very convenient and efficient for rigid impact analyses, where the primary quantity of interest is the post-impact velocities of the system, given the pre-impact velocities. Since, time is very small while the contact force are very large, neither time or forces are considered useful in such analysis. However, the force, deformation and time evolution during rigid impacts are useful for certain applications. Since no object is truly rigid, hard objects that may be considered rigid for some analyses, actually do exhibit very small deformations that characterizes the contact forces on the body during collision. Nevertheless, deformation based contact models are inefficient for very hard or rigid objects, compared to the Darboux-Keller model. Hence in this work an extension to the rigid impact model is also proposed where a rigid collision model is augmented with contact force model to yield force, deformation and time evolution information of an impact along with the post-impact states. This scheme maintains the overall rigidity of the body while allowing tiny deformations in the neighborhood of the contact points, and as a result allows for the calculation of forces and elapsed-time, as efficiently. Since the overall rigidity in the impact model is maintained, the dynamic associated with rigid collision model is unaffected by the forces and deformations, instead the rigid collision model dictates the nature of the force, deformation and time evolution during impact. The contact force model used for this augmentation is a visco-elastoplastic force model is taken from the contact mechanics literature [55, 58–67], that allows permanent (plastic) deformations, and is discussed in details in Chapter 7. The analysis presented in Chapter , also establishes a link between the permanent deformations and global ECOR, and thereby helps define the relationships governing the evolution of deformation, forces and time in terms of the states of the rigid impact model i.e. velocities, energy dissipation and impulses.

The short duration of rigid body collisions produces large forces and thus it is more useful to examine the problem in the *impulse domain* rather than the time domain. The impulse-domain impact analysis takes place after the time-domain integration of the equations of motion is stopped when a collision is detected. This method of simulation is known as *event-based* or *hybrid dynamic simulation*, where standard numerical integration techniques are used to simulate the time-dependent equations of motions between various impact events. One of the difficulties encountered with the event-based simulation approach is the accumulation of events because of the high frequency *chattering* behavior as the impact transitions to a contact. In the hybrid dynamic simulation of rigid bodies, chattering takes place when a rigid body impacts a contact surface with a small amount of rebound. These small rebounds lead to a succession of impact events that, in effect, stop the time based simulation. Chattering is common in a variety of hybrid dynamic simulation problems, and has been studied extensively from a numerical integration point of view in the literature [68–71]. The goal here is not to use an advanced numerical integration scheme to eliminate the chattering behavior. Instead a smooth time-domain contact dynamics model is developed that uses online constraint embedding to remove degrees of freedom (DOFs), which eliminates the chattering behavior.

Constraint enforcement in multibody dynamics can be performed by *redundant coordinate* techniques or *coordinate reduction/constraint-embedding* techniques [72]. Techniques based on *redundant coordinate* sets solve the equations of motion and the constraints simultaneously in a differential algebraic equation (DAE) framework. DAE solvers typically satisfy constraints and reduce "drift-off effects" by employing error-minimization techniques based on Baumgarte's stabilization method [72–76] or Lagrange multiplier based penalty methods [73, 77, 78]. In contrast, coordinate reduction methods reformulate the equations of motion based on a minimal set of independent generalized coordinates. Constraint embedding techniques are based on coordinate-partitioning techniques originally proposed in [79], that make use of the constraint equations to resolve dependent coordinates in terms of independent generalized coordinates based on the SVD [73,80,81], LU [81] or QR [82–85] decomposition methods. This work uses a QR based constraint embedding technique to enforce non-penetrability and frictional constraints during the no-rebound contact phase.

In Chapter 2 a general overview of modeling and simulation technique for constrained dynamic systems is presented. The goal of this chapter is to introduce a method of *online constraint embedding* that is used throughout this work. Chapter 2 presents a broad background on the two types of constraints common in multibody dynamic systems: *Bilateral* and *Unilateral* constraints. Although this work is mainly concerned with modeling unilateral constraints (contact constraints), the online constraint embedding technique allows both types of constraints using a similar framework. The method for enforcing frictional contact constraints (a type of unilateral constraints), is revisited in Chapters 3 and 5. Chapter 3 develops the method for solving planar multi-point impact problems. The planar impact problem offers certain simplifications to the general three-dimensional problem, nevertheless the fundamental problem of resolving indeterminacy in multi-point impact remains in both. So this chapter presents a great deal of discussion on the overall approach of resolving indeterminacy. Chapter 4 presents some simulation results for planar impact problems. Chapter 5 generalizes some of the techniques used in Chapter 2 and develops solution method for three-dimensional (spatial) impact problem. Chapter 5 also discuses to great length about the problem of multi-point stick-slip transition and slip-reversal that occurs in three-dimensional impacts. It also presents a non-iterative solution method for the slip-reversal problem. Chapter 6 presents some simulation results obtained based on the method presented in Chapter 5. Lastly, Chapter 7 develops the method of estimating forces, deformations, and time-evolution during rigid collisions. Simulation results based on the method proposed in Chapter 7 are presented in Chapter 8.

CHAPTER 2

CONSTRAINED DYNAMICS AND CONTACT MODELING

This chapter presents a general framework for modeling constrained dynamic systems that would be used throughout the remainder of this work. Multibody dynamic systems in their most general form can be represented in terms of *Differential Algebraic Equations* (DAE) systems. DAE systems are systems of ordinary or partial differential equations (ODE or PDE), whose states are constrained by an algebraic equation. Although it is possible to represent multibody dynamic systems using both ordinary and partial DAEs, partial DAEs are rarely used in practice because they are significantly harder to solve. Hence within the domain of multibody dynamics, by DAE it is implied that the differential equation component of the system is an ordinary differential equation.

The ordinary differential equation portion of a DAE for a multibody dynamic system, represents the dynamics or force-acceleration relationship for the system, and is referred to as the *equations of motion* for the system, which can be derived using a number of different methods viz. *Newton-Euler*, *Kane/Maggi*, *Euler-Lagrange*, etc. Where as the algebraic portion of a multibody DAE system arises due to all kinematic or contact constraints on the system. The constraints on a multibody system are essentially restrictions on the configuration-space that reduces the degrees of freedom (DOF) of the system, with respect to number of defined coordinates. A standard method for solving DAE systems is to convert it into a standard ODE problem. This can be done by taking derivatives of the associated algebraic equation to match the order of the differential equations in the DAE system. Hence, this allows for a DAE to be evaluated as an ODE, provided the initial conditions satisfy the constraints (or are zeros of the algebraic equation). The conversion of DAEs to

ODEs may be performed symbolically to yield minimal sets of differential equations that can be integrated numerically. In multibody dynamics vernacular, this approach is often referred to as *offline constraint embedding*. The offline constraint embedding approach is suitable for small systems (less number of bodies) with persistent kinematic constraints. However, this approach is not efficient for multibody systems with large number of bodies or contact constraints. Contact constraints in multibody systems can activate and deactivate during numerical integration, which makes them difficult to enforce with the offline constraint embedding method. Hence, numerical evaluation of the DAEs are more suitable for contact problems.

In multibody dynamics, the class of methods used to numerically solve DAEs by conversion to ODEs, are often referred to as *online constraint embedding*. The *online constraint embedding* methods in the literature can be classified into two groups: *redundant coordinate* [72–78] approaches or coordinate-partitioning approaches [72, 73, 79–85]. In this work a coordinate-partitioning approach is used to numerically solve DAEs with contact constraints.

2.1 General Form of Equations of Motion

The general form of the equations of motion for any arbitrary multibody dynamic system is can be written as,

$$A(\mathbf{q})\ddot{\mathbf{q}} + \mathbf{B}(\mathbf{q}, \dot{\mathbf{q}}) = \mathbf{\Gamma}(\mathbf{q}) = J^T(\mathbf{q})\mathbf{F} + E(\mathbf{q})^T \mathbf{\Upsilon} \tag{2.1}$$

where $\mathbf{q}$ is a set of generalized coordinates used to describe the configuration of the multibody system, and $A(\mathbf{q})$ is a mass matrix that contains all of the masses and moments of inertia of the system. The vector $\mathbf{B}(\mathbf{q}, \dot{\mathbf{q}})$ contains a number of other terms, and can be broken down as,

$$\mathbf{B}(\mathbf{q}, \dot{\mathbf{q}}) = \mathbf{b}(\mathbf{q}, \dot{\mathbf{q}}) + \mathbf{g}(\mathbf{q}) \tag{2.2}$$

where $\mathbf{b}(\mathbf{q}, \dot{\mathbf{q}})$ and $\mathbf{g}(\mathbf{q})$ are the Coriolis and gravity terms, respectively. The left-hand side of the generalized equations of motion in (2.1), given by $\mathbf{\Gamma}(\mathbf{q})$, contain terms related to the *generalized active forces*, or external forces applied to the system. The generalized active forces $\mathbf{\Gamma}(\mathbf{q})$ is composed of two terms $J^T(\mathbf{q})\mathbf{F}$ and $E(\mathbf{q})^T\mathbf{\Upsilon}$, which represent contributions of the constraint forces and applied input forces, respectively. The constraint forces given by $\mathbf{F}$, are the forces applied to the system by all kinematic or contact constraints on the system, and is related to the generalized active forces through a *constraint Jacobian* matrix $J(\mathbf{q})$. Υ consists of all the applied input forces/torques to the system, and is related to $\Gamma(\mathbf{q})$ by a matrix $E(\mathbf{q})$, which is a diagonal matrix consisting of all gear ratios associated with the applied input forces/torques as diagonal elements. Hence, the general form of equations of motion in (2.1), representing the dynamics of an arbitrary system forms the ordinary differential equation (ODE) portion of the DAE for the multibody dynamics system, and can be rewritten as an initial value problem (IVP) as,

$$\ddot{\mathbf{q}} = A^{-1}\left(J^T\mathbf{F} + E^T\mathbf{\Upsilon} - \mathbf{B}\right) \quad \text{with} \quad \mathbf{q}(0) = \mathbf{q}_0, \quad \dot{\mathbf{q}}(0) = \dot{\mathbf{q}}_0 \tag{2.3}$$

where $\mathbf{q}_0$ and $\dot{\mathbf{q}}_0$ are the initial values of the states for the second order ODE. Here the mass matrix A has been assumed to be a full-rank and invertible. However, note that A may not be invertible if *quaternions* are used to represent the orientations of the system. In such cases, additional constraints are required for the inversion [86]. In this work all orientations are represented using euler angles.

2.2 Constraints

Constraints in multibody systems that reduce the system's degrees of freedom, can be classified as either *Bilateral Constraints* or *Unilateral Constraints*. Although, this work mainly deals with unilateral constraints related to contact problems, for completeness, both types of constraints are briefly discussed in the following sections.

2.2.1 Bilateral Constraints: Joints

Bilateral constraints are the type of constraints used to model various types of joints in multibody dynamic systems. These constraints can be further classified into *holonomic* or *non-holonomic* constraints. The holonomic constraints are only functions of generalized coordinates $\mathbf{q}$, whereas non-holonomic constraints can be functions of $\mathbf{q}$, $\dot{\mathbf{q}}$ or t. If the non-holonomic constraint is a function is time t, then it is called *rheonomic*, otherwise it's called *scleronomic*. Despite these classification, the general approach for solving these different types of constraints remain the same. Hence, the approach discussed here is derived using rheonomic bilateral constraint of the type:

$$\mathbf{\Phi}(\mathbf{q}, t) = \mathbf{0} \tag{2.4}$$

The constraint in (2.4) would be called an *index - 2* constraint, which means two time-derivative operations are required for the constraint to have same order as the order of the ODE in (2.3). The *index - 2* constraint function $\mathbf{\Phi}(\mathbf{q}, t)$ is a time-dependent position-level constraint function. Consequently, $\dot{\mathbf{\Phi}}$ and $\ddot{\mathbf{\Phi}}$ would be velocity-level and acceleration-level constraints and are given by,

$$\begin{aligned} \dot{\mathbf{\Phi}} &= \frac{\partial \mathbf{\Phi}}{\partial \mathbf{q}}\dot{\mathbf{q}} + \frac{\partial \mathbf{\Phi}}{\partial t} = J\dot{\mathbf{q}} + \mathbf{a} = \mathbf{0} \\ \text{and,} \qquad \ddot{\mathbf{\Phi}} &= \frac{\partial \mathbf{\Phi}}{\partial \mathbf{q}}\ddot{\mathbf{q}} + \frac{d}{dt}\left(\frac{\partial \mathbf{\Phi}}{\partial \mathbf{q}}\right)\dot{\mathbf{q}} + \frac{\partial^2 \mathbf{\Phi}}{\partial t^2} = J\ddot{\mathbf{q}} + \dot{J}\dot{\mathbf{q}} + \dot{\mathbf{a}} = \mathbf{0} \end{aligned} \tag{2.5}$$

Note, that the constraint Jacobian J obtained in (2.5) identical to the constraint Jacobian in (2.1) and (2.3). This property is very important as it allows for the unknown constraint forces $\mathbf{F}$ to be eliminated out of the reduced equations of motion.

2.2.2 Unilateral Constraints: Contact

Unlike bilateral constraints, the unilateral constraints are not always active. These constraints are conditionally activated, and are useful in modeling contact and friction in dynamic systems. The conditions for activating these constraint while modeling rigid contact and impact are presented in Sections 3.3 and 5.3, in the form of certain complimentarity conditions. Nevertheless, when these constraints are activated, they are enforced as velocity and acceleration level constraints similar to (2.5).

2.3 Constraint Embedding - Coordinate Partitioning

This section presents an overview of the coordinate-partitioning based method used to enforce constraints in this work. The method essentially relies on partitioning the constraint Jacobian obtained in (2.5) to express the generalized speeds and accelerations in terms of a minimal independent sets of their components. The constraint Jacobian can be partitioned into dependent and independent columns using QR decomposition as,

$$J = QR = Q\,[R_D \;\; R_I] = [QR_D \;\; QR_I] = [J_D \;\; J_I]$$

where J_D and J_I columns associated with the dependent and independent generalized speed components. J_D is selected such that its is full-rank and invertible. Similarly, $\dot{\mathbf{q}}$ can be partitioned into dependent and independent parts as $\dot{\mathbf{q}} = [\dot{\mathbf{q}}_D \;\; \dot{\mathbf{q}}_I]^T$. Then the Jacobian in the first equation of (2.5) can be decomposed as,

$$\mathbf{0} = \dot{\mathbf{\Phi}} = J\dot{\mathbf{q}} + \mathbf{a} = \begin{bmatrix} J_D & J_I \end{bmatrix} \begin{bmatrix} \dot{\mathbf{q}}_D \\ \dot{\mathbf{q}}_I \end{bmatrix} + \mathbf{a} \tag{2.6}$$

The dependent components of the generalized speeds can be expressed in terms of the independent components by inverting J_D matrix. Thus, all generalized speeds can be defined in terms of the independent generalized speeds,

$$\dot{\mathbf{q}} = \begin{bmatrix} -J_D^{-1}J_I \\ I \end{bmatrix} \dot{\mathbf{q}}_I + \begin{bmatrix} -J_D^{-1}\mathbf{a} \\ \mathbf{0} \end{bmatrix} = G\dot{\mathbf{q}} + \mathbf{h} \tag{2.7}$$

Taking the time-derivative of (2.7) yields,

$$\ddot{\mathbf{q}} = G\ddot{\mathbf{q}}_I + \dot{G}\dot{\mathbf{q}}_I + \dot{\mathbf{h}} \tag{2.8}$$

Repeating the same process with the acceleration equations in (2.5), and then comparing with (2.8) yields,

$$\dot{G}\dot{\mathbf{q}} = \begin{bmatrix} -J_D^{-1}\dot{J}\dot{\mathbf{q}} \\ \mathbf{0} \end{bmatrix} \quad \text{and} \quad \dot{\mathbf{h}} = \begin{bmatrix} -J_D^{-1}\dot{\mathbf{a}} \\ \mathbf{0} \end{bmatrix} \tag{2.9}$$

The equation (2.8) defines shows the relationship of all generalized acceleration with the set of independent generalized accelerations $\mathbf{q}_I$. Now, substituting (2.8) into the equations of motion in (2.1), and pre-mutiplying both sides with G^T yields,

$$G^T AG\ddot{\mathbf{q}}_I + G^T A\dot{G}\dot{\mathbf{q}}_I + G^T A\dot{\mathbf{h}} + G^T\mathbf{B} = G^T J^T\mathbf{F} + G^T E^T\boldsymbol{\Upsilon} \tag{2.10}$$

Considering the decomposition of the constraint Jacobian, the term $G^T J^T$ in (2.10) vanishes as,

$$G^T J^T = (JG)^T = \left(\begin{bmatrix} J_D & J_I \end{bmatrix} \begin{bmatrix} -J_D^{-1} J_I \\ I \end{bmatrix} \right)^T = (-J_I + J_I)^T = 0 \tag{2.11}$$

Hence, all of the constraint forces $\mathbf{F}$ defined on the system get eliminated once the constraints $\boldsymbol{\Phi}$ are enforced, thereby reducing the degrees of freedom of the system. The independent set of generalized acceleration can now be solved as,

$$\ddot{\mathbf{q}}_I = \left(G^T AG\right)^{-1} \left(G^T E^T\boldsymbol{\Upsilon} - G^T A\dot{G}\dot{\mathbf{q}}_I - G^T A\dot{\mathbf{h}} - G^T\mathbf{B}\right) \tag{2.12}$$

Therefore, the constrained dynamic system could be numerically integrated using equations (2.7), (2.7) and (2.12). Thus the constrained dynamic system could be summarized as,

$$\begin{cases} \ddot{\mathbf{q}} = G\ddot{\mathbf{q}}_I + \dot{G}\dot{\mathbf{q}}_I + \dot{\mathbf{h}} \\ \text{where,} \quad \ddot{\mathbf{q}}_I = \left(G^T AG\right)^{-1} \left(G^T E^T\boldsymbol{\Upsilon} - G^T A\dot{G}\dot{\mathbf{q}}_I - G^T A\dot{\mathbf{h}} - G^T\mathbf{B}\right) \\ \text{and,} \quad \dot{\mathbf{q}} = G\dot{\mathbf{q}} + \mathbf{h} \end{cases} \tag{2.13}$$

The reduced equations of motion in (2.13) represents constrained dynamics for a given set of constraints $\mathbf{\Phi}(\mathbf{q}, t)$. The constraints $\mathbf{\Phi}$ can be either bilateral or unliateral constraints. In case of bilateral constraints $\mathbf{\Phi}$ remains constant throughout the simulation, whereas in case of unlateral constraints the elements of $\mathbf{\Phi}$ are conditionally activated or deactivated. The application of unilateral constraints in this work arise due to the problem of modeling contact between rigid bodies, where certain components of $\mathbf{\Phi}$, say Φ_{z_i}, represent the normal component of the position vector between a surface and a contact point. The contact constraints cannot be applied until the contact point touches the surface, i.e. when $\Phi_{z_i} \leq 0$. So when the condition, $\Phi_{z_i} \leq 0$ is satisfied, the contact constraints applied between a pair of contact point and contact surface include 1) non-penetration constraints and 2) frictional constraints. The details pertaining to 1) non-penetration and 2) frictional constraints are presented in Chapters 3 an 5. However, an important thing to note about frictional constraints, which is based on Coulomb's law, is that these constraints are actually force-based inequality constraints. Chapters 3 and 5 shows how the force inequality constraints based on Coulomb's law can be enforced via the aforementioned method.

CHAPTER 3

PLANAR RIGID IMPACT MODEL

The motivation for this work is to develop an analytical framework for modeling interactions between mechanical systems (e.g. buildings, legged robots, etc.) and their surroundings. This work presents a two-dimensional analysis of this problem using a rigid multibody approach assuming small deformations of the bodies. The modeling approaches used in multibody dynamics might be considered a coarse approximation, but their simplicity often leads to useful insights about the behavior of the mechanical systems studied. This work is fundamentally focused on developing an energetically consistent method of modeling planar indeterminate contact and impact while considering the stick-slip transition. The tangential impulses and forces during impacts and sustained contacts respectively are modeled using Coulomb friction. The slip-direction may change during contact or impact due to the discontinuity associated with the friction force, such that the post-impact velocities are affected during impact events. The point(s) in contact during an impact event or sustained contact phase may stick (no-slip), slide (slip) or enter a stick-slip transition. The stick-slip transition refers to the instants when one or more contact points with initial tangential velocities come to rest. Following the stick-slip transition these points may stick, slip-reverse or resume slipping [28, 87]. Analysis of the stick-slip transition leads into an analysis of the transition between impact and contact. After an impact event, points on the surface may rebound from the surface or remain in sustained contact with it. This work is intended to address all phases of this analysis from impact to contact in an energetically consistent manner.

A considerable amount of work related to contact and impact in multibody systems can be found in the literature. Interactions between rigid bodies are referred to as impacts when they occur over an infinitesimally small time-period. Rigid impacts take place in the presence of very large forces, such that the bodies experience a sudden change in velocity. These events can be treated as continuous, discontinuous or hybrid processes. The continuous approaches use regularized [8], non-colliding [9], or compliant [88, 89] contact force models and often involve penalty methods. These models allow small local deformations between the impacting bodies since they incorporate stiffness due to springs and dampers into the model [10]. In the discontinuous approach impacts between rigid bodies are treated as discrete events. This approach, also referred to as piecewise [8] or nonsmooth [11, 26, 90], treats the impact event as an instantaneous change in velocities of the impacting bodies. The post-impact velocities are resolved based on impulse-momentum theory with the help of constraints as shown in [21]. The hybrid or impact and continuous [9], approaches treat the impact event as discontinuous in time-domain but continuous in impulse-domain [2, 32, 33]. The hybrid approach is used in this work.

One of the key issues addressed in this work is the problem of resolving indeterminacy in multi-point impact based on rigidity. As shown in [36] velocity constraints can be derived based on the rigid body assumption. Then the indeterminacy can be resolved by applying these constraints at the velocity level of the equations of motion. The work in [36] used this method and solved for the post-impact velocities using an optimization technique. This work proposes a further development such that the post-impact velocities may be solved analytically based on constraints arising from the rigid body assumption. An alternative method found in literature, involves allowing compliance at the impact points [29], thereby adding degrees of freedom (DOFs) and equations of motion. These additional equations of motion remove the indeterminacy associated with multiple point impacts. In [34], a distributing law was developed for frictionless multiple impacts and later extended to consider friction [35]. This theoretical approach produces consistent results in comparison to experiments and explores the complex behaviors that arise with friction. Similar to [36], this work utilizes the constraints available from the rigid body assumption. However, the present work converts the velocity constraints into force constraints using the dual property of the impact Jacobian and applies them at the force level. These aspects of the analysis allow a conversion of physically meaningful velocity constraints into force or impulse constraints.

Another key issue addressed here is the energy consistency of rigid body collision simulations. Herein, an energetic coefficient of restitution is used to guaranty energetic consistency. An extensive body of work exists on the estimation of coefficients of restitution (CORs) based on the material properties of the impacting bodies [55–57]. However, the objective of this work is not to estimate COR values for impacts, but rather to implement classical hypotheses for rigid body collision to model energy dissipation. The efficacy of these hypotheses lies in their ability to represent physically consistent behavior. For example, it has been established that Newton's COR may lead to energy gains during impacts and thereby yield energetically inconsistent simulation results [18, 19]. Poisson's COR yields energetically consistent solutions but was formulated as a mathematical convenience to allow resolution of the post-impact velocities [29]. Stronge's energetic coefficient of restitution (ECOR) stems from work in [30, 31], and incorporates work-energy theory to yield energetically consistent results for rigid body impact modeling [2, 22, 33]. In this work, the application of the ECOR is extended to model the *global* dissipation of energy for multiple point impact problems, similar to the breakthrough works in [26, 52], as opposed to defining local ECORs for each impact point as in [28, 53, 54].

A rigid body model provides a simplified or coarse analysis of a collision. Thus the goal in this work is to determine whether the proposed framework can capture realistic behavior after in response to a collision. It is possible to use more detailed models that include deformations and other surface phenomena to obtain a prediction of a system's post-impact behavior based on material properties [55,57,91]. The remarkable thing in this work is that such a simplified model can capture system behavior to the level of accuracy that will be shown later. The current state of this work provides a tool for analyzing energy losses in a recorded collision. This is similar to several current works which use experimental data to determine the CORs for different types of collisions [19,92].

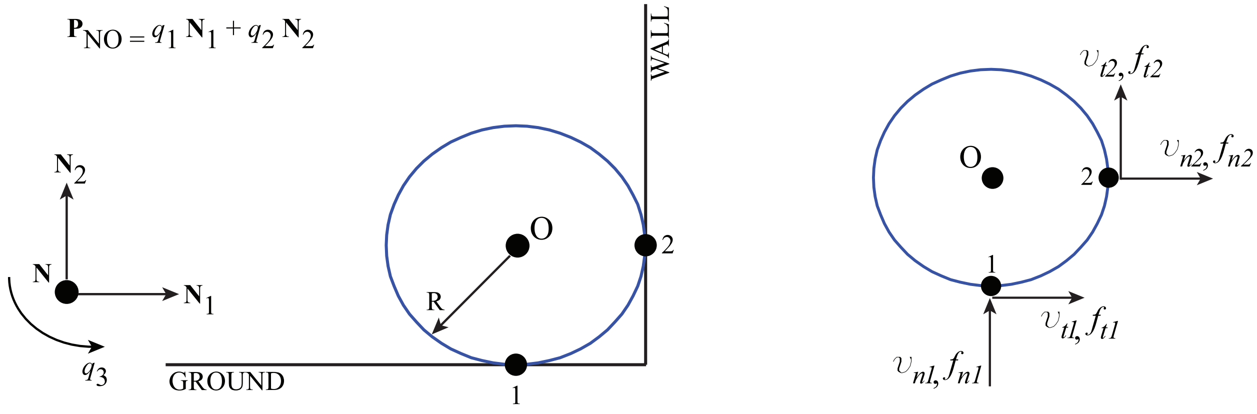

(a) (b)

Figure 3.1: (a) Planar model of the ball example, (b) velocities and forces at impact points 1 (ground) and 2 (wall).

This work presents an analytical framework for the treatment of simultaneous, multi-point impact problems in the presence of friction. Djerassi developed an analytic approach, similar to the present work, for analyzing single point planar impact problems [2]. Extending a similar analysis to multiple point impact problems results in indeterminacy, as the number of impact forces exceeds the number of available equations to solve for them. For example, consider the planar ball of radius R, as shown in Fig. 3.1(a). The position and orientation of this planar ball can be described in terms of three generalized coordinates q_1, q_2, and q_3, which are associated with the three degrees of freedom of the system. When the two different impact points, namely 1 and 2 in Fig. 3.1(a), are considered with friction, there are four unknown impact forces f_{t1}, f_{n1}, f_{t2}, and f_{n2}, as shown in Fig. 3.1(b). The subscripts n_i and t_i for $i = 1, 2$ shown in Fig. 3.1(b) refer to the normal and tangential terms respectively. Note that there are four forces but only three equations of motion to solve for them, thereby making the impact problem indeterminate.

3.1 Impact Modeling

This section presents the analytic framework for impact analysis used in this work. The proposed method treats impacts as discrete events within the transient simulation of the system's equations of motion. During these impact events the time is held fixed, while the impact states evolve in the *impulse-domain*, similar to [21, 33–37]. The relations that govern the evolution of the system states during impact events are dependent on the frictional constraints enforced by the Coulomb friction law. Application of Coulomb friction for the analysis of impacts, inevitably leads to a set of complimentarity conditions which accounts for the discontinuities in the tangential velocities as impact points transition between slipping and sticking. In the case of multi-point impacts, frictional constraints are often insufficient to fully establish the governing relationships. Additional constraints are necessary to determine the contribution of each point toward the net impulse induced on the system during impact. This work proposes the use of rigid-body constraints along with the Coulomb friction law for this purpose. Here the proposed analysis is demonstrated with the help of the example in Fig. 3.1, a rigid body undergoing simultaneous two-point impact. However, the method is generalizable to any planar rigid multibody system and any number of points.

3.1.1 General State Equations during Impact

The configuration of the rigid body system used for this example is defined by a set of generalized coordinates, $\mathbf{q}$. A general form of the governing equations of motion for the system can be expressed as

$$A(\mathbf{q})\ddot{\mathbf{q}} + \mathbf{b}(\dot{\mathbf{q}}, \mathbf{q}) + \mathbf{g}(\mathbf{q}) = \mathbf{\Gamma}(\mathbf{q}) = J^T(\mathbf{q})\mathbf{F} = J^T(\mathbf{q}) \begin{bmatrix} f_{t_1} & f_{n_1} & f_{t_2} & f_{n_2} \end{bmatrix}^T \tag{3.1}$$

where A is the mass matrix for the system. The terms $\mathbf{b}$ and $\mathbf{g}$ define the Coriolis and gravity terms respectively. The generalized active forces are represented by $\mathbf{\Gamma}$ and are related to the impact forces, $\mathbf{F}$, through the *impact Jacobian matrix*, J. The impact Jacobian matrix also forms an important relationship between the velocities of the impact points and the generalized speeds. This dual relationship property of the impact Jacobian matrix will later be used in the application of the rigid-body constraints. Since, the impact event takes place over a small period of time, a definite integration of the equations of motion in Eq. (3.1) over the interval $[t, t+\epsilon]$ yields

$$\int_t^{t+\epsilon} \left(A(\mathbf{q})\ddot{\mathbf{q}} + \mathbf{b}(\dot{\mathbf{q}}, \mathbf{q}) + \mathbf{g}(\mathbf{q})\right) dt = \int_t^{t+\epsilon} J^T(\mathbf{q})\mathbf{F} dt \tag{3.2}$$

where ϵ is the small time period representing the duration of the impact event. This yields,

$$A\left(\dot{\mathbf{q}}(t+\epsilon) - \dot{\mathbf{q}}(t)\right) = J^T\mathbf{p} = J^T \begin{bmatrix} p_{t_1} & p_{n_1} & p_{t_2} & p_{n_2} \end{bmatrix}^T \tag{3.3}$$

where $\mathbf{p}$ is a vector containing all of the impulse parameters. The terms p_{t_i} and p_{n_i} represent the tangential and normal impulse parameters for the i^{th} point where $i = 1, 2$. Based on the assumption that the configuration of the block does not change during an impact event, the Coriolis and gravity terms disappear upon integration over the infinitesimally small time-period, ϵ. Also, A and J, which were defined as functions of the generalized coordinates $\mathbf{q}$ in Eq. (3.1), remain constant during the impact event. The generalized speeds, as a result of Eq. (3.3), can be rewritten as,

$$\dot{\mathbf{q}} = \dot{\mathbf{q}}(0) + A^{-1}J^T\mathbf{p} \tag{3.4}$$

where $\dot{\mathbf{q}}(0)$ and $\dot{\mathbf{q}}$ refer to the pre- and post-impact generalized speeds of the system. Note that in Eq. (3.4), the generalized speeds $\dot{\mathbf{q}}$ are linearly dependent on the impulses $\mathbf{p}$. Therefore, Eq. (3.4) describes the equations of motion for the impact event in the *impulse-domain*, as opposed to Eq. (3.1) which is in *time-domain*. The generalized speeds are expressed in terms of the *operational space* velocities of the impact points to facilitate the proposed analysis. Hence, Eq. (3.4) is pre-multiplied by the impact Jacobian,

$$\boldsymbol{\vartheta} = \begin{bmatrix} v_{t_1} & v_{n_1} & v_{t_2} & v_{n_2} \end{bmatrix}^T = \boldsymbol{\vartheta}(0) + JA^{-1}J^T\mathbf{p} \tag{3.5}$$

where $\boldsymbol{\vartheta}(0)$ and $\boldsymbol{\vartheta}$ stand for the pre- and post-impact velocities of the impact points. The tangential and normal velocities of the impact points are represented by v_{t_i} and v_{n_i} respectively, where $i = 1, 2$.

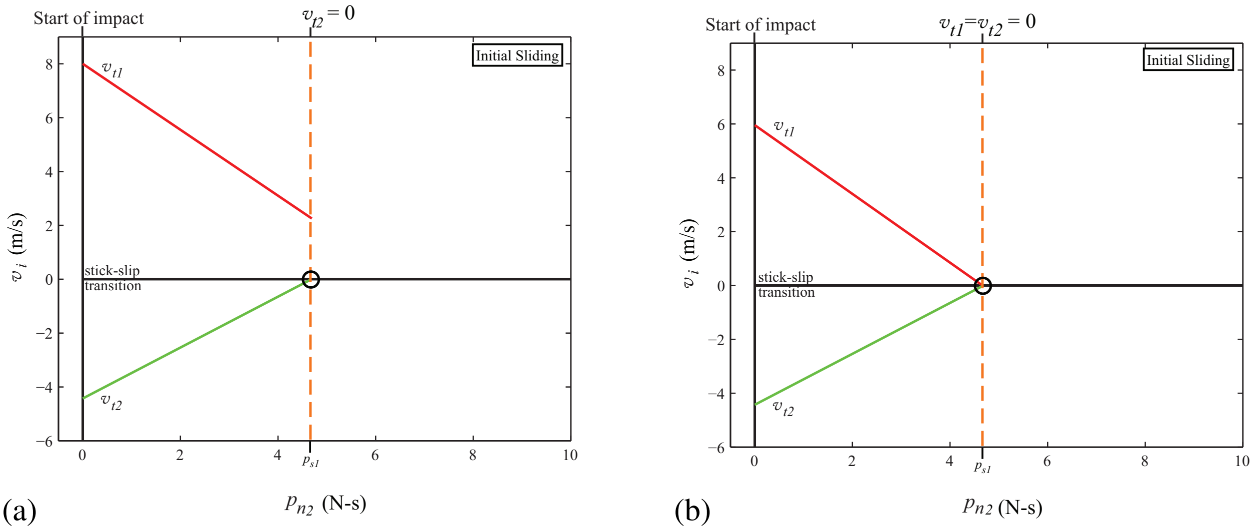

Figure 3.2: Typical friction behaviors after the stick-slip transition if (a) one point, or (b) two points come to rest.

During an impact events, various contact points in a rigid-body system may experience what is known as the *Stick-Slip Phenomenon*. The stick-slip phenomenon is characterized by discontinuous changes in the velocities of the contact points. An idealized version

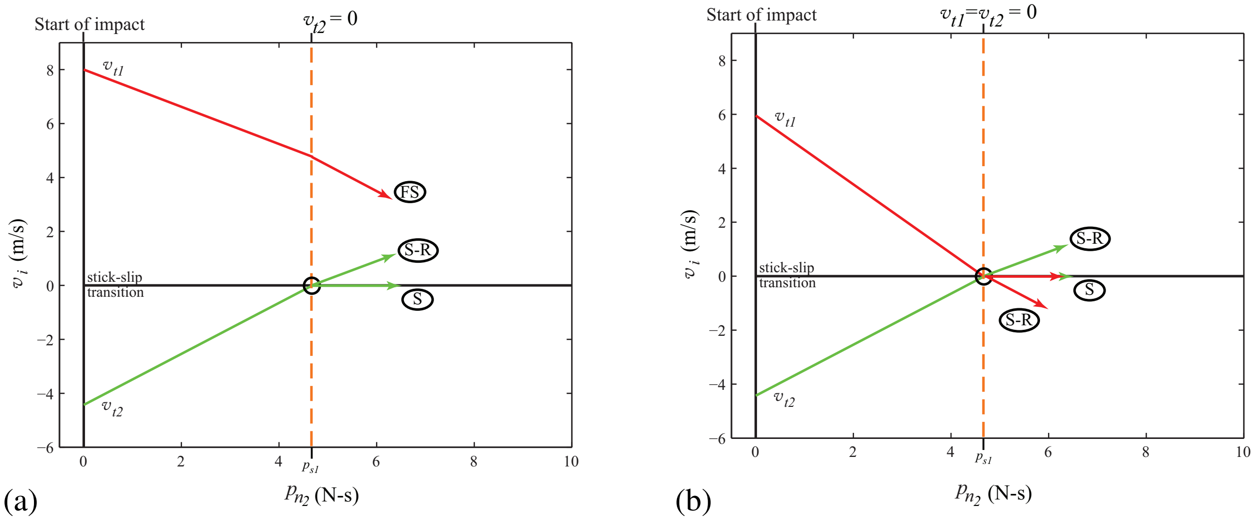

Figure 3.3: Typical friction behaviors after the stick-slip transition if (a) one point, or (b) two points come to rest.

of this behavior can be modeled using the Coulomb friction law [2, 21, 32]. Coulomb friction models introduce discontinuities in the velocities of the contact points that closely resemble reality. These discontinuities occur as a result of points transitioning between sticking and slipping.

In Eq. (3.5), $\mathbf{p} = \begin{bmatrix} p_{t_1} & p_{n_1} & p_{t_2} & p_{n_2} \end{bmatrix}^T$ represents all of the impulses at different contact points. The impulses in $\mathbf{p}$ can be resolved in terms of one arbitrarily chosen independent impulse parameter,

$$\mathbf{p} = \mathbf{C} p_{n_2} \qquad \text{where} \qquad p_{n_2} \geq 0 \tag{3.6}$$

Here p_{n_2} is the arbitrarily chosen impulse parameter. The coefficient $\mathbf{C}$, which depends upon the slip-state of the various contact points, is derived using frictional and rigid-body constraints. Sec. 3.2 presents the details of this derivation. Therefore, using Eq. (3.5) and Eq. (3.6), the contact point velocities $\boldsymbol{\vartheta}$ during an impact event may be expressed as,

$$\boldsymbol{\vartheta} = \boldsymbol{\vartheta}(0) + J A^{-1} J^T \mathbf{C} p_{n_2} \tag{3.7}$$

where $p_{n_2} \geq 0$. Eq. (3.7) shows that the contact velocities $\boldsymbol{\vartheta}$ evolve linearly as a function of the independent impulse parameter p_{n_2}. However this linear relationship is disrupted when one (or more) contact points experience the stick-slip transition.

Consider the case of an impact event with non-zero pre-impact velocities. In such an impact the first stick-slip transition takes place when $v_{t_i} = 0$. Fig. 3.2 shows the occurrence of stick-slip transitions when the tangential velocities of one (or more) contact points becomes equal to zero. The stick-slip transition shown in Fig. 3.2 marks the end of a phase in which the contact points undergo an initial sliding. After the stick-slip transition, contact points may enter *sticking* (S) or *slip-reversal* or *slip-resumption* (S-R), as shown in Fig. 3.3. Slip resumption occurs when the tangential speed of the contact point equals zero momentarily and then the point resumes slipping in the same direction. Therefore the frictional constraints on the impulse parameters change depending on the situation following a stick-slip transition. Hence the coefficient $\mathbf{C}$ in Eq. (3.7) is updated whenever a contact point enters the stick-slip transition, its tangential velocity becomes equal to zero.

Let the velocities at the various stick-slip transitions be defined as $\boldsymbol{\vartheta}_k$, where the subscript $k = 0, ..., N$ refer to the stick-slip transitions, including the pre-impact velocities $\boldsymbol{\vartheta}_0 = \boldsymbol{\vartheta}(0)$. The total number of stick-slip transitions N cannot be determined a priori, it depends upon the number of times the tangential velocities of one (or more) contact point reaches zero. The value of the independent impulse parameter, p_{n_2} at kth stick-slip transition will be referred to as p_{sk}. Fig. 3.4 shows an example of velocity evolution through different sticking and slipping conditions. Based on the definition of the velocities at different stick-slip transitions k, Eq. (3.7) may be rewritten as,

$$\boldsymbol{\vartheta} = \boldsymbol{\vartheta}_k + JA^{-1}J^T\mathbf{C}(p_{n_2} - p_{sk}) \qquad \text{where} \qquad p_{n_2} \geq 0 \tag{3.8}$$

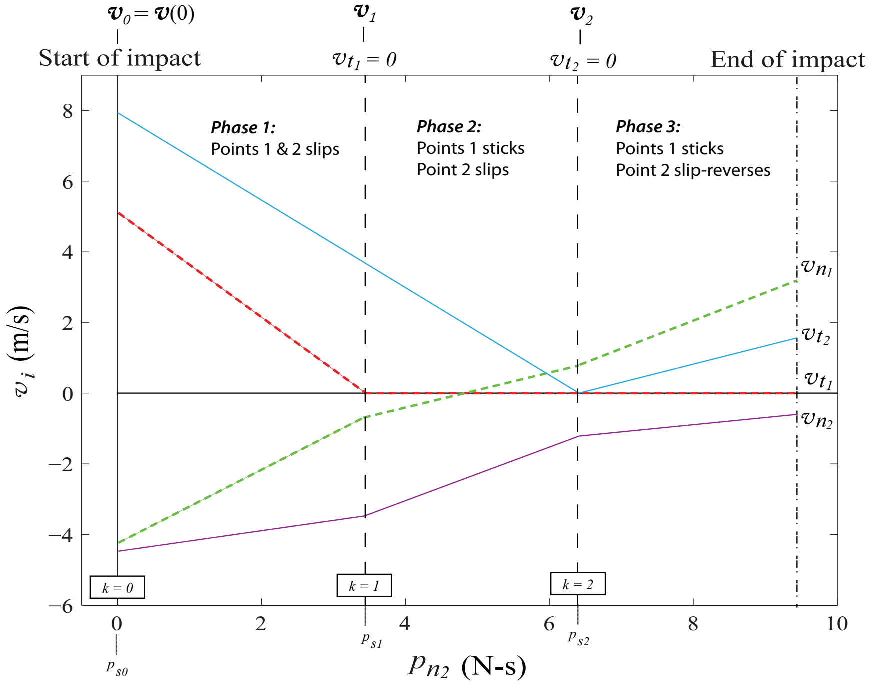

Figure 3.4: Example of velocity evolution plot during impact event.

The values for the independent impulse parameters, p_{sk} at the different stick-slip transitions $k = 1, ..., N$ can be easily determined using the tangential components of $\boldsymbol{\vartheta}_{k-1}$ and there corresponding slope from $JA^{-1}J^T\mathbf{C}$.

Equation (3.8) essentially expresses the post-impact velocities of the contact points as a function of one independent impulse parameter, p_{n_2}. The relationship between post-impact velocities and the independent impulse parameter is linear. However at stick-slip transitions the frictional force constraints change and therefore the term $\mathbf{C}$ which is associated with the frictional and rigid body constraints is updated. The remaining portion of this section, which deals with the termination of the impact event or in other words determining the impulse p_{n_2} at the end of the impact event, is presented with the assumption that $\mathbf{C}$ is known in all situations.

3.1.2 Energetic Termination of Impact Events

The criterion for the termination of impact events is based on *Stronge's Hypothesis* on rigid impacts [22, 32]. Stronge's hypothesis places an energetic constraint on the evolution of the contact point velocities as a function of the independent impulse parameter as shown in Eq. (3.8). The work done during an impact event is given by the difference in kinetic energy between the pre- and post-impact states of the rigid body system, which is given by,

$$\begin{aligned} W &= \frac{1}{2}\dot{\mathbf{q}}^T A\dot{\mathbf{q}} - \frac{1}{2}\dot{\mathbf{q}}^T(0)A\dot{\mathbf{q}}(0) && (3.9)\\ &= \frac{1}{2}\boldsymbol{\vartheta}^T(J^+)^T A(J^+)\boldsymbol{\vartheta} - \frac{1}{2}\boldsymbol{\vartheta}^T(0)(J^+)^T A(J^+)\boldsymbol{\vartheta}(0) && (3.10)\end{aligned}$$

where J^+ is the pseudo-inverse of the impact Jacobian matrix J. Since, the pre- and post-impact generalized speeds or contact point velocities depend upon the independent impulse p_{n_2}, the work itself becomes a function of the independent impulse parameter. The net work done during an impact event can be decoupled between work done by normal impulses and work done by tangential impulses. The energetic constraint based on Stronge's hypothesis, is placed only on the work due to the normal components. The normal work is given by,

$$\begin{aligned} W_n = &\left\{{\boldsymbol{\vartheta}_t}^T(J_t^+)^T A(J_n^+)\boldsymbol{\vartheta}_n - {\boldsymbol{\vartheta}_t}^T(0)(J_t^+)^T A(J_n^+)\boldsymbol{\vartheta}_n(0)\right\}\\ &+\frac{1}{2}\left\{{\boldsymbol{\vartheta}_n}^T(J_n^+)^T A(J_n^+)\boldsymbol{\vartheta}_n - {\boldsymbol{\vartheta}_n}^T(0)(J_n^+)^T A(J_n^+)\boldsymbol{\vartheta}_n(0)\right\} \qquad (3.11)\end{aligned}$$

where $\boldsymbol{\vartheta}_t$ and $\boldsymbol{\vartheta}_n$ are the tangential and normal velocities of the contact point, while J_t and J_n are their corresponding Jacobian matrices. The definition of the normal work, and therefore the ECOR, is similar to that in [52]. Note that $\boldsymbol{\vartheta}_t$ and $\boldsymbol{\vartheta}_n$ are linearly related to p_{n_2} within any phase. Therefore, based on Eq.(3.11) W_n would be a quadratic function on p_{n_2} with constant coefficients for each stick-slip phase. However, the constant coefficients of this quadratic function must be updated at every stick-slip transition, because they depend upon the vector $\mathbf{C}$ as defined in Eq. (3.6). Figure 3.5 shows an example plot of normal work W_n as a function of p_{n_2}. As expected, the quadratic relationship between the normal work and the independent impulse parameter yields a parabolic trend in the plot. The shifts shown in Fig. 3.5 are a result of the stick-slip transition.

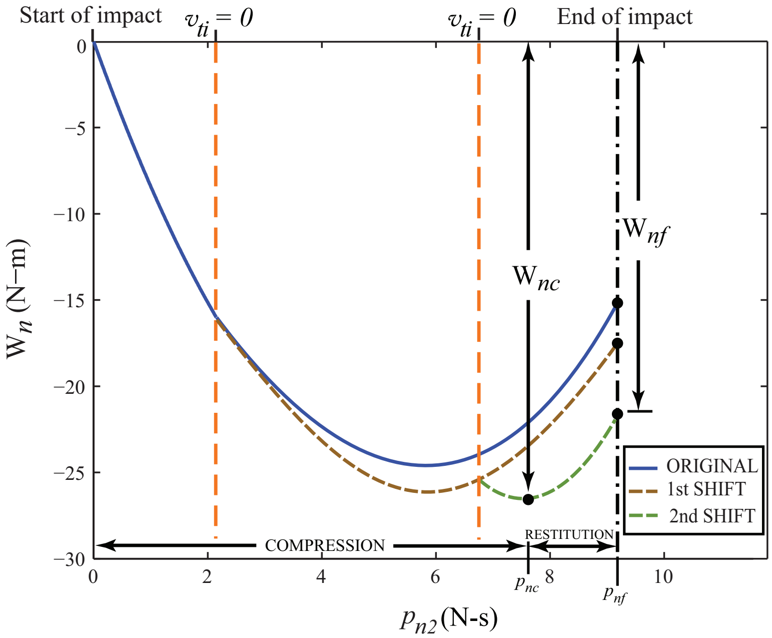

Figure 3.5: Example plot of the normal work for an impact event showing the shifts that occur from the stick-slip transition.

The normal work written as a function of p_{n_2} is given by,

$$W_n(p_{n_2}) = W_{nk} + a(p_{n_2} - p_{sk})^2 + b\,(p_{n_2} - p_{sk}) \qquad (3.12)$$

where a and b are the constant coefficients that can be found by substituting Eq. (3.8) into Eq. (3.11). These constant coefficients define the parabolic curve for normal work for a given phase following stick-slip transition k. The terms a and b are dependent upon $\mathbf{C}$, but are independent of the initial velocities $\boldsymbol{\vartheta}(0)$. The term W_{nk} is the normal work at stick-slip transitions $k = 0, .., N$, such that $W_{n0} = 0$.

According to *Stronge's Hypothesis*, the energy change during an impact takes place over two consecutive energetic phases: a compression phase followed by a restitution phase. As shown in Fig. 3.5, compression takes place over the interval of p_{n_2} when the normal work is generally decreasing. The end of the compression phase is marked by the minimum normal work W_{nc} in Fig. 3.5, where the corresponding value for the independent impulse parameter is p_{nc}. The normal work at the end of the compression phase W_{nc} is given by,

$$W_{nc} = \min W_n(p_{n_2}) \tag{3.13}$$

Note that in Eq. (3.13) the value of W_{nc} can be found analytically.

The energetic phase following the end of compression is the restitution. The restitution phase ends when the impact event terminates. The value of normal work and the independent impulse parameter at this point are given by W_{nf} and p_{nf}. The terminal normal work W_{nf} is related to the normal work at the end of the compression phase W_{nc} as,

$$W_{nf} = (1 - e_*^2) W_{nc} \tag{3.14}$$

where $e_* \in [-1, 1]$ is defined as the *Global Energetic Coefficient of Restitution* which accounts for the amount of energy dissipated during an impact event. Using Eq. (3.12) it can be shown that *Stronge's model* in Eq. (3.14) is equivalent to *Poisson's model* for planar impact problems. The *Poisson's model* for impact is given by,

$$p_{nf} = (1 + e_*) p_{nc} \tag{3.15}$$

The global ECOR e_*, is similar to the traditional definitions of ECOR in the way that it describes an energetic relationship between compression and restitution for a single contact point. However due to the application of rigid-body constraints in this work, e_* assumes a broader role by providing a system-level energetic constraint during impacts, such that it eliminates the need for defining local ECORs at different contact points. Unlike traditional ECORs which exist within the range $\in [0, 1]$, the global ECOR can take both positive and negative values as, $e_* \in [-1, 1]$. The global ECOR e_* is necessarily positive for single point impact events, but it may assume both positive and negative values for simultaneous multi-point impact analysis. Here $e_* < 0$ implies that the impact event terminates before the end of compression phase. It is evident from Eq. (3.14) that the net energy loss during an impact cannot be altered with a sign change of $e*$. However a sign change of e_* affects the amount of impulse experienced at the contact points. When an ECOR is chosen such that $e_* < 0$, the post-impact velocities in the normal direction of all contact-points are not guaranteed to be positive. This leads to a successive impact event involving the points with negative post-impact velocities at the end of the first impact event. Thus, in a series of successive impact events the final impact event must have a positive value of e_*. Some of the results shown in Sec. 4 demonstrate the usefulness of $e_* < 0$ values for replicating post-impact behavior.

3.2 Stick-Slip Analysis during Impact Events using Coulomb friction and Rigid Body Constraints

Rigid bodies undergoing impact in the presence of dry friction typically exhibit a slipping (sliding) and halting (sticking) behavior. In the literature, this behavior is often represented mathematically as a set of complementarity conditions that establish the relations between friction and contact forces [27]. Classical Coulomb friction defines the conditions for stick-slip in terms of tangential velocities and accelerations,

$$\begin{cases} \boldsymbol{\vartheta}_{ti} = \mathbf{0} \text{ and } \dot{\boldsymbol{\vartheta}}_{ti} = \mathbf{0} & \text{then} \quad \|\mathbf{f}_{ti}\| \leq \mu_s \left| f_{ni} \right| \text{ sticking} \\ \boldsymbol{\vartheta}_{ti} = \mathbf{0} \text{ and } \dot{\boldsymbol{\vartheta}}_{ti} \neq \mathbf{0} & \text{then} \quad \|\mathbf{f}_{ti}\| = \mu_s \left| f_{ni} \right| \text{ stick-slip transition} \\ \boldsymbol{\vartheta}_{ti} \neq \mathbf{0} & \text{then} \quad \|\mathbf{f}_{ti}\| = \mu_d \left| f_{n_i} \right| \text{ slipping} \end{cases} \tag{3.16}$$

where μ_s and μ_d are the static and dynamic coefficients of friction [27].

The relations in Eq. (3.16) state the conditions for sticking, the stick-slip transition and slipping respectively. The conditions in Eq. (3.16) capture the discontinuities in frictional forces during contact or impact (assuming $\mu_s \neq \mu_d$). These discontinuities lead to an abrupt transition between sticking and slipping, also referred to as *impending motion*. Fig. 3.3 shows the discontinuities in the contact point velocities caused due to stick-slip transitions.

Equations (3.16) form the basis for linear complementarity problem (LCP) relevant to optimization-based solutions of contact and impact problems [93]. Complementarity conditions based on moments can also be found in the literature [94, 95]. Certain friction models eliminate the need for complementarity conditions by allowing a continuous stick-slip transition [96, 97]. In this work, a discontinuous friction model based on impulsive forces is used for stick-slip transition, as presented in [23]. The complementarity conditions based on Coulomb friction in Eq. (3.16) are relevant for the more general 3D contact problems, where the tangential components of velocities are resolved in terms of two basis directions that define a contact plane. This work is only concerned with planar contact and impact problems, such that the tangential components are constrained along a single direction. Also, as was discussed in Sec. 3.1, an impact event can consist of a number of different phases, during which the changes in the velocities and impulses are characterized by the slip-state at different contact points. The complementarity conditions used in this work to describe the stick-slip states are,

$$\begin{cases} v_{t_i}(p_{n_2}) = 0 \text{ and } \dot{v}_{t_i}(p_{n_2}) = 0 & \text{then} \quad p_{t_i} \leq \mu_s p_{n_i} \;\; \text{sticking} \\ v_{t_i}(p_{n_2}) = 0 \text{ and } \dot{v}_{t_i}(p_{n_2}) \neq 0 & \text{then} \quad p_{t_i} = \mu_s p_{n_i} \;\; \text{stick-slip transition} \\ v_{t_i}(p_{n_2}) \neq 0 & \text{then} \quad p_{t_i} = \mu_d p_{n_i} \;\; \text{slipping} \end{cases} \tag{3.17}$$

where the subscript i refers to the contact point and k represents a point in the impulse domain when an impact point comes to rest, having no tangential velocity. The velocity-impulse relation shown in Eq. (3.8), depends upon the vector $\mathbf{C}$. This section shows how $\mathbf{C}$ is derived using the rigid body constraints and Coulomb friction as shown in Eq. (3.17).

3.2.1 Frictional Constraints for Slipping

When a contact point i slips during an impact event, the tangential impulse on the point is related to the normal impulse as,

$$p_{t_i} = -x_i \mu_i p_{n_i} \tag{3.18}$$

where x_i is a multi-valued signum function such that $x_i \in \{-1, 1\}$, which represents the direction of the tangential pre-impact velocity of the point v_{t_i}. The term x_i may be also defined as $x_i = v_{t_i}/||v_{t_i}||$. Here the coefficient of the point i is selected as $\mu_i = \mu_s$. The frictional constraint for slipping can be rewritten as,

$$p_{t_i} + x_i \mu_i p_{n_i} = \mathbf{u}_i \mathbf{p} = 0 \tag{3.19}$$

where the row vector $\mathbf{u}_i$ contains coefficients from frictional constraint equation for the ith point.

3.2.2 Frictional Constraints for Sticking

When a point i sticks, both the tangential velocity and acceleration of the point remain equal to zero. In Eq. (3.5) the velocities of all the contact points are related to their respective impulses by,

$$M = JA^{-1}J^T = \begin{bmatrix} \mathbf{m}_{t_1} \\ \mathbf{m}_{n_1} \\ \mathbf{m}_{t_2} \\ \mathbf{m}_{n_2} \end{bmatrix} \tag{3.20}$$

where $\mathbf{m}_{t_i}$ and $\mathbf{m}_{n_i}$ are the rows of M corresponding to the tangential and normal components, respectively. Hence constraining the tangential velocity of point i using Eq. (3.5) yields.

$$v_{t_i} = 0 = \mathbf{m}_{t_i} \mathbf{p} \tag{3.21}$$

where the row vector $\mathbf{m}_{t_i}$ gives the coefficients for $\mathbf{p}$ for the point to remain in sticking. Therefore when the point i sticks the frictional constraint is replaced by,

$$\mathbf{u}_i\mathbf{p} = \mathbf{m}_{t_i}\mathbf{p} = 0 \tag{3.22}$$

3.2.3 Rigid-Body Constraints

The frictional constraints based on the Coulomb friction law can only resolve the tangential impulses in terms of the normal impulses of the contact point. In case of simultaneous muli-point impact analysis, constraint relationships must be established to resolve all of the unknown impulse parameters in terms of one independent impulse parameter. Here such constraint relationships are derived based on the assumption of rigidity. These rigid body constraints were originally used to develop the equations of motion in Eq. (3.1). To remain consistent with the original equations, it is necessary to apply these constraints in the impact analysis as well.

Consider for the two-point impact example, $\mathbf{v}_1 = \begin{bmatrix} v_{t_1} & v_{n_1} \end{bmatrix}^T$ and $\mathbf{v}_2 = \begin{bmatrix} v_{t_2} & v_{n_2} \end{bmatrix}^T$ are the velocities of points 1 and 2. The direction cosines of the line defined by the two contact points is given by,

$$\hat{\boldsymbol{\eta}} = \frac{(\mathbf{P}_{O1} - \mathbf{P}_{O2})}{||\mathbf{P}_{O1} - \mathbf{P}_{O2}||} = \begin{bmatrix} \eta_x & \eta_y \end{bmatrix}^T$$

where $\mathbf{P}_{Oi}$ is the position of the contact point $i = 1, 2$ with respect to the body's center of mass. The rigid body assumption restricts any relative motion between the contact points during impact. Therefore the velocities of the two contact points are constrained along $\hat{\boldsymbol{\eta}}$ as,

$$(\mathbf{v}_1 - \mathbf{v}_2) \cdot \hat{\boldsymbol{\eta}} = 0 \tag{3.23}$$

Upon expansion,

$$(v_{t_1} - v_{t_2})\eta_x + (v_{t_1} - v_{t_2})\eta_y = \underbrace{\begin{bmatrix} \eta_x & \eta_y & -\eta_x & -\eta_y \end{bmatrix}}_{\mathbf{w}} \begin{bmatrix} v_{t_1} \\ v_{n_1} \\ v_{t_2} \\ v_{n_2} \end{bmatrix} = \mathbf{w}\boldsymbol{\vartheta} = 0 \qquad (3.24)$$

Equation (3.24) gives the constraint equations that relate the velocities of the two contact points undergoing impact. The velocity projection method in Appendix A shows that the rigid body constraints that are applicable at the velocity level can also be enforced at the force/impulse level. Hence, the rigid-body constraint in Eq. (3.24) can be expressed in terms of impulses as,

$$\mathbf{wp} = \begin{bmatrix} \eta_x & \eta_y & -\eta_x & -\eta_y \end{bmatrix} \begin{bmatrix} p_{t_1} \\ p_{n_1} \\ p_{t_2} \\ p_{n_2} \end{bmatrix} = 0 \qquad (3.25)$$

The constraint in Eq. (3.25) gives the relationship between the impulse parameters of the two points used in this example. If the number of contact points is increased, additional constraint equations similar to Eq. (3.25) would be necessary to resolve all of the associated impulse parameters in terms of one independent parameter. The remainder of this section is dedicated to the solution method used in this work to resolve the frictional and rigid-body constraints.

3.2.4 Solution to Friction and Rigid Body Constraints and Analysis of Slip-Reversal

Here the frictional constraints due to sticking and slipping as shown in Eq. (3.22) and Eq. (3.19) respectively, and the rigid-body constraints in Eq. (3.25) are used to resolve all of the impulse parameters in terms of a single independent impulse parameter. Also the conditions for slip-reversal are shown and analyzed here.

The frictional and rigid-body constraints from Eq. (3.19), Eq. (3.22) and Eq. (3.25) can be rewritten as,

$$H\mathbf{p} = \mathbf{0} \qquad \text{where} \qquad H = \begin{bmatrix} \mathbf{w} \\ \mathbf{u}_1 \\ \mathbf{u}_2 \end{bmatrix} \tag{3.26}$$

where $\mathbf{u}_i$ for points $i = 1, 2$ are the coefficients of the frictional constraint equation. Depending upon whether the point i sticks or slips, the row vector $\mathbf{u}_i$ is chosen from the relations Eq. (3.19) or Eq. (3.22). The matrix $H \in \mathbb{R}^{3\times 4}$ is rank deficient by one. This rank deficiency will persist if the number of contact points are increased. For an n-point impact, the number of frictional constraints would be $2n$, the number of rigid-body constraint equations would be $2n - 1$, and the number of impulse parameters would be $4n$. Thus, H would be rank deficient by one, for any arbitrary number of contact points n.

The linearly dependent and independent columns of H can be separated as,

$$H = \begin{bmatrix} H_s & H_r \end{bmatrix} \tag{3.27}$$

where $H_s \in \mathbb{R}^{3\times 3}$ are the linearly independent columns and $H_r \in \mathbb{R}^{3\times 1}$ is the single dependent column. Here H_r is selected as the last column of H, which is consistent with the choice of the independent impulse parameter p_{n_2} Since H is rank deficient by one and H_r is a column vector, H_s is full rank and invertible. Thus, the impulse parameters for all of the points can be computed as,

$$\mathbf{p} = \begin{bmatrix} -{H_s}^{-1} H_r \\ 1 \end{bmatrix} p_{n_2} = \mathbf{C} p_{n_2} = \begin{bmatrix} c_1 \\ c_2 \\ c_3 \\ 1 \end{bmatrix} p_{n_2} \tag{3.28}$$

where $\mathbf{C}$ relates all of the impulse parameters to one independent impulse. The partitioning carried out in Eq. (3.27) to obtain H_s and H_r, can be performed using QR, SVD or LU decomposition methods. This work uses the QR decomposition method.

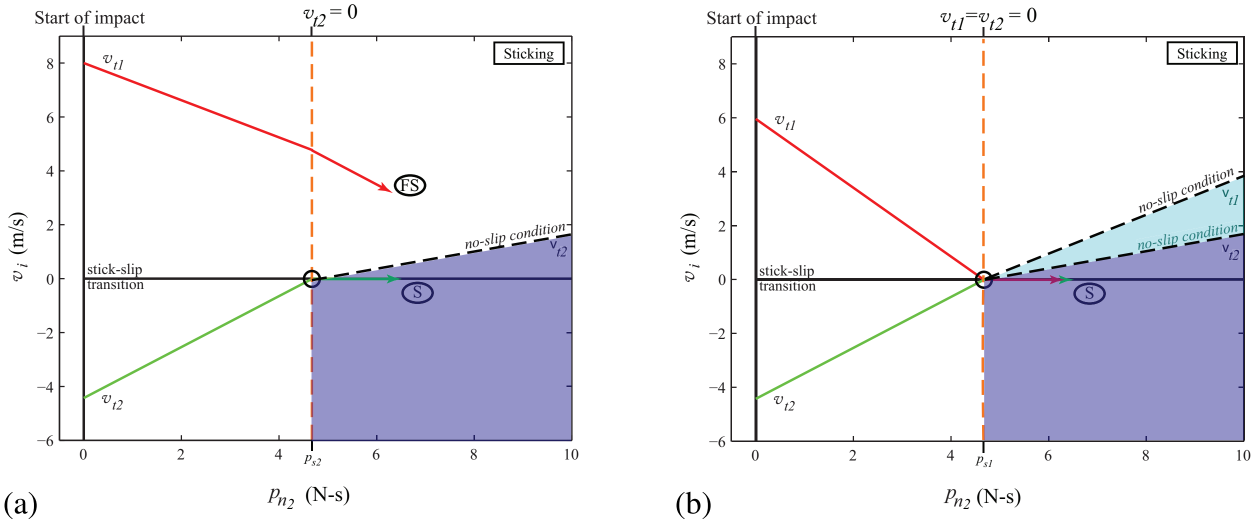

Figure 3.6: The no-slip condition defined by the value of μ_s for (a) one point and (b) two point stick-slip transition

The vector $\mathbf{C}$ can be used in Eq. (3.8), and is recomputed and updated for every stick-slip transition k. However the conditions for slip-reversal must be checked before using $\mathbf{C}$ in Eq. (3.8), if the points are stationary in the tangential direction. If $v_{t_1} = 0$ and/or $v_{t_2} = 0$ at the beginning of a stick-slip phase then according to the complimentarity conditions in Eq. (3.17), for the points to stick the impulses must satisfy: $p_{t_i} \leq \mu_s p_{n_i}$, where μ_s is the coefficient of static (limiting) friction and the subscript i refers to the points in sticking. The constraint used for sticking friction in Eq. (3.22), enforces a *critical coefficient of friction*, $\bar{\mu}_i$ for the equality relation of the Coulomb friction law $p_{t_i} = -x_i \bar{\mu}_i p_{n_i}$, such that $v_{t_i} = 0$.

Hence based on Eq. (3.28), the *critical coefficients of friction* for the two contact points are given by

$$\bar{\mu}_1 = -\frac{c_1}{x_1 c_2} \qquad \bar{\mu}_2 = -\frac{c_3}{x_2} \tag{3.29}$$

Therefore the no-slip condition for the contact points is given by,

$$\bar{\mu}_i \leq \mu_s \tag{3.30}$$

Any contact point i, with tangential velocity $v_{t_i} = 0$ sticks if the no-slip condition in Eq. (3.30) is satisfied. The no-slip condition for any given value of μ_s can be plotted on a velocity-impulse plot, as denoted by the shaded regions in Fig. 3.6. Violation of Eq. (3.30) leads to slip-reversal which causes the slip direction to change such that the coefficient of friction becomes $\bar{\mu}_i = -\mu_d$.

When a point i slip-reverses, the vector $\mathbf{C}$ is recomputed by resetting $\mathbf{u}_i$ based on the equality constraint of Coulomb friction law parameterized by a negative coefficient of friction $\bar{\mu}_i = -\mu_i$,

$$p_{t_i} - x_i \mu_i p_{n_i} = \mathbf{u}_i \mathbf{p} = 0 \tag{3.31}$$

3.3 Transition to Contact

The discussion presented in Sec. 3.1 and Sec. 3.2, is primarily relevant to *impulse-domain* analysis of impact events, during which the time remains fixed. The *impulse-domain* analysis takes place after the *time-domain* integration of the equations of motion is stopped upon impact detection. This method of simulation is known as *event-based* or *hybrid dynamic simulation approach*, where standard numerical integration techniques are used to simulate the time-dependent equations of motions between various impact events. Impulse-domain analysis with event-based simulation approach is appropriate for rigid body impacts which occur over infinitesimally small time-periods. However, one of the difficulties encountered with the event-based simulation approach is the accumulation of events due to high frequency *chattering* behavior for low-speed contacts. In the hybrid dynamic simulation of rigid bodies, chattering takes place when a rigid body touches a contact surface but does not rebound, which leads to a successive series of impact events that, in effect, stop the *time-domain* simulation. This chattering has been studied extensively in the literature [68–71].

Here the chattering behavior is caused by the non-smooth dynamic model used for the treatment of impact events during a transient simulation. The impulse-domain analysis presented earlier is inadequate for handling no-rebound contact. In this work, a no-rebound contact is represented by smooth dynamics where non-penetrability conditions are enforced. Frictional constraints are also enforced during the contact phase.

Constraint enforcement for multibody dynamics can be performed by either *redundant coordinate* techniques and *coordinate reduction/constraint-embedding* techniques [72]. Techniques based on *redundant coordinate* sets solve the equations of motion and the algebraic constraints simultaneously, in a differential-algebraic equation (DAE) framework. DAE solvers typically satisfy algebraic constraints and curb what is known as "drift-off effects" using several methods. One approach is Baumgarte's stabilization method [72–76], which essentially treats the contact constraint forces as a PD feedback control input computed using the constraint violations and their derivatives. Other approaches include a penalty based formulations, such as the staggered stabilization technique [73, 77], and the augmented Lagrangian method [73, 78]. Coordinate reduction methods on the other hand, reformulate the equations of motion based on a minimal set of independent generalized coordinates. These methods can be performed offline or online while the simulation is running. Online constraint embedding is based on the coordinate-partitioning techniques originally proposed in [79] that make use of the constraint equations to resolve dependent coordinates in terms of independent generalized coordinates using the SVD [73, 80, 81], LU [81] or QR [82–85] decomposition methods. The proposed analysis uses a QR based constraint embedding technique to enforce non-penetrability and frictional constraints during the no-rebound contact phase.

This work uses a simple criteria for distinguishing between contacts, impacts and separation:

$$\begin{cases} \text{if} \quad |v_{ni}(t)| \leq \epsilon_v \quad \text{and} \quad \dot{v}_{ni}(t) < 0 & \text{Contact (Constraint Embedding)} \\ \text{if} \quad v_{ni}(t) < -\epsilon_v \quad \text{and} \quad \dot{v}_{ni}(t) < 0 & \text{Impact (Impulse-Domain Analysis)} \\ \text{if} \quad v_{ni}(t) > \epsilon_v \quad \text{or} \quad \dot{v}_{ni}(t) > 0 & \text{Separation (Floating-Base EOM)} \end{cases} \tag{3.32}$$

where ϵ_v is a small threshold value selected to determine if the contact points have near-zero normal velocity. During contact, the non-penetrability constraint always needs to be satisfied. However, similar to the impulse-domain analysis, the frictional constraints can switch during contact depending upon whether a contact point sticks or slips. The proposed method first embeds non-penetrability and sticking friction constraints. Then a method based on the rigid body constraints is used to compute the reaction forces. The reaction forces are checked using the friction cone defined by Coulomb's law to identify contact points that are slipping. Finally sliding frictional constraints are enforced for the relevant points.

3.3.1 Reaction Forces due to Contact Constraints Assuming Sticking

Initially, during a no-rebound contact phase, all of the points satisfying the contact criteria in Eq. (3.32) are assumed to stick. Therefore both the tangential and the normal components are constrained to be equal to zero. Consider the velocities and accelerations of the contact points that satisfy the contact constraint in Eq. (3.32)

$$\mathbf{0} \;=\; \boldsymbol{\vartheta}_c \;=\; \begin{bmatrix} v_{t_1} \\ v_{n_1} \\ \vdots \end{bmatrix} \;=\; J_c\,\dot{\mathbf{q}} \tag{3.33}$$

and,

$$\mathbf{0} \;=\; \dot{\boldsymbol{\vartheta}}_c \;=\; \begin{bmatrix} \dot{v}_{t_1} \\ \dot{v}_{n_1} \\ \vdots \end{bmatrix} \;=\; J_c\,\ddot{\mathbf{q}} \;+\; \dot{J}_c\,\dot{\mathbf{q}} \tag{3.34}$$

where J_c is the Jacobian matrix associated with $\boldsymbol{\vartheta}_c$. Substituting the expression for $\ddot{\mathbf{q}}$ from Eq.(3.1),

$$\mathbf{0} \;=\; \dot{\boldsymbol{\vartheta}}_c \;=\; J_c\,A^{-1}J_c^{\,T}\mathbf{F} \;-\; J_cA^{-1}\left(\mathbf{b}(\mathbf{q},\dot{\mathbf{q}}) \;+\; \mathbf{g}(\mathbf{q})\right) \;+\; \dot{J}_c\,\dot{\mathbf{q}} \tag{3.35}$$

Similar to the impulse domain analysis, the contact forces $\mathbf{F}$ are going to be constrained by the rigid body constraints and frictional constraints. Hence the contact constraint forces may be resolved as,

$$\mathbf{F} \;=\; \mathbf{C}\,F_r \tag{3.36}$$

where F_r is an independent force parameter. The vector $\mathbf{C}$ is recomputed for the contact condition, using the method shown in Sec. 3.2. Now substituting Eq. (3.36) into Eq.(3.35) yields,

$$\bar{\mathbf{c}}\,F_r \;=\; J_c\,A^{-1}J_c^{\,T}\mathbf{C}\,F_r \;=\; J_cA^{-1}\left(\mathbf{b}(\mathbf{q},\dot{\mathbf{q}}) \;+\; \mathbf{g}(\mathbf{q})\right) \;-\; \dot{J}_c\,\dot{\mathbf{q}} \tag{3.37}$$

Hence, the full set of reaction forces $\mathbf{F}$ would be given by,

$$\mathbf{F} \;=\; \mathbf{C}\,F_r \;=\; \mathbf{C}\,\frac{\bar{\mathbf{c}}^T}{\bar{\mathbf{c}}^T\bar{\mathbf{c}}}\,\left(J_cA^{-1}\left(\mathbf{b}(\mathbf{q},\dot{\mathbf{q}}) \;+\; \mathbf{g}(\mathbf{q})\right) \;-\; \dot{J}_c\,\dot{\mathbf{q}}\right) \tag{3.38}$$

The reaction forces in $\mathbf{F}$ in Eq. (3.38) are calculated assuming that all of the points are sticking. Now Coulomb's law is used to check whether the contact points stick or slip,

$$|f_{t_i}| \leq \; \mu_s\, f_{n_i} \tag{3.39}$$

where μ_s is the coefficient of static (limiting) friction. A contact point sticks if equation Eq. (3.39) is satisfied, otherwise the point slips. When a contact point slips, the contact-plane tangential velocities have unknown non-zero values. Thus, the velocity and acceleration constraint in Eq. (3.33) and Eq. (3.34) need to be restricted to only the normal components for the slipping points. The constraint for the tangential forces are then given by Coulomb's friction law.

Enforcing the slip and no-slip constraints is accomplished by partitioning the reaction forces as follows:

$$\mathbf{F} = \begin{bmatrix} \mathbf{F}_{slip} \\ \mathbf{F}_{stick} \end{bmatrix} = S_c \begin{bmatrix} \mathbf{F}_{slip_n} \\ \mathbf{F}_{stick} \end{bmatrix} \tag{3.40}$$

where $\mathbf{F}_{slip}$ and $\mathbf{F}_{stick}$ are the forces at the contact points that are slipping and sticking, respectively and $\mathbf{F}_{slip_n}$ are the normal forces at the points i that are slipping,

$$\mathbf{F}_{slip} = \begin{bmatrix} f_{t_1} \\ f_{n_1} \\ \vdots \end{bmatrix} \qquad \mathbf{F}_{slip_n} = \begin{bmatrix} f_{n_1} \\ \vdots \end{bmatrix} \tag{3.41}$$

In Eq. (3.40) the matrix S_c relates the normal forces of the slipping points to the tangential forces using the equality relation of Coulomb friction law,

$$S_c = \left[\begin{array}{c|c} -x_i \mu_i & \\ 1 & 0 \\ \hline 0 & \mathrm{I} \end{array}\right] \tag{3.42}$$

where $x_i = v_{t_i}/||v_{t_i}||$ gives the direction of the contact point, $\mu_i = \mu_d$ is the dynamic coefficient of friction at point i, and I is an identity matrix. Eq. (3.42) shows the matrix S_c as if i refers to a single point. S_c should be suitably adjusted when defining Coulomb friction relations for more than one point.

Using dual property of the Jacobian matrix, the generalized active forces, $\mathbf{\Gamma}$ in Eq. (3.1), are related to the constraint forces as

$$\mathbf{\Gamma} \;=\; J_c^T\,\mathbf{F} \;=\; J_c^T\,S_c \begin{bmatrix} \mathbf{F}_{slip_n} \\ \mathbf{F}_{stick} \end{bmatrix} \tag{3.43}$$

Based on the dual property of the Jacobian matrix, as shown in the Appendix A, the force constraint in Eq. (3.43) may be written as a velocity constraint,

$$\mathbf{0} \;=\; \begin{bmatrix} \boldsymbol{\vartheta}_{stick} \\ \boldsymbol{\vartheta}_{slip_n} \end{bmatrix} \;=\; S_c^T\,J_c\,\dot{\mathbf{q}} \;=\; J_{\mathrm{I}}\,\dot{\mathbf{q}}_{\mathrm{I}} \;+\; J_{\mathrm{D}}\,\dot{\mathbf{q}}_{\mathrm{D}} \tag{3.44}$$

where $\boldsymbol{\vartheta}_{stick}$ refers to both the normal and tangential velocity components of the points that are sticking, $\boldsymbol{\vartheta}_{slip_n}$ refers to only the normal velocity components of the points that are slipping, and $\dot{\mathbf{q}}_{\mathrm{D}}$ and $\dot{\mathbf{q}}_{\mathrm{I}}$ are the dependent and independent generalized speeds. Now $\dot{\mathbf{q}}$ and $\ddot{\mathbf{q}}$ can be expressed as

$$\dot{\mathbf{q}} \;=\; \begin{bmatrix} \dot{\mathbf{q}}_{\mathrm{D}} \\ \dot{\mathbf{q}}_{\mathrm{I}} \end{bmatrix} \;=\; \begin{bmatrix} -J_{\mathrm{D}}^{-1}J_{\mathrm{I}} \\ \mathrm{I} \end{bmatrix} \dot{\mathbf{q}}_{\mathrm{I}} \;=\; G\,\dot{\mathbf{q}}_{\mathrm{I}} \tag{3.45}$$

and

$$\ddot{\mathbf{q}} \;=\; G\,\ddot{\mathbf{q}}_{\mathrm{I}} \;+\; \dot{G}\,\dot{\mathbf{q}}_{\mathrm{I}} \qquad\qquad \dot{G}\,\dot{\mathbf{q}}_{\mathrm{I}} \;=\; \begin{bmatrix} -J_{\mathrm{D}}^{-1}\left(\dot{S}_c^T J_c + S_c^T \dot{J}_c\right)\dot{\mathbf{q}} \\ 0 \end{bmatrix} \tag{3.46}$$

Substituting Eq. (3.44) and Eq. (3.46) into Eq. (3.1) and pre-multiplying with G^T yields,

$$G^T\,A\,G\,\ddot{\mathbf{q}}_{\mathrm{I}} \;+\; G^T\left(A\,\dot{G}\,\dot{\mathbf{q}}_{\mathrm{I}} \;+\; \mathbf{b} \;+\; \mathbf{g}\right) \;=\; G^T J_c^T S_c \begin{bmatrix} \mathbf{F}_{slip_n} \\ \mathbf{F}_{stick} \end{bmatrix} \tag{3.47}$$

From Eq. (3.44) and Eq. (3.45), it can be easily shown that,

$$G^T J_c^T S_c = 0 \tag{3.48}$$

Hence, the reduced set of equations of motion are given by,

$$G^T\,A\,G\,\ddot{\mathbf{q}}_{\mathrm{I}} \;+\; G^T\left(A\,\dot{G}\,\dot{\mathbf{q}}_{\mathrm{I}} \;+\; \mathbf{b} \;+\; \mathbf{g}\right) \;=\; \mathbf{0} \tag{3.49}$$

Thus, during contact Eq. (3.49), Eq. (3.45) and Eq. (3.46) are used to integrate the states of dynamic system.

3.3.2 Summary of the Proposed Method

This section presents a brief summary of the proposed simulation method for rigid body contacts and impacts. In this approach the simulation takes place in two different domains: 1) *time-domain* in which the system's states evolve with respect to time and 2) *impulse domain* in which the states are dependent on a single parameter of impulse. The switch between the *time-domain* and *impulse domain* model takes place when an impact is detected according to the criteria Eq. (3.34). The conditions in Eq. (3.32) also present the criteria for embedding contact constraints during the *time-domain* simulation of the system. *Note that if a single point is experiencing impact, all points are considered to be experiencing impact.*; the contact analysis is not used when an impact event is detected.

The *time domain* model is given by a set of ordinary differential equations, and may be expressed without any loss in generality as an initial value problem (IVP) as,

$$\begin{cases} \text{IVP :} & \ddot{\mathbf{q}} = G\ddot{\mathbf{q}}_{\mathrm{I}} + \dot{G}\dot{\mathbf{q}}_{\mathrm{I}}, \quad \mathbf{q}(0) \quad \text{and} \quad \dot{\mathbf{q}}(0) \\[2ex] \text{where} & \ddot{\mathbf{q}}_{\mathrm{I}} = -(G^T A G)^{-1} G^T (A\dot{G}\dot{\mathbf{q}}_{\mathrm{I}} + \mathbf{b}(\mathbf{q},\dot{\mathbf{q}}) + \mathbf{g}(\mathbf{q})), \quad \dot{\mathbf{q}} = G\dot{\mathbf{q}}_{\mathbf{I}} \\[2ex] \text{and} & \dot{G}\,\dot{\mathbf{q}}_{\mathrm{I}} \;=\; \begin{bmatrix} -J_{\mathrm{D}}^{-1}\left(\dot{S}_c^T J_c + S_c^T \dot{J}_c\right)\dot{\mathbf{q}} \\ 0 \end{bmatrix}, \quad G = \begin{bmatrix} -J_{\mathrm{D}}^{-1} J_{\mathrm{I}} \\ \mathrm{I} \end{bmatrix} \end{cases} \tag{3.50}$$

the matrices J_{D} and J_{I} is found by partitioning the matrix ${S_c}^T J_c$ into dependent and independent columns. Note that if system is not in contact at any point $G = I$, where I is an identity matrix, and $\dot{G} = 0$. Substituting these into Eq.(3.50) would lead to IVP equivalent to an IVP formed by setting the right hand side of (3.1) to zero.

The *impulse-domain* model for impact analysis is given by the following set of equations:

$$\begin{cases} \boldsymbol{\vartheta} = \boldsymbol{\vartheta}_k + JA^{-1}J^T\mathbf{C}(p_{n_2} - p_{sk}) \qquad \text{where} \qquad p_{n_2} \geq 0 \\ \mathbf{C} = \begin{bmatrix} -{H_s}^{-1}H_r \\ 1 \end{bmatrix} \text{ and } H = \begin{bmatrix} \mathbf{w} \\ \mathbf{u}_1 \\ \mathbf{u}_2 \end{bmatrix} = [H_s \;\; H_r] \\ W_n(p_{n_2}) = W_{nk} + a(p_{n_2} - p_{sk})^2 + b\,(p_{n_2} - p_{sk}) \end{cases} \tag{3.51}$$

Here the relationship between velocity and the independent impulse parameter is given by a piece-wise linear algebraic equation, and the normal work is given by a piece-wise quadratic equation. The idea is to evolve $\boldsymbol{\vartheta}(p_{n_2})$ and $W_n(p_{n_2})$ with respect to $p_{n_2} \geq 0$, and find the solution of p_{nc} such that, $p_{nc} = \arg\min W_n(p_{n_2})$. Then the value of the independent impulse parameter at the end of the impact event would be $p_{nf} = (1 + e_*)p_{nc}$. Hence the post-impact velocities of the contact points are found by further evolving the system until $\boldsymbol{\vartheta}(p_{n_2} = p_{nf})$. If all the normal components of the post-impact velocities are positive or close to zero, then the *time-domain* simulation is resumed. Otherwise the impact analysis is repeated for the points with negative normal velocities at the end of the first impact event.

CHAPTER 4

SIMULATIONS OF CONTACT AND IMPACT IN PLANAR RIGID SYSTEMS

This section presents results of some benchmark examples of multi-point impact problems using the proposed method. First, an example is presented for a planar block impact with a horizontal, stationary surface. This problem is analyzed using both frictionless and frictional models of impacts. Simulation results using the proposed method are compared with experimental results found in the literature, which gives an indication of the energy loss during the impact. Another set of results pertaining to the angular response of a planar rocking block model is also presented. The time-domain simulation of the rocking block model requires a switching scheme for the pivoting between the two vertex contact points. The contact transition technique that was discussed in Sec. 3.3 is used to accomplish this switching between contact constrained points. The angular responses generated using the proposed method are then compared against experimental results for validation and analysis of the energy losses. Lastly an example of a planar ball two-point impact is presented, to illustrate the effect of stick-slip transition on the post-impact states.

4.0.1 Simulation Technique

The hybrid simulation technique implemented for this work uses *Matlab's* `ode45`, which is an adaptive Runge-Kutta integrator based on the Dormand-Prince method [98,99]. The results in this section were simulated in Matlab on an Intel(R) Core(TM) 2 Duo CPU with 3 GHz processor and 4 GB RAM. The examples used in this work do not have complex geometries, so a simple collision detection scheme is used here. The collision detection scheme tracks the distances of certain a priori selected points from the contact surface, and collision is detected when one or more of these distance values are equal (or less than) zero. If the proposed contact and impact modeling is to be used for more complicated geometries, a variety of advanced collision detection methods are available in the literature, see [100–102].

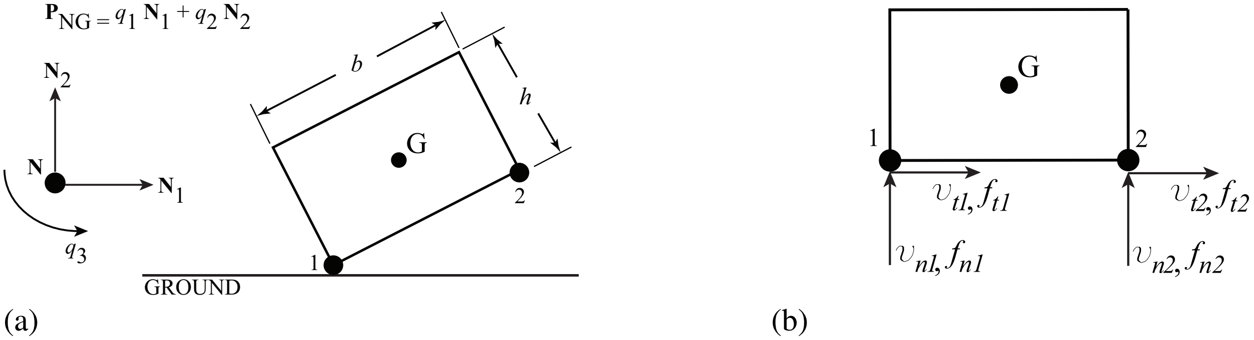

Figure 4.1: (a) Model description for the planar rocking block example, (b) velocities and forces at the impact points.

4.0.2 Example 1: Planar Rocking Block

The rocking block problem is of great interest in the multibody dynamics community [26, 53, 103, 104]. The interest in this particular problem is facilitated partly due to its relevance in applications such as robotics [105,106] and earthquake engineering [107,108], and also due to a number of issues that arise in its modeling. One of the main issues faced in planar rocking block modeling is the resolution of the indeterminate system of equations when multiple point impacts are considered. Another key issue is the switching of pivot points during the rocking motion. The proposed method addresses both of these issues.

The planar rocking block model in Fig. 4.1a has three DOFs and its center of mass is located at point G. The configuration of the block is given by a set of generalized coordinates $\mathbf{q} = \begin{bmatrix} q_1 & q_2 & q_3 \end{bmatrix}^T$, where q_1 and q_2 represent the block's position and q_3 denotes its orientation. The dimensions of the the block are defined by its breadth b and height h, such that $b/h > \sqrt{2}$ (flat block [53, 104]) for two of the cases studied here. The contact between the bottom surface of the block and the ground is assumed at the two vertex points 1 and 2, as shown in Fig. 4.1. The terms in Eq. (3.4) that represent the dynamics of the planar rigid block are given by,

$$A = \begin{bmatrix} m & 0 & 0 \\ 0 & m & 0 \\ 0 & 0 & \frac{m(b^2+h^2)}{12} \end{bmatrix} \qquad J = \begin{bmatrix} 1 & 0 & \frac{h\cos(q_3)+b\sin(q_3)}{2} \\ 0 & 1 & \frac{h\sin(q_3)-b\cos(q_3)}{2} \\ 1 & 0 & \frac{h\cos(q_3)-b\sin(q_3)}{2} \\ 0 & 1 & \frac{h\sin(q_3)+b\cos(q_3)}{2} \end{bmatrix} \tag{4.1}$$

$$\dot{\mathbf{q}}(0) = \begin{bmatrix} 0.344 & -0.500 & -9.199 \end{bmatrix}^T$$

Based on this assumption the planar rocking block poses an indeterminate problem when both vertex points 1 and 2 touch the surface. The rigid body constraints introduced in Sec. 3.2 resolve this indeterminacy by harnessing the rigidity property of the block. If additional contact points are introduced, the indeterminacy can still be resolved due to the availability of additional rigid body constraint equations, which are derived based on pairs of contact points.

4.0.2.1 Rocking Block: Frictionless Case

Here the results of the frictionless version of the planar rocking block example are compared with an experimental result from the study in [53]. The block has a mass of $m = 2.5\ kg$, breadth of $b = 0.1087\ m$ and a height of $h = 0.0645\ m$, similar to the experimental specimen used in [53]. Here the coefficients of friction for the two contact points are assumed to be $\mu_1 = \mu_2 = 0$. This leads to the tangential friction forces f_{t_1} and f_{t_2}, shown in Fig. 4.1, being equal to zero. The simulation starts with point 1 in contact and the impact event takes place when point 2 hits the ground. Note, that both points 1 and 2 would be used for the impact analysis, although impact takes place only at point 2. In the context of the experimental results shown in [53], $\theta_1 = \theta_2 = 0^\circ$ is used to represent a flat ground surface.

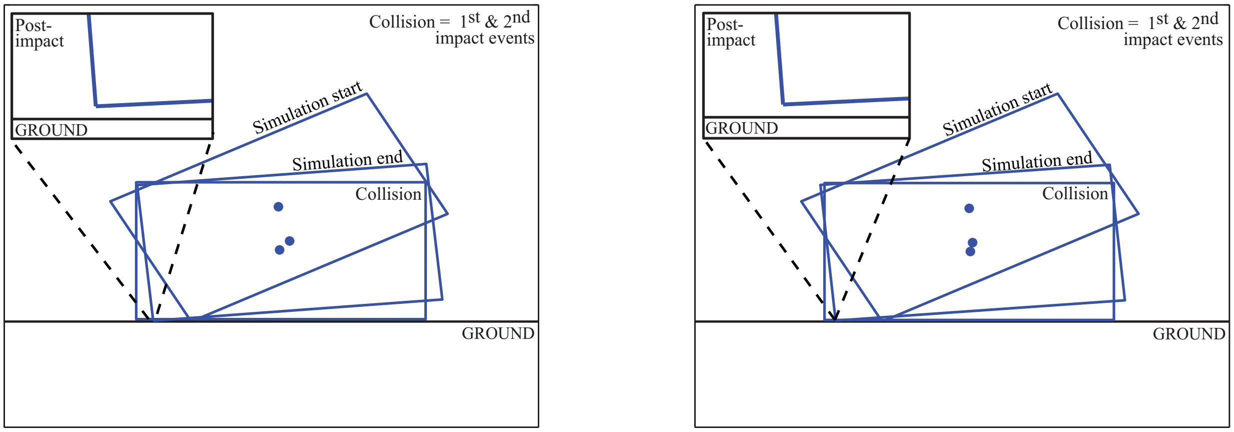

(a) (b)

Figure 4.2: Simulation of the (a) frictionless (CPU Time: 0.28 s) and (b) frictional (CPU Time: 0.26 s) rocking block examples—a similar post-impact state is obtained for both cases.

Some configurations from the simulation results are shown in Fig. 4.2a. A plot of the system energy is included in Fig. 4.7 to show energy consistency for the simulation performed. The entire impact process shown in this example takes place over two consecutive impact events. At the end of the first impact event the post-impact normal velocity of point 2 remains negative, while the normal velocity of point 1 becomes positive. Thus a secondary impact event takes place that only includes point 2 in the impact analysis. The post-impact state for point 2 is determined at end of the second impact event, whereas the velocities at end of the first impact event are used as the post-impact state for point 1. The post-impact states are used to compute the initial conditions needed to restart the simulation after the impact.

The analysis of the first impact event is illustrated in Fig. 4.3. Particularly Fig. 4.3a shows the normal work for $e_* = -0.8$, where the first impact event is terminated in its

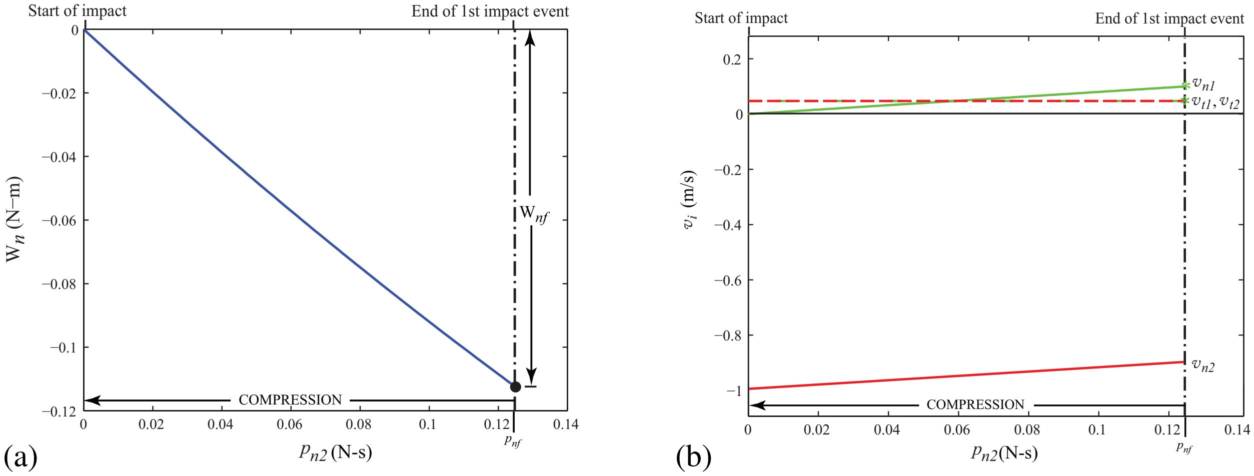

Figure 4.3: (a) Normal work done, and (b) evolution of velocities throughout the first impact event for the frictionless rocking block example.

compression phase by the start of the second impact event, recall Fig. 3.5. Figure 4.3b depicts the evolution of velocities throughout the first impact event. This figure shows how the normal, v_{n_1}, and tangential, v_{t_1}, velocity of point 1 evolve, indicating that point 1 rebounds slightly from the surface, while the normal velocity of point 2 is negative, which initiates a second impact event. Analysis of the second impact event is shown in Fig. 4.4 and only involves the velocities of point 2, v_{n_2} and v_{t_2}. It begins with the velocity of point 2 at the end of the first impact event. In the second impact event $e_* = 0.6667$. The evolution of velocities in Fig. 4.4b shows that point 2 rebounds from the surface. The inset plot in Fig. 4.2a shows a close-up view of the post-impact state of the entire block rebounding away from the surface after the collision. An ECOR equal to one, $e_* = 1$ would indicate no energy loss. Therefore ECORs of $e_* = \{-0.8, 0.67\}$ indicate a significant loss of energy during this first collision, which is also indicated by the substantial difference in the rebound configuration of the block as compared to its initial configuration in Fig. 4.2a.

The results obtained for this benchmark are compared to experimental data reported in Fig. 8 of [53].. The *global* ECOR values of $e_* = \{-0.8, 0.67\}$ yield an identical match

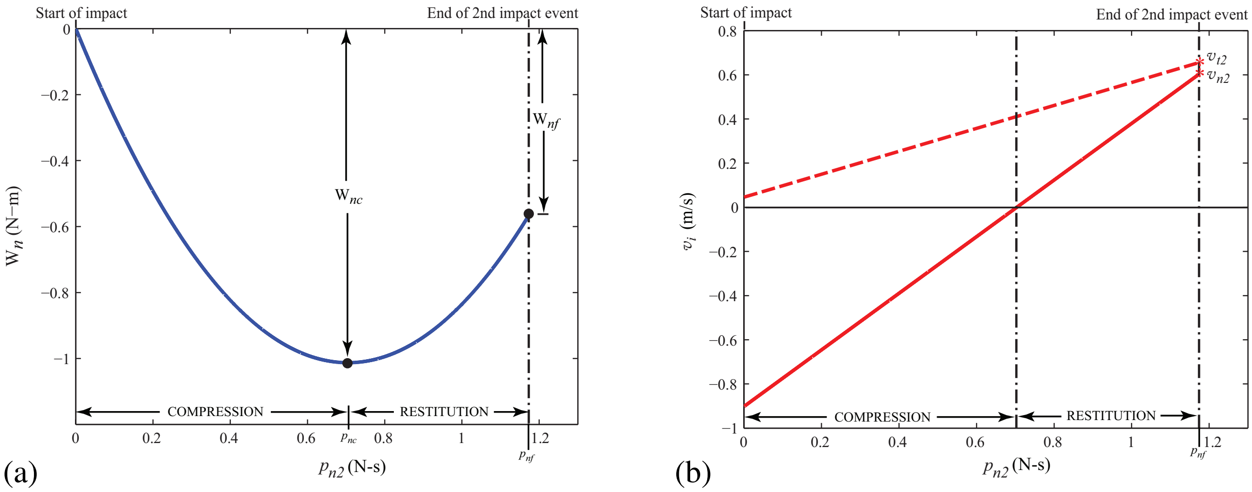

Figure 4.4: (a) Normal work done, and (b) evolution of velocities throughout the second impact event for the frictionless rocking block example.

to the results in [53]. The post-impact velocities for the two methods given in Table 4.1 for points 1, v_1^+, and 2, v_2^+, are normalized with respect to the pre-impact velocity of point 2, v_2^-, to directly compare the two results. Note that these are only the normal components of the velocities of points 1 and 2. The impact analysis method shown in [53] uses local ECORs corresponding to each contact point. These local ECOR values were experimentally found to be $e_1 = 0.43$ and $e_2 = 0.64$ corresponding to points 1 and 2 respectively. Intuitively, one would expect $e_1 < e_2$ for the local ECORs because point 2 rebounds higher than point 1, but it is not clear that this intuition is valid. The global ECORs give a different view of the collision, which suggests that the collision loses more energy during the interaction at point 2 than at point 1. This is because point 2 is solely involved in the second impact event, where a larger portion of the system energy is lost, even though it rebounds higher than point 1. It is possible to reach the opposite conclusion from the local ECORs if there was no other indication of how the system loses energy. One can also consider the small difference in the initial and final position of point 1, compared to the large difference for point 2, as an indication of where most of the energy is lost.

4.0.2.2 Rocking Block: Frictional Case

A rocking block with friction is explored here to observe the effects of considering friction at the impact points. The same model parameters and initial conditions, as in Sec. 4.0.2.1, are used in this simulation aside from friction at the impact points, where initially $\mu_1 = \mu_2 = 0.35$. The coefficients of friction do not have to be the same but it makes sense for this example because the points impact the same surface.

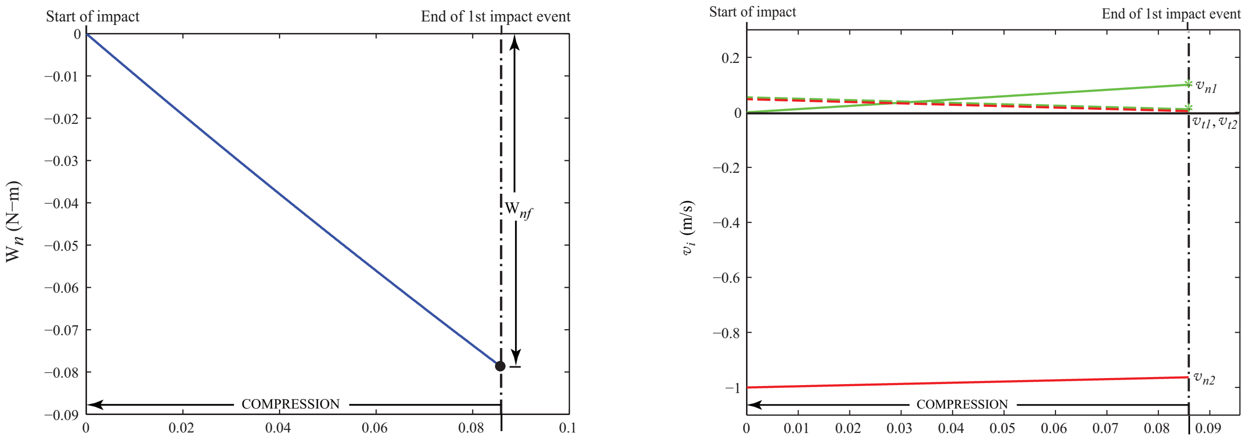

(a) (b)

Figure 4.5: (a) Normal work done, and (b) evolution of velocities throughout the first impact event for the frictional rocking block example.

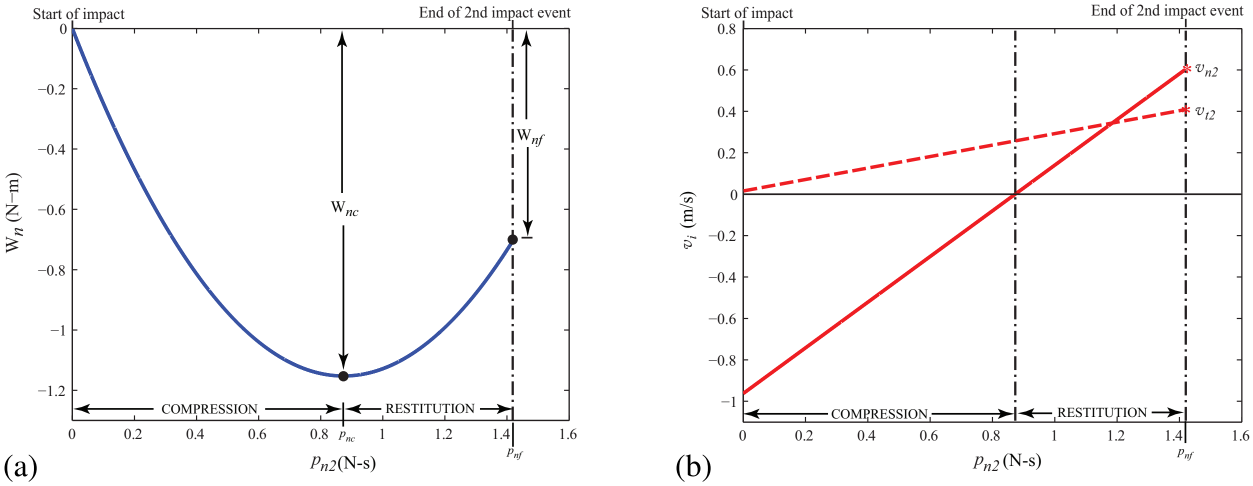

(a) (b)

Figure 4.6: (a) Normal work done, and (b) evolution of velocities throughout the second impact event for the frictional rocking block example.

The results of the simulation are depicted in Fig. 4.2b and a plot of the system energy is included in Fig. 4.7 to show energy consistency for the simulation performed. Similar to the frictionless case, the collision of point 2 with the ground results in two impact events which are representative of the entire collision of the block with the ground. The first impact event is the only indeterminate one in the simulation, which involves the simultaneous impact of points 1 and 2. The post-impact velocity of point 2 at the end of the first impact event is negative which indicates that it is still moving toward the ground surface. This situation is interpreted as a second impact event involving only point 2, a determinate collision. Furthermore, point 1 has a positive velocity after the first impact event, which is interpreted as having reached its post-impact state, as in the frictionless case. This second impact event is resolved before restarting the simulation to find the post-impact velocity of point 2.

The result obtained for this case is similar to the frictionless case analyzed in Sec. 4.0.2.1 and [53]. The difference is that the *global* ECORs is $e_* = -0.863$ for the first and $e_* = 0.623$ for the second impact event. The first impact event, illustrated in Fig. 4.5, shows a plot of the normal work and evolution of velocities. The inclusion of friction for this case does not cause the tangential velocities to come to rest at the stick-slip transition; this is almost the case at the end of the first impact event. Thus, the slope of the velocities never changes and the impact points maintain a slip-state of forward sliding throughout the impact event. The plot of the normal work in Fig. 4.5a shows that the first impact event terminated in its compression phase due to the start of the second impact event. As in the frictionless case, Fig. 4.5b shows how the normal, v_{n_1}, and tangential, v_{t_1}, velocity of point 1 evolve, which shows that point 1 slightly rebounds from the surface. Meanwhile, the normal velocity of point 2 is negative which indicates that it is still impacting the ground, initiating a second impact event. The analysis of the second impact event is shown in Fig. 4.6 and only involves point 2. Fig. 4.6a shows the characteristic parabolic shape of the normal work where a compression and restitution phase are clearly defined. Fig. 4.6b shows how the velocities of point 2, v_{n_2} and v_{t_2} evolve, such that point 2 rebounds from the surface.

Table 4.1: Comparison of a frictional rocking block to theoretical and experimental results of a frictionless case. (The ECORs (e_1, e_2) used in [53] are local for each impact point; in this work, two impact events are detected for this case so two *global* ECORs are used here in the order specified.)

		v_1^+/v_2^-	v_2^+/v_2^-	ECORs
Experimental	Yilmaz, et al. [53]	-0.100	-0.600	e_1 = 0.43, e_2 = 0.64
Theoretical	Chatterjee-Rodriguez-Bowling			
	no friction	-0.100	-0.600	e_* = -0.8, 0.6667
	with friction	-0.100	-0.600	e_* = -0.863, 0.623

The results from this case are summarized in Table 4.1, along with the results for the frictionless case examined in Sec. 4.0.2.1. Fig. 4.2(b) also shows a close up view of the post-impact state of the block leaving the ground surface after the simultaneous collision. The post-impact velocities of points 1, v_1^+, and 2 v_2^+, are normalized with respect to the pre-impact velocity of point 2, v_2^-. The solution to the post-impact velocities of points 1 and 2 are also identical to the result obtained for the frictionless case. Friction is dissipative by nature and it is observed that this leads to an increase in the global ECOR for the first impact event and a reduction for the second, to obtain the same post-impact result.

The conclusions concerning the energy losses from the frictionless case in Sec. 4.0.2.1 also apply here, but the inclusion of friction includes a second means of energy dissipation that alters the ECORs in a manner that is difficult to predict. Because the final motion is identical to the frictionless case, it appears that friction dissipated more energy at points 1 and 2 than in the frictionless case during the first impact because the global ECOR increased while yielding the same post-impact velocities; recall that the global ECOR determines only the loss of normal work even though it is dependent on friction. Yet the global ECOR decreases for the second impact event, which means that more energy is lost for the normal work to obtain the same post-impact velocities as in the frictionless case.

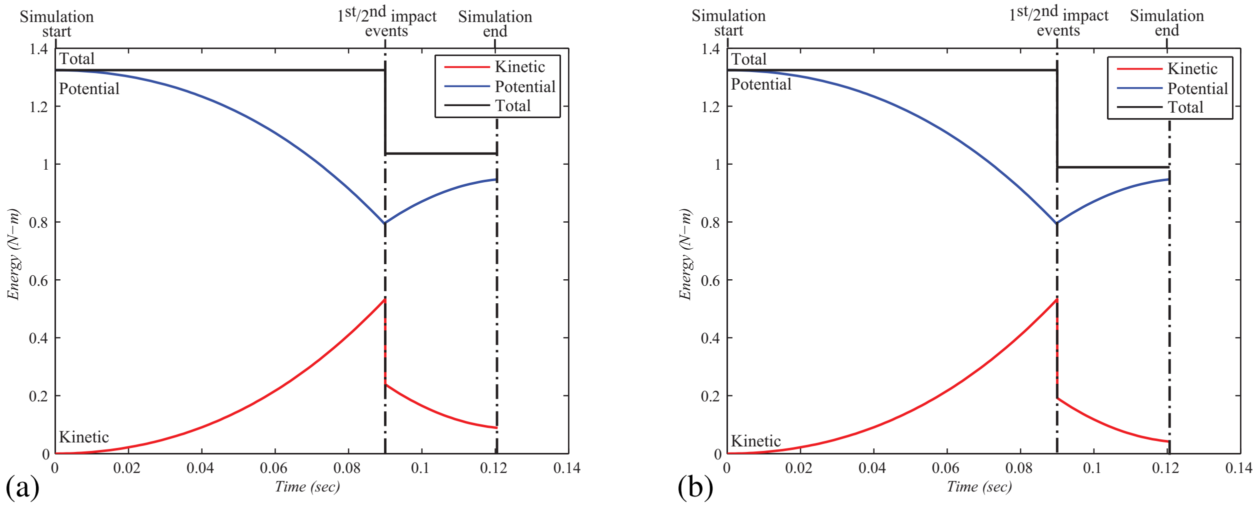

Figure 4.7: Energy consistency throughout the simulation for (a) frictionless rocking block, and (b) frictional rocking block examples.

4.0.3 Example 2: Angular Response of Planar Rocking Block

The results in Sec. 4.0.2 show that the proposed method can be used to analyze the energy losses during a single collision in the rocking block problem. However, the method also applies to cases of multiple collisions over time and shows the energy dissipation over the entire motion of the system. To examine successive collisions, the method must address the transition to contact that can occur if a point on the block sticks to the surface. This problem of simulating successive collisions has been studied extensively in the literature [34, 54, 109–115]. These models use stiffness properties [113], local energy dissipation properties [34, 109] or global kinematic restitution properties [115].

The data analyzed in this example comes from [113,114], which reports experimental data on different specimens of concrete blocks for the cases of free-rocking and rocking with base excitation; herein, only the free-rocking block results are considered. The work in [103] showed that these experimental results can be predicted using the LZB model, which was proposed in [34, 54, 109–112]. The LZB model uses local ECORs for each contact point and relates the local energy losses by a distributing law, based on parameters defined as contact stiffness ratios and elasticity coefficients. This is different from the proposed approach where the stiffness and elasticity between different contact points is lumped into a global ECOR as was discussed in Sec. 3.1.2.

Table 4.2: Choice of effective width

Block Specimen	Geometric width(m) [114]	LZB model width(m) [103]	CRB model width(m)
1	0.25	0.23	0.23
2	0.17	0.155	0.155
4	0.16	0.115	0.115

Three different specimens were used for the free-rocking block experiments in [114]: 1) *Specimen 1* with a width of 0.25 m, height of 1 m and mass of 503 kg, 2) *Specimen 2* with width and height 0.17 m and 1 m respectively and a mass of 228 kg, and 3) *Specimen 4* of width 0.16 m, height 0.457 m and mass 245 kg. The width of the block needs to be calibrated, since the angular response to a rocking block problem is highly sensitive to variations in width [116]. A detailed discussion on this presented in [103, 116]. The *effective width* selected herein for all of the specimens are the same as in [103, 116], and are tabulated in Table. 4.2.

Fig. 8.40 compares the simulated and experimental angular response of the three specimens. Here, Pena refers to the measured angular response from the experiments done

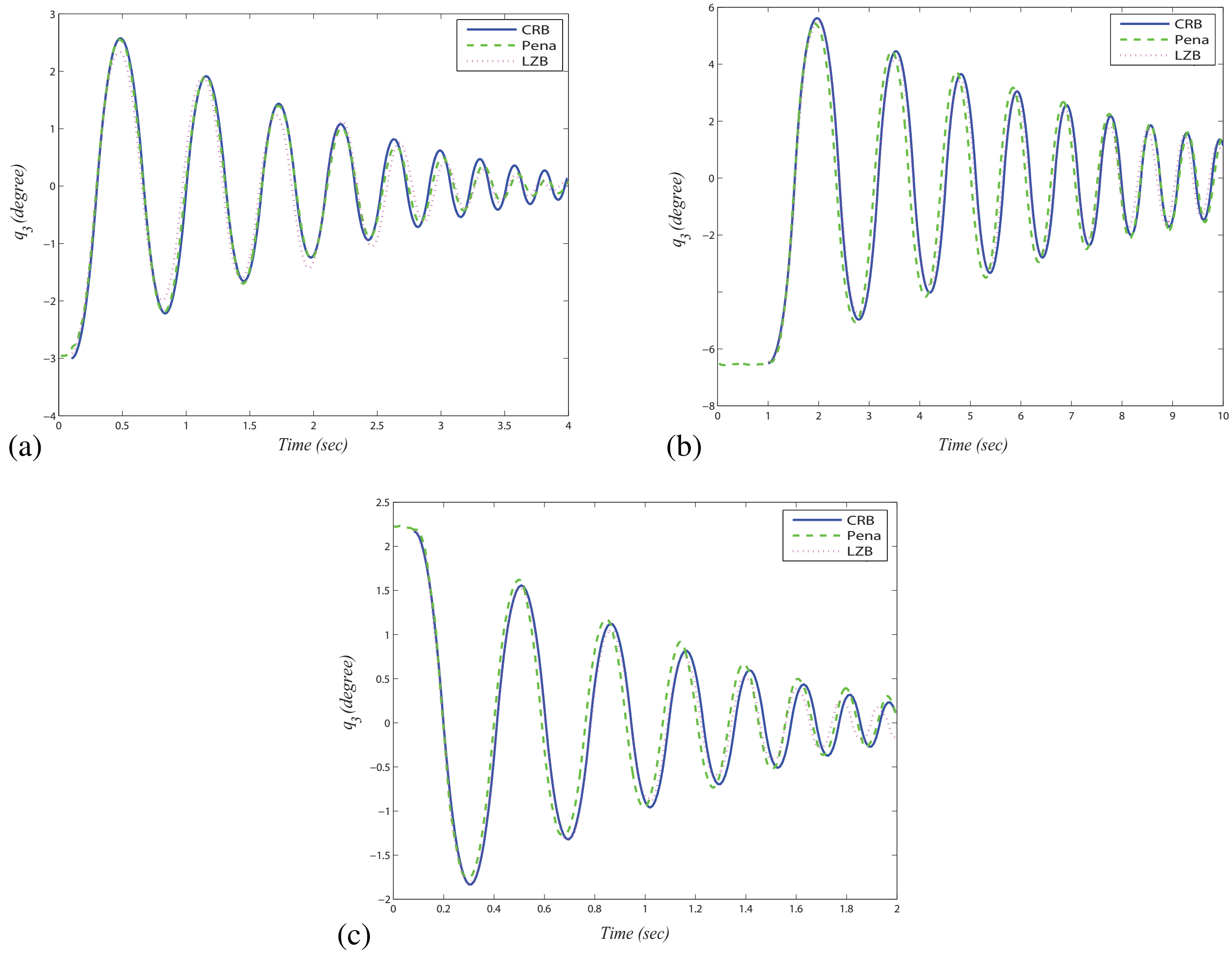

Figure 4.8: Angular Response for (a) Specimen 1 (CPU Time: 59.06 s) (b) Specimen 2 (CPU Time: 79.33 s) (c) Specimen 4 (CPU Time: 56.37 s). The angular response data for Pena and LZB, were obtained from plots shown in Fig.5 of [103].

by Pena et.al [114], LZB refers to the simulated response using the LZB model [103], and CRB is the simulated angular response based on the approach proposed in this work. The static and dynamic coefficient of friction used for the simulation are $\mu_s = 0.577$ and $\mu_d = 0.3$ respectively, identical to [103].

To match this data, a negative global ECOR is used for the multi-point impacts and a positive global ECOR is used for the single point impacts. Thus, for each specimen a pair of ECOR values are chosen The response for Specimen 1, shown as CRB in Fig. 8.40a

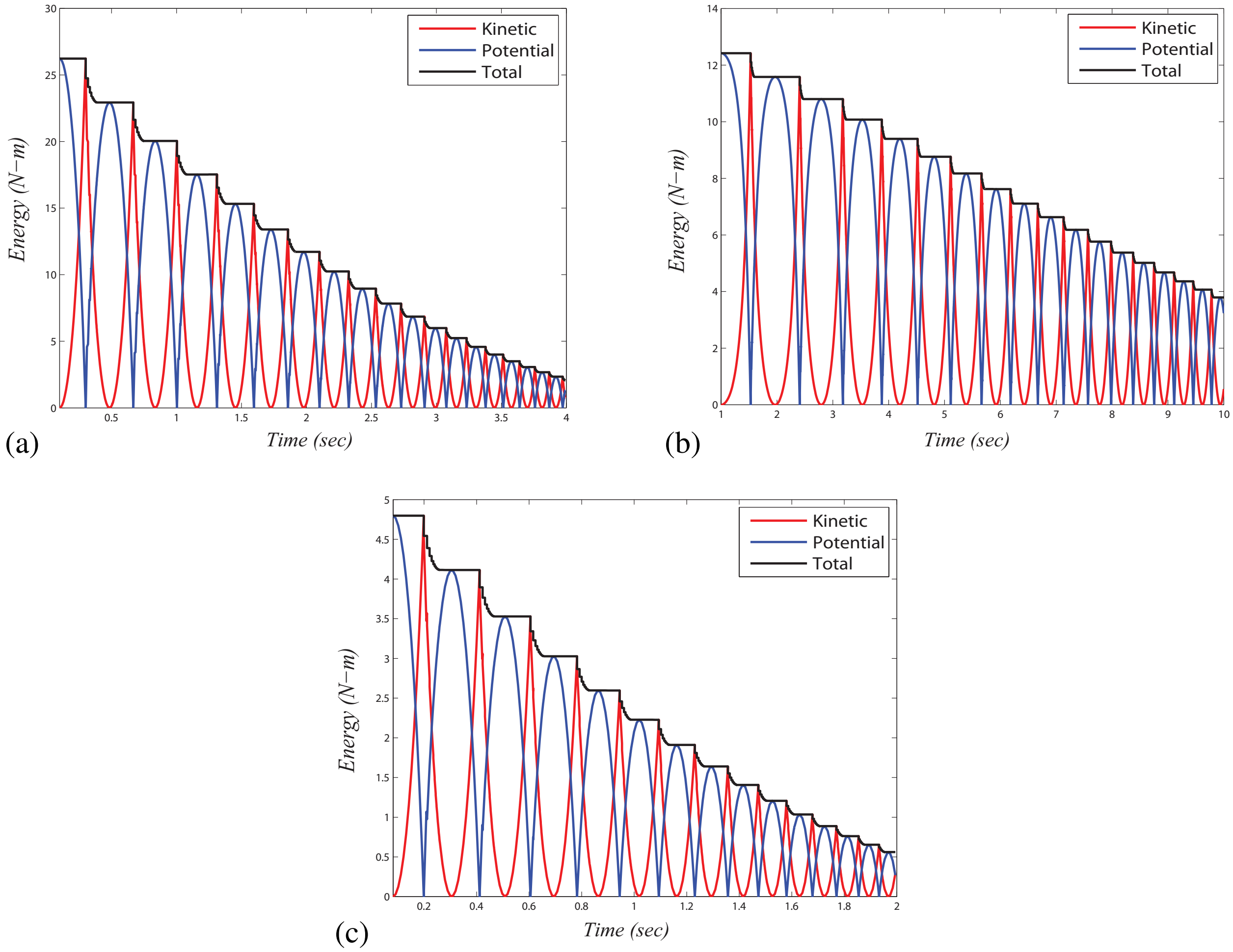

Figure 4.9: Energy consistency throughout the simulation for (a) Specimen 1 (b) Specimen 2 (c) Specimen 4 .

was obtained using $e_* = -0.73$ for all two-point impacts and $e_* = 0.8$ for all single point impacts. Also shown in Fig. 8.40a, is the angular response of the same specimen using the LZB model where an ECOR value, $e_n = 0.97$ is used until 2.83 seconds, after which it is updated with $e_n = 0.88$ [103]. Note, that the e_n used in [103] are local ECORs at each point, as opposed to the global ECOR e_* used in this work. Similarly, the global ECORs used to match the angular response for Specimen 2 in Fig. 8.40b and Specimen 4 in Fig. 8.40c are $e_* = \{-0.95, 0.8\}$ and $e_* = \{-0.96, 0.8\}$, respectively. The LZB model simulates the response for Specimen 2 with an ECOR of $e_n = 0.999$, and for Specimen 4 the ECOR values are $e_n = \{0.99, 0.87\}$ before and after 0.85 seconds. All of the simulation parameters used for the LZB and CRB models are summarized in Table 4.3. The interesting thing to note is that all of the local ECORs have higher values than the global ECORs, especially in the case of Specimen 1. The global ECORs also indicate that most of the system energy was lost during single point impacts, rather than the multiple point impacts. This same trend was true for the previous analyses in Sec. 4.0.2.

Table 4.3: Simulation Parameters

	Specimen 1		Specimen 2		Specimen 4	
	LZB	CRB	LZB	CRB	LZB	CRB
μ_d	0.3	0.3	0.3	0.3	0.3	0.3
μ_s	0.577	0.577	0.577	0.577	0.577	0.577
ECORs	$\{0.97, 0.88\}$	$\{-0.73, 0.8\}$	0.999	$\{-0.95, 0.8\}$	$\{0.99, 0.87\}$	$\{-0.96, 0.8\}$

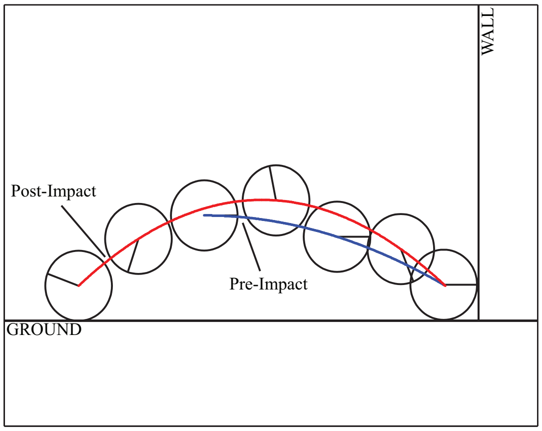

(a)

	Initial	Pre-impact	Post-impact
Position			
q_1	0.000 m	3.614 m	3.614 m
q_2	1.500 m	0.500 m	0.500 m
q_3	0.000 rad	0.000 rad	0.000 rad
Speeds			
$\dot{q}_1$	8.000 m/s	8.000 m/s	-5.504 m/s
$\dot{q}_2$	0.000 m/s	-4.430 m/s	4.893 m/s
$\dot{q}_3$	0.000 rad/s	0.000 rad/s	-9.786 rad/s
Velocities			
v_{t1}	8.000 m/s	8.000 m/s	-10.397 m/s
v_{n1}	0.000 m/s	-4.430 m/s	4.893 m/s
v_{t2}	0.000 m/s	-4.430 m/s	0.000 m/s
v_{n2}	8.000 m/s	8.000 m/s	-5.504 m/s

(b)

Figure 4.10: (a) Simulation of the planar ball example (CPU Time: 0.54 s), and (b) table of velocities and generalized speeds for the simulation.

4.0.4 Example 3: Planar Ball With Friction

Here, a simulation of a planar ball impacting a corner, as in Fig. 3.1a, is performed to show the effect of the stick-slip transition on the post-impact behavior of a system. The dynamics of the planar ball are shown in Eq. (3.4):

$$A = \begin{bmatrix} m & 0 & 0 \\ 0 & m & 0 \\ 0 & 0 & \frac{mR^2}{2} \end{bmatrix} \qquad J = \begin{bmatrix} 1 & 0 & R\cos(q_3) \\ 0 & 1 & R\sin(q_3) \\ 0 & 1 & R\cos(q_3) \\ 1 & 0 & -R\sin(q_3) \end{bmatrix} \qquad \dot{\mathbf{q}}(0) = \begin{bmatrix} 8.000 \\ -4.430 \\ 0.000 \end{bmatrix} \tag{4.2}$$

The planar ball has a mass $m = 1.0\ kg$ and radius $R = 0.5\ m$. The simulation of the ball is depicted in Fig. 4.10a and ends when a second collision is detected with the ground. A plot of the system energy is shown in Fig. 4.11 to show energy consistency for the simulation performed. Only one impact event occurs during the collision of the ball and the corner, which is an indeterminate collision involving points 1 and 2. A global ECOR of $e_* = 0.5$ and $\mu_1 = \mu_2 = 0.35$ are used to generate the simulation data given in Fig. 4.10b.

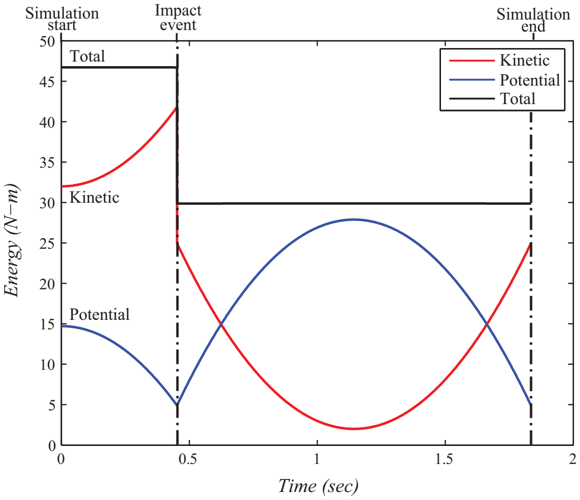

Figure 4.11: Energy consistency throughout the simulation for the planar ball example.

The ball has no angular velocity prior to impact but rebounds with a negative angular velocity after impact. This angular velocity is attributed to the slip-state of the ground contact point undergoing slip reversal, while the wall contact point sticks to the surface until it separates from it at the end of the collision. This is also consistent with the post-impact trajectory of the ball's mass center shown in Fig. 4.10a, which is higher than its pre-impact trajectory.

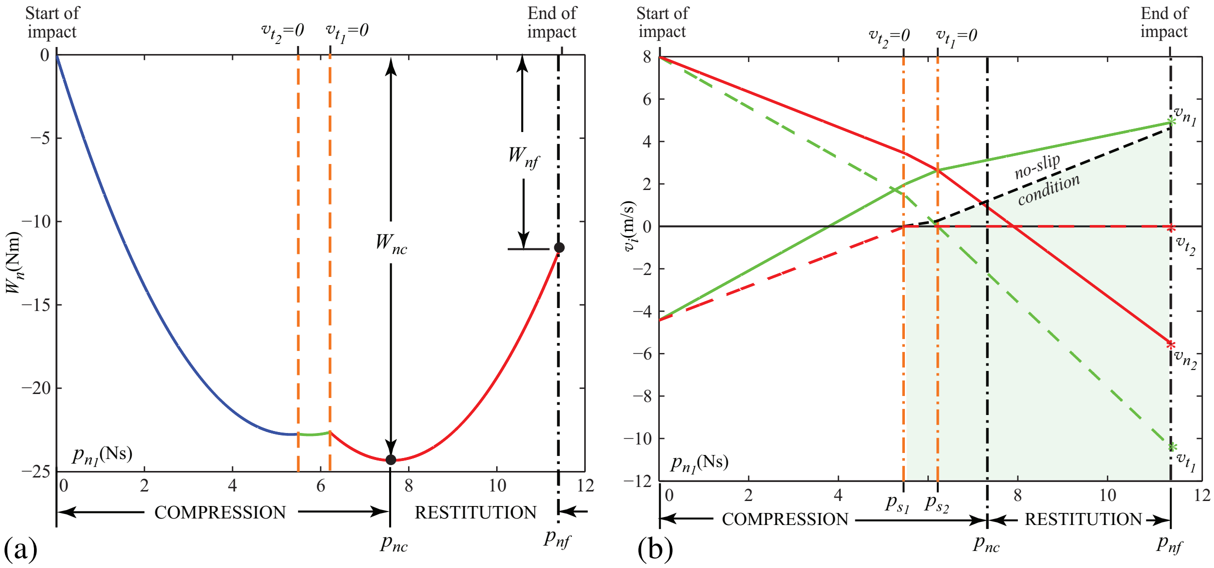

Figure 4.12: (a) Normal work done, and (b) evolution of velocities throughout the impact event for the planar ball example.

The evolution of the velocities were determined by accounting for the change in slip-state of points 1 and 2 throughout the impact event. The result of these processes is shown in Fig. 4.12. A plot of the normal work throughout the collision is shown in Fig. 4.12a. The two shifts in the normal work curve are a result of evaluating the stick-slip transition, which occur at the points where $v_{t_2} = 0$ and $v_{t_1} = 0$. These shifts indicate the importance of knowing where the tangential velocities come to rest so that the stick-slip transition can be analyzed. The effects of a change in friction direction are illustrated in the evolution of velocities, seen in Fig. 4.12b. Both tangential velocities reach the stick-slip transition during this single impact event. The tangential velocity at the wall comes to rest first at p_{s1} and sticks to the surface. The no-slip condition for this impact point is derived and plotted in Fig. 4.12b to allow a check if the slip-state changes during the remainder of the impact event. The tangential velocity of the ground impact point comes to rest next in the impact event at p_{s1}. This impact point slip-reverses so that the friction direction changes, which is consistent with the negative angular velocity of the ball after the collision. Figure 4.12b illustrates an abrupt shift in the direction for all of the velocities at the stick-slip transitions.

The energy plots are included here to show energy consistency for the collisions simulated for the planar rocking block (frictionless and frictional) and planar ball examples. The drops in total energy shown in Fig. 4.7, Fig. 4.11, and Fig. 8.42 correspond to the energy losses specified by the *global* ECOR and friction analyzed in the previous sections.

CHAPTER 5

SPATIAL RIGID IMPACT MODEL

5.1 Overview of Impact Modeling

The proposed method treats impacts as discrete events within the *time-domain* simulation of the equations of motion. The impact evolves to its final state in the impulse domain rather than the time domain. The goal is to express all of the impulses in terms of a single independent impulse so that the work-energy theorem can govern the evolution of the single impulse in an energetically consistent manner. This section derives this approach using as an example the three-dimensional rigid block undergoing a four-point impact shown in Fig. 5.1. However, the proposed method may be generalized for any type of multibody system and any number of contact points.

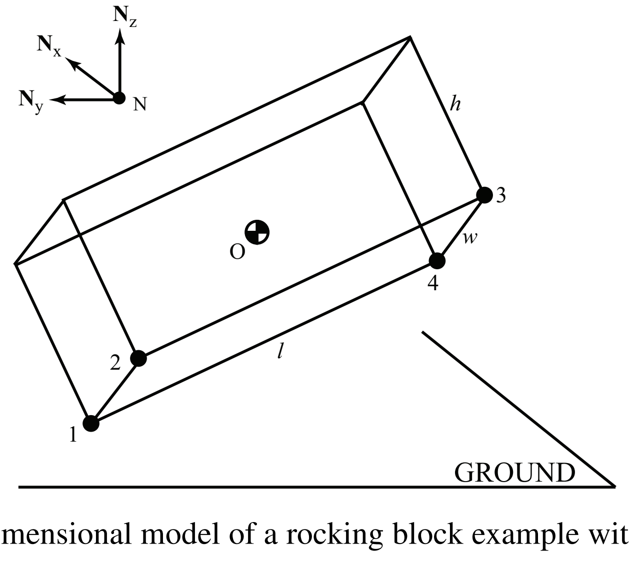

Figure 5.1: Three-dimensional model of a rocking block example with four corner impact points.

The configuration of the rigid block shown in Fig. 5.1, is represented by a minimal set of generalized coordinates,

$$\mathbf{q} \;=\; [\, q_1 \;\; q_2 \;\; q_3 \;\; q_4 \;\; q_5 \;\; q_6 \,]^T \tag{5.1}$$

where q_1, q_2, and q_3 represent the position of the body's reference point O, and q_4, q_5, and q_6 define the orientation of the body. In the Fig. 5.1, the four impact points are denoted as $i = \{1, ..., 4\}$, and there positions with respect to the inertial reference frame and point are defined as $\mathbf{P}_{Ni} = [x_i \;\; y_i \;\; z_i]^T$. The equations of of motion for this system are,

$$A\ddot{\mathbf{q}} \;+\; \mathbf{b}(\mathbf{q}, \dot{\mathbf{q}}) \;+\; \mathbf{g}(\mathbf{q}) \;=\; \mathbf{\Gamma}(\mathbf{q}) \;=\; J^T(\mathbf{q})\,\mathbf{F} \tag{5.2}$$

where A is the mass matrix of the system. The vector $\mathbf{b}(\mathbf{q}, \dot{\mathbf{q}})$ and $\mathbf{g}(\mathbf{q})$ are the Coriolis and gravity terms respectively. Note that for the simple block example in Fig. 5.1, the Coriolis terms would be equal to zero. The generalized active forces are represented by $\mathbf{\Gamma}$ and are related to the impact forces, $\mathbf{F}$, through the contact Jacobian matrix J. The post-impact states can be obtained by performing a definite integration over the very small time period $[t, t+\epsilon]$,

$$\int_t^{t+\epsilon} (A\ddot{\mathbf{q}} + \mathbf{b}(\mathbf{q}, \dot{\mathbf{q}}) + \mathbf{g}(\mathbf{q}))\, dt \;=\; \int_t^{t+\epsilon} J^T(\mathbf{q})\,\mathbf{F}\, dt \tag{5.3}$$

This yields,

$$A\,(\dot{\mathbf{q}}(t+\epsilon) \;-\; \dot{\mathbf{q}}(t)) \;=\; J^T \int_t^{t+\epsilon} \mathbf{F}\, dt \;=\; J^T\mathbf{p} \tag{5.4}$$

where,

$$\mathbf{p} = [p_{x_1} \;\; p_{y_1} \;\; p_{z_1} \;\; \ldots \;\; p_{x_4} \;\; p_{y_4} \;\; p_{z_4}]^T$$

The vector $\mathbf{p}$ contains all of the impulses induced at the impact points during the impact event. The terms p_{x_i} and p_{y_i} are the tangential impulses and p_{z_i} is the normal impulse, at impact point $i = 1, ..., 4$. It is assumed that there is no change in configuration during an impact event. The definite integration over the small time-period $[t, t+\epsilon]$ causes the

Coriolis force and gravity terms to vanish in the (5.4). The mass matrix, A and contact Jacobian J are assumed to remain constant during the impact event.

The velocities of the impact points can be obtained by inverting the mass matrix A and pre-multiplying the resulting equation by the Jacobian matrix,

$$\boldsymbol{\vartheta} = [v_{x_1} \; v_{y_1} \; v_{z_1} \; \ldots \; v_{x_4} \; v_{y_4} \; v_{z_4}]^T = \boldsymbol{\vartheta}(0) + JA^{-1}J^T \, \mathbf{p} = \boldsymbol{\vartheta}(0) + M \, \mathbf{p} \quad (5.5)$$

where and $\boldsymbol{\vartheta}(0)$ and $\boldsymbol{\vartheta}$ are the pre- and post-impact velocities of the impact points. v_{x_i} and v_{y_i} are the tangential components, and v_{z_i} is the normal component of the velocity at impact point $i = 1, ..., 4$. It is noteworthy that at this point the velocities of the contact points are only dependent on the impulses. Hence, (5.5) shows the *impulse-domain* version of the equations of motion [1,2,20–22,26].

In addition to impulses and momentum in (5.5), the proposed analysis also considers the effect of friction on system behavior during the collision. Here the Coulomb friction law is used to determine the stick or slip state of the impact points. Unlike the planar analysis, the three dimensional analysis of the stick-slip transition must be addressed in force space. The Coulomb friction law in three-dimensions, cannot be analytically integrated. Hence, the impulses $\mathbf{p}$ in (5.5) need to be numerically integrated. In addition to Coulomb friction, this work also uses constraints based on the rigidity of the body, this allows for the impulses to be represented in terms of an arbitrarily selected normal impulse parameter $p_n \geq 0$. For the example in Fig. 5.1, $dp_n = dp_{z_4}$ will be used. Thus, the impulses $\mathbf{p}$ in (5.5) would be given by,

$$\frac{d\mathbf{p}}{dt} = \mathbf{F} = \mathbf{C}\,\frac{dp_n}{dt} \qquad \mathbf{p} = \int_0^{p_n} \mathbf{C}\, dp_n \quad (5.6)$$

where $\mathbf{C}$ is a force gradient vector in terms of the independent impulse term. The derivation of $\mathbf{C}$ will be discussed in Sec. 5.2. Thus (5.5), (5.6) and (5.7) govern the impact point velocities. As it can be seen in (5.6), the impulses $\mathbf{p}$ is defined in terms of definite integral with respect to p_n as a dummy variable. Thus, the post-impact states depend upon the final value of p_n. This work uses an energetic constraint based on the work-energy theorem to determine the final value of p_n, such that the energy consistency of the system is guaranteed.

Unlike planar impacts, in three dimensions the slip direction may vary during an impact event, which requires a different treatment of the stick-slip transition. The first difference is that Cartesian velocities will be examined in cylindrical coordinates:

$$\boldsymbol{\vartheta}_{cyl} = [s_1 \;\; \phi_1 \;\; v_{z_1} \;\; \dots \;\; s_4 \;\; \phi_4 \;\; v_{z_4}]^T \tag{5.7}$$

$$s_i = \sqrt{{v_{x_i}}^2 + {v_{y_i}}^2} \qquad \phi_i = \arctan(v_{x_i}, v_{y_i}) \tag{5.8}$$

where s_i and ϕ_i are the sliding speed and sliding direction in the impact plane. This change of coordinates is carried out at the velocity-level, not the position-level, to avoid singularities in the transformation [4, 22].

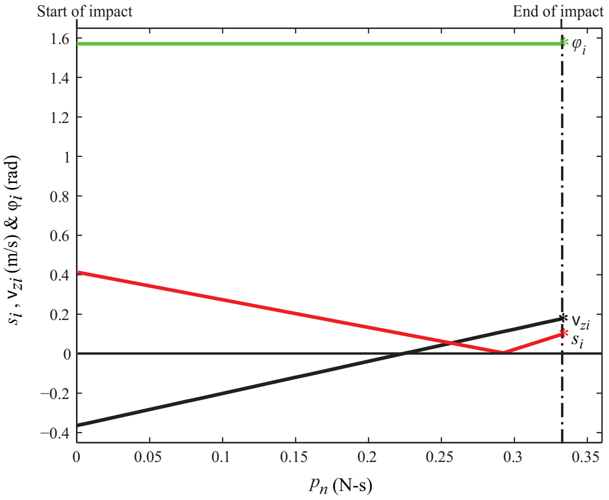

Figure 5.2: Example of the evolution of velocities with p_n.

Fig. 5.2 shows an example of the evolution of velocities with respect to an independent impulse parameter required to address impact events. The analysis begins by assuming all impact points with a nonzero tangential velocity are slipping. If an initial tangential velocity is equal to zero, $\mathbf{C}$ is determined assuming that this point is sticking. The resulting impulses are checked to if they satisfy the sticking condition; see Sec. 5.2.4. If not, the point is assumed to be slipping and the analysis continues.

The numerical integration of $\mathbf{C}$ in (5.6) then begins to find a new value of $\mathbf{p}$. This value is substituted into the impulse-momentum relationship in (5.5) to determine new velocities of the impact points. These velocities are then converted into the cylindrical coordinates in (5.7), shown in Fig. 5.2. The goal is to evolve the velocities until a tangential velocity becomes equal to zero, or the final impulse is reached. If a tangential velocity crosses zero, then the stick-slip transition is evaluated to determine whether the impact point will slip or stick; an event function tracks s_i to catch a zero crossing. Again, it is assumed to stick and the resulting forces are checked. However, $\mathbf{C}$ must be re-evaluated each time any tangential velocity becomes equal to zero. Thus, the integration shown in (5.6) is not trivial. The end of the collision is specified using the global ECOR, which defines the value of the final impulse, p_{nf}. However, to find the final impulse, it is necessary to locate the impulse at the end of the compression phase, p_{nc}, as the integration progresses. The final and compression impulse will be discussed in Sec. 5.2.6.

Even if the integration in (5.6) reaches the final impulse, it is possible that the velocity of some impact points will still cause the surfaces to penetrate. In this case, a second impact event is triggered which will include only the impact points that are attempting to penetrate. The whole process is performed again for this subset of impact points. If some velocities in this second event are still attempting to penetrate the surfaces, a third event is triggered and so on until all points have post-impact velocities where they are not attempting to penetrate the surfaces. This is considered the end of the collision. Thus a collision may consist of several impact events.

At the end of the collision, it is possible that the surfaces may remain in contact with each other. In this case the impacts comprising the collision transition into a contact scenario. Sec. 5.3 will discuss how the transition from impact to contact is modeled in the proposed approach. In this work, it is necessary to address the transition from impact to contact to match some experimental data.

5.2 Friction, Rigid Body, and Energetic Constraints

This section discusses the derivation of **C** in (5.6) as well as the energetic termination condition for the impact events. During impact events, points may stick, slip or slip-reverse. The slip-state of any given impact point is characterized in terms of the sliding speed along the impact plane,

$$\begin{cases} s_i = 0 \quad \text{and} \quad \dot{s}_i = 0 & \text{sticking} \\ s_i = 0 \quad \text{and} \quad \dot{s}_i \neq 0 & \text{stick-slip transition} \\ s_i \neq 0 & \text{slipping} \end{cases} \tag{5.9}$$

where the subscript i refers to the impact point. In the literature, stick-slip behavior is represented as a set of complementarity conditions [27], which establish frictional force relationships for different slip states. These complementarity conditions are defined based on Coulomb fricton [27, 95, 117], and form the basis for the LCP, which are solved using optimization techniques [117, 118]. This work uses a similar set of complementarity conditions based on Coulomb friction law,

$$\begin{cases} \text{sticking} & dp_{t_i} \leq \mu_s \, dp_{z_i} \\ \text{stick} - \text{slip transition} & dp_{t_i} = \mu_s \, dp_{z_i} \\ \text{slipping} & dp_{t_i} = \mu_d \, dp_{z_i} \end{cases} \tag{5.10}$$

where $dp_{t_i} = \sqrt{{dp_{x_i}}^2 + {dp_{y_i}}^2}$, and $i = 1, ..., 4$. μ_s and μ_d are the static and dynamic coefficients of friction. The relations in (5.10) express the complementarity conditions in terms of force components, where dt is multiplied on both sides, leaving the differential impulses.

5.2.1 Frictional Constraint for Slipping

According to (5.10), if a given contact point i slips during an impact, the relationships between the tangential and normal differential impulses are given by,

$$\frac{dp_{x_i}}{dt} = -\mu_i \cos(\phi_i)\, \frac{dp_{z_i}}{dt} \qquad\qquad \frac{dp_{y_i}}{dt} = -\mu_i \sin(\phi_i)\, \frac{dp_{z_i}}{dt} \tag{5.11}$$

where $\mu_i = \mu_d$ is the coefficient of friction for point $i = 1, ..., 4$. The equations in (5.11) also govern the force relations during slip-reversal. The frictional constraints in (5.11) can be expressed as,

$$\begin{bmatrix} dp_{x_i} \;+\; \mu_i\; \cos(\phi_i)\; dp_{z_i} \\ dp_{y_i} \;+\; \mu_i\; \sin(\phi_i)\; dp_{z_i} \end{bmatrix} \;=\; U_i\, d\mathbf{p} \;=\; \mathbf{0} \tag{5.12}$$

5.2.2 Frictional Constraint for Sticking

If a contact point i sticks during impact, the sliding speed is constrained to be zero, $s_i = 0$, and therefore $v_{x_i} = v_{y_i} = 0$. The differential velocities of the sticking points are obtained from (5.5) as

$$d\boldsymbol{\vartheta} \;=\; M\; d\mathbf{p} \;=\; \begin{bmatrix} \mathbf{m}_{x_1}^T & \mathbf{m}_{y_1}^T & \mathbf{m}_{z_1}^T & \ldots \end{bmatrix}^T d\mathbf{p} \tag{5.13}$$

When an impact point sticks [22],

$$\begin{bmatrix} dv_{x_i} \\ dv_{y_i} \end{bmatrix} \;=\; \begin{bmatrix} \mathbf{m}_{x_i} \\ \mathbf{m}_{y_i} \end{bmatrix} d\mathbf{p} \;=\; U_i\, d\mathbf{p} \;=\; \mathbf{0} \tag{5.14}$$

5.2.3 Rigid-Body Constraints

In case of a single-point impacts, the differential impulses can be resolved just by using the slipping or sticking frictional constraints. However, for multi-point impact additional constraints are required for the distribution of the forces (differential impulses) to various contact points. This work uses the rigidity property of the impacting body to derive additional constraints. These constraints can be expressed in terms of the direction cosines associated with pairs of points on the rigid body,

$$\hat{\boldsymbol{\eta}} \;=\; \frac{(\mathbf{P}_{Oi} - \mathbf{P}_{Oj})}{||\mathbf{P}_{Oi} - \mathbf{P}_{Oj}||} \;=\; [\; \eta_x \;\; \eta_y \;\; \eta_z \;]^T \tag{5.15}$$

where $\mathbf{P}_{Oi}$ and $\mathbf{P}_{Oj}$ are the position vectors from the body-attached reference point O to the impact points $i, j = 1, ..., 4$, $i \neq j$. The relative motion of two impact points on the same rigid body must be equal to zero when observed from the body-attached reference frame and point, therefore

$$\begin{gathered} (\mathbf{v}_i - \mathbf{v}_j) \cdot \hat{\boldsymbol{\eta}} \;=\; 0 \\ (v_{x_i} - v_{x_j})\eta_x + (v_{y_i} - v_{y_j})\eta_y + (v_{z_i} - v_{z_j})\eta_z \;=\; \mathbf{w}_{ij}\, \boldsymbol{\vartheta} \;=\; 0 \end{gathered} \tag{5.16}$$

Equation (5.16) provides a constraint equation which relates the velocities of points i and j. The velocity projection method in Appendix A and [36–38] shows that velocity-level rigid-body constraints may be transformed into force-level constraints as,

$$\mathbf{w}_{ij}\, d\mathbf{p} \;=\; 0 \tag{5.17}$$

The rigid body constraint shown in (5.17) is an approximate force distribution law, which assumes no deformation in the body during impact. In reality, objects composed of any material would show some deformation during impact. So the assumption made here regarding the rigidity of the body is an idealization, that is admissible only for materials of high stiffness that exhibit negligible amounts of deformation under compression. This assumption significantly simplifies the analysis of multi-point impact analysis, and therefore is advantageous in the context of hybrid dynamic simulation.

5.2.4 Final Frictional and Rigid Body Constraints

Sections 5.2.1, 5.2.2, and 5.2.4 presented the frictional and rigid body constraints that can be imposed on the differential impulses. This section will demonstrate how these constraint may be used to resolve the differential impulses with respect to a single independent impulse parameter. In order to resolve the differential impulses for an n-point impact in terms of a single independent parameter, $n-1$ rigid body constraints and $2n$ frictional constraint are required. The frictional and rigid body constraints from (5.12), (5.14) and (5.17) for the example block in Fig. 5.1 can be expressed as,

$$H\,d\mathbf{p} \;=\; \begin{bmatrix} U_1 \\ \vdots \\ U_4 \\ \mathbf{w}_{14} \\ \mathbf{w}_{24} \\ \mathbf{w}_{34} \end{bmatrix} d\mathbf{p} \;=\; 0 \tag{5.18}$$

Note that the $\mathbf{w}_{ij}$ will always be linearly independent as long as $i \neq j$. The matrix $H \in \mathbb{R}^{11\times 12}$ is rank deficient by one row. The linearly dependent and independent columns of H can be separated as, $H \;=\; [H_s \;\; H_r]$. Where $H_s \in \mathbb{R}^{11\times 11}$ is a full rank matrix, $H_r \in \mathbb{R}^{11\times 1}$ is a linearly dependent column in H, such that

$$d\mathbf{p} \;=\; \begin{bmatrix} -H_s^{-1}H_r \\ 1 \end{bmatrix} dp_n \;=\; \mathbf{C}\,dp_n \tag{5.19}$$

where $\mathbf{C}$ relates all of the differential impulses to the single independent impulse parameter dp_n.

If $s_i = 0$, the differential impulses must satisfy the no-slip condition,

$$\sqrt{dp_{x_i}^2 \,+\, dp_{y_i}^2} \;\leq\; \mu_s\, dp_{z_i} \qquad \Longrightarrow \qquad \sqrt{C_{x_i}^2 \,+\, C_{y_i}^2} \;\leq\; \mu_s\, C_{z_i} \tag{5.20}$$

where C_{x_i}, C_{y_i} and C_{z_i} are the element of $\mathbf{C}$ associated with dp_{x_i}, dp_{y_i}, and dp_{z_i} respectively. Thus (5.20) implies that the slip state of an impact point is dependent on the friction and rigid body constraints, rather than the value of p_n. If the no-slip condition is not satisfied, then point i slips along a new direction $\hat{\phi}_i$. This is known as *Slip-Reversal*. The following section presents how this new slip direction $\hat{\phi}_i$ is calculated. Since this work considers rigid bodies, if two or more impact points stick, then sticking is enforced in all other contact points. Hence there can be only three possibility during stick-slip transition: 1) all points enter sticking, 2) a single point sticks, while the rest slip-reverse or 3) all points slip-reverse in some new directions. If the slip states of any of the impact points must be altered, H must be re-evaluated and all conclusions of sticking and slipping must be rechecked.

5.2.5 Stick-Slip Transition

This section presents the methods used in this work to solve for the unique and invariant slip-direction at stick-slip transition and during slip-reversal. The invariant slip direction at the stick-slip transition can only be solved by reformulating the differential velocities in (5.5) in cylindrical coordinates [41]. The tangential components of the cartesian differential velocities can be expressed in terms of cylindrical coordinates as,

$$\left.\begin{aligned} v_{x_i} &= s_i \cos(\phi_i) \\ v_{y_i} &= s_i \sin(\phi_i) \end{aligned}\right\} \implies \begin{bmatrix} dv_{x_i} \\ dv_{y_i} \end{bmatrix} = \underbrace{\begin{bmatrix} \cos(\phi_i) & -\sin(\phi_i) \\ \sin(\phi_i) & \cos(\phi_i) \end{bmatrix}}_{R} \begin{bmatrix} ds_i \\ s_i d\phi_i \end{bmatrix} \tag{5.21}$$

The cartesian coordinate differential velocities may be further expressed in terms of differential impulse parameters, as shown in (5.13). Also note that the transformation R in (5.21) is orthogonal. Hence the cylindrical coordinate differential velocities can be expressed as,

$$\begin{bmatrix} ds_i \\ s_i d\phi_i \end{bmatrix} = R^T \begin{bmatrix} dv_{x_i} \\ dv_{y_i} \end{bmatrix} = \begin{bmatrix} \cos(\phi_i) & \sin(\phi_i) \\ -\sin(\phi_i) & \cos(\phi_i) \end{bmatrix} \begin{bmatrix} \mathbf{m}_{x_i} \\ \mathbf{m}_{y_i} \end{bmatrix} d\mathbf{p} \tag{5.22}$$

When the point i enters stick-slip transition the sliding velocity s_i becomes zero and results in a change in sliding direction. The new sliding direction $\hat{\phi}_i$ can be calculated by substituting $s_i = 0$ in (5.22) and solving for ϕ_i, as shown in [22]. However this is a difficult task considering that (5.22) has nonlinear trigonometric functions of ϕ_i. Hence, these trigonometric functions are expressed in terms of differential impulse parameters using (5.11),

$$\cos(\phi_i) = -\frac{dp_{x_i}}{\mu_i dp_{z_i}} \qquad \sin(\phi_i) = -\frac{dp_{y_i}}{\mu_i dp_{z_i}}$$

Substituting these into (5.22) yields two equations,

$$\begin{bmatrix} ds_i \\ s_i d\phi_i \end{bmatrix} = -\frac{1}{\mu_i dp_{z_i}} \begin{bmatrix} dp_{x_i} & dp_{y_i} \\ -dp_{y_i} & dp_{x_i} \end{bmatrix} \begin{bmatrix} \mathbf{m}_{x_i} \\ \mathbf{m}_{y_i} \end{bmatrix} d\mathbf{p} \tag{5.23}$$

The stick-slip transition takes place when the sliding velocity s_i for any point i comes to rest. This situation may occur either 1) when a single contact point i comes to rest, $s_i = 0$ while all other points continue to slip or 2) when all contact points come to rest simultaneously. These scenarios are analyzed separately here.

5.2.5.1 Case: Single Point Enters Stick-Slip Transition

First, lets consider case when a single point $i = 1$ enters stick-slip transition, while the other points 2, 3, and 4 are in slip. This yields $s_1 = 0$, and consequently the first equation of (5.23) for the point $i = 1$ would be given by,

$$0 = \begin{bmatrix} dp_{x_1} & dp_{y_1} \end{bmatrix} \begin{bmatrix} \mathbf{m}_{y_1} \\ -\mathbf{m}_{x_1} \end{bmatrix} d\mathbf{p} \tag{5.24}$$

The frictional constraints on the other points and the rigid body constraints may be written in terms of matrix H^*, and partitioned into H_s^* and H_r^* as,

$$H^* d\mathbf{p} = \begin{bmatrix} U_2 \\ U_3 \\ U_4 \\ \mathbf{w}_{14} \\ \mathbf{w}_{24} \\ \mathbf{w}_{34} \end{bmatrix} d\mathbf{p} \;=\; H_s^* d\mathbf{p}_s + H_r^* \begin{bmatrix} dp_{x_1} \\ dp_{y_1} \\ dp_{z_1} \end{bmatrix} \;=\; \mathbf{0} \tag{5.25}$$

where $d\mathbf{p}_s$ are the differential impulse parameters of the points in slip. H_s^* and H_r^* are columns of H^*, corresponding to the slipping and stick-slip transition point differential impulses. Hence, solving for the impulses using (5.25) and substituting into (5.24) yields,

$$
\begin{aligned}
0 &= \begin{bmatrix} dp_{x_1} & dp_{y_1} \end{bmatrix} \overbrace{\begin{bmatrix} \mathbf{m}_{y_i} \\ -\mathbf{m}_{x_i} \end{bmatrix} \begin{bmatrix} -(H_s^*)^{-1} H_r^* \\ I \end{bmatrix}}^{Q} \begin{bmatrix} dp_{x_1} \\ dp_{y_1} \\ dp_{z_1} \end{bmatrix} \\
&= \begin{bmatrix} dp_{x_1} & dp_{y_1} \end{bmatrix} \left(Q_o \begin{bmatrix} dp_{x_1} \\ dp_{y_1} \end{bmatrix} + Q_r dp_{z_1} \right)
\end{aligned}
\tag{5.26}
$$

where,

$$
Q = \left[\begin{array}{cc:c} Q_{11} & Q_{12} & Q_{13} \\ Q_{21} & Q_{22} & Q_{23} \end{array} \right] = \left[\begin{array}{c:c} Q_o & Q_r \end{array} \right]
$$

When a contact point enters stick-slip transition, the tangential differential impulses on the point are related to the normal differential impulse according to coulomb law of slipping friction. However the slip direction changes to $\phi_i = \hat{\phi}_i$, which is an unique direction such that $s_i = 0$ and $ds_i > 0$ at stick-slip transition. Therefore the tangential differential impulses during stick-slip transition may be normalized by the normal differential impulse parameters as,

$$
\begin{bmatrix} dp_{x_1} \\ dp_{y_1} \end{bmatrix} = dp_{z_1} \begin{bmatrix} d\hat{p}_{x_1} \\ d\hat{p}_{y_1} \end{bmatrix}
\tag{5.27}
$$

Now, substituting (5.27) into (5.26) and diving through with $dp_{z_1}^2$ yields,

$$
0 = \begin{bmatrix} d\hat{p}_{x_1} & d\hat{p}_{y_1} \end{bmatrix} Q_o \begin{bmatrix} d\hat{p}_{x_1} \\ d\hat{p}_{y_1} \end{bmatrix} + Q_r^T \begin{bmatrix} d\hat{p}_{x_1} \\ d\hat{p}_{y_1} \end{bmatrix}
\tag{5.28}
$$

Also, based on the Coulomb slipping friction law the normalized differential impulses form the constraint,

$$
d\hat{p}_{x_1}^2 + d\hat{p}_{y_1}^2 = \mu_1^2
\tag{5.29}
$$

Next, lets define a variable $u = \tan\phi_1$, which represents the tangent of the unknown slip-direction such that, $d\hat{p}_{y_1} = ud\hat{p}_{x_1}$, then (5.28) and (5.29) may be rewritten as,

$$\begin{gathered}\left[Q_{22}u^2 + \left(Q_{12} + Q_{21}\right)u + Q_{11}\right]d\hat{p}_{x_1} + \left(Q_{13} + uQ_{23}\right) = 0 \\ \left(1 + u^2\right)d\hat{p}_{x_1}^2 = \mu_1^2\end{gathered} \tag{5.30}$$

Now solving the two equations in (5.30) to eliminate $\hat{p}_{x_1}$, yields a quartic polynomial equation of a single variable,

$$c_0u^4 + c_1u^3 + c_2u^2 + c_3u + c_4 = 0 \tag{5.31}$$

where c_0, c_1, c_2, c_3 and c_4 are coefficients formed by the elements of the matrix Q and the coefficient of friction μ_i.

Equation (5.31) has four roots u_k where $k = 1, .., 4$, each of which is associated to a slip direction $\hat{\phi}_{1k} = \tan^{-1}u_k$, known as *isoclines* [22]. The roots of the quartic equation (5.31) can be calculated by forming a Frobenius companion matrix.

$$L = \begin{bmatrix} 0 & 0 & 0 & -{}^{c_4}\!/_{c_0} \\ 1 & 0 & 0 & -{}^{c_3}\!/_{c_0} \\ 0 & 1 & 0 & -{}^{c_2}\!/_{c_0} \\ 0 & 0 & 1 & -{}^{c_1}\!/_{c_0} \end{bmatrix} \tag{5.32}$$

The Frobenius Companion matrix L would yield a characteristic equation identical to the quartic equation (5.31). Therefore the eigenvalues of L, λ_k are equal to the roots of the quartic polynomial in (5.31). So, the four roots of (5.31) are $u_k = \lambda_k$ for $k = 1, ..., 4$. Using the Coulomb friction relation in (5.29) and the relation $d\hat{p}_{y_1} = ud\hat{p}_{x_1}$, the tangential differential impulses of the point in stick-slip transition are given by,

$$d\hat{p}_{x_{1k}} = -\frac{\mu_1}{\sqrt{1 + u_k^2}} \qquad\qquad d\hat{p}_{y_{1k}} = -\frac{\mu_1 u_k}{\sqrt{1 + u_k^2}}$$

Thus, the *isocline* associated with each root of (5.31) can be calculated as,

$$\hat{\phi}_{1k} = \tan^{-1}\left(\frac{d\hat{p}_{y_{1k}}}{d\hat{p}_{x_{1k}}}\right) \tag{5.33}$$

Based on the criteria for slip-reversal, if the contact point continues to slip after stick-slip transition the slip-direction is reset to one of the isoclines. This selection is made by computing $\frac{ds_1}{dp_{z_1}}(\phi_{1k})$ using the second equation form (5.23) and checking if the differential tangential work is negative for a given isocline ϕ_{1k},

$$\text{if} \qquad \frac{ds_1}{dp_{z_1}}(\phi_{1k}) > 0 \qquad \text{and} \qquad dW_t(\phi_{1k}) < 0 \qquad \text{then} \qquad \phi_1 = \hat{\phi}_{1k} \tag{5.34}$$

for $k = 1, ..., 4$. $dW_t(\phi_{1k})$ is the differential tangential work for the given isocline. The differential tangential work is must be negative. Note that, it may be still possible to have more than slip direction remaining, even after eliminating certain isoclines based on (5.34). In such a situation, the unique slip direction $\hat{\phi}$ is chosen as the one that results in least amount of energy loss due to friction, or $\phi_1 = \underset{\phi_{1k}}{\operatorname{argmin}} - dW_t(\phi_{1k})$.

5.2.5.2 Case: All Points Enter Stick-Slip Transition

A different scenario may arise such that multiple contact points enter stick-slip transition simultaneously. Note, that this case may only occur when all of the contact points are impacting the same plane, or in other words, the normal velocity/force direction for all of the points are parallel to each other. In case of impacts involving multiple impact planes (*viz.* a block simultaneously impacting a wall and a floor), the tangential velocity of one contact point depends upon the normal velocity of another contact point. Therefore, in this case, if multiple contact point simultaneously enters stick-slip transition, the normal velocity components for these points must also be zero. Note that the only way the normal velocities of these contact points can be simultaneously zero in this configuration, would be if all initial velocities were zero at the beginning of the impact event, which contradicts the definition of impacts (initial normal velocities for an impact event must be negative).

On the other hand, if all contact point impacting a common impact plane simultaneously enter stick-slip transition, it would be necessary to evaluate the slip-direction for all these point at this instant. Based on the rigidity assumption, a natural conclusion for this situation is that the tangential velocities of all of the contact points must be zero, and consequently all slip-directions ϕ_i are unknown. Although this scenario requires the solution for all four contact points simultaneously, the number of unknown variable in this problem can be reduced by taking advantage of the fact that all of contact point accelerations are related to one another. Let us consider an independent contact point $j = 4$, having an acceleration $\dot{\mathbf{v}}_j$ then all other contact point accelerations are defined by the relationship,

$$\dot{\mathbf{v}}_k = \dot{\mathbf{v}}_j + \dot{\mathbf{\Omega}} \times \mathbf{P}_{jk} + \mathbf{\Omega} \times (\mathbf{\Omega} \times \mathbf{P}_{jk}) \tag{5.35}$$

where $k = 1, 2, 3$. $\mathbf{\Omega} = \begin{bmatrix} 0 & 0 & \omega \end{bmatrix}^T$ and $\dot{\mathbf{\Omega}}$ are the angular velocities and accelerations of the body. $\mathbf{P}_{jk} = [x_{jk}, y_{jk}, z_{jk}]^T$ is the position vector between the points j and k. At the stick-slip transition, the sliding speed of the contact points vanishes to $s_i = 0$. This implies that the angular velocity of the body at stick-slip transition should also vanish, $\mathbf{\Omega} = \mathbf{0}$. Therefore, the tangential acceleration components of the contact points $k = 1, 2, 3$ based on (5.35), may be written in differential form as,

$$\begin{bmatrix} dv_{x_k} \\ dv_{y_k} \end{bmatrix} = \begin{bmatrix} dv_{x_j} \\ dv_{y_j} \end{bmatrix} + \begin{bmatrix} -d\omega y_{jk} \\ d\omega x_{jk} \end{bmatrix} \tag{5.36}$$

Thus, the tangential components of the differential velocities of all contact points may be rewritten in terms of the impulses as,

$$\begin{bmatrix} dv_{x_1} \\ dv_{y_1} \\ \vdots \\ dv_{x_4} \\ dv_{y_4} \end{bmatrix} = S \begin{bmatrix} dv_{x_j} \\ dv_{y_j} \\ d\omega \end{bmatrix} = \underbrace{\begin{bmatrix} \mathbf{m}_{x_1} \\ \mathbf{m}_{y_1} \\ \vdots \\ \mathbf{m}_{x_4} \\ \mathbf{m}_{y_4} \end{bmatrix}}_{M_t} d\mathbf{p} \tag{5.37}$$

where S is a matrix containing the coefficients from (5.35). The differential impulses $d\mathbf{p}$ may be resolved using the rigid body constraints,

$$H^* d\mathbf{p} = \begin{bmatrix} \mathbf{w}_{14} \\ \mathbf{w}_{24} \\ \mathbf{w}_{34} \end{bmatrix} d\mathbf{p} = \begin{bmatrix} H_s^* & H_r^* \end{bmatrix} \begin{bmatrix} d\mathbf{p}_s \\ d\mathbf{p}_r \end{bmatrix} = \mathbf{0} \tag{5.38}$$

where,

$$d\mathbf{p}_s = [dp_{z_1} \;\; dp_{z_2} \;\; dp_{z_3}]^T \quad \text{and} \quad d\mathbf{p}_r = [dp_{x_1} \;\; dp_{y_1} \;\; \ldots \;\; dp_{x_4} \;\; dp_{y_4} \;\; dp_{z_4}]^T$$

Now (5.37) may be expressed in terms of $d\mathbf{p}_r$ as,

$$S \begin{bmatrix} dv_{x_j} \\ dv_{y_j} \\ d\omega \end{bmatrix} = \underbrace{M_t \begin{bmatrix} -(H_s^*)^{-1} H_r^* \\ I \end{bmatrix}}_{G} d\mathbf{p}_r = \begin{bmatrix} G_s & G_r \end{bmatrix} \begin{bmatrix} d\mathbf{p}_t \\ dp_n \end{bmatrix} \tag{5.39}$$

where G_s and G_r are the dependent and independent columns of the matrix G. The vector $d\mathbf{p}_r$ is further partitioned into $d\mathbf{p}_t$ and the independent impulse parameter $dp_n = dp_{z_4}$. Hence, from (5.39) the dependent impulses may be solved as,

$$d\mathbf{p}_t = \left[\begin{array}{c:c} (G_s)^{-1}S & -(G_s)^{-1}G_r \end{array}\right] \begin{bmatrix} dv_{x_j} \\ dv_{y_j} \\ d\omega \\ dp_n \end{bmatrix} \tag{5.40}$$

Thus, the differential impulses $d\mathbf{p}$ on the system during stick slip transition may be resolved in terms of
$\mathbf{u} = \begin{bmatrix} \frac{dv_{x_j}}{dp_n} & \frac{dv_{y_j}}{dp_n} & \frac{d\omega}{dp_n} & 1 \end{bmatrix}^T$ as,

$$d\mathbf{p} = \underbrace{\begin{bmatrix} -(H_s^*)^{-1}H_r^* \\ I \end{bmatrix} \left[\begin{array}{c:c} (G_s)^{-1}S & -(G_s)^{-1}G_r \\ \hdashline \multicolumn{2}{c}{0 \;\; \ldots \;\; 0 \;\; 1} \end{array}\right]}_{\Lambda} \mathbf{u}\, dp_n \;\; = \begin{bmatrix} \mathbf{\Lambda}_{x_i} \\ \mathbf{\Lambda}_{y_i} \\ \vdots \\ \mathbf{\Lambda}_{z_4} \end{bmatrix} \mathbf{u}\, dp_n \tag{5.41}$$

Therefore, the tangential impulses for point $i = 1, ..., 4$ would be given by,

$$dp_{x_i} = \mathbf{\Lambda}_{x_i}\mathbf{u}\, dp_n \qquad dp_{y_i} = \mathbf{\Lambda}_{y_i}\mathbf{u}\, dp_n \tag{5.42}$$

The sliding speeds at all contact points vanishes, if all of the contact points simultaneously enter stick-slip transition. Thus, setting $s_i = 0$ for all contact points $i = 1, ..., 4$ in (5.23) yields,

$$0 = \begin{bmatrix} dp_{x_i} & dp_{y_i} \end{bmatrix} \begin{bmatrix} \mathbf{m}_{y_1} \\ -\mathbf{m}_{x_1} \end{bmatrix} d\mathbf{p} \tag{5.43}$$

Now substituting (5.41) and (5.42) in (5.43) and dividing both sides by ${dp_n}^2$ yields,

$$0 = \mathbf{u}^T \underbrace{\begin{bmatrix} {\mathbf{\Lambda}_{x_i}}^T & {\mathbf{\Lambda}_{y_i}}^T \end{bmatrix} \begin{bmatrix} \mathbf{m}_{y_i} \\ -\mathbf{m}_{x_i} \end{bmatrix} \Lambda}_{Q_i} \mathbf{u} \tag{5.44}$$

for the contact points $i = 1, ..., 4$.

Now, in order to solve for the invariant slip-direction the solution to $\mathbf{u}$ needs to be computed by simultaneously solving the quadratic form expression in (5.44) for all four contact points $i = 1, ..., 4$. This poses a multipolynomial root finding problem. Equation (5.44) can be rewritten as set of multipolynomial system in terms of $\bar{\mathbf{u}} = \begin{bmatrix} u_1 & u_2 & u_3 \end{bmatrix}$ as,

$$\begin{aligned} f_1(u_1, u_2, u_3) &= 0 \\ f_2(u_1, u_2, u_3) &= 0 \\ f_3(u_1, u_2, u_3) &= 0 \\ f_4(u_1, u_2, u_3) &= 0 \end{aligned} \tag{5.45}$$

where $u_1 = \frac{dv_{x_1}}{dp_n}$, $u_2 = \frac{dv_{y_1}}{dp_n}$, and $u_3 = \frac{d\omega}{dp_n}$. Since, it is important to locate all possible roots of (5.44), traditional line-search based root-finding methods such as Newton-Raphson, Secant or Broyden methods are not adequate, as they only converge to one among the many possible solutions, subject to good initial guess. Hence, the feasible solution set for the given multi-polynomial system requires a slightly more sophisticated treatment. Appendix. B shows a general procedure for computing all roots of a multi-polynomial system.

Note that the solutions $\bar{\mathbf{u}}_k = [u_{1_k}, u_{2_k}, u_{3_k}]^T$ thus obtained for (5.45) may contain both real and complex solutions. Only the real solutions are admissible for the calculation of the unknown slip-direction. Hence, using the real solutions $\bar{\mathbf{u}}_k$, the *isoclines* $\hat{\phi}_{i_k}$ for each point may be calculated.

$$\hat{\phi}_{ik} = \tan^{-1}\left(\frac{\mathbf{\Lambda}_{x_i}\mathbf{u}_k}{\mathbf{\Lambda}_{y_i}\mathbf{u}_k}\right) \qquad \text{where} \qquad \mathbf{u}_k = \begin{bmatrix} \bar{\mathbf{u}}_k \\ 1 \end{bmatrix} \tag{5.46}$$

Finally, the unique slip-directions $\hat{\phi}_i$ are selected from the set of isoclines based on the criteria,

$$\text{if} \quad \begin{cases} ds_1(\hat{\phi}_{i_k}) > 0 \\ ds_2(\hat{\phi}_{i_k}) > 0 \\ ds_3(\hat{\phi}_{i_k}) > 0 \\ ds_4(\hat{\phi}_{i_k}) > 0 \end{cases} \quad \text{and} \quad dW_t(\phi_{ik}) < 0 \quad \text{then} \quad \hat{\phi}_i = \hat{\phi}_{i_k} \tag{5.47}$$

Similar, to the single-point stick-slip transition case, it is possible to end up with more than one feasible solution set for the given multipolynomial system. In such cases the solution is selected from the feasible set as the one that results in the least amount of energy loss due to frictional forces.

5.2.6 Energetic Termination of Impact Events

In non-smooth impact models, the post-impact velocities are characterized in terms of a coefficient of restitution (COR) parameter. There are three types of COR: Newton's COR (Kinematic), Poisson's COR (Impulsive) and Stronge's ECOR (Energetic). Newton's COR has been known for yielding in energy gain for certain frictional impacts [18, 19]. Glocker showed that Newton's COR can violate energy consistency for certain types mechanisms, and developed a method for determining the bounds of COR that ensures energy consistency, based on the condition number of the Delaussus matrix [119]. Poisson's COR has been generally proven to ensure energy consistency for frictional systems and for systems containing one single frictional contact [119]. However, it has been shown that Poisson's COR can lead to energy gains for systems with more than one frictional contact [119]. Stronge's ECOR on the other hand always ensures energy consistency, since this type of COR directly enforces a constraint on the energy of the system [2, 22, 33]. This work uses a global energetic coefficient of restitution based on the Stronge's ECOR. The global energetic coefficient of restitution enforces a constraint on the energy dissipation throughout the system, unlike the standard Stronge's ECOR which constrains the energy dissipation at each contact point.

This section discusses the criterion for terminating an impact event which defines the final impulse, p_{nf}, and compression impulse, p_{nc}, that were discussed toward the end of Sec. 5.1. The energetic constraint used in this work is based on Stronge's ECOR [22, 26, 32]. Stronge's ECOR places an energetic constraint on the normal work, which is an extension of the restitution expression given by Boulanger [30] and Routh [31]. In Stronge's approach, impact events take place in two phases, *compression* and *restitution*. The ECOR determines energy loss in the system. However, it was originally formulated for single point impacts. This work uses an extension of this concept, the *global* ECOR, which determines the system energy loss for multi-point impacts.

The expression for the normal work during impact may be expressed as the summation of the energy dissipation at all of the contact points given by,

$$\begin{aligned} W_n &= \int_0^{z_1} f_{z_1} dz_1 + \ldots + \int_0^{z_4} f_{z_4} dz_4 \\ &= \int_0^{p_{z_1}} dp_{z_1} \frac{dz_1}{dt} + \ldots + \int_0^{p_{z_4}} dp_{z_4} \frac{dz_4}{dt} \end{aligned} \tag{5.48}$$

This yields the expression,

$$W_n(p_n) = \int_0^{p_n} \boldsymbol{\vartheta}(p_n)^T \mathbf{C}_n \, dp_n \tag{5.49}$$

where $\boldsymbol{\vartheta}_n(p_n)$ and $\mathbf{C}_n$ are the normal components from the vectors $\boldsymbol{\vartheta}(p_n)$ and $\mathbf{C}$ respectively. The normal work is a piecewise quadratic curve with respect to the independent impulse parameter p_n, as shown in Fig. 5.3. The normal work generally decreases during the *compression phase* and starts to increase in *restitution phase*. Hence, the compression phase ends when the normal work assumes a minimum value W_{nc}, given by,

$$W_{nc} = \min\left(W_n(p_n)\right) \quad \longrightarrow \quad p_n\left(W_{nc}\right) = p_{nc} \tag{5.50}$$

where p_{nc} is the impulse at the end of the compression phase.

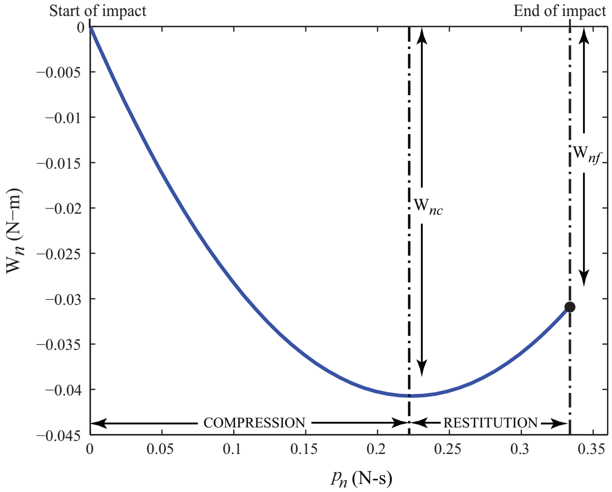

Figure 5.3: Example of a normal work plot.

It is difficult to find p_{nc} analytically, because of the integration involved. Hence, the value of p_{nc} and $W_{nc} = W_n(p_{nc})$ is found by numerically integrating (5.6) along with (5.49), and using an event-location scheme to terminate this integration when the condition in (5.50) is satisfied. The value of the normal work at the end of the compression phase, W_{nc}, can be related to W_{nf}, the normal work value at the end of the impact event, as

$$W_{nf} \;=\; (1 - {e_*}^2)\, W_{nc} \tag{5.51}$$

where $e_* \in [-1, 1]$ is the global ECOR. Unlike the traditional ECOR which $\in [0, 1]$, the global ECOR may assume negative values. A negative value occurs when the impact event terminates before the end of compression. Termination of impact events before full compression is reached is a feature of multi-point impact analysis, and is not relevant for single point impacts. This situation occurs when some impact points begin to separate while the other points continue to be in impact. This type of impact event is typically followed by another impact event involving only the points that remain in impact ($v_{n_i} < 0$) at the end of the preceding impact event.

The global ECOR parameter e_* is used to impose a constraint on the total energy dissipation of the system during collision. Therefore, an $e_* \in [-1, 1]$ always guarantees the energy consistency for simultaneous multi-point impact analysis. The objective of this work is not to quantify or characterize this parameter, rather it is to use this definition of coefficient to restitution and adjust its value to obtain simulation results, that can be either compared against experimental results or qualitatively analyzed for validity. The global ECOR, similar to other definitions of coefficient of restitution (e.g. Newton's, Poisson's or Stronge's), is fitting parameter, that can be determined experimentally. However, since e_* is a system level parameter, its experimental determination may require the control of a multitude of variable viz. material properties, contact geometries, configurations, initial speeds and accelerations, etc.

The value of the independent impulse parameter at the end of the restitution phase p_{nf} is the solution of the integral equation in (5.49) for a normal work value of W_{nf}. Similar to p_{nc}, the value of p_{nf} is found using event location during the numerical integration of (5.6) and (5.49). Since $W_n(p_n)$ is a piece-wise quadratic function, for any given value of W_{nf}, there must exist atleast two solutions of p_{nf}, $p_{nf} < p_{nc}$ and $p_{nf} > p_{nc}$. The velocities at the end of the collision are used as the initial conditions when the time-domain integration is restarted.

5.3 Transition from Impact to Contact

Typically, surfaces rebound after a collision, but after the energy is lost in successive collisions, the amount of rebound decreases. As the magnitude of the normal velocities for the rebound decrease, the time duration between impacts essentially converges to zero. This results in an accumulation of impact events and causes the numerical integrator to stop or fail. This situation is known as *chattering* or the *zeno phenomenon* and is a feature of hybrid dynamic simulation. This situation is sometimes addressed using more advanced numerical schemes [68–71]. However use of such numerical schemes would neglect the dynamics of the system engaged in sustained contact, which is well understood. Hence, in this work the idea is to transition to a contact mode by enforcing some constraints based on the non-penetrability criteria and Coulomb friction, when the simulation starts to chatter.

The criteria used in this work for enforcing these contact constraints constraints is given by,

$$\begin{cases} |v_{z_i}(t)| \le \epsilon_v \quad \text{and} \quad \dot{v}_{z_i}(t) < 0 & \text{Contact} \\ \\ v_{z_i}(t) < -\epsilon_v \quad \text{and} \quad \dot{v}_{z_i}(t) < 0 & \text{Impact} \\ \\ v_{z_i}(t) > \epsilon_v \quad \text{or} \quad \dot{v}_{z_i}(t) > 0 & \text{Separation} \end{cases} \tag{5.52}$$

where ϵ_v is a small threshold value selected to determine if the contact points have near-zero normal velocity. During contact, the non-penetrability constraint must always be satisfied. However, similar to the impulse-domain analysis, the frictional constraints can switch during contact depending upon whether a contact point sticks or slips. In the proposed method, the contact constraint forces are first calculated by assuming all of the contact points are sticking. Then the reaction forces are checked using the Coulomb friction law to identify contact points that are slipping. Finally, sliding frictional forces are enforced for the sliding points.

Initially, during a no-rebound contact phase, all of the points satisfying the contact criteria in (5.52) are assumed to be sticking. Therefore both the tangential and normal components of velocity are constrained to be equal to zero. Consider the velocities $\boldsymbol{\vartheta}_c$ and accelerations $\dot{\boldsymbol{\vartheta}}_c$ of a set of contact points c that satisfies the contact constraint in (5.52),

$$\mathbf{0} = \boldsymbol{\vartheta}_c = [\, v_{x_1} \;\; v_{y_1} \;\; v_{z_1} \;\; \cdots \,]^T = J_c\, \dot{\mathbf{q}} \tag{5.53}$$

and,

$$\mathbf{0} = \dot{\boldsymbol{\vartheta}}_c = [\, \dot{v}_{x_1} \;\; \dot{v}_{y_1} \;\; \dot{v}_{z_1} \;\; \cdots \,]^T = J_c\, \ddot{\mathbf{q}} + \dot{J}_c\, \dot{\mathbf{q}} \tag{5.54}$$

where J_c is the Jacobian matrix associated with $\boldsymbol{\vartheta}_c$. Substituting the expression for $\ddot{\mathbf{q}}$ from (5.2),

$$\mathbf{0} \;=\; J_c\, A^{-1} {J_c}^T \mathbf{F} \;-\; J_c A^{-1} \left(\mathbf{b}(\mathbf{q},\dot{\mathbf{q}}) \;+\; \mathbf{g}(\mathbf{q})\right) \;+\; \dot{J}_c\, \dot{\mathbf{q}} \tag{5.55}$$

Similar to the impulse domain analysis, the contact forces $\mathbf{F}$ are constrained by the rigid body and frictional constraints. The contact constraint forces may be resolved as,

$$\mathbf{F} \;=\; [\, f_{x_1} \;\; f_{y_1} \;\; f_{z_1} \;\; \ldots \;\; f_{x_4} \;\; f_{y_4} \;\; f_{z_4} \,]^T \;=\; \mathbf{C}\, F_r \tag{5.56}$$

where F_r is an independent force parameter. The vector $\mathbf{C}$ constrains the forces based on the Coulomb friction and the rigid body constraints, as shown in Sec. 5.2. First $\mathbf{C}$ is computed considering all of the contact points to be in sticking, then the no-slip condition in (5.20) is checked to identify the points that slipping. If a contact point sticks, both tangential and normal components of the velocity and acceleration for the point is constrained to be zero. When a contact point slips, the tangential velocities have unknown non-zero values. Thus, the velocity and acceleration constraints in (5.53) and (5.54) need to be restricted to only the normal components for the slipping points. The tangential forces are then given by Coulomb's friction law.

Enforcing the slip and no-slip constraints is accomplished by partitioning the reaction forces as follows:

$$\mathbf{F} \;=\; \begin{bmatrix} \mathbf{F}_{slip} \\ \mathbf{F}_{stick} \end{bmatrix} \;=\; S_c \begin{bmatrix} \mathbf{F}_{slip_n} \\ \mathbf{F}_{stick} \end{bmatrix} \tag{5.57}$$

where $\mathbf{F}_{slip}$ and $\mathbf{F}_{stick}$ are the forces at the contact points that are slipping and sticking, respectively and $\mathbf{F}_{slip_n}$ are the normal forces at the points i that are slipping,

$$\mathbf{F}_{slip} \;=\; [\, f_{x_1} \;\; f_{y_1} \;\; f_{z_1} \;\; \cdots]^T \qquad \mathbf{F}_{slip_n} \;=\; [\, f_{z_1} \;\; \cdots]^T \tag{5.58}$$

In (5.57) the matrix S_c relates the normal forces of the slipping points to the tangential forces using the equality relation of the Coulomb friction law,

$$S_c = \left[\begin{array}{cc|c} -\mu_i \cos(\phi_i) & 0 & \multirow{2}{*}{0} \\ -\mu_i \sin(\phi_i) & 0 & \\ \hline \multicolumn{2}{c|}{0} & \mathrm{I} \end{array}\right] \tag{5.59}$$

where $\mu_i = \mu_d$ is the dynamic coefficient of friction at point i, and I is an identity matrix. Equation (5.59) shows the matrix S_c as if i refers to a single point, but it should be suitably adjusted when considering more than one point.

Using the dual property of the Jacobian matrix, the generalized active forces, $\mathbf{\Gamma}$ in (5.2), are related to the constraint forces as

$$\mathbf{\Gamma} = J_c^T \, \mathbf{F} = J_c^T \, S_c \begin{bmatrix} \mathbf{F}_{slip_n} \\ \mathbf{F}_{stick} \end{bmatrix} \tag{5.60}$$

Based on the dual property of the Jacobian matrix, as shown in the Appendix A, the force constraint in (5.60) may be written as a velocity constraint,

$$\mathbf{0} = \begin{bmatrix} \boldsymbol{\vartheta}_{stick} \\ \boldsymbol{\vartheta}_{slip_n} \end{bmatrix} = S_c^T \, J_c \, \dot{\mathbf{q}} = J_{\mathrm{I}} \, \dot{\mathbf{q}}_{\mathrm{I}} + J_{\mathrm{D}} \, \dot{\mathbf{q}}_{\mathrm{D}} \tag{5.61}$$

where $\boldsymbol{\vartheta}_{stick}$ refers to both the normal and tangential velocity components of the points that are sticking, $\boldsymbol{\vartheta}_{slip_n}$ refers to only the normal velocity components of the points that are slipping, and $\dot{\mathbf{q}}_{\mathrm{D}}$ and $\dot{\mathbf{q}}_{\mathrm{I}}$ are the dependent and independent generalized speeds.

In (5.61), the matrix $S_c^T \, J_c$ is partitioned as $S_c^T \, J_c = QR = Q \begin{bmatrix} R_{\mathrm{D}} & R_{\mathrm{I}} \end{bmatrix} = \begin{bmatrix} J_{\mathrm{D}} & J_{\mathrm{I}} \end{bmatrix}$ with the help of the QR decomposition with column pivoting. Now $\dot{\mathbf{q}}$ and $\ddot{\mathbf{q}}$ can be expressed as

$$\dot{\mathbf{q}} = \begin{bmatrix} \dot{\mathbf{q}}_{\mathrm{D}} \\ \dot{\mathbf{q}}_{\mathrm{I}} \end{bmatrix} = \begin{bmatrix} -J_{\mathrm{D}}^{-1} J_{\mathrm{I}} \\ \mathrm{I} \end{bmatrix} \dot{\mathbf{q}}_{\mathrm{I}} = G \, \dot{\mathbf{q}}_{\mathrm{I}} \tag{5.62}$$

and,

$$\ddot{\mathbf{q}} \;=\; G\,\ddot{\mathbf{q}}_{\mathrm{I}} \;+\; \dot{G}\,\dot{\mathbf{q}}_{\mathrm{I}} \tag{5.63}$$

where

$$\dot{G}\,\dot{\mathbf{q}}_{\mathrm{I}} \;=\; \begin{bmatrix} -J_{\mathrm{D}}^{-1}\left(\dot{S}_c^T J_c + S_c^T \dot{J}_c\right)\dot{\mathbf{q}} \\ 0 \end{bmatrix} \tag{5.64}$$

Substituting (5.61) and (5.63) into (5.2) and pre-multiplying with G^T yields,

$$G^T\,A\,G\,\ddot{\mathbf{q}}_{\mathrm{I}} \;+\; G^T\left(A\,\dot{G}\,\dot{\mathbf{q}}_{\mathrm{I}} \;+\; \mathbf{b} \;+\; \mathbf{g}\right) \;=\; G^T J_c^T S_c \begin{bmatrix} \mathbf{F}_{slip_n} \\ \mathbf{F}_{stick} \end{bmatrix} \tag{5.65}$$

From (5.61) and (5.62), it can be easily shown that,

$$G^T J_c^T S_c \;=\; 0 \tag{5.66}$$

Hence, the reduced set of equations of motion are given by,

$$G^T\,A\,G\,\ddot{\mathbf{q}}_{\mathrm{I}} \;+\; G^T\left(A\,\dot{G}\,\dot{\mathbf{q}}_{\mathrm{I}} \;+\; \mathbf{b} \;+\; \mathbf{g}\right) \;=\; \mathbf{0} \tag{5.67}$$

Thus, during contact (5.67), (5.62) and (5.63) are used to integrate the states of dynamic system. Hence the *time-domain* equations of motion (EOM) during contact can be summarized as,

$$\left\{\begin{array}{ll} \text{EOM :} & G^T\,A\,G\,\ddot{\mathbf{q}}_{\mathrm{I}} \;+\; G^T\left(A\,\dot{G}\,\dot{\mathbf{q}}_{\mathrm{I}} \;+\; \mathbf{b} \;+\; \mathbf{g}\right) \;=\; \mathbf{0} \\ \text{where} & \ddot{\mathbf{q}}_{\mathrm{I}} = -(G^T A G)^{-1} G^T (A\dot{G}\dot{\mathbf{q}}_{\mathrm{I}} + \mathbf{b}(\mathbf{q},\dot{\mathbf{q}}) + \mathbf{g}(\mathbf{q})) \\ \text{and} & \dot{\mathbf{q}} = G\dot{\mathbf{q}}_{\mathbf{I}}, \quad G = \begin{bmatrix} -J_{\mathrm{D}}^{-1} J_{\mathrm{I}} \\ \mathrm{I} \end{bmatrix}, \\ & \dot{G}\,\dot{\mathbf{q}}_{\mathrm{I}} \;=\; \begin{bmatrix} -J_{\mathrm{D}}^{-1}\left(\dot{S}_c^T J_c + S_c^T \dot{J}_c\right)\dot{\mathbf{q}} \\ 0 \end{bmatrix} \end{array}\right. \tag{5.68}$$

Note that when the system is not in contact at any point the matrix ${S_c}^T J_c \;=\; [J_{\mathrm{D}} \;\; J_{\mathrm{I}}]$ is empty. Consequently, $G \;=\; I$, where I is an identity matrix and $\dot{G} \;=\; 0$. Substituting these back into (5.68), gives back (5.2) with the right-hand side (forcing terms) set to zero. Hence, (5.68) represents both the constrained and unconstrained *time-domain* dynamics of the system.

CHAPTER 6

SIMULATIONS OF CONTACT AND IMPACT IN SPATIAL RIGID SYSTEMS

6.1 Simulation Technique

This section discusses the techniques used in this work to simulate the aforementioned hybrid dynamic system, in which the dynamics evolve while switching back and forth between the *impulse domain* and the *time domain*. The simulation is initialized with a set of initial conditions on the generalized coordinates $\mathbf{q}(0)$ and generalized speed $\dot{\mathbf{q}}(0)$. The first step is to identify a set of contact points (if any) indexed i, such that, $z_i \leq 0$, $v_{z_i} \leq \epsilon_v$ and $\dot{v}_{z_i} < 0$. The parameter ϵ_v is a small threshold value used to determine if $|v_{z_i}| \to 0$. Next all these contact points are checked for the impact criteria, i.e. $v_{z_i} < -\epsilon_v$, in accordance to (5.52). If one or more contact point(s) test positive to the impact criteria in (5.52), the impulse domain analysis is performed considering all of the contact points. The contact point velocities are numerically integrated using the differential equations in (5.6). The numerical integration is terminated using an event-location scheme. The contact point velocities are rechecked at the end of the impact event. If the normal velocities of any of the contact points remain $v_{z_i} < -\epsilon_v$, a following impact event takes place involving only the contact points with $v_{z_i} < -\epsilon_v$. This process is repeated until all of the contact point velocities are $v_{z_i} > -\epsilon_v$. The post-impact velocities thus obtained, are then used to initialize the *time-domain* dynamics. The *time-domain* dynamics is represented by the set of differential equations in (5.68). Again during the *time domain* dynamics, if there exists any contact point(s) such that, $z_i \leq 0$, $|v_{z_i}| \leq \epsilon_v$ and $\dot{v}_{z_i} < 0$, then the non-penetrability and Coulomb friction constraints are embedded. During the *time domain* simulation, an event location scheme is used to detect impacts based on the conditions specified in (5.52).

6.2 Results

This section presents a number of simulation results on example of multi-point contact and impact problems using the proposed method. The first two simulations presented in this section pertain to examples of a three-dimensional rigid block undergoing a four-point impact against the ground and a three-dimensional sphere undergoing a three-point impact against a wall corner. These examples are presented to demonstrate how the proposed method is used to solve multi-point impact problems. The next example shows a set results for a three-dimensional block undergoing a series of impact and contact. In this example the number of points used for the contact/impact analysis varied. The objective of presenting this result is to show that the proposed method can be used to model contacts and impacts between generalized surfaces involving a large number of contact points. The final example presents a set of results on the angular response of a free three-dimension rocking block model. The results presented in this example is validated using experimental results from another study.

The hybrid dynamic simulation technique used in this work was implemented with the help of Matlab's `ode45`, which is an adaptive Runge-Kutta integrator based on Dormand-Prince method [98,99]. The results presented in this section were simulated on an Intel(R) Core(TM) 2 Duo CPU with 3 GHz processor and 4 GB RAM.

6.2.1 Example-1: 3D Block 4 point Impact

This section presents the example of a three-dimensional block model impacting a ground, as shown in Fig.5.1. The block model identifies four impact points, denoted by 1, 2, 3, and 4, which are located at the corner points of the impacting surface of the block and its center of mass at point O. The system has six DOFs described by six generalized coordinates - three translation q_1, q_2, q_3 and three orientation q_4, q_5, q_6 coordinates. The block has length $l = 0.1$m, width $b = 0.2$m, and height $h = 0.05$m with mass $m = 0.25\ kg$.

It is assumed in the simulations that follow, that the impact of the block's bottom surface with the ground occurs only at the points identified in Fig. 5.1. A static and dynamic coefficient of friction are $\mu_s = 0.6$ and $\mu_d = 0.35$, respectively. The global ECOR value for this impact is chosen to be $e_* = 0.50$.

The simulation starts with a configuration of the block such that the edge defined by the points 1 and 2 is in contact with the ground. Contact constraints prevent the block from penetrating into the ground, so the block pivots along the edge until a collision takes place with the ground surface. All four points are in contact when this collision takes place, hence all these points are considered for the impact analysis. This presents an indeterminate case, as the number of contact forces exceed the number of degrees of freedom of the system. The frictional and rigid body constraints as presented in Sec. 5.2 resolve this indeterminacy. The energetic termination criteria in Sec. 5.2.6, guarantees energy consistency in the post-impact states. The results of the simulation are depicted in Fig. 6.1a. A plot of the system energy is included in Fig. 6.1b to show energy consistency for the simulation performed.

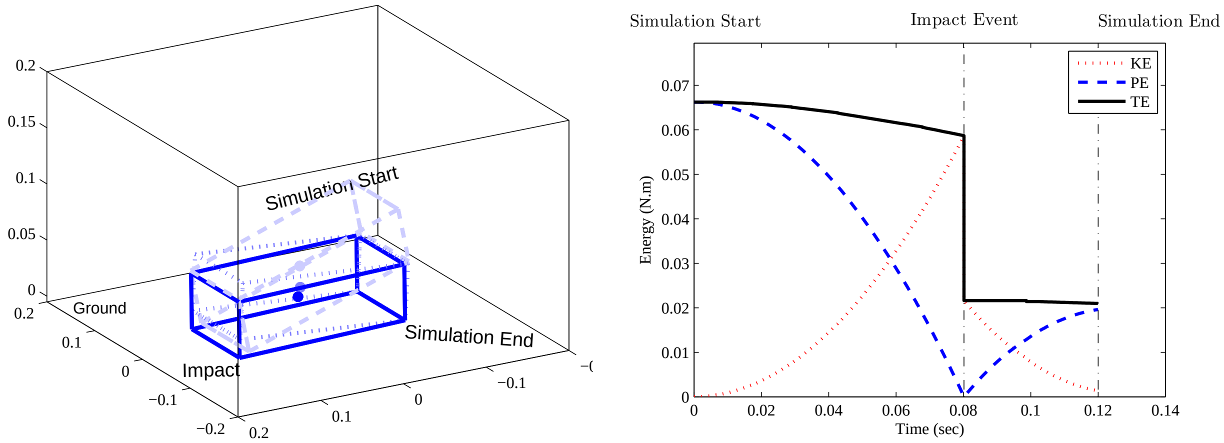

(a) (b)

Figure 6.1: (a) Simulation of the 3D rocking block example with four corner impact points and (b) energy consistency for the simulation.

The impact problem shown here is an example of multi-point impact analysis, where the indeterminacy is resolved by application of rigid body constraints. The impact problem consists of two consecutive impact events. The first impact event is the only indeterminate one in the simulation, which involves the simultaneous impact of points 1, 2, 3, and 4. The post-impact velocity of points 3 and 4 at the end of the first impact event are negative which indicate that they are still moving toward the ground surface. This situation is interpreted as a second impact event involving only points 3 and 4, a determinate collision. Furthermore, points 1 and 2 have a positive velocity after the first impact event, which are interpreted as having reached their post-impact state. The second impact event is resolved before restarting the simulation. The result for this case is obtained by using *global* ECORs

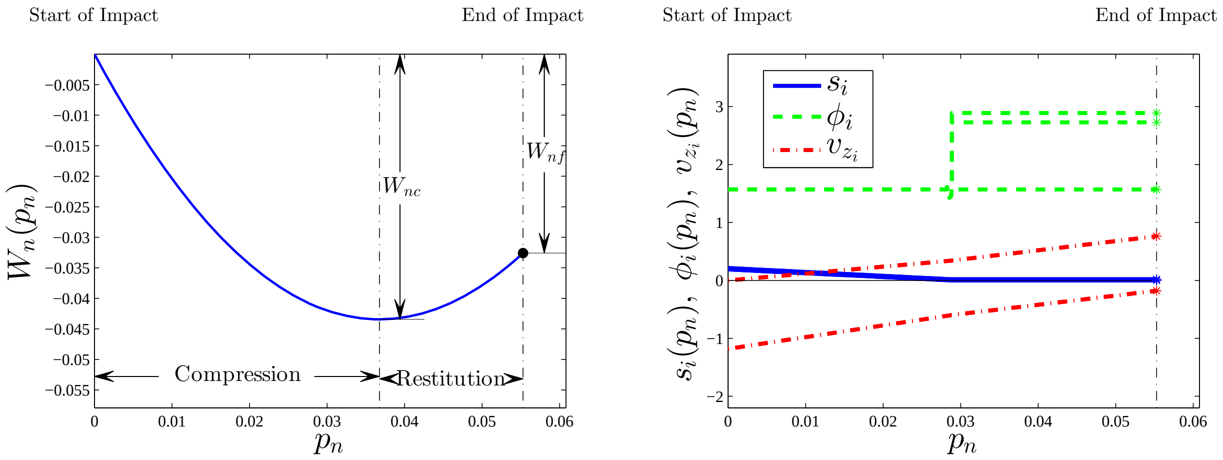

(a) (b)

Figure 6.2: (a) Evolution of sliding velocities, sliding directions, and normal velocities and (b) Normal work done throughout the first impact event for the 3D rocking block example with four corner impact points.

$e_* = 0.50, 0.50$ for the first and second impact events, respectively. The first impact event, illustrated in Fig. 6.2, shows a plot of the normal work and evolution of sliding velocities, sliding directions, and normal velocities. The inclusion of friction for this case does cause the tangential velocities to come to rest together at the stick-slip transition in the first impact

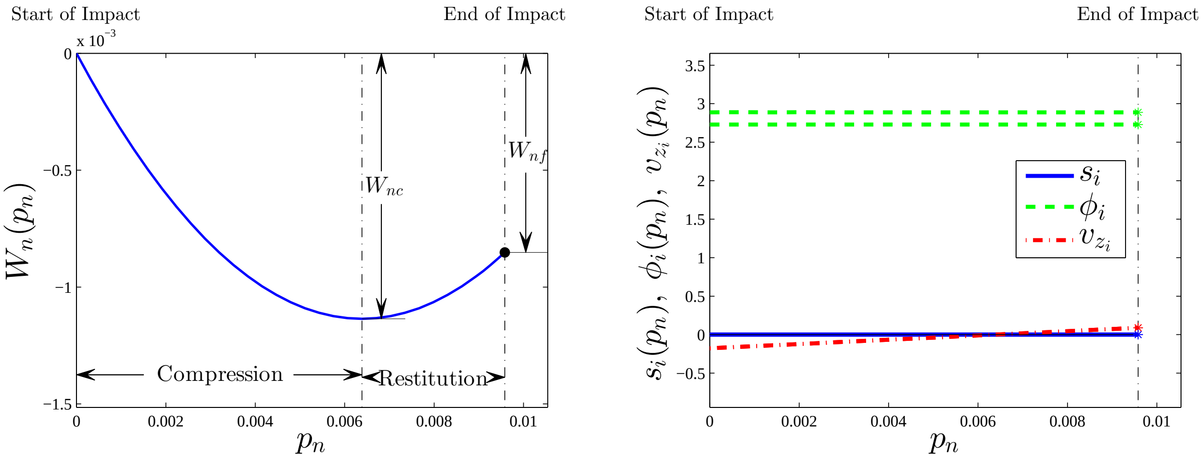

(a) (b)

Figure 6.3: (a) Evolution of sliding velocities, sliding directions, and normal velocities and (b) Normal work done throughout the second impact event for the 3D rocking block example with four corner impact points.

event. Analysis of this stick-slip transition using the techniques discussed in Sec. 5.2, yield new feasible slip-directions, however all of these new slip-directions violate the condition (5.47). This implies that the assumed estimate of the static coefficient of friction $\mu_s = 0.6$ is invalid for the given configuration, and the contact points must stick. The plot of the normal work in Fig. 6.2a shows its characteristic shape. Figure 6.2b shows the velocities during this impact event. As it can be seen in Fig. 6.2b, the normal velocities of all contact points do not reach positive values at the end of the impact event, hence a second impact event follows. Figures 6.3a and 6.3b shows the normal work and velocities plots for the second impact event, which involves only two contact points which had negative velocities at the end of the first impact event. The tangential velocities Fig. 6.3b continue to be zero during the second impact event due to sticking constraints, and both normal velocity values reach positive values as the impact event terminates.

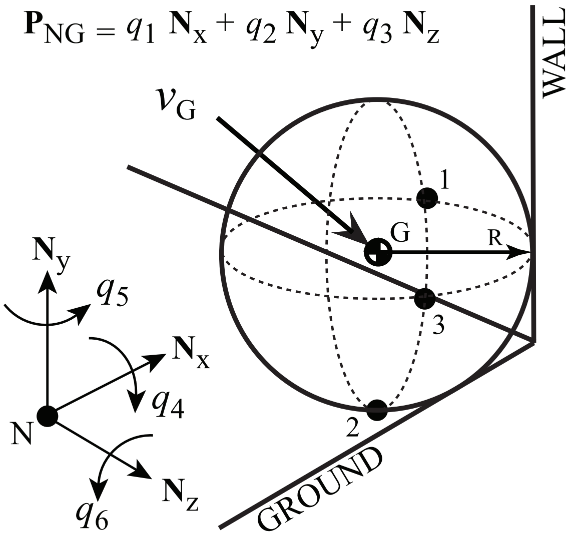

Figure 6.4: Three dimensional model of a sphere impacting a corner.

6.2.2 Example-2: 3D Ball 3 point Impact

The three-dimensional model of the sphere is shown in Fig. 6.4. The sphere has three impact points denoted by 1, 2, and 3. This system has six degrees-of-freedom (DOF) defined by six generalized coordinates - three translation q_1, q_2, q_3 and three orientation q_4, q_5, q_6 coordinates. The sphere has mass, $m = 1\ kg$ and radius R $= 0.50\ m$.

An arbitrary initial position and translational velocity was used for the ball simulation with no initial angular velocity. The simulation of the sphere is depicted in Fig. 6.5a, as it impacts a corner formed by the ground and two wall planes, and ends when a second impact is captured with the ground. This corner impact event is an indeterminate collision involving points 1, 2, and 3. An $e_* = 0.50$ and $\mu_B = \mu_C = \mu_D = 0.35$ is used. After impacting the corner, the position of the impact points 1, 2, and 3 change which demonstrate the sphere's post-impact angular velocity as a result of impact. A plot of the system energy is shown in Fig. 6.5(b) to show energy consistency throughout the simulation.

After impact, the sphere follows a lower trajectory which suggests that the system lost energy from the impact. This is supported by the energy plot in Fig. 6.5(b), which is

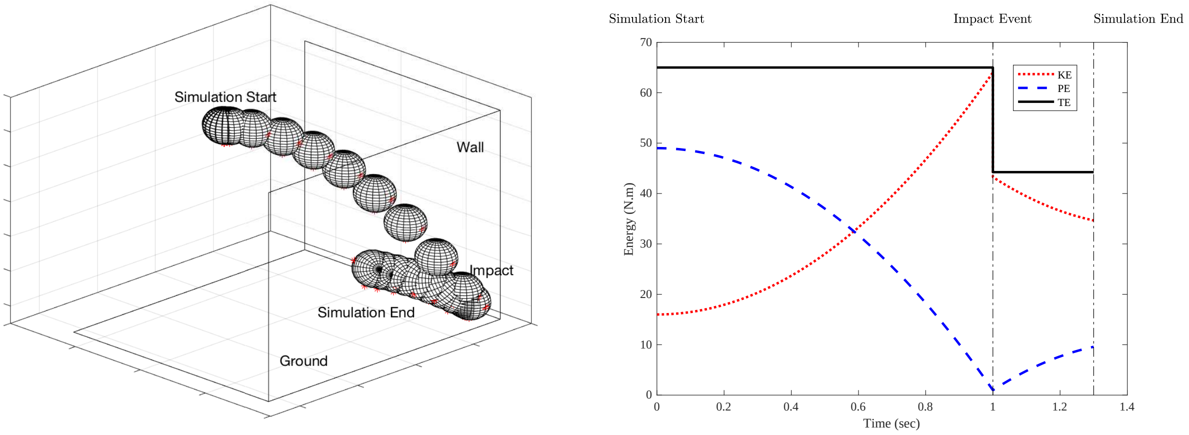

(a) (b)

Figure 6.5: (a) Simulation results and (b) Energy consistency of the 3D sphere example impacting a corner.

further used to determine that no energy gains were encountered throughout the simulation.

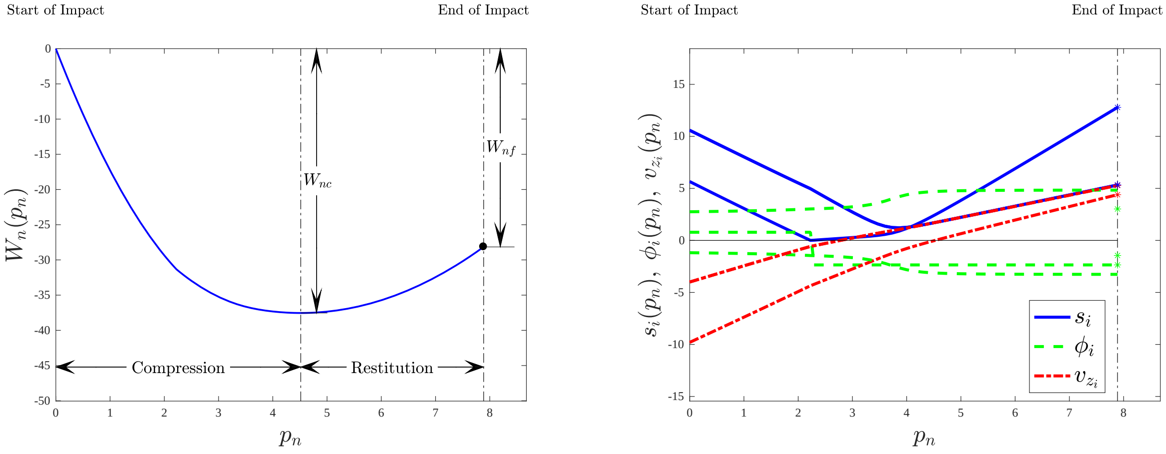

(a) (b)

Figure 6.6: (a) Normal work done and (b) evolution of sliding velocities, sliding directions, and normal velocities throughout the impact event for the 3D sphere example.

The result of this three-dimensional case was obtained using the developed numerical framework. First, the impulse at the end of the compression phase is determined and used to find W_{nc}, and the net work done on the system W_{nf} with the *global* ECOR. The evolution of the sliding velocities, sliding directions, and normal velocities were determined by the numerical integration of the system equations in (5.5) throughout the impact event, and shown in Fig. 6.6b. A plot of the normal work throughout the impact event is shown in Fig. 6.6a. In this particular simulation, none of the sliding velocities come to rest at the stick-slip transition, which result in no shifts in the normal work plot.

The end condition for the normal impulse p_{nf} is evaluated with the knowledge of W_{nf}, which marks the end of the impact event. The post-impact velocities at the impact end serve as the initial conditions for restarting the simulation to model the system after impact.

6.2.3 Example-3: 3D Block Surface-Surface Contact and Impact

The example presented in this section demonstrates that the proposed method of contact and impact analysis may be used to model general surface to surface contact and impact problems. Multibody dynamics simulation systems typically store geometry information of bodies as a collection of points, in the form of a mesh or a grid. Contact and impact analysis may be performed on these points upon collision detection. The preceding examples demonstrated that by using the proposed method contact and impact analysis may be performed for a given set of points. However, it is important to show that the results obtained using this technique is invariant to the number of points used for a given contact/impact configuration. This is to show that if the geometries of the impacting bodies are represented using some mesh, the contact and impact analysis results are not affected by the mesh density. In this example a three-dimensional rigid block model of mass 2.5 kg and dimensions $1.5\text{m} \times 1.5\text{m} \times 1\text{m}$ is dropped from a height of $1.5m$ (the distance between the center of mass and the ground), with a roll angle of -0.2rad. The values for static and dynamic coefficients of friction are selected to be $\mu_s = 0.1$ and $\mu_d = 0.2$, respectively. The

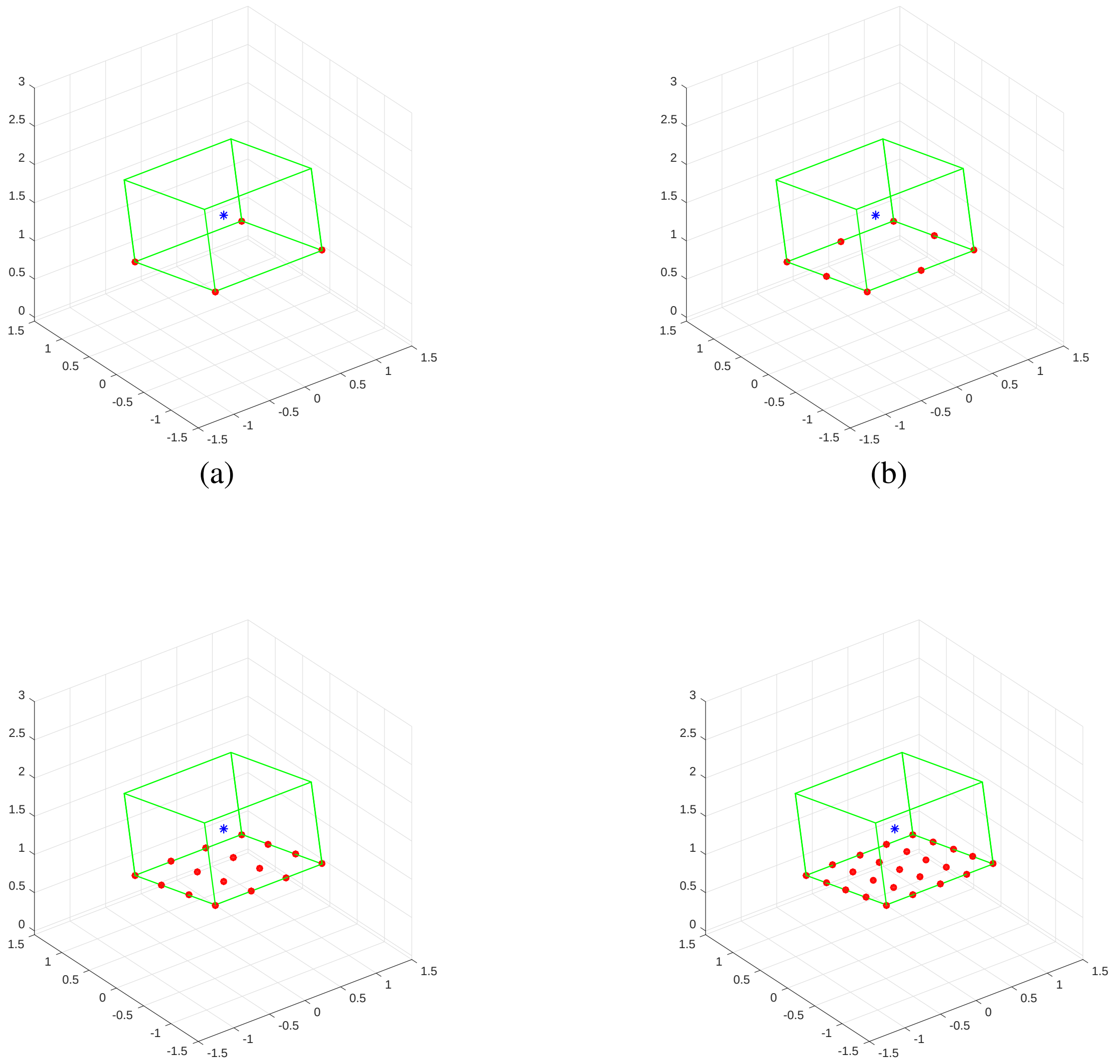

(a) (b)

(c) (d)

Figure 6.7: Block with (a) four points (b) eight points (c) sixteen points (d) twenty-five points

global ECOR value is chosen to be $e_* = 0.5$. The bottom face of the block interacts with the ground throughout the simulation. In this example, the simulation is performed for four different cases, while using the same initial configuration and simulation parameters. In these four cases the bottom surface of the block is represented using 1) four corner points, 2) eight points evenly distributed on the edges, 3) sixteen points and 4) twenty-five points distributed throughout the bottom surface. These four cases are shown in Fig. 6.7. Results were generated using the proposed method over a 2 seconds period, while considering all the points that came in contact for the contact and impact analysis.

Figure 6.8 shows the evolution of the generalized coordinates for the 1) Four Point, 2) Eight Point, 3) Sixteen Point, and 4) Twenty-Five Point cases for the 2 second simulation. It is clear from these plots, that the trajectories of the generalized coordinates for these cases remains very close to one another throughout the simulation period. The small errors between the trajectories are mainly a consequence of numerical tolerance, and can be considered negligible. The energy dissipation exhibited by the system during all these simulations are shown in Fig. 6.9. Again the energy dissipation plots reaffirm that the overall behavior of the simulation is not affected due to the redundant number of points used for the contact and impact analysis. The steps on the total energy plot reflect the energy dissipation due to impact.

Another interesting feature of the proposed contact/impact analysis technique is revealed by investigating individual impact events. Fig. 6.10 shows a comparison of the normal work plot for the first impact event during the simulation. Notice, that for all four cases the values of W_{nc} and W_{nf} are identical. However, the p_{nf} values are different for the four cases. The final value of of the independent impulse parameter is reduced for greater number of points. This indicates that the rigid-body constraints used in the model is in effect distributing the net impulse over the constituent points. Hence, for a greater number

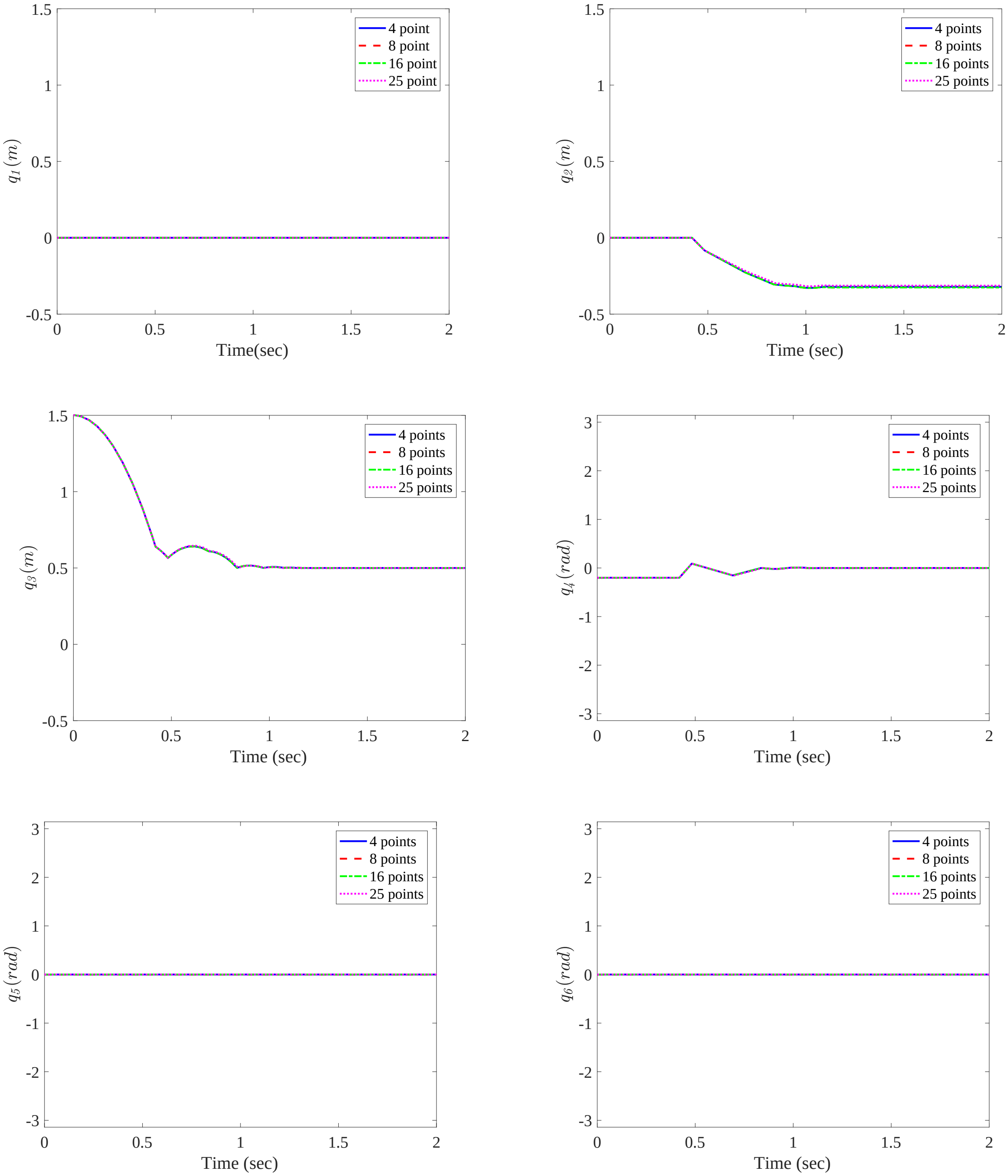

Figure 6.8: Comparison of the generalized coordinates of the block

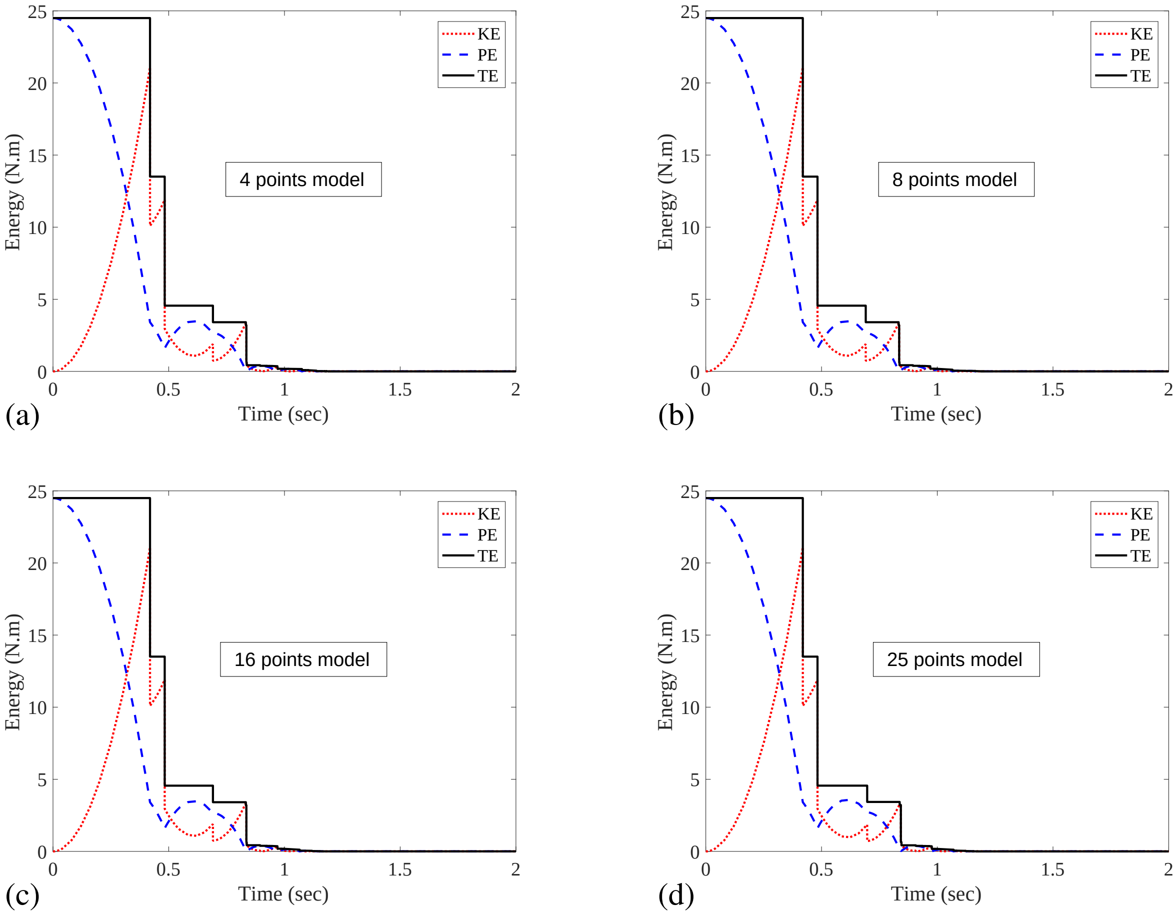

Figure 6.9: Energy Dissipation for (a) Four Point (CPU Time: 21.52 s), (b) Eight Point (CPU Time: 18.66 s), (c) Sixteen Point (CPU Time: 27.98 s) and, (d) Twenty-Five Point Cases (CPU Time: 35.67 s)

of points, each point contributes a lesser amount towards the net impulse induced on the system.

6.2.4 Example-4: 3D Rocking Block Angular Response

The example provides an experimental validation for the proposed method. Here the benchmark problem of rocking block is simulated and compared against experimental results. The rocking block problem has be been extensively studied in the literature [34,35,

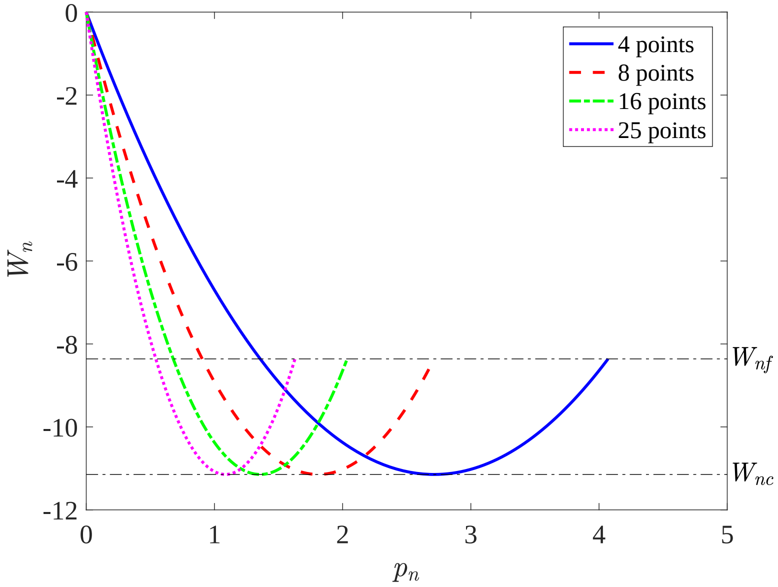

Figure 6.10: Comparison of the Normal Work plot for the first impact event.

109–115]. These models use stiffness properties [113], local energy dissipation properties [34, 109] or global kinematic restitution properties [115].

The data analyzed in this example comes from [113,114], which reports experimental data on different specimens of concrete blocks for the cases of free-rocking and rocking with base excitation; herein, only the free-rocking block results are considered. The work in [103] matched these experimental results while considering a planar block, using what is known as the LZB model, which was proposed in [34, 35, 109–112]. The LZB model uses local ECORs for each contact point and relates the local energy losses by a distributing law, based on parameters defined as contact stiffness ratios and elasticity coefficients. The work in [38] also matches the data from [113, 114] using a planar block model, and considering different global ECOR values for single and multiple(two)-point impacts. The approach used in [38] is essentially a planar version of the method proposed in this work.

Table 6.1: Choice of effective width

Block Specimen	Geometric width(m) [114]	LZB model width(m) [103]	CRB model width(m)
1	0.25	0.23	0.23
2	0.17	0.155	0.155
4	0.16	0.115	0.115

Three different specimens were used for the free-rocking block experiments in [114]: 1) *Specimen 1* with a width of 0.25 m, height of 1 m and mass of 503 kg, 2) *Specimen 2* with width and height 0.17 m and 1 m respectively and a mass of 228 kg, and 3) *Specimen 4* of width 0.16 m, height 0.457 m and mass 245 kg. The width of the block needs to be calibrated, since the angular response to a rocking block problem is highly sensitive to variations in width [116]. A detailed discussion on this presented in [103, 116]. The *effective width* selected herein for all of the specimens are the same as in [103, 116], and are tabulated in Table. 6.1. The length of the three specimens were selected to be the same as in [114]: 0.7594m, 0.502m and 0.705m for *Specimen 1*, *Specimen 2* and *Specimen 4* respectively.

Fig. 6.11 compares the simulated and experimental angular response of the three specimens. Here, Pena refers to the measured angular response from the experiments done by Pena et.al [114], LZB refers to the simulated response using the LZB model [103], which is based on a two-dimensional block, CRB-2D refers to the planar model proposed in [38], and CRB-3D is the response using the three-dimensional model proposed in this work. The static and dynamic coefficient of friction used for the simulation are $\mu_s = 0.577$ and $\mu_d = 0.3$ respectively, identical to [103].

The angular responses shown as CRB-2D in 6.11, from [38] were matched using two ECOR values; a positive ECOR value for single point impact and a negative ECOR value for two-point impacts. This work uses the same ECOR values as [38] to match the

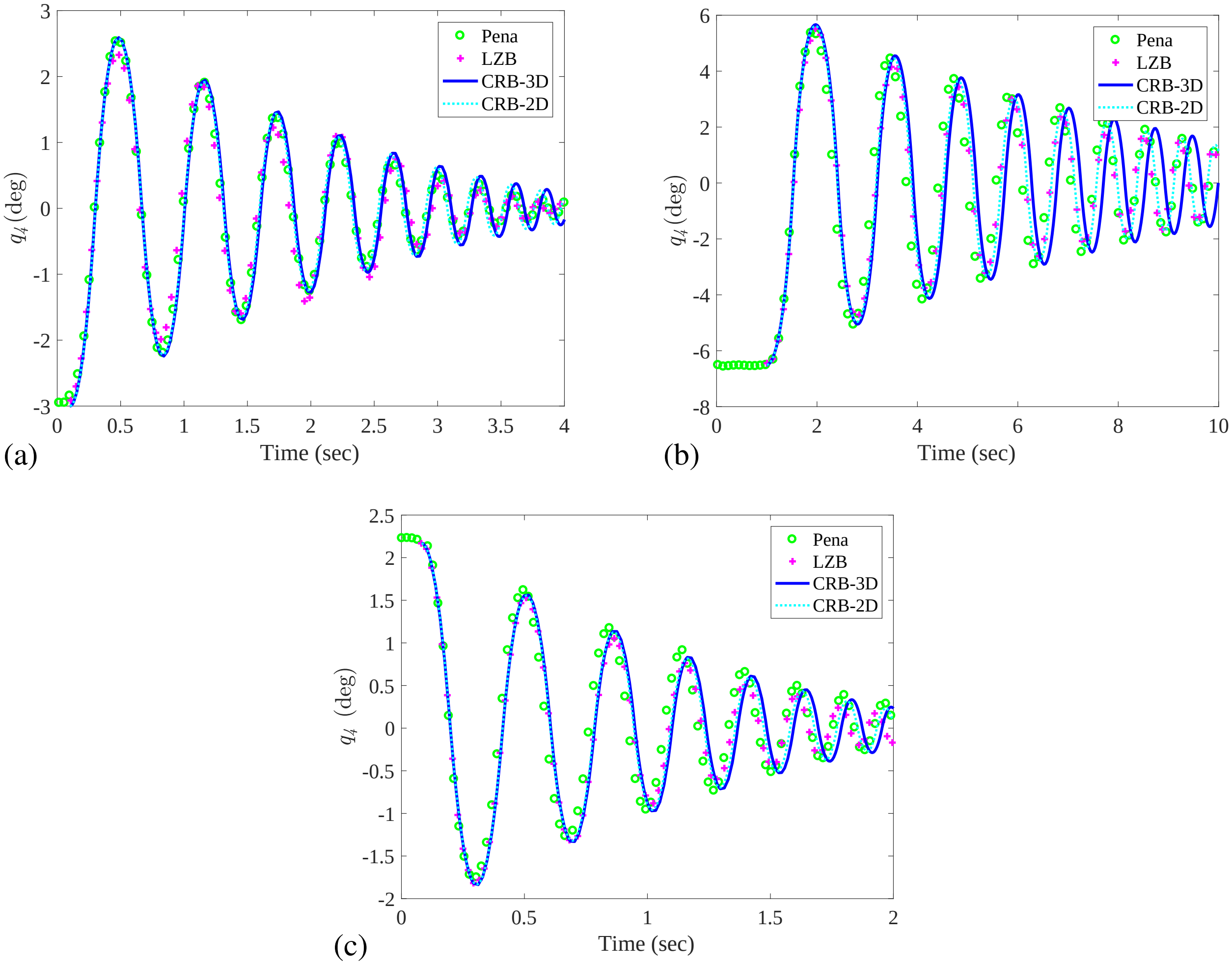

(a) (b) (c)

Figure 6.11: Angular Response for (a) Specimen 1 (CPU Time: 186.89 s) (b) Specimen 2 (CPU Time: 136.98 s) (c) Specimen 4 (CPU Time: 74.20 s). The angular response data for Pena and LZB, were obtained from plots shown in Fig.5 of [103].

the angular response data. Here the positive ECOR values identical to [38] are chosen for all 1-point and 2-point impact events, and the negative ECOR values are selected for all 3-point and 4-point impact events. The angular response plots in Fig. 6.11 show very little difference in results between the 2D and 3D models listed as CRB-2D and CRB-3D respectively while using the same values of ECOR. Fig. 6.11 also shows the responses from the planar LZB model from [103]. The LZB model also used two ECOR values to match the angular response data, however these are local ECORs which had to be switched in the middle of the simulation. All of the simulation parameters used for the LZB and CRB-2D/3D models are summarized in Table 6.2. Fig. 6.12 shows the energy dissipation during rocking for all the specimen. The curved steps of the total energy plots indicate that a considerable amount of energy is lost in friction during contact.

Table 6.2: Simulation Parameters

	Specimen 1		Specimen 2		Specimen 4	
	LZB	CRB-2D/3D	LZB	CRB-2D/3D	LZB	CRB-2D/3D
μ_d	0.3	0.3	0.3	0.3	0.3	0.3
μ_s	0.577	0.577	0.577	0.577	0.577	0.577
ECORs	$\{0.97, 0.88\}$	$\{-0.73, 0.8\}$	0.999	$\{-0.95, 0.8\}$	$\{0.99, 0.87\}$	$\{-0.96, 0.8\}$

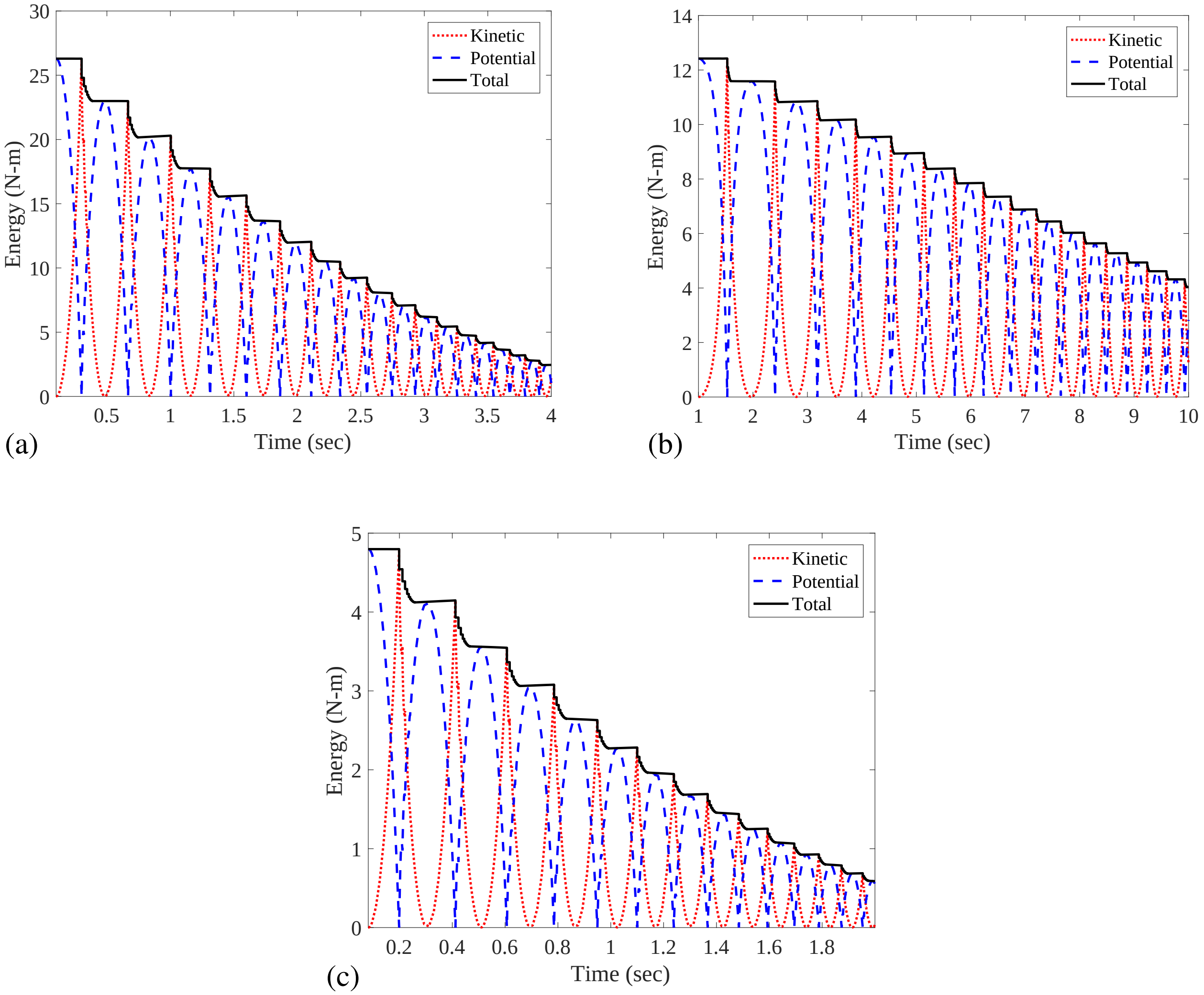

Figure 6.12: Energy consistency throughout the simulation for (a) Specimen 1 (b) Specimen 2 (c) Specimen 4 .

CHAPTER 7

AUGMENTED IMPACT MODEL TO EVOLVE FORCES, DEFORMATIONS AND TIME DURING COLLISIONS

A significant disadvantage of rigid collision models [22, 28, 38, 43, 48, 49], which which analyze impacts in the impulse domain, is that they all lose critical information like the force history and deformation history during the impact event. This work attempts to reformulate the rigidity based impulse-domain equations in [41, 42] to derive a model of impact that includes the force and deformation history during the impact. However, in order to do this, it would be necessary to slightly relax the rigidity assumption and use a deformation based force model from contact mechanics. The proposed model would retain the rigidity property among the contact points within the impacting bodies, but relax the intra-body non-penetration condition to allow tiny deformations, such that the forces during the impact could be calculated. The rigid body constraints along with the frictional constraints, as shown in [38, 42], help resolve all contact forces with respect to a single independent normal force parameter. Hence, in the present work a force model is used only for the independent force parameter, such that all other contact forces on the system may be calculated in terms of the independent force parameter.

A vast variety of contact force models can be found in the literature. These contact models may be broadly classified into a number of categories namely purely elastic [58–60], visco-elastic [61–63], elastoplastic [55, 64, 65] and visco-elastoplastic models [66, 67]. In purely elastic models, the forces depend solely on the deformation of the bodies. A popular example of purely elastic model of contact is the Hertz's contact model [58], which was proposed by Hertz in 1882, and subsequently became the foundation for much of the later works in contact mechanics. Purely elastic contact force models are suitable force static contacts, but they don't capture very well the dynamic behaviour involved in impacts. The visco-elastic models take into account the viscous(damping) effects involved in contact dynamics. Some of the well-known examples of visco-elastic models would include Hunt-Crossley [60, 62], Kelvin-Voigt [60, 61], Lankarani-Nikravesh [60, 120], Flores [60, 121], Gharib-Hurmuzlu [60, 122] models. Visco-elastic contact models have very popular usage in the modeling of impacts in multibody dynamic simulations. However, both purely elastic and visco-elastic models do not take into account the permanent deformations typically associated with impacts. Impacts between rigid bodies usually result in observable permanent deformations in the bodies. In order to take into account the effects of permanent deformations, it is important to allow some plastic behaviour in the contact models. Both elastoplastic and visco-elastoplastic models incorporate the effects of plasticity in the contact force model. Elastoplastic and visco-elastoplastic models consist of two phases: *compression phase* and *restiutution phase*. The contact forces increase during the compression phase with respect to the induced deformation till contact point accelerations reach zero. The compression phase is always followed by a restitution phase where the forces decrease till they become zero. In elastoplastic and visco-elastoplastic models the compression phase is typically subdivided into three parts: 1) elastic regime, 2) mixed elastic-plastic regime and 3) fully plastic regime. These three regimes within the compression phase, capture both elastic and plastic behaviour of the material in contact. The restitution phase unloads the maximum compressive force reached at the end of the compression phase. Hence, the restitution phase is usually modelled as a purely elastic phase. The elastoplastic models only dependent upon the deformation of the contact point and do not consider the viscous behaviour of the materials in contact, so they are more appropriate for static contacts. The visco-elastoplastic models of forces introduce a damping term based on the deformation rates to the elastoplastic models, which make them more suitable for capturing the velocity dependent dynamic behavior involved in impacts. This work uses a visco-elastoplastic model of contact force for the model of impact, similar to the one proposed in [67]. Although this work uses the visco-elastoplastic contact force model in [67] to define the independent force parameter, the general approach proposed in this work can be applied to any contact force model from the contact mechanics literature, viz. [55, 58, 62].

7.1 Contact Forces during Impact Event

The previous section showed that the contact point velocities of a rigid object may be evolved in terms of a single independent impulse parameter. This type of treatment of the impact problem discards certain information such as elapsed-time, force history and indentations at the contact point. The goal of this section is to modify the non-smooth model of impact shown in Sec. 5.1, with the help of a classical contact-mechanical model, such that the forces at the various contact points during the impact event could be obtained. In contact mechanics, the forces over a contact patch are defined in terms of the material stiffness properties and the deformations associated with the applied contact force. Although the impulse-domain model of impact, as presented in Sec. 5.1 assumes no change in configuration during the impact event, in reality there are small deformations associated with each contact point. In this work, we analyze these small deformations within the framework of a rigid body collision analysis.

7.1.1 Contact Deformations

Consider the side-view schematic of the rigid block impacting the ground in Fig. 7.1. The deformations associated with contact points $i = \{1, ..., 4\}$ are represented by δ_i. In this work, the deformation δ_i is defined as the relative displacement of the ground with respect to the region around the contact points. Note that δ_i is not defined as the deformation of

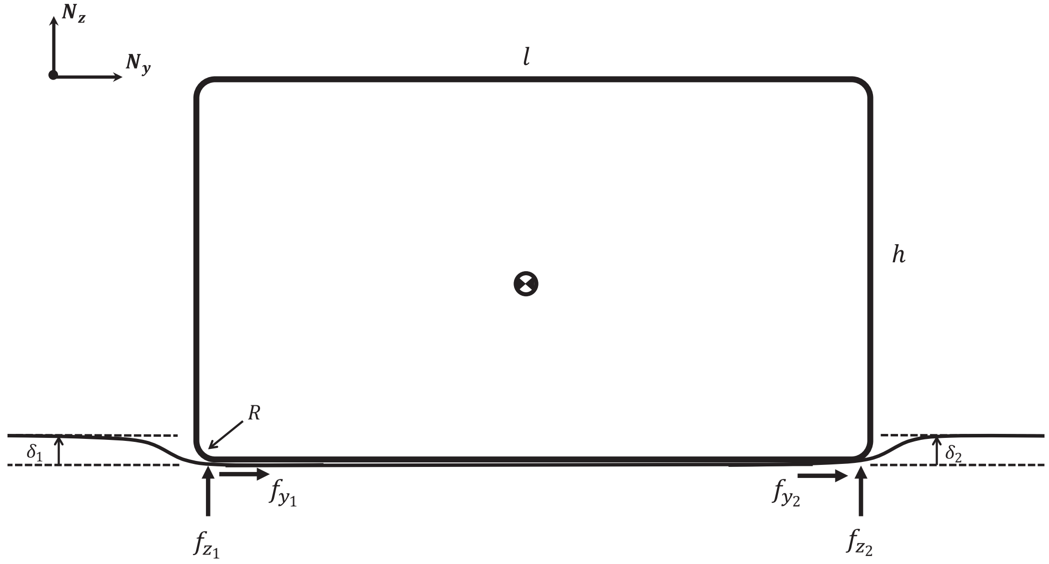

Figure 7.1: Side-view of the rigid block from $\hat{\mathbf{N}}_y - \hat{\mathbf{N}}_z$ plane, showing the indentation of the ground during an impact event

the ground, rather it is a value representing the combined deformation of both the ground and the block. Adhering to the notation used in Sec. 5.1, the two tangential and one normal force components at contact points $i = \{1, ..., 4\}$ are f_{x_i}, f_{y_i}, and f_{z_i} respectively. The tangential forces f_{x_i} and f_{y_i} are related to the normal forces f_{z_i} based on Coulomb friction, similar to (5.10). The normal forces are non-adhesive and depend upon the local deformation and deformation rates, $f_{z_i} = f_{z_i}\left(\delta_i, \dot{\delta}_i\right)$. In Sec. 5.1, the rigid impact model was derived such that all impact states can be evolved with respect to an independent normal impulse parameter p_n. Hence, here it is necessary to identify the force and deformation parameters associated with p_n. Let the deformation and normal force associated with p_n be δ_n and $f_n = f_n\left(\delta_n, \dot{\delta}_n\right)$, respectively. Then the change in time during the impact event can be expressed in terms of the deformation as,

$$v_n = -\frac{d\delta_n}{dt} \qquad \longrightarrow \qquad dt = -\frac{1}{v_n}d\delta_n = \frac{1}{\dot{\delta}_n}\, d\delta_n \tag{7.1}$$

where, $v_n = -\dot{\delta}_n$ is the normal velocity or the deformation rate of the contact point associated with the independent normal impulse parameter. Also, the sign convention between normal velocity and deformation is important in (7.1). Note that the relation (7.1) becomes singular when $v_n \to 0$. Thus, an alternative definition for the change in time can be expressed in terms of the independent normal force,

$$dt = \frac{1}{f_n}\, dp_n \tag{7.2}$$

Equation (7.2) becomes singular when $f_n \to 0$. Therefore, the definition of the change in time needs to be switched from (7.1) to (7.2), when $v_n = 0$, and vice-verse when $f_n = 0$. This would lead to two different sets of equations; one for each of these conditions. The two sets of equations would be integrated with respect to two different variables i.e. δ_n and p_n. Hence it is more convenient represent the relationships in (7.1) and (7.2) in terms of a new variable β, which is defined in differential form as,

$$d\beta = \begin{cases} \dfrac{\dot{\delta}_n}{\bar{\epsilon}|\dot{\delta}_n|}\, d\delta_n & \text{if} \qquad v_n \neq 0 \ \text{ and } \ f_n = 0 \\[2ex] dp_n & \text{if} \qquad f_n > 0 \end{cases} \tag{7.3}$$

Now the required integration for the two cases can be carried out in terms of this new variable β. The advantage of deriving the differential equations in terms of this new variable β is that they can be integrated without requiring an event-based scheme to account for the change in the independent variable. Here the relationship (7.3) is designed such that the equations in (7.1) and (7.2) could be integrated such that $d\beta$ is always positive. Note that according to the first relationship of (7.3), $d\delta_n$ would change sign with respect to $\frac{\dot{\delta}_n}{|\dot{\delta}_n|}$, if $d\beta > 0$. This takes care of the restitution phase of an impact; as it would be seen later δ_n decreases during the restitution phase. In the first relationship, $d\beta$ is also inversely scaled by an arbitrarily small scaling term $\bar{\epsilon}$. Typically in impacts the impulse values are larger than the deformation values by several orders of magnitude, i.e. $p_n >> \delta_n$. Therefore, the addition of the small scaling term $\bar{\epsilon}$ helps in the smooth transition between δ_n and p_n. Lastly, note that during an impact the condition $v_n = f_n = 0$ can only occur when the contact point(s) enters a "stable contact" (no-rebound contact). In other words, the impact event would terminate when $v_n = f_n = 0$ is reached.

7.1.1.1 Case: $v_n \neq 0$ and $f_n = 0$

In the case when $v_n \neq 0$ and $f_n = 0$, recall (7.3), the differential of the elapsed time is expressed in terms of (7.1). The independent differential impulse parameter can be expressed in terms of its corresponding deformation as,

$$dp_n \;=\; f_n dt \;=\; -\frac{f_n}{v_n}\, d\delta_n \tag{7.4}$$

The normal deformations for all of the contact points may be related to the deformation associated with the independent normal impulse. Let the normal deformations for all contact points be $\boldsymbol{\delta} = \begin{bmatrix} \delta_1 & \dots & \delta_4 \end{bmatrix}^T$, then by using (7.1), the differential of $\boldsymbol{\delta}$ would be given by,

$$d\boldsymbol{\delta} = \dot{\boldsymbol{\delta}} dt = \frac{\mathbf{v}_z}{v_n} d\delta_n \tag{7.5}$$

where $\mathbf{v}_z$ are the normal velocity components for all contact points, and are related to the normal deformation rates of the contact points as $\dot{\boldsymbol{\delta}} = -\mathbf{v}_z$. Using (7.4), the differential equations associated with the velocities and the normal work from (5.5) and (5.49) respectively, can be expressed in terms of the independent deformation parameter δ_n. Thus, the system states can be evolved with respect to the variable β when $v_n \neq 0$ and $f_n = 0$, and the set of differential equations to be integrated for this case can be summarized as,

$$\text{Velocities}: \quad \begin{cases} d\boldsymbol{\vartheta}_{cyl} = -\bar{\epsilon} P M \mathbf{C} \dfrac{f_n}{v_n} \dfrac{\dot{\delta}_n}{|\dot{\delta}_n|} d\beta & \text{if} \quad \textit{Slipping} \\ d\boldsymbol{\vartheta} = -\bar{\epsilon} M \mathbf{C} \dfrac{f_n}{v_n} \dfrac{\dot{\delta}_n}{|\dot{\delta}_n|} d\beta & \text{if} \quad \textit{Sticking} \end{cases}$$

$$\text{Impulses}: \quad d\mathbf{p} = -\bar{\epsilon} \mathbf{C} \frac{f_n}{v_n} \frac{\dot{\delta}_n}{|\dot{\delta}_n|} d\beta \ , \qquad \text{Normal Work}: \quad dW_n = -\bar{\epsilon} \mathbf{v}_z^T \mathbf{C}_z \frac{f_n}{v_n} \frac{\dot{\delta}_n}{|\dot{\delta}_n|} d\beta$$

$$\text{Deformations}: \quad d\boldsymbol{\delta} = \bar{\epsilon} \frac{\mathbf{v}_z}{v_n} \frac{\dot{\delta}_n}{|\dot{\delta}_n|} d\beta \ , \qquad \text{Elapsed Time}: \quad dt = -\bar{\epsilon} \frac{1}{v_n} \frac{\dot{\delta}_n}{|\dot{\delta}_n|} d\beta \tag{7.6}$$

where, P is a transformation matrix between Cartesian and cylindrical coordinate differential velocities.

7.1.1.2 Case:$f_n > 0$

When $fn > 0$, the system can be integrated with respect to the independent normal impulse parameter p_n. The differential time expression in (7.2) is used for this case. Then, the differential deformations for all contact points would be given by $d\boldsymbol{\delta} = -\frac{\mathbf{v}_z}{f_n} dp_n$. Thus, the system of equations to be integrated with respect to $\beta = p_n$ for this case, can be summarized as,

$$\text{Velocities}: \quad \begin{cases} d\boldsymbol{\vartheta}_{cyl} = P M \mathbf{C} d\beta & \text{if} \quad \textit{Slipping} \\ d\boldsymbol{\vartheta} = M \mathbf{C} d\beta & \text{if} \quad \textit{Sticking} \end{cases}$$

$$\text{Impulses}: \quad d\mathbf{p} = \mathbf{C} d\beta \ , \qquad \text{Normal Work}: \quad dW_n = \mathbf{v}_z^T \mathbf{C}_z d\beta$$

$$\text{Deformations}: \quad d\boldsymbol{\delta} = -\frac{\mathbf{v}_z}{f_n} d\beta \ , \qquad \text{Elapsed Time}: \quad dt = \frac{1}{f_n} d\beta \tag{7.7}$$

Hence, evolving the sets of equations given for the two cases in (7.6) and (7.7), would yield the deformations of the contact points and elapsed time of impact, along with the the other quantities with respect to the integration variable β, as defined in (7.3). Figure 7.2 shows an example of impact states viz. velocities, normal work, deformation and time being integrated together with respect to β. Since, f_n is the force associated with the independent impulse parameter p_n, the forces at all the contact points can be projected in terms of f_n using the force gradient vector $\mathbf{C}$ as, $\mathbf{F} = \mathbf{C}f_n$. However, doing so would imply that the forces at all contact points are proportional to f_n. Although the rigid hypothesis proposed in [38, 42] and used in this work, states that the differential impulses of all points may be resolved in terms of the differential impulse of a single point, as in $d\mathbf{p} = \mathbf{C}dp_n$, the forces calculated the same way can yield incorrect force-history results for certain impacts. Projecting the independent force parameter f_n to calculate the force $\mathbf{F}$ assumes that the maximum compression (or minimum normal work at the end of compression phase) coincides for the forces at all contact points. This is actually an artifact of the rigid-body assumption as it simplifies the multi-point impact analysis by reducing the problem in terms of a single contact point and simultaneously characterizing the compression and restitution phases of all points in terms of the global normal work. In reality, the compression and restitution phases of each point depend upon their respective deformations and velocities. Hence, the forces at all contact points needs to be calculated, as a post-process, explicitly in terms of the deformations and velocities obtained from the proposed model. The contact force model used in this work (discussed in Sec.7.1.2) yields only the normal force component based on the deformations and velocities. Since, the tangential forces are to be modeled using Coulomb's friction law which has been embedded in $\mathbf{C} = [C_{x_1} \;\; C_{y_1} \;\; C_{z_1} \;\; \cdots \;\; C_{x_4} \;\; C_{y_4} \;\; C_{z_4}]^T$, the correct contact forces for all point $\mathbf{F}$ can be calculated by re-scaling the relationship $\mathbf{F} = \mathbf{C}f_n$ such that all normal forces are independent and are explicitly defined in terms of deformations and velocities of individual points. Thus, the expression for all contact forces can be expressed as,

$$\mathbf{F} = \bar{C}\,\mathbf{F}_z = \begin{bmatrix} C_{x_1}/C_{z_1} & \cdots & 0 \\ C_{y_1}/C_{z_1} & & \vdots \\ 1 & & \vdots \\ 0 & \ddots & \vdots \\ \vdots & & C_{x_4}/C_{z_4} \\ \vdots & & C_{y_4}/C_{z_4} \\ 0 & \cdots & 1 \end{bmatrix} \begin{bmatrix} f_{z_1}(\delta_1, \dot{\delta}_1) \\ \vdots \\ f_{z_4}(\delta_4, \dot{\delta}_4) \end{bmatrix} \tag{7.8}$$

Note that although the forces at each contact point in (7.8) may appear to be independent of the deformation and velocity histories of all other contact points, they actually do depend upon the deformations and velocities of all contact points. This is because the deformations and velocities obtained from the model in (7.6) and (7.7) are constrained by the rigid-body constraints, such that the deformation and velocity each point depends on every other point. Thereby the forces **F** calculated using (7.8) also implicitly depend upon the rigid body constraints and the overall deformation and velocity history during an impact. Nevertheless it is important to note that this approach is only an approximation for the very complicated dynamics associated with multi-point impact analysis. In reality, there would be some relative displacement between the contact points depending upon the stiffness of the material. The relative displacement between the points are negligible for very stiff materials. Therefore, the proposed approach is a good approximation for objects with very high stiffness, which allow minimal deformation upon impact.

So far in this work, the focus has been on the development of an augmented model for rigid-body impacts that utilizes the *Darboux-Keller* based impact model shown in [41,42]. When provided with a normal contact-force model $f_{z_i} = f_{z_i}(\delta_i, \dot{\delta}_i)$, the deformation and force histories during the impact event can also be calculated. Now having defined the framework for the augmented impact model, the following sections discuss the contact-force model used in this work.

7.1.2 Contact Force Model

This work uses the visco-elastoplastic contact force model, given in [55,67], to model the normal contact force. However, in order to apply this model to the example problem of the rigid block that has been analyzed thus far, it is necessary to consider some geometric and material properties of the block. Although the block has been said to be impacting at the four dimensionless corner points labeled in $i = \{1, ..., 4\}$ in Fig. 5.1, in reality each of these contact points on the body represent a small contact patch on the surface, such that the forces at each point depends upon the contact patch area and the stiffness of the material. The shape of the contact patch depends upon the surface profiles of the body near the contact points. In this work, the region around the contact points is assumed to have a spherical surface profile that yields a circular contact patch of radius a during impact. This assumption allows for the usage of hertzian contact theory for the analysis of the forces. In the literature, one can find more exact models for different types of surface profiles [14, 123, 124]. However the goal of this work is to determine an approximate solution of the forces during impacts, therefore a simpler spherical contact model is used here. Let the radii of the spherical corner points of the block have the radii R_1, and the radius for the flat ground be $R_2 = \infty$. The Young's moduli for the block and the ground are E_1 and E_2, respectively. Similarly, let ν_1 and ν_2 be the Poisson's ratio of the block and the ground, respectively. Then, the equivalent Young's modulus and radius to be used for the contact model are given by,

$$E = \left(\frac{1 - \nu_1^2}{E_1} + \frac{1 - \nu_2^2}{E_2} \right)^{-1} \qquad \text{and} \qquad R = \left(\frac{1}{R_1} + \frac{1}{R_2} \right)^{-1} \tag{7.9}$$

Let, S_{y1} be the yield strength for the block, and likewise S_{y2} be the yield strength of the ground. Then, the equivalent yield strength for the contact S_y is considered to be the same as the yield strength of the material that yields first,

$$S_y \; = \; \min \left[S_{y1}, S_{y2} \right] \tag{7.10}$$

Similarly, the equivalent Poisson's ratio, ν is the same as the poisson ratio of the material that yields first. At any point during an impact event, the contact points may either be in compression or restitution. Note that the compression and restitution of individual contact points may not coincide with the global compression and restitution phases defined based on the global normal work Wn, shown in Figs. 5.3b, 7.2b and 7.3. Hence to make this distinction, the compression and restitution phases of individual contact points will be referred to as *Local Compression Phase* and Local Restitution Phase. Similarly, the compression and restitution phases of the entire system would be referred to as the *Global Compression Phase* and *Global Restitution Phase*. Figure 7.3 shows an example of a normal work plot for a 2-point impact-event where the *Local Compression* and *Local Restitution* phases do not coincide with the *Global Compression* and *Global Restitution*. The normal works at the end of local compression phases for the two points in Fig. 7.3 are labeled as W_{c1} and W_{c2}, whereas the normal work at the end of global compression phase is labeled as W_{nc}.

According to the rigid impact model in Sec. 5.1, every impact event consists of a *global compression* phase, which may be followed by a *global restitution* phase if $e_* > 0$. However, it is worth noting that this pattern does not necessarily apply, when considering compression and restitution of individual points. For example, if in a multi-point impact some of the points being considered are already in contact with zero pre-impact velocities, then these contacting points will not have a *local compression* phase. Instead the contacting points will *locally restitute* through the impact event. This happens because the contacting points are pre-loaded with compression forces during the contact phase before the onset of the impact event. Therefore, these contact forces get unloaded throughout the impact-event, in the form of a *local restitution* phase, such that these points come out of contact at the end of the impact event. On the other hand, if a point is impacting with negative pre-impact normal velocity, there would always exist a *local compression* phase that may be followed by a *local restitution* phase.

7.1.2.1 Force Model for Local Compression Phase

The visco-elastoplastic force model used in this work is based on [67], where the contact force $f_{z_i}\left(\delta_{z_i}, \dot{\delta}_{z_i}\right)$ during a local compression phase contains a stiffness part and a damping part, similar in form to that of the Hunt-Crossley model,

$$f_{z_i}\left(\delta_{z_i}, \dot{\delta}_i\right) = f_s(\delta_i) + f_d(\dot{\delta}_i) \tag{7.11}$$

where $f_s(\delta_i)$ is the force due to the stiffness, which depends only on the deformation of the contact point δ_i. The damping portion of the force $f_d(\dot{\delta}_i)$, has a constant functional form throughout the local compression and is given by,

$$f_d(\dot{\delta}_n) = b\dot{\delta}_n^{\frac{3}{2}} \frac{\dot{\delta}_n}{|\dot{\delta}_n|} \tag{7.12}$$

Unlike the damping term, the stiffness term $f_s(\delta_i)$ does not have a fixed functional form throughout the impact; it is peicewisely defined across different regimes of the local compression phase. The various regimes within the local compression phase considered here are 1) *Elastic*, 2) *Elastic-Plastic* and 3) *Plastic* regimes. One drawback of the force model presented in [67] is that the nonlinear stiffness model is not guaranteed to be continuous, and may yield discontinuous forces. Hence, in this work the nonlinear stiffness portion is updated with the model presented in [55], which guarantees smooth force profiles. According to the nonlinear stiffness model presented in [55], the compression phase begins with the elastic phase and persists till the material starts to yield. The deformation at the yield point is given by δ_y, which can be calculated using the yield strength S_y, is used to determine end of the elastic regime. The force due to the stiffness during elastic phase is calculated using hertz contact model [55, 67]. The elastic regime is usually followed by a mixed elastic-plastic regime, which acts as a transition phase between the perfectly elastic and perfectly plastic phases [55, 67]. Finally, the contact enters a perfectly plastic regime, during which the deformations are considered to be permanent [55, 67]. The details of this stiffness model during the three regimes are summarized below,

- Elastic Regime $(0 \leq \delta_i < \delta_y)$: The contact force at point i during the elastic regime is given by the Hertz model for spherical contact,

  $$f_s = \frac{4}{3} E R^{\frac{1}{2}} {\delta_i}^{\frac{3}{2}} \text{ when } 0 \leq \delta_i < \delta_y \tag{7.13}$$

  where, the initiation of yield, δ_y is the deformation at the end of the elastic regime, which is given by,

  $$\delta_y = \frac{R}{F(\nu)} \left(\frac{\pi S_y}{2E} \right)^2$$

  The function $F(\nu)$ defines the maximum amplitude stress, according to the von Mises criteria, and is given by,

  $$F(\nu) = \max_{u \in \mathbb{R}} \left(-(1+\nu) \left(1 - u \text{atan} \left(\frac{1}{u} \right) + \frac{3}{2} \frac{1}{1+u^2} \right) \right)^2$$

  The maximum amplitude stress function $F(\nu)$, cannot be solved analytically. However, the solution can be approximated via a curve fit proposed by Jackson and Green [125, 126],

  $$F(\nu) \approx \frac{1}{C} \text{ where } C = 1.295 e^{0.736\nu}$$

  The force at the end of the elastic regime is given by,

  $$f_y = \frac{4}{3} E R^2 \left(\frac{3\pi\nu S_y}{4E} \right)^3$$

  The derivative of the force at yield is given by,

  $$f'_y = 2E(R\delta_y)^{\frac{1}{2}}$$

- Elastic-Plastic Regime ($\delta_y \leq \delta_i < \delta_p$): As shown in [55], the force function during the elastic-plastic regime may be approximated as a cubic hermite interpolation, such that the contact force smoothly transitions between elastic and plastic regimes. The interpolation force model for the elastic-plastic phase is given by,

$$\begin{aligned} f_s \;=\; & \left(2f_y - 2f_p + (\delta_p - \delta_y)\left(f'_y + f'_p\right)\right)\left(\tfrac{\delta_i - \delta_y}{\delta_p - \delta_y}\right)^3 \\ & + \left(-3f_y + 3f_p + (\delta_p - \delta_y)\left(-2f'_y - f'_p\right)\right)\left(\tfrac{\delta_i - \delta_y}{\delta_p - \delta_y}\right)^2 \\ & + (\delta_p - \delta_y) f'_y \left(\tfrac{\delta_i - \delta_y}{\delta_p - \delta_y}\right) \end{aligned} \tag{7.14}$$

where f_p is the forces at the onset of the plastic regime and f'_p is it's derivative. δ_p is the deformations at the onset of the plastic regime, respectively. Based on the analysis presented in [55], the formulas for these quantities are:

$$f_p = \left(\frac{3R}{4E}\right)^2 (\pi p_0)^3 \qquad f'_p = 2R\pi p_0 \qquad \delta_p = \left(\tfrac{p_0}{S_y}\right)^2 \delta_y$$

where, the quantity of p_0 is the uniform contact pressure on the contact patch during the plastic regime. p_0 depends upon the hardness of the material, and is given by,

$$p_0 = \bar{H} g (10^6)$$

where $\bar{H}$ is the effective hardness of the two materials, $g = 9.8\text{m/s}^2$ is the gravitational constant.

- Plastic Regime ($\delta_i \geq \delta_p$): During plastic regime the contact pressure p_0, over the contact patch remains constant, while the area of the contact patch changes. Thus, the force is defined in terms of the area of the circular contact patch as,

$$f_s = p_0 \pi a^2 \tag{7.15}$$

where, a is the radius of the circular contact patch. During the plastic regime, the contact patch radius can be defined in terms of the deformation,

$$a = \left(2R(\delta_i - \delta_p) + a_p^2\right)^{\frac{1}{2}}$$

where a_p is the contact patch radius at the initiation of the plastic regime, and is given by

$$a_p = R\frac{3\pi}{4}\frac{p_0}{E}$$

A given point undergoing local compression may not enter all three possible regimes defined for local compression. The end of local compression occurs when the normal work induced by the given point reaches its minimum value. Hence for a given point i, the end of its local compression phase is reached when,

$$\frac{d}{d\beta}\int_0^{z_i} f_{z_i} dz_i = \frac{d}{d\beta}\int_0^{z_i} v_{z_i} dp_{z_i} = 0 \qquad \text{Or equivalently,} \qquad v_{z_i} = 0$$

The force model changes to the local restitution phase model after the maximum local compression is reached.

7.1.2.2 Force Model for Local Restitution Phase

The local restitution phase takes place after the end of local compression phase for a given point i, if the pre-impact normal velocity is negative, i.e. $v_{z_i}(\beta = 0) < 0$. On the other hand, if the point i was initially in contact, i.e. $v_{z_i}(\beta = 0) = 0$, then the point enters the impact event in *local restitution*. The forces approach zero at the end of the restitution phase (end of the impact event). During the restitution phase, the forces are usually modeled as elastic unloading forces [55, 67]. In this work, a purely elastic hertzian model is used to characterize the restitution force, similar to [67]. Thus, at a contact point i, the force f_{z_i}, during the restitution phase is given by,

$$f_{z_i} = f_0\left(\frac{\delta_i - \delta_{if}}{\delta_{ic} - \delta_{if}}\right)^{3/2} \tag{7.16}$$

where f_0 is the force at the onset of the local restitution phase. If the pre-impact normal velocity of the point i is negative f_0 takes the value of the force at end of compression phase $f_{z_{ic}}$, whereas if the point i was initially in contact it takes the value of the pre-impact contact constraint force,

$$f_0 = f_{z_{ic}} \qquad \text{if} \qquad v_{z_i}(\beta = 0) < 0$$

$$f_0 = f_{z_i}(\beta = 0) \qquad \text{if} \qquad v_{z_i}(\beta = 0) = 0$$

The pre-impact contact constraint forces $f_{z_i}(\beta = 0)$ can be calculated by imposing the non-penetration and frictional constraints of the point i to the general equations of motion (5.2), and then solving for the forces. [38, 42] shows a method for doing this using a co-ordinate partitioning technique. δ_{ic} and δ_{if} are the deformations of point i at the end of local compression phase and local restitution phase, respectively. Note that in this work the forces at all contact points are calculated as a post-process, with the help of (7.8), after the full deformation-history is obtained. So the local restitution force model in (7.16) is only used when the values of δ_{ic} and δ_{if} is known from the deformation history. However, this raises the question: *how can the deformations be evolved using the independent force model f_n during the global restitution phase, if f_n itself depends upon the final-value of the deformation?* This question is answered in the following section.

7.1.2.3 Independent Force Model during Global Restitution Phase

As shown in the augmented impact model in (7.6) and (7.7), the impact states, which include the deformations δ_i, is evolved with the help of an independent force parameter, f_n. If for a given impact event, the global ECOR value is positive, $e_* > 0$, then the impact event enters a *global restitution* phase. The force model for the *local restitution* phase shown in (7.16) uses the final value of the deformation δ_{if}, which is unknown during the evolution of the augmented impact model. δ_{if} are essentially some unknown boundary conditions that influence the force trajectories during the restitution phase. The unknown boundary conditions of δ_{if} are also constrained by the total energy dissipation W_{nf}, which is calculated a priori using the e_* (ECOR) parameter. This type of problems are commonly known as *Two Point Boundary Value Problems* (TPBVP), and can be solved using well-known numerical techniques viz. Shooting Method [127]. However in this case, as it shall be seen, it is actually possible to eliminate the permanent deformation δ_{if} from the restitution force equations in (7.17), by making an intuitive approximation.

The force associated with the independent impulse parameter f_n, during the global restitution phase is given by,

$$f_n = f_{nc}\left(\frac{\delta_n - \delta_{nf}}{\delta_{nc} - \delta_{nf}}\right)^{3/2} \tag{7.17}$$

where f_{nc} is the maximum force at the end of the local compression phase for the point associated with independent normal impulse parameter p_n. δ_{nc} and δ_{nf} are the deformations associated p_n, at the end of the local compression phase and at the end of the local restitution phase, respectively. Similarly, the normal force component f_{z_i} at any given contact point i, also follows the purely elastic unloading model during local restitution phase,

$$f_{z_i} = f_{z_{ic}}\left(\frac{\delta_i - \delta_{if}}{\delta_{ic} - \delta_{if}}\right)^{3/2} \tag{7.18}$$

where, $f_{z_{ic}}$ is the normal force at point i at the end of the compression phase. δ_i is the deformation associated with contact point i during the restitution phase. Let the normal work corresponding to a deformation δ_n be given by $W_n(\delta_n)$. Then, the normal work till the end of the restitution phase can be derived using the normal force component expression shown in (7.18) as,

$$\int_{W_n(\delta_n)}^{W_{nf}} dW_n = \sum_{i=1}^{4}\int_{z_i}^{z_{if}} f_{z_i} dz_i = -\sum_{i=1}^{4}\int_{\delta_i}^{\delta_{if}} f_{z_{ic}}\left(\frac{\delta_i - \delta_{if}}{\delta_{ic} - \delta_{if}}\right)^{3/2} d\delta_i \tag{7.19}$$

which yields,

$$W_{nf} - W_n(\delta_n) = \frac{2}{5}\sum_{i=1}^{4} f_{z_{ic}}\left(\delta_{ic} - \delta_{if}\right)\left(\frac{\delta_i - \delta_{if}}{\delta_{ic} - \delta_{if}}\right)^{5/2} \tag{7.20}$$

Now, lets consider the normal force component for a given point $i = \{1, ..., 4\}$, in terms of the force component associated with the independent normal impulse parameter. As shown in Chapter 5, using the rigid hypothesis, the forces at all contact points are constrained by the frictional and rigid body constraints. Hence, by using (5.19), the normal force component at any contact point $i = \{1, ..., 4\}$ can be defined as,

$$dp_{z_i} = C_{z_i} dp_n \qquad \rightarrow \qquad f_{z_i} = C_{z_i} f_n \tag{7.21}$$

where C_{z_i} is the normal component of the force gradient vector $\mathbf{C}$, associated with the ith contact point. Similarly, at the end of the compression phase, the normal force of any point i, can be described in terms of the normal force associated with the independent impulse parameter at the end of the compression phase,

$$dp_{z_{ic}} = C_{z_{ic}} dp_{nc} \qquad \rightarrow \qquad f_{z_{ic}} = C_{z_{ic}} f_{nc} \tag{7.22}$$

where $C_{z_{ic}}$ is the ith normal component of $\mathbf{C}$ at the end of the local compression phase of i. Now, solving the equations (7.17), (7.18), (7.21), and (7.22) yields the relationship,

$$\left(\frac{\delta_i - \delta_{if}}{\delta_{ic} - \delta_{if}}\right)^{3/2} = \frac{C_{z_i}}{C_{z_{ic}}} \left(\frac{\delta_n - \delta_{nf}}{\delta_{nc} - \delta_{nf}}\right)^{3/2} \tag{7.23}$$

The relationship in (7.23) can be used to redefine the forces at all contact points $i = \{1, ..., 4\}$, in terms of the independent displacement parameter δ_n. Likewise, the change in normal work from $W_n(\delta_n)$ to the final normal work W_{nf}, as shown in (7.20), could be redefined in terms of δ_n. Hence, substituting (7.23) to (7.20) yields,

$$W_{nf} - W_n(\delta_n) = \frac{2}{5} \left[\sum_{i=1}^{4} C_{z_{ic}} \left(\delta_{ic} - \delta_{if}\right) \left(\frac{C_{z_i}}{C_{z_{ic}}}\right)^{5/3} \right] \left(\frac{\delta_n - \delta_{nf}}{\delta_{nc} - \delta_{nf}}\right)^{5/2} \tag{7.24}$$

C_{z_i} and $C_{z_{ic}}$ are elements of the force gradient vector $\mathbf{C}$ at the δ_i and δ_{ic}. Note that the force gradient vector $\mathbf{C}$ varies only if the contact points are slipping; $\mathbf{C}$ is constant if all contact points are slipping. However, during the global restitution phase the changes in the normal components of **C** are typically very small, and their effect on the normal work, according to the formulation in (7.24) is diminished by the very small deformation quantity $(\delta_{ic} - \delta_{if}) \sim 0$. Hence, $\frac{C_{z_i}}{C_{z_{ic}}}$ can be approximated as,

$$\frac{C_{z_i}}{C_{z_{ic}}} \approx 1 \quad \rightarrow \quad \left(\frac{C_{z_i}}{C_{z_{ic}}}\right)^{5/3} \approx 1 \tag{7.25}$$

Thus, after applying this approximation, (7.24) can be simplified as,

$$W_{nf} - W_n(\delta_n) = \frac{2}{5}\left[\sum_{i=1}^{4} C_{z_{ic}}\left(\delta_{ic} - \delta_{if}\right)\right]\left(\frac{\delta_n - \delta_{nf}}{\delta_{nc} - \delta_{nf}}\right)^{5/2} \tag{7.26}$$

Now using the formulation of normal work as in (7.26), the change in normal work through the local restitution phase, starting from the end of maximum local compression of the independent point δ_{nc}, is given by,

$$W_{nf} - W_n(\delta_{nc}) = \frac{2}{5}\left[\sum_{i=1}^{4} C_{z_{ic}}\left(\delta_{ic} - \delta_{if}\right)\right] \tag{7.27}$$

Note here $W_n(\delta_{nc})$ is the total normal work at the end of the local compression phase for the independent point, associated with the independent impulse parameter p_n. Now, dividing (7.26) by (7.27), yields the relationship,

$$\frac{W_{nf} - W_n(\delta_n)}{W_{nf} - W_n(\delta_{nc})} = \left(\frac{\delta_n - \delta_{nf}}{\delta_{nc} - \delta_{nf}}\right)^{5/2} \tag{7.28}$$

Hence, the expression for the force associated with the independent impulse parameter f_n during the local restitution phase, as given in (7.17), can be rewritten as,

$$f_n = f_{nc}\left(\frac{W_{nf} - W_n(\delta_n)}{W_{nf} - W_n(\delta_{nc})}\right)^{3/5} \tag{7.29}$$

The definition of the independent force during the restitution phase in terms of the normal work, as shown in (7.29) is much more advantageous compared to (7.17), which requires an a priori estimate of the permanent deformation δ_{nf}, which is difficult to obtain accurately. The independent force during the restitution phase, f_n obtained using (7.29), is used to evolve the augmented impact model given in (7.6) and (7.6). Once, the deformation histories of all contact points are obtained, the forces at these points can be calculated using (7.8). Figure 7.4 shows an example of the force history during an impact event. The compression and restitution phase force models presented in (7.11), (7.13), (7.14), (7.15) and (7.29) respectively, causes the force to initially increase (loading) during the impact till a point of maximum compression and then decrease (unloading) to become zero, as shown in Fig. 7.4a. Note that in Fig. 7.4a, the deformation at the end of restitution phase does not reach zero; there exists some permanent deformation. The permanent deformation during the impact event contribute towards the hysteresis typically observed in rigid body collision, and is characterized by the choice of global coefficient of restitution. Figure 7.4b shows an example of the time-history of the forces during an impact.

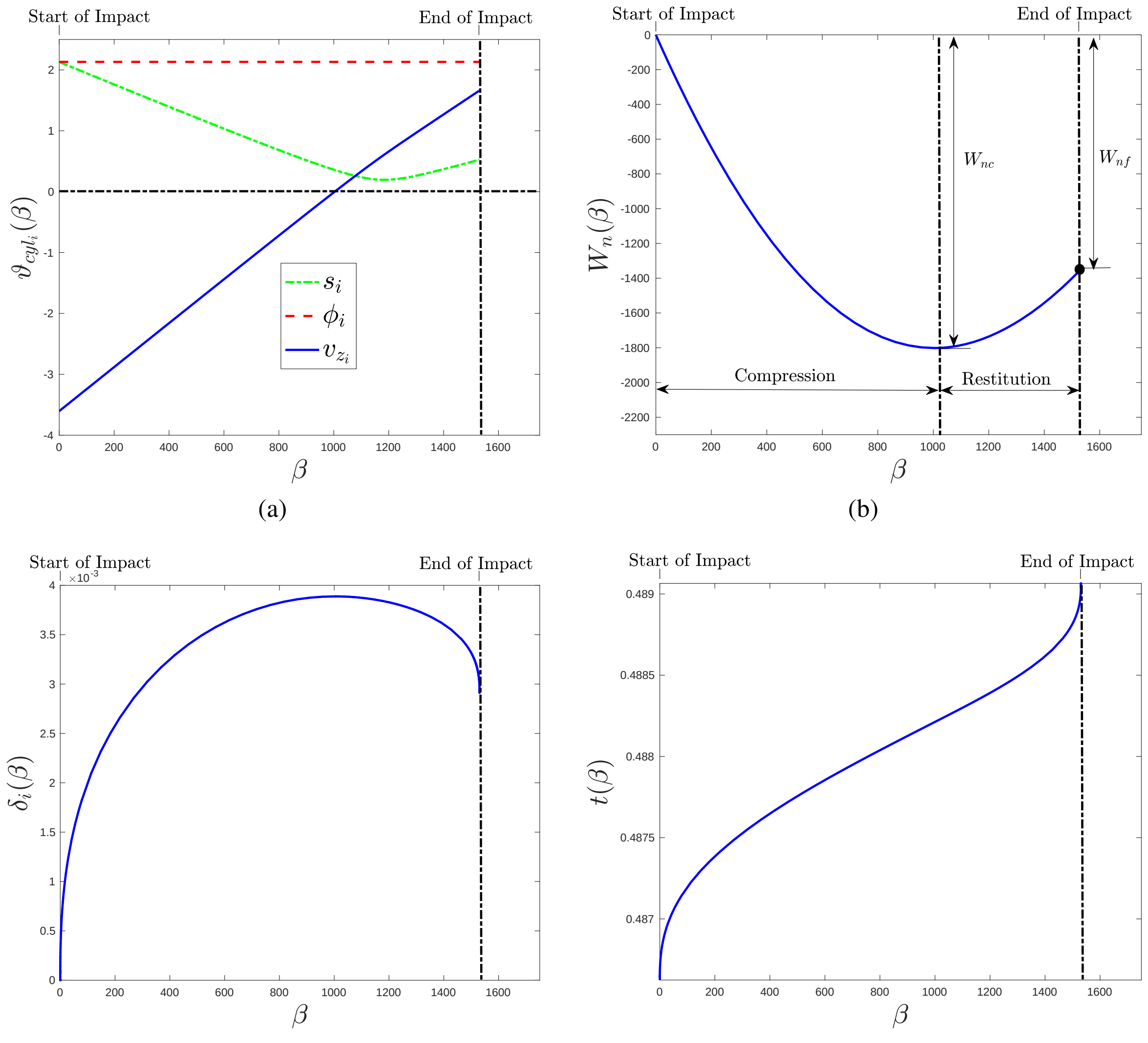

(a) (b)

(c) (d)

Figure 7.2: Evolution of (a) velocities, (b) normal work, (c) normal deformation and (d) time with respect to β, during the first impact event

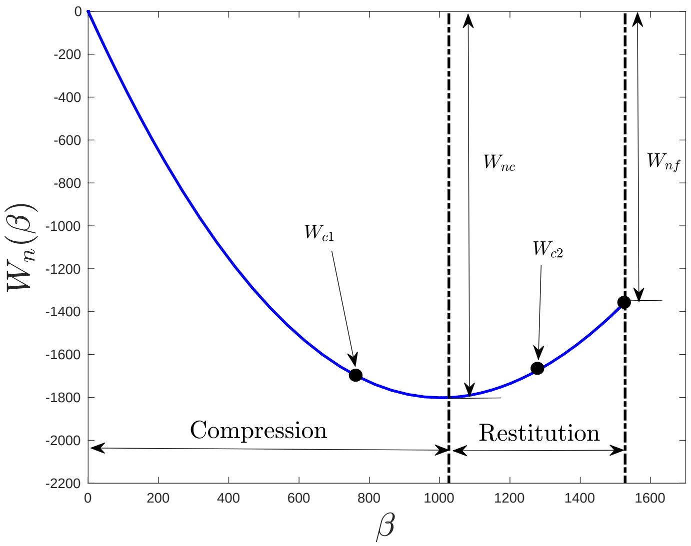

Figure 7.3: An hypothetical example of normal work plot showing the maximum global compression, W_{nc} and two maximum local compression for two distinct points labeled W_{c1} and W_{c2}

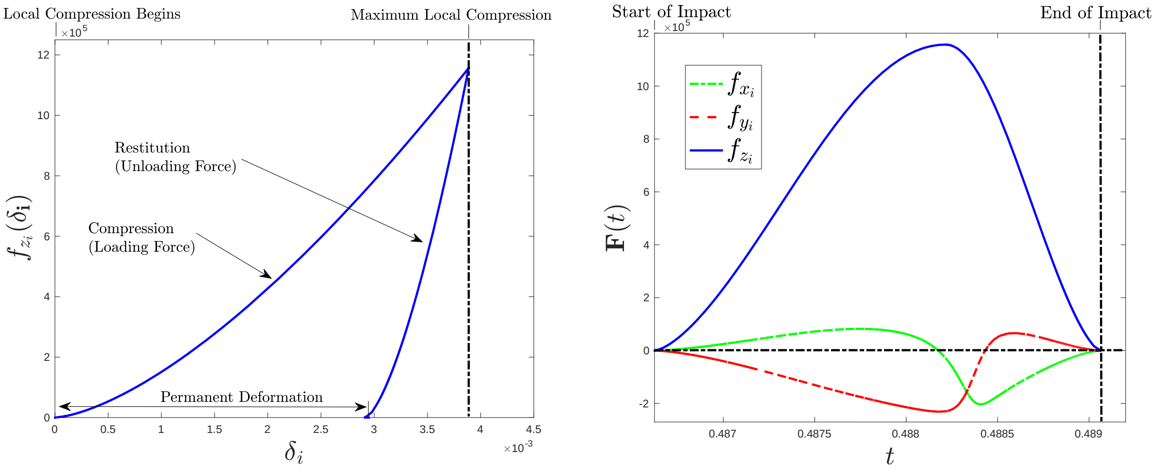

(a) (b)

Figure 7.4: Force history during the impact in terms of (a) normal deformation and (b) time

CHAPTER 8

SIMULATIONS USING AUGMENTED IMPACT MODEL

8.1 Simulation Technique

The previous sections derived a model for rigid impacts that retains the force and deformation history during the impact, while performing impulse-domain impact analysis. The proposed model augments the purely rigid impact model presented in [38,41] with a set of additional differential equations used to evolve the states of contact point deformations and elapsed time of impact. The differential equations associated with the deformation and time are based on the visco-elastoplastic contact force model presented in Sec. 7.1.2, which in turn depends upon the deformations and the velocities of the contact point. Hence, the contact force can be thought of as a closed-loop feedback input to the dynamic system that governs the evolution of the impact states. The impact states during an impact can be written as,

$$\mathbf{x} = \left[\boldsymbol{\vartheta}_{cyl}^T \;\; \mathbf{p}^T \;\; \boldsymbol{\delta}^T \;\; t \;\; W_n\right]^T \tag{8.1}$$

then the set of differential equations representing the state dynamics from (7.6) and (7.7) is given by,

$$\frac{d\mathbf{x}}{d\beta} = \mathbf{f}(\mathbf{x}, f_n), \qquad \mathbf{x}(0) = \left[\boldsymbol{\vartheta}_{cyl}^T(0) \;\; \mathbf{p}^T(0) \;\; \boldsymbol{\delta}^T(0) \;\; t(0) \;\; W_n(0)\right]^T \tag{8.2}$$

where f_n is the normal force at the independent contact point, and acts as the input to the impact state dynamics. The initial conditions $\mathbf{x}(0)$ consists of $\boldsymbol{\vartheta}_{cyl}(0)$ and $t(0)$, which are known at the beginning of the impact event. The deformations and impulses are zero at initially, $\mathbf{p}(0) = \boldsymbol{\delta}(0) = \mathbf{0}$. Also there is no energy loss due to normal forces at the start of an impact event, so $W_n(0) = 0$. Based on the contact force model presented in Sec. 7.1.2, the force f_n can be written as,

$$f_n = h(\mathbf{y})$$

$$\text{where,} \quad \mathbf{y} = \begin{bmatrix} \delta_n \\ \dot{\delta}_n \end{bmatrix} = \begin{bmatrix} \delta_n \\ -v_n \end{bmatrix} = \underbrace{\begin{bmatrix} 0 & \cdots & 0 & 0 & 0 & \cdots & 0 & 1 & 0 & \cdots & 0 \\ 0 & \cdots & 0 & -1 & 0 & \cdots & 0 & 0 & 0 & \cdots & 0 \end{bmatrix}}_{D_\delta} \mathbf{x} = D_\delta \mathbf{x} \tag{8.3}$$

In (8.3), $h(\mathbf{y})$ represents the visco-elastoplastic contact force model used in this work. The vector $\mathbf{y}$ consists the deformation and the rate of deformation at the independent contact point, and is treated as an output obtained from the state dynamics in (8.2). The output $\mathbf{y}$ is selected from the states $\mathbf{x}$, using the an output coefficient matrix D_δ, as shown in (8.3). Similarly, the normal work W_n and the sliding speeds s_i during the impact can be defined in terms of an output coefficient matrix D_w and D_{s_i} respectively such that,

$$W_n = \underbrace{\begin{bmatrix} 0 & \cdots & 0 & 1 \end{bmatrix}}_{D_w} \mathbf{x} = D_w \mathbf{x} \qquad s_i = \underbrace{\begin{bmatrix} 0 & \cdots & 0 & 1 & 0 & \cdots & 0 \end{bmatrix}}_{D_{s_i}} \mathbf{x} = D_{s_i} \mathbf{x}$$

The overall system defined in (8.2) and (8.3) very closely resembles closed-loop feedback system, it can be visualized in block-diagram form, as shown in Fig. 8.1. When a contact point enters stick-slip transition, at $s_i = 0$, the slip-direction is reset to a new unique slip-direction that depends only on the configuration of the impacting body. Details on the method for determining this new slip-direction at stick-slip transition can be found in [41]. The impact process, as presented in block diagram format in Fig. 8.1, terminates when the normal work $W_n(\beta)$ reaches the final normal work W_{nf}. The final value of normal work at the end of an impact event W_{nf} is calculated using the global coefficient of restitution e_* parameter and the normal work value at maximum compression W_{nc}. After the impact process, as shown in Fig. 8.1 ends, the deformation and velocity histories are used to recalculate the force-histories of all points during the collision.

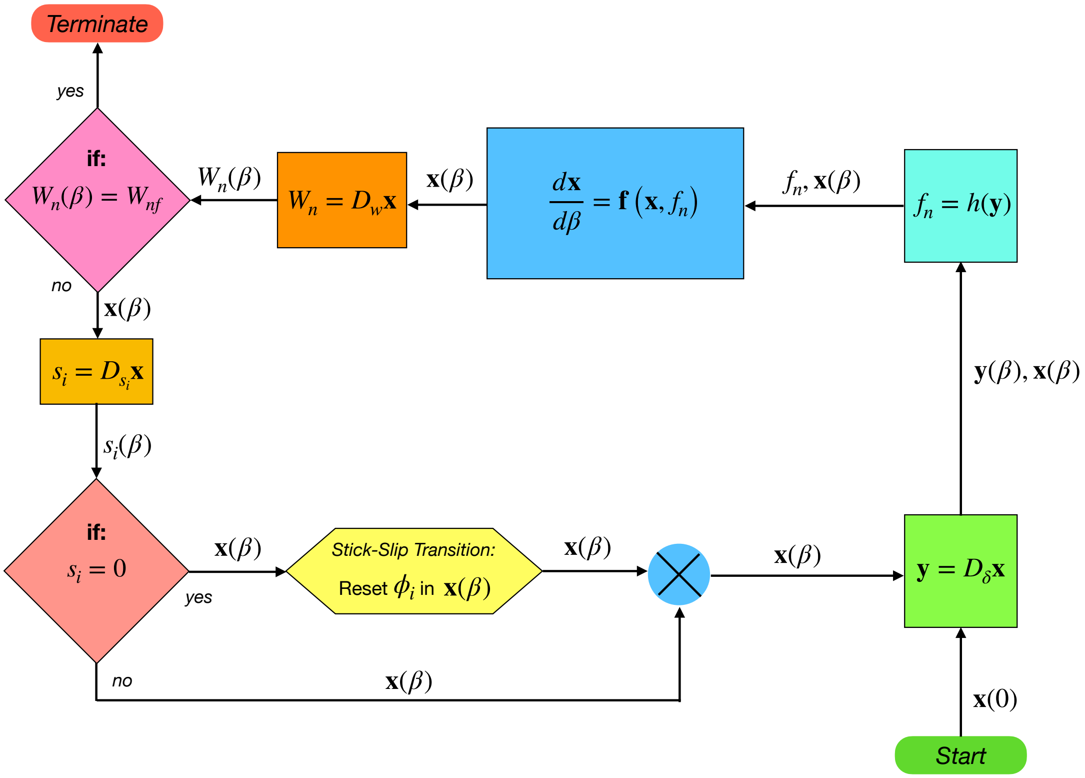

Figure 8.1: Block Diagram representation of the proposed impact analysis method

8.2 Results

This section presents a number of simulation results based on the augmented rigid impact model proposed in this article. The examples shown here are identical to the ones in shown in [42]. Since, the model proposed here is an extension of the rigid impact model in [42], all results of velocities, normal work and generalized coordinates shown ahead exactly match the ones from [42]. In addition to these matching results, the simulation results here also demonstrate the evolution deformations, forces and time during the impacts. Also, some of the examples here rely on transitioning between contacts and impacts, which are modeled as a *hybrid dynamic system* that switches dynamics between contact constraints in the *time-domain* and β-*domain*. This hybrid dynamics setup and contact constraints are not discussed in this article, in the interest of space. These are nevertheless same as in [42], hence the readers are referred to [42] for the related discussion on rigid contact modeling and the hybrid dynamics modeling.

The simulations presented here were implemented on `MATLAB` with the help of `ode45`, which is an adaptive Runge-Kutta integrator that uses the Dormand-Prince algorithm [98, 99]. Lastly, the value of the scaling parameter $\bar{\epsilon}$ used in (7.6), was chosen to be the floating-point relative accuracy value in `MATLAB`. This can be obtained by using the `eps` command on `MATLAB`, which yields the value 2.204×10^{-16}.

8.2.1 Example-1: 3D Block 2-point Impact

The example problem analyzed here is that of a block rocking against the ground. In this example, two consecutive collisions between the block and the ground is analyzed, over a span of 6 seconds long simulation. Both the block, and the ground is assumed to be composed of `SUJ2 Steel`, with density of $\rho = \rho_1 = \rho_2 = 7825\ \mathrm{kg/m}^3$, Young's modulus of $E = E_1 = E_2 = 206$ GPa, Poisson's ratio of $\nu = \nu_1 = \nu_2 = 0.3$, Hardness of $barH = \bar{H}_1 = \bar{H}_2 = 290\ \mathrm{kgf/mm}^2$ and Yield's strength of $\sigma_y = \sigma_{y_1} = \sigma_{y_2} = 350$ MPa. The damping coefficient pertaining to the visco-elastoplastic force model used in this result is $b = 0.1\ \mathrm{kg} \cdot \mathrm{m}^{-\frac{1}{2}} \cdot \mathrm{s}^{-\frac{1}{2}}$. As shown in Sec. 7.1, the contact force model used in this work is based on the hertzian theory of contact, where all contact points are assumed to be of spherical geometry. In this example, the impacts between the block and the ground is analyzed at the four corner points of the bottom face of the block. These corner points are assumed to be of spherical shape with the radius $R_1 = 0.001$ m. The ground is assumed to be perfectly flat with a radius of $R_2 = \infty$. The dimensions used for the block are $0.6 \times 0.8 \times 0.4\ \mathrm{m}^3$, hence the mass is calculated using the volume and the density ρ_1. All simulation parameters are listed in Table 8.1.

Parameters	**Block**	**Ground**
Mass	$m = 1502$ kg	-
Radius	$R_1 = 0.001$ m	$R_2 = \infty$ m
Young's Modulus	$E_1 = 206$ GPa	$E_2 = 102$ GPa
Poisson's Ratio	$\nu_1 = 0.3$	$\nu_2 = 0.3$
Yield Strength	$\sigma_{y_1} = 350$ MPa	$\sigma_{y_2} = 120$ MPa
Hardness	$\bar{H}_1 = 290 \;\; \mathrm{kgf/mm^2}$	$\bar{H}_1 = 290 \;\; \mathrm{kgf/mm^2}$
Damping Coefficient	$b = 0.1 \;\; \mathrm{kg \cdot m^{-\frac{1}{2}} \cdot s^{-\frac{1}{2}}}$	
Coefficient of friction	$\mu_s = 0.6$, $\mu_d = 0.35$	
ECOR	$e_* = 0.50$	

Table 8.1: Parameters used to simulate 2-point consecutive block-ground impacts

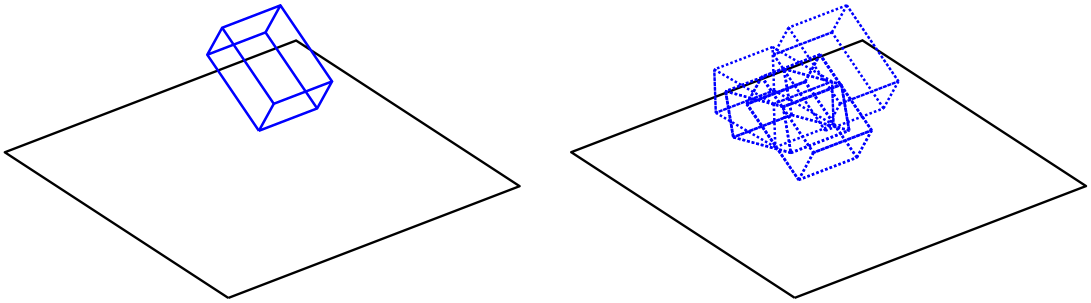

(a)

(b)

Figure 8.2: (a) Initial configuration of the block and (b) motion capture of the rocking block simulation

In this example, the steel block is dropped on the ground from a configuration as shown in Fig. 8.2(a). The block is also given an initial transnational velocity along the $\hat{\mathbf{N}}_y$ direction. Hence, the initial generalized coordinates and speeds of the block is given by,

$$\mathbf{q}(0) = \begin{bmatrix} 0 & -0.5 & 1 & \frac{\pi}{6} & 0 & 0 \end{bmatrix}^T \qquad \text{and} \qquad \dot{\mathbf{q}}(0) = \begin{bmatrix} 0 & 1 & 0 & 0 & 0 & 0 \end{bmatrix}^T$$

The block undergoes two consecutive impact events during the 6 seconds long simulation. Fig. 8.2 shows the motion of the block throughout the simulation period. Given, the initial condition, first a time-domain simulation of the equations of motion is performed, until the block comes in contact with the ground. An event based approach is used to stop the

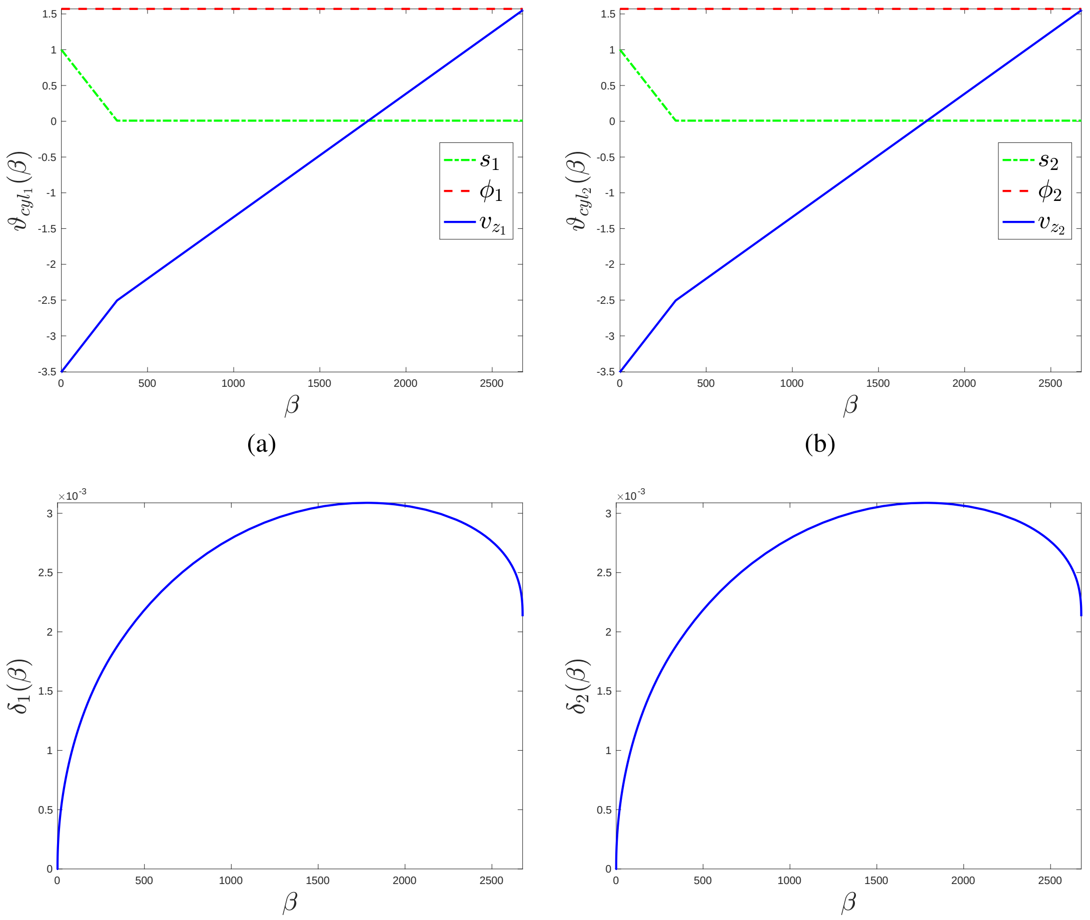

(a) (b) (c) (d)

Figure 8.3: Evolution of the velocities at (a) point 1 and (b) point 2, and the deformation histories of (c) point 1 and (d) point 2 with respect to β, during the first impact event

time-domain integration of the equations of motion upon collision detection. The impulse domain analysis presented in Sec. 5.1 and [38,41] can be used to analyze the impact events. However, the impact model proposed in this work augments the impulse-domain impact model in [41] with a force based model, as presented in Sec. 7.1 to determine the force and deformation histories during the impact event.

The model used to evolve the impact states during an impact-event is concisely presented in equations (7.6) and (7.7). In these models the impact states are evolved with respect to the independent parameter β, which either takes the value of the independent de-

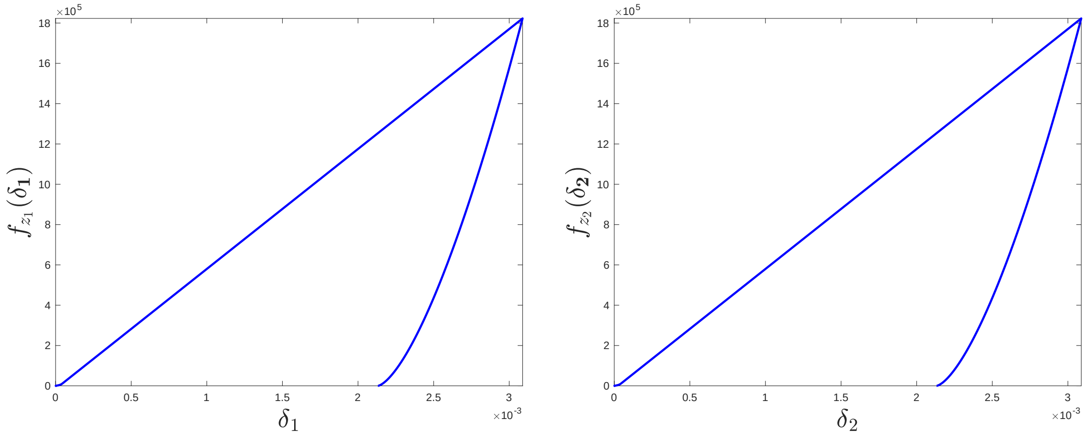

(a) (b)

Figure 8.4: Normal forces at (a) point 1 and (b) point (2) varying with the corresponding deformations, during the first impact event

formation parameter δ_n or the independent impulse parameter p_n, depending upon whether the independent normal force is zero or not. The value of the independent normal force can be calculated based on the deformation or normal work, along with the deformation rates using the contact force model presented in Sec. 7.1.2. The impact states evolved using the models in (7.6) and (7.7) include the velocities, deformations, the impulses of the contact points, the elapsed time of impact and the normal work. Figures 8.3(a) and 8.3(b) show evolution of the velocities of the contact points during the first impact event. Similarly, figures 8.3(c) and 8.3(d) show the deformations during the first impact event. The velocities shown in Fig. 8.3(a) and 8.3(b) are in cylindrical coordinates, where s_i and ϕ_i are the sliding speeds and sliding directions, respectively. Note, that in these plots the sliding speed s_i starts at a positive non-zero value and then reaches zero (stick-slip transition), and continues to be a zero till the end of impact event. Hence, the contact points initially slip and then sticks after entering stick-slip transition. The normal velocities are also affected as the contact points transition from slipping to sticking.

The deformations at the contact points evolved by integrating (7.6) or (7.7) with respect to β, allow for the computation of the independent normal force parameter, $f_n(\delta_n \dot{\delta}_n)$. The deformation rates at the contact points can be expressed in terms of the normal velocity components of the same points $\dot{\delta}_n = -\vartheta_n$. The contact force model, defined in the most general form in (7.11), changes according to different contact regimes namely, *elastic*, *elastic-plastic*, and *plastic* regimes during compression, as shown in (7.13), (7.14) and (7.15). A separate contact force model for the restitution phase developed in this work (7.29), is used as the collision enters the restitution phase. The force distribution (gradient) vector $\mathbf{C}$ is used to calculate the forces at all contact points from the independent force parameter using (7.8). Fig. 8.4(a) and (b) shows the normal force components at the two contact points with respect to the deformations during the impact event. Note that the normal forces shown Fig. 8.4 has a loading phase (during which the forces increase), and the unloading phase (during which the forces decrease). The loading and unloading phases correspond to the compression and restitution phases of the impact model. The normal forces first increase to a maximum along with maximum deformation of the contact points. After reaching maximum compression the normal forces and the associated deformations start decreasing, and the normal forces reach zero and the end of the restitution phase, where the impact event terminates. The residual deformation at the end of the impact event is the permanent deformation the contact point experiences due to the plasticity of the material, at end of impact. The permanent deformation induced in this model also characterizes the hysteresis in Fig. 8.4, such that the total area under the normal force curves (both points combined) represent the amount of energy lost due to the normal forces during the impact event. However, note that the proposed model does not depend upon a priori determination of the permanent deformation, rather in this work, the net energy loss (in terms of the global energetic coefficient of restitution, e_*) is used to determine the permanent deformation.

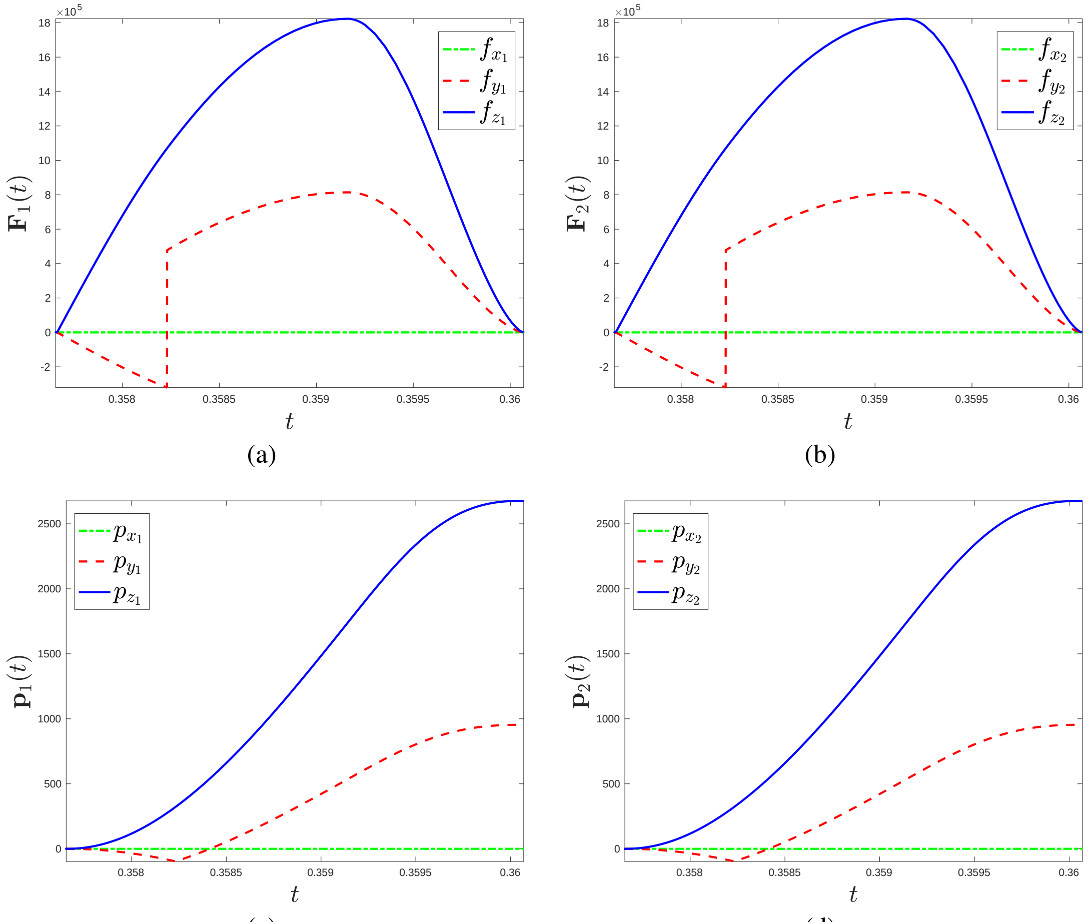

(a) (b)

(c) (d)

Figure 8.5: Evolution of (a) forces at point 1, (b) forces at point 2, (c) impulses at point 1, (d) impulses at point 2 with respect to time, during the first impact event

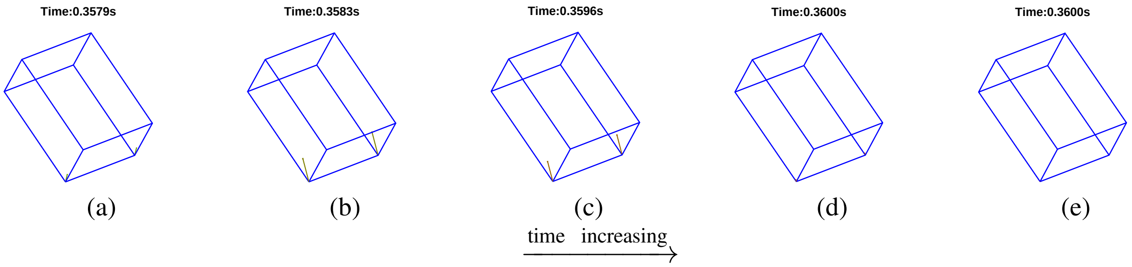

(a) (b) (c) (d) (e)

Figure 8.6: Visualization of the contact forces on the block at different times block during the first impact event (time increases from left (a) to right (e))

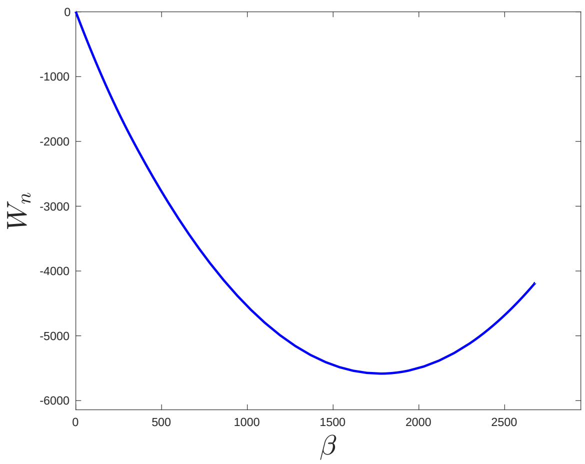

Figure 8.7: Evolution of Normal Work with respect β, during the first impact event

The impact states evolved by integrating (7.6) or (7.7), also includes the elapsed time of impact, impulses at all contact points and the normal work done by the block. Therefore, the time-histories of the forces and impulses is also known. Fig. 8.5(a) and (b) shows how the forces change with time during the event. Similarly, Fig. 8.5(a) and (b), shows the trajectories of the impulses at the two contact points with respect to the time of impact. The forces on the block at different times during impact can also be visually depicted, as shown in Fig. 8.6(a)-(e). In Fig. 8.6, time increases left (a) to right (e), and the force at each contact point is represented with an arrow whose length is scaled according to the magnitude of the force. Note, that the arrow is not visible at the beginning, Fig. 8.6(a) and the end, Fig. 8.6(e) of the impact event. The length of the arrow in Fig. 8.6 first increases and then decreases during the restitution phase. Also note the change in the arrow direction between Fig. 8.6(c) and 8.6(d), indicating the change in force directions at the stick-slip transition. Fig. 8.7 shows the evolution of the normal work with respect to β, during the impact event. As seen in the prior studies [38, 41], the normal work follows a parabolic trajectory with respect to β, whose minima represent the maximum compression, and the

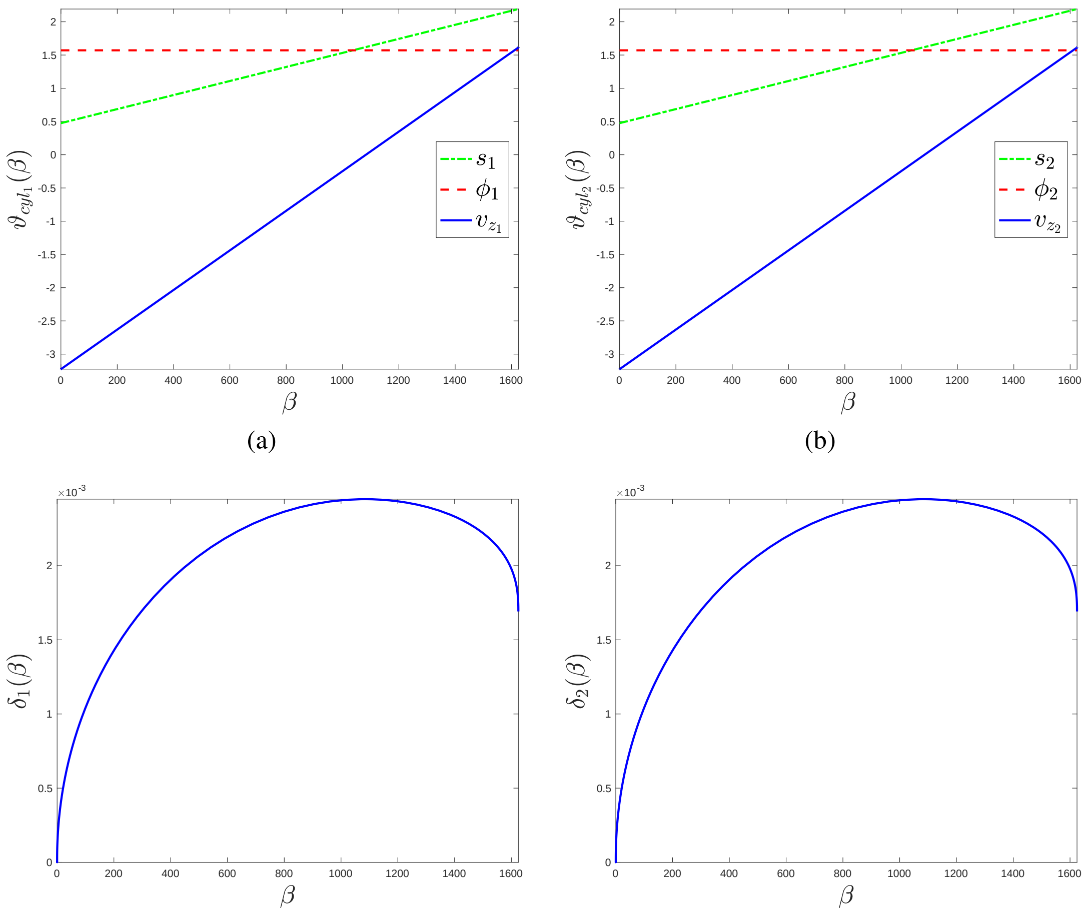

(a) (b)

(c) (d)

Figure 8.8: Evolution of the velocities at (a) point 3 and (b) point 4, and the deformation histories of (c) point 1 and (d) point 2 with respect to β, during the second impact event

normal work value at the maximum compression is used to determine the end of the impact event.

Similar to the results of the first impact event, the results from the second impact analysis is also presented here. The second impact event also involves two contact points named point 3 and point 4. Fig. 8.8(a) and 8.8(b) show the evolution of the velocities, and Fig. 8.8(c) and 8.8(d) show the evolution of deformations with respect to β, during the second impact event. It can be seen from Fig. 8.8(a) and 8.8(b), that both contact points slip throughout the impact event. The normal forces in terms of the deformations during

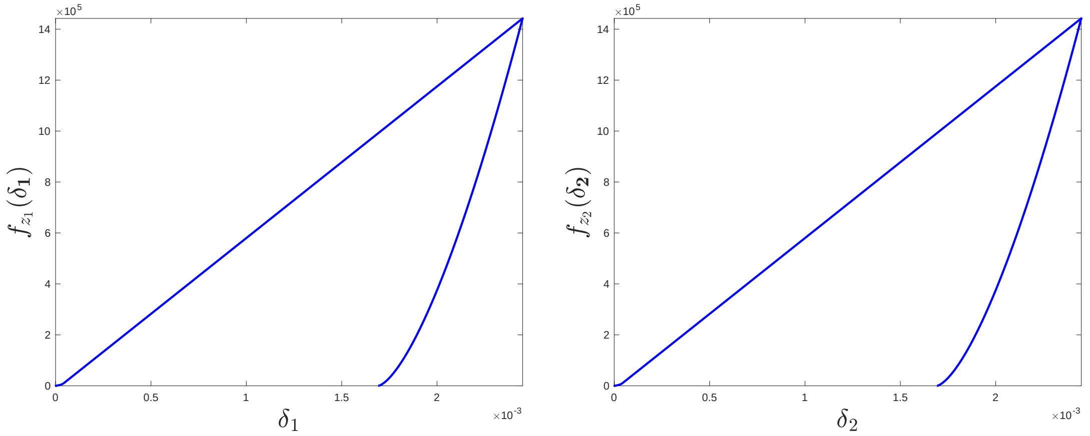

(a) (b)

Figure 8.9: Normal forces at (a) point 1 and (b) point (2) varying with the corresponding deformations, during the second impact event

the second impact event is shown in Fig. 8.9(a) and 8.9(b). The time-histories of the forces and impulses are presented in Fig. 8.10. Fig. 8.11 presents a visual representation of the forces at the contact points during the impact event, and Fig. 8.12 shows the evolution of normal work with respect to the parameter β during the second impact event.

The post-impact states computed using the proposed impact analysis method was used to reset the generalized speeds of the system after collision and resume time domain integration. Fig. 8.13(a) and 8.13(b) show the generalized coordinates and the generalized speeds throughout the simulation. Notice, that the discontinuities in the generalized coordinates $\mathbf{q}(t)$, correspond with the sharp changes in generalized speeds $\dot{\mathbf{q}}(t)$. Fig. 8.14(a) shows the contact forces applied to the four corner points throughout the simulation. The spikes on the contact force plot indicate the applied contact forces during impact events. Fig. 8.14(b) shows the kinetic, potential and total energies during the impact event. Each stepped decrease in total energy of the system indicate the net energy loss during impacts. Also, note that the total energy of the system never increases during the simulation. Hence

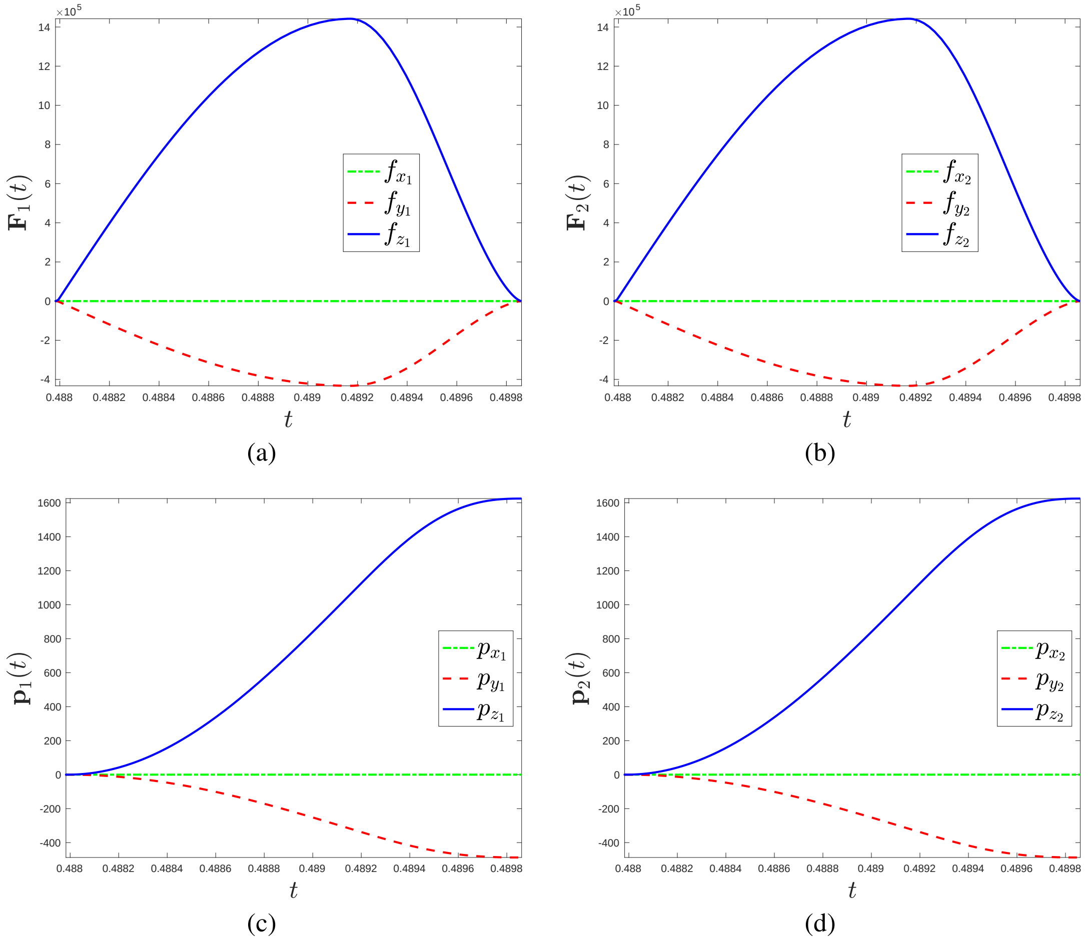

Figure 8.10: Evolution of (a) forces at point 1, (b) forces at point 2, (c) impulses at point 1, (d) impulses at point 2 with respect to time, during the second impact event

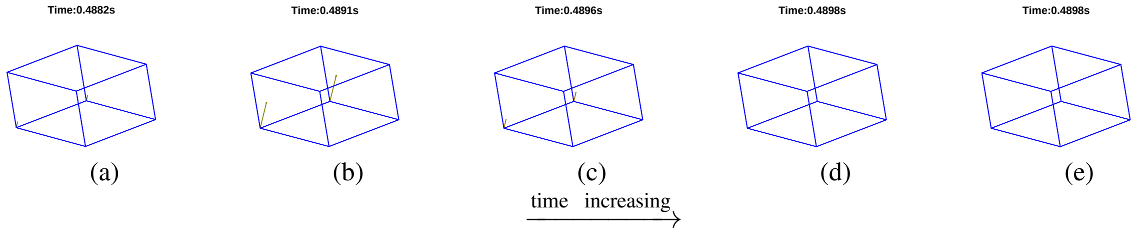

Figure 8.11: Visualization of the contact forces on the block at different times block during the second impact event (time increases from left (a) to right (e))

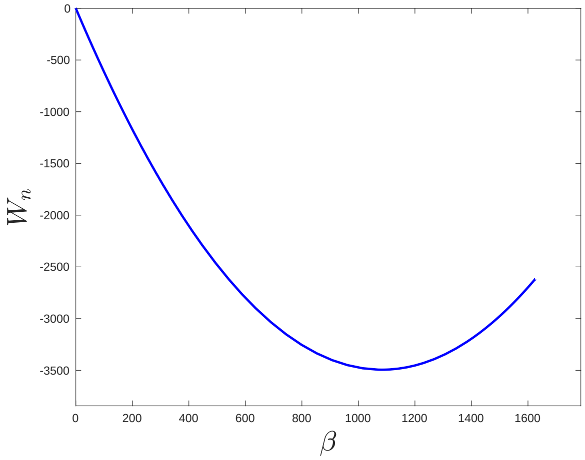

Figure 8.12: Evolution of Normal Work with respect β, during the second impact event

it may be concluded that the proposed approach for impact analysis is energetically consistent.

8.2.2 Example-2: 3D Sphere 3-point Impact

This section presents a simulation example of a three-dimensional model of the sphere is shown in Fig. 8.15, undergoing impact at three separate points denoted by 1, 2, and 3, against two walls and a ground. This system has six degrees-of-freedom (DOF) defined by six generalized coordinates - three translation q_1, q_2, q_3 and three orientation q_4, q_5, q_6 coordinates. The sphere is assumed to be made out of `SUJ2 Steel`, which has a mass of $m = 1$ kg and a radius of $R_1 = 0.50$ m. The sphere has a Young's modulus of $E_1 = 206$ GPa, Poisson's Ratio of $\nu_1 = 0.3$ and a Yield's strength of $\sigma_{y_1} = 350$ MPa. The wall and the ground is assumed to be composed of a material whose Young's modulus is $E_2 = 102$ GPa, Poisson's Ratio is $\nu_2 = 0.4$ and Yield strength is $\sigma_{y_2} = 120$ MPa. The wall and the ground are assumed to be completely flat and therefore have the radii, $R_2 = \infty$. The effective hardness values for the sphere, wall and the ground is considered to be $\bar{H} = 290$ $\mathrm{kgf/mm}^2$. The damping coefficient used for this impact was $b = 0.1\ \mathrm{kg} \cdot \mathrm{m}^{-\frac{1}{2}} \cdot \mathrm{s}^{-\frac{1}{2}}$. All parameters used in this simulation are summarized in Tab. 8.2.

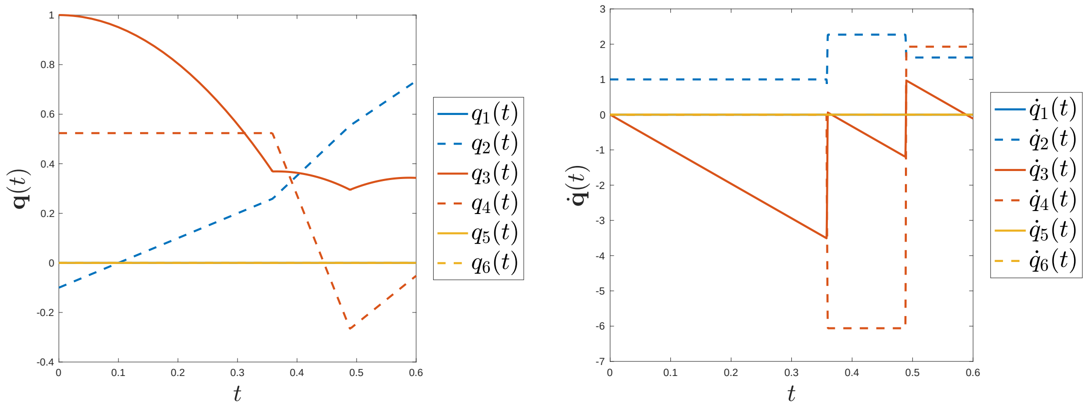

(a) (b)

Figure 8.13: Generalized (a) coordinates and (b) speeds with respect to time, throughout the simulation

An arbitrary initial position and translational velocity was used for the sphere simulation with no initial angular velocity. The simulation of the sphere is depicted in Fig. 8.16a, as it impacts a corner formed by the ground and two wall planes, and ends when a second impact is captured with the ground. This corner impact event is an indeterminate collision involving points 1, 2, and 3. An ECOR of $e_* = 0.50$ is used. The static and dynamic coefficients of restitution are chosen to be $\mu_s = 0.6$ and $\mu_d = 0.35$. After impacting the corner, the position of the impact points 1, 2, and 3 change which demonstrate the sphere's post-impact angular velocity as a result of impact. A plot of the system energy is shown in Fig. 8.16b to show energy consistency throughout the simulation.

After impact, the sphere follows a lower trajectory which suggests that the system lost energy from the impact. This is supported by the energy plot in Fig. 8.16b, which is further used to determine that no energy gains were encountered throughout the simulation.

The result of this three-dimensional case was obtained using the proposed method. The augmented impact model in (7.6) and (7.7) is used along with an independent force model $f_n(\delta_n, \dot{\delta}_n)$ from Sec. 7.1, to evolve the velocities and deformations of the three points

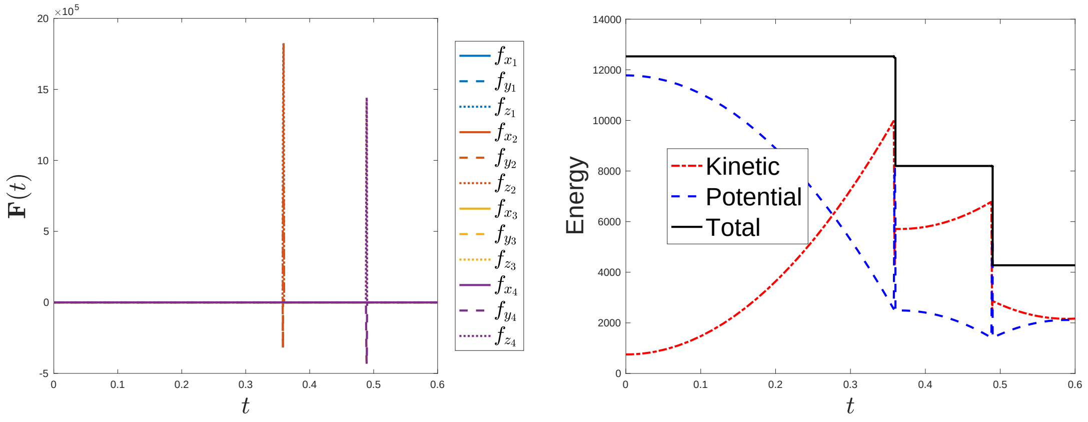

(a) (b)

Figure 8.14: (a) Forces and (b) Energies with respect to time throughout the simulation

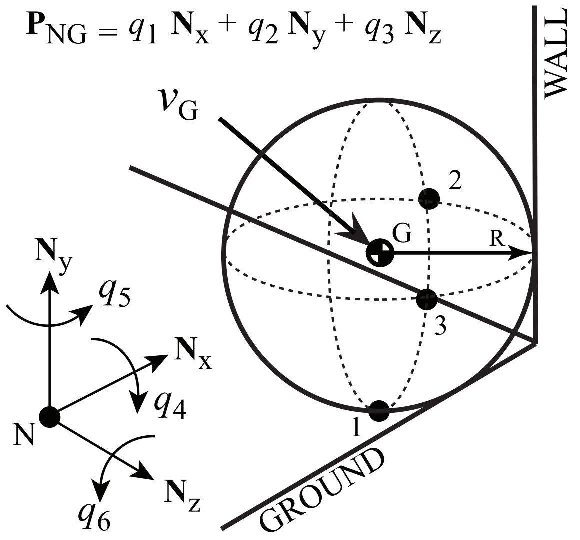

Figure 8.15: Three dimensional model of a sphere impacting a corner.

along with the normal work and elapsed time of impact. The end of the global compression phase is determined by checking the slope of normal work as it is being evolved. The global ECOR parameter, $e_* = 0.5$ is used to determine the end of impact event. The evolution of the normal work and the velocities during the impact with respect to β is shown in plots Fig. 8.17a and Fig. 8.17b. These results are identical to the ones shown in [42].

Parameters	**Sphere**	**Ground/Wall**
Mass	$m = 1$ kg	-
Radius	$R_1 = 0.50$ m	$R_2 = \infty$ m
Young's Modulus	$E_1 = 206$ GPa	$E_2 = 102$ GPa
Poisson's Ratio	$\nu_1 = 0.3$	$\nu_2 = 0.4$
Yield Strength	$\sigma_{y_1} = 350$ MPa	$\sigma_{y_2} = 120$ MPa
Hardness	$\bar{H}_1 = 290 \ \mathrm{kgf/mm^2}$	$\bar{H}_1 = 290 \ \mathrm{kgf/mm^2}$
Damping Coefficient	$b = 0.1 \ \mathrm{kg \cdot m^{-\frac{1}{2}} \cdot s^{-\frac{1}{2}}}$	
Coefficient of friction	$\mu_s = 0.6$, $\mu_d = 0.35$	
ECOR	$e_* = 0.50$	

Table 8.2: Parameters used to simulate 3-point sphere impact

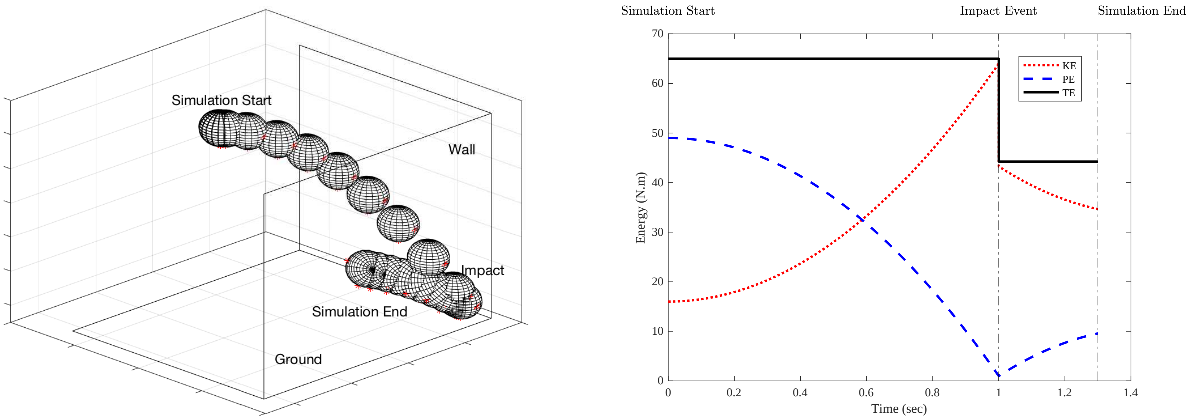

(a) (b)

Figure 8.16: (a) Simulation results and (b) Energy consistency of the 3D sphere example impacting a corner.

Evolution of systems in (7.6) and (7.7) also yield the deformation histories of the three contact points and the elapsed time of impact. These quantities depend upon the independent force model which is characterized by the material properties. After obtaining the deformation history of all contact points during the impact, the forces at these points can be calculated based on 7.8. Fig. 8.18 shows the normal force-deformation curves of the three contact points during the impact. Note, that both the normal and the deformation

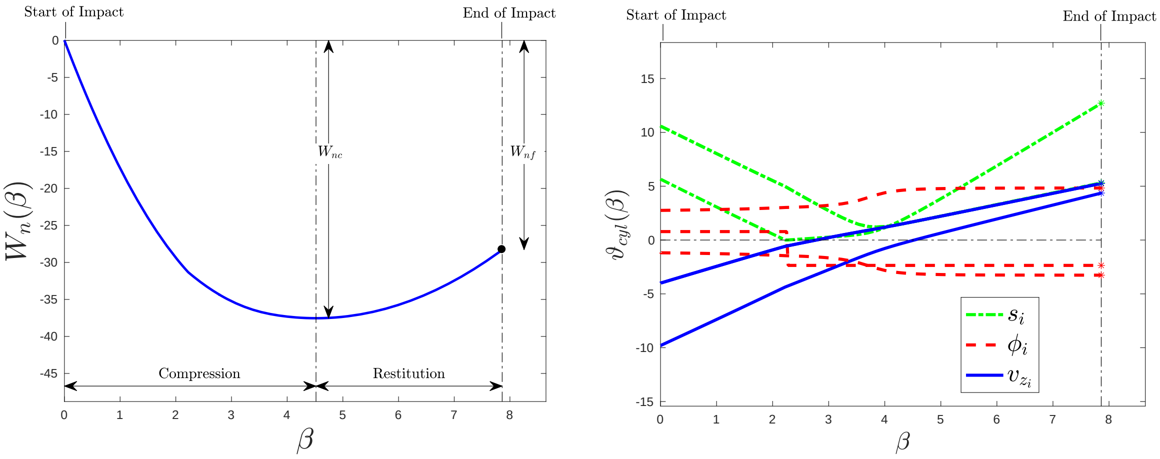

(a) (b)

Figure 8.17: (a) Normal work done and (b) evolution of sliding velocities, sliding directions, and normal velocities throughout the impact event for the 3D sphere example.

increases during the compression phase and then decreases during the restitution phase. Also, notice that the force increases to a very high value in the order of 10^4, whereas the deformation changes by a very small value in the order 10^{-4}. Hence, these plots represent characteristic properties of rigid-body impacts which negligible deformations and very high forces. Fig. 8.18 also highlights a hysteresis phenomenon which leads to some permanent deformations at the contact points. Fig. 8.19a and Fig. 8.19b show the evolution of all impulses and forces with respect to the elapsed time during the impact. As it is to be expected from rigid-body impacts, the elapsed time during the impact event is very small ans is in the order of 10^{-5}. Note that there exist some discontinuities in the tangential forces shown in Fig. 8.19b. These discontinuities are associated with stick-slip transition, and coincide with the discontinuities seen in the velocities plot in 8.17b. The forces during the impact event is can be visualized using Fig. 8.20, which give a sense of the direction and magnitude of the forces during the impact at various time instances. FIg. 8.21 shows the forces at the three points throughout the simulation. The collision of the ball with the wall-ground corner is marked by a sharp spike in forces at 1 second time into the simulation.

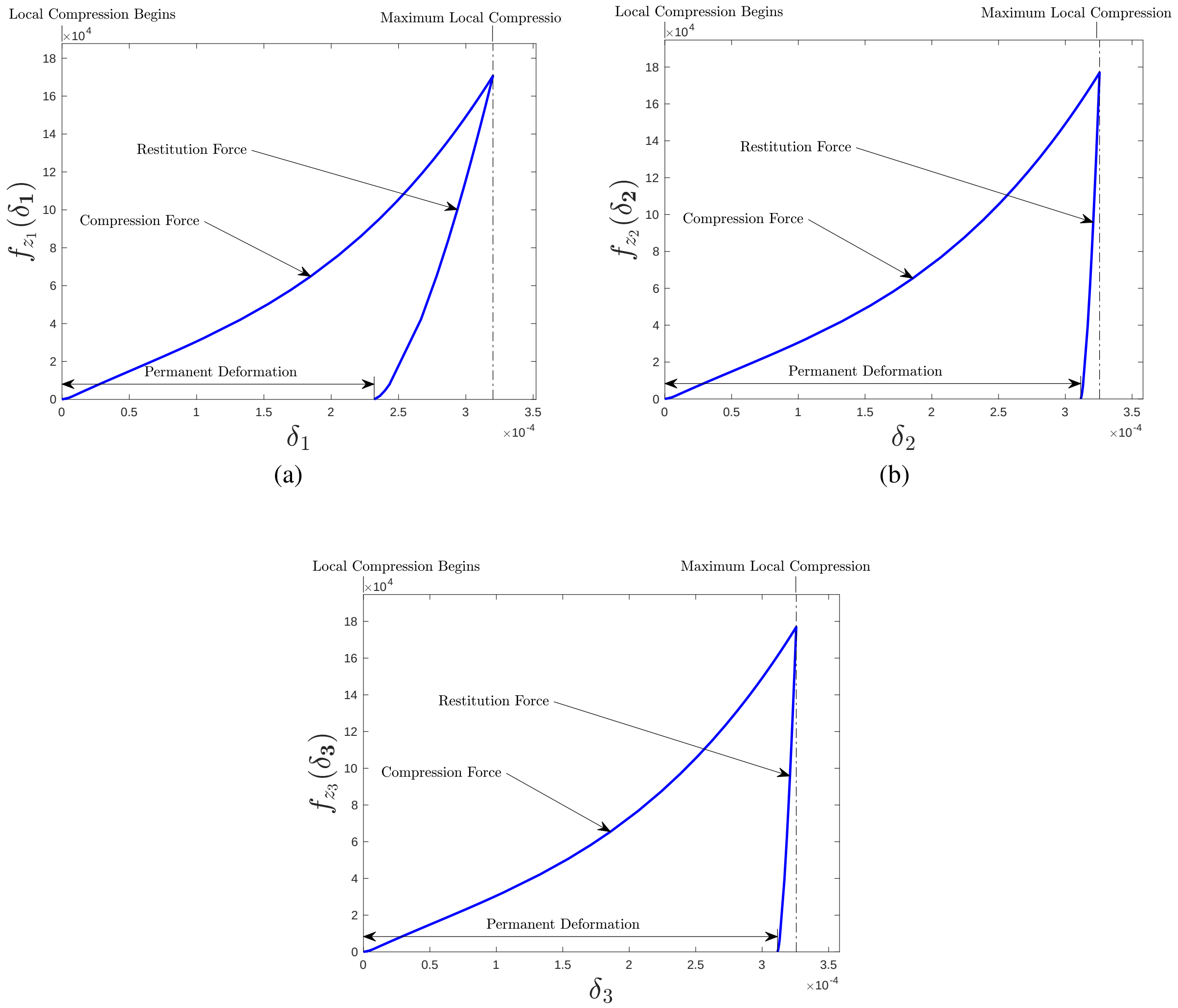

Figure 8.18: Normal Force-Deformation curves for (a) point 1 (b) point 2 and (c) point 3

8.2.3 Example-3: 3D Block 4-point Impact

This section revisits the example of a three-dimensional block model impacting a ground from [42], as shown in Fig.5.1. The block impacts the ground at four different points, denoted by 1, 2, 3, and 4, which are located at the corner points of the impacting surface of the block and its center of mass at point O. The system has six DOFs described by three translation q_1, q_2, q_3 and three orientation q_4, q_5, q_6 coordinates. The block has length $l = 0.1$m, width $b = 0.2$m, and height $h = 0.05$m with mass $m = 0.25\ kg$. The

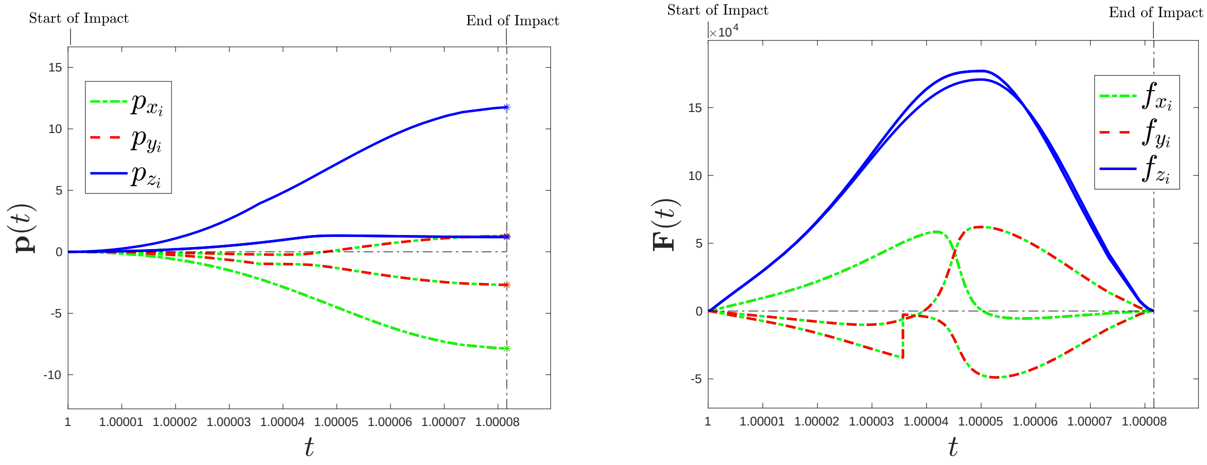

(a) (b)

Figure 8.19: Changes in (a) impulses and (b) forces with respect to time during the impact event.

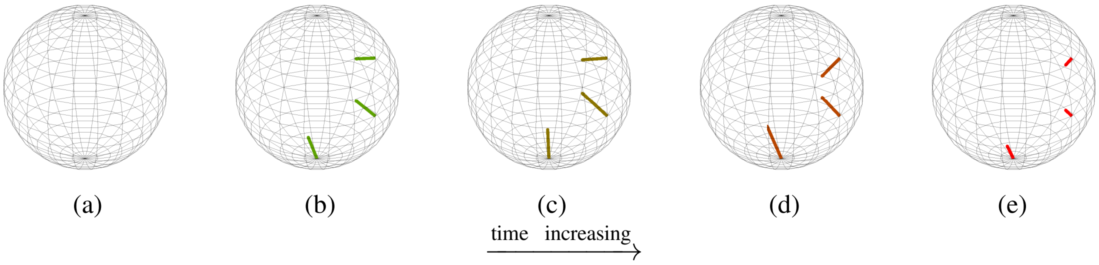

Figure 8.20: Visualization of the contact forces on the 3D sphere at different times block during the impact event (time increases from left (a) to right (e))

four corners of the bottom face of the block, where the points 1, 2, 3 and 4 are located are assumed to be rounded with a radius of $R_1 = 0.01$ m. The block is considered to be made out of `SUJ2 Steel` which has a Young's modulus of $E_1 = 206$ GPa, Poisson's Ratio of $\nu_1 = 0.3$ and a Yield's strength of $\sigma_{y_1} = 350$ MPa. The ground is assumed to be composed of a material whose Young's modulus is $E_2 = 102$ GPa, Poisson's Ratio is $\nu_2 = 0.4$ and Yield's strength is $\sigma_{y_2} = 120$ MPa. Also, since the ground is perfectly flat, the radius is selected as, $R_2 = \infty$. The hardness values for both the ball and the wall is selected to be $\bar{H} = 290\ \mathrm{kgf/mm}^2$. The damping coefficient used in this impact is $b = 10\ \mathrm{kg} \cdot \mathrm{m}^{-\frac{1}{2}} \cdot \mathrm{s}^{-\frac{1}{2}}$.

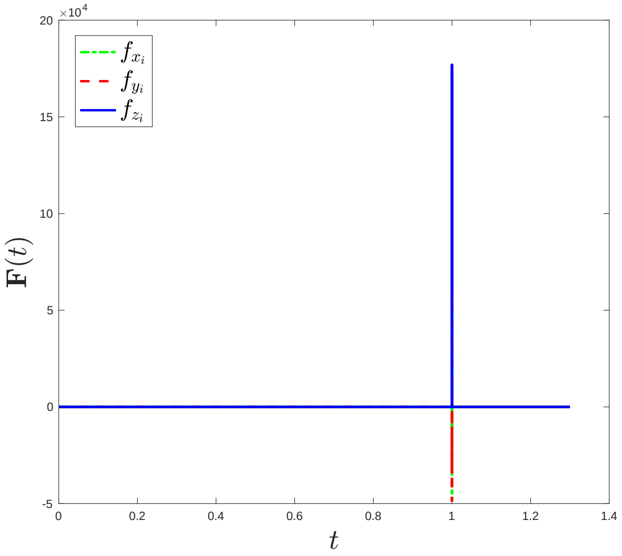

Figure 8.21: Forces vs. Time for the ball throughout the simulation

The static and dynamic coefficient of friction of $\mu_s = 0.6$ and $\mu_d = 0.35$, respectively are used in this simulation The global ECOR value for this impact is chosen to be $e_* = 0.50$. All parameters used for this simulation are listed in Tab. 8.3

Parameters	**Block**	**Ground**
Mass	$m = 0.25$ kg	-
Radius	$R_1 = 0.01$ m	$R_2 = \infty$ m
Young's Modulus	$E_1 = 206$ GPa	$E_2 = 102$ GPa
Poisson's Ratio	$\nu_1 = 0.3$	$\nu_2 = 0.4$
Yield Strength	$\sigma_{y_1} = 350$ MPa	$\sigma_{y_2} = 120$ MPa
Hardness	$\bar{H}_1 = 290 \ \text{kgf}/\text{mm}^2$	$\bar{H}_2 = 290 \ \text{kgf}/\text{mm}^2$
Damping Coefficient	$b = 10 \ \text{kg} \cdot \text{m}^{-\frac{1}{2}} \cdot \text{s}^{-\frac{1}{2}}$	
Coefficient of friction	$\mu_s = 0.6$, $\mu_d = 0.35$	
ECOR	$e_* = 0.50$	

Table 8.3: Parameters used to simulate 4-point impact of the 3D block

The simulation is started at time $t = 0$s with points 3 and 4 of the block in contact with the ground, at an initial angle of $-15°$, such that the block drops with a pivots along the edge defined by points 3 and 4 and undergoes a 4-point collision. Contact constraints based on [42] are imposed on points 3 and 4 such that they remain in contact with the ground till the 4-point collision (involving points 1, 2, 3 and 4) takes place. During the drop, points 3 and 4 also go through a number of 2-point collisions with the ground. The 4-point collision of the block with the ground takes place such that the points 3 and 4 are in contact with the ground initially. The results in this example primarily focus on the analysis of this 4-point collision, with two of the points in contact initially. After the 4-point collision the block resumes its motion with a new set of generalized speeds The simulation is ended at time $t = 0.12$s. A motion capture of this 3D block trajectory is shown in Fig. 8.22a, which demonstrate the overall motion of the block. The kinetic, potential and total energies of the system throughout this motion has been shown in Fig. 8.22b. Evidently, it can be seen from Fig. 8.22b, that the system loses energy during its trajectory till the 4-point collision. This loss in energy is due to slipping frictional contact constraints imposed on points 3 and 4, based on [42]. There is also some minor loss in energy due to a number of 2-point collisions involving points 3 and 4, which take place during this part of the block motion. One can see in Fig. 8.22b, the 4-point collision also results in a significant loss in energy of the system. This loss of energy takes place instantaneously (during the time-period of the collision), and can be characterized by the global ECOR e_* values during the impact events. Energy is again lost due to frictional contact constraints, as the motion of the block resumes after the 4-point collision.

The 4-point collision between points 1, 2, 3, and 4 of the 3D block and the ground consists of two separate impact events. In the 1st impact event all four points are simultaneously analyzed for impact. Since, points 3 and 4 come into the impact event while in contact, they have zero normal velocities initially, whereas points 1 and 2 have negative normal velocities initially. The velocities, normal work, deformations and the elapsed time are evolved using the augmented impact model in (7.6) and (7.7). The global ECOR,

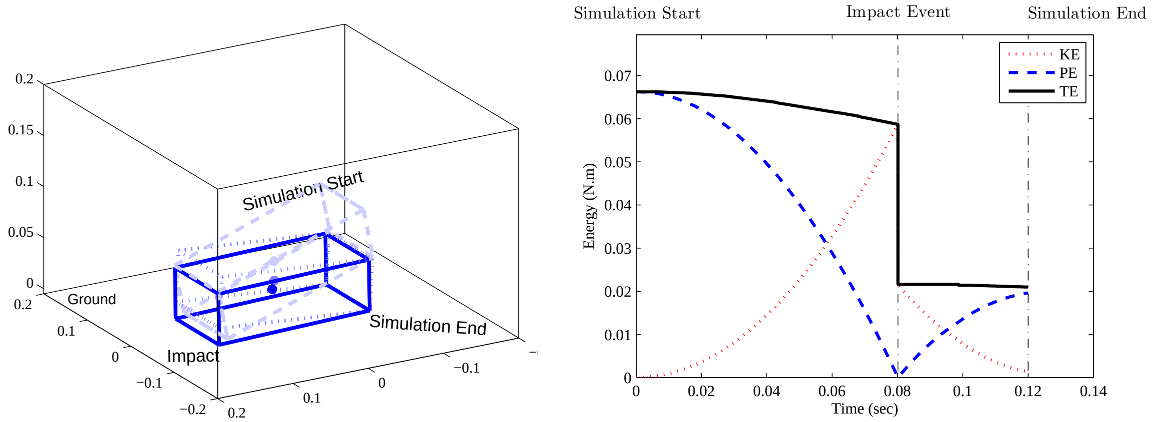

(a) (b)

Figure 8.22: (a) Simulation of the 3D rocking block example with four corner impact points and (b) energy consistency for the simulation.

$e_* = 0.5$ value characterizes the termination criteria for this impact event. Fig. 8.23a and Fig. 8.23b shows the evolution of the velocities and normal work with respect to the parameter β. It can be seen from Fig. 8.23, that the velocities and normal work plots for this 1st impact event is identical to the results in [42], which is based on only the rigid impact model. The contact points during this 1st impact event undergo stick-slip transition, exhibit slip-reversal, similar to the result obtained in [42]. Stick-slip transitions and slip-reversal phenomenon are discussed in great details in [42]. The normal work plot in Fig. 8.23b shows a decrease in the energy of the system during the 1st impact event. Note, that the normal velocities of all contact points do not reach positive values by the end of the 1st event. Hence, after the end of the 1st impact event there is a 2nd impact event that follows immediately. Only the points whose normal velocities did not reach a positive vale at the end of the 1st impact event, are analyzed in the 2nd impact event, with $e_* = 0.5$. Fig. 8.24a and Fig. 8.24b shows the evolution of the normal work respectively. Once again the velocities and normal work plots in Fig. 8.24 are very similar to the ones obtained in [42]. Note that the normal velocities of the two contact points at the end of the 2nd impact event reach positive values. Hence, the 4-point collision ends with the 2nd impact event, and the new post-impact velocities and impulses are used to restart the simulation.

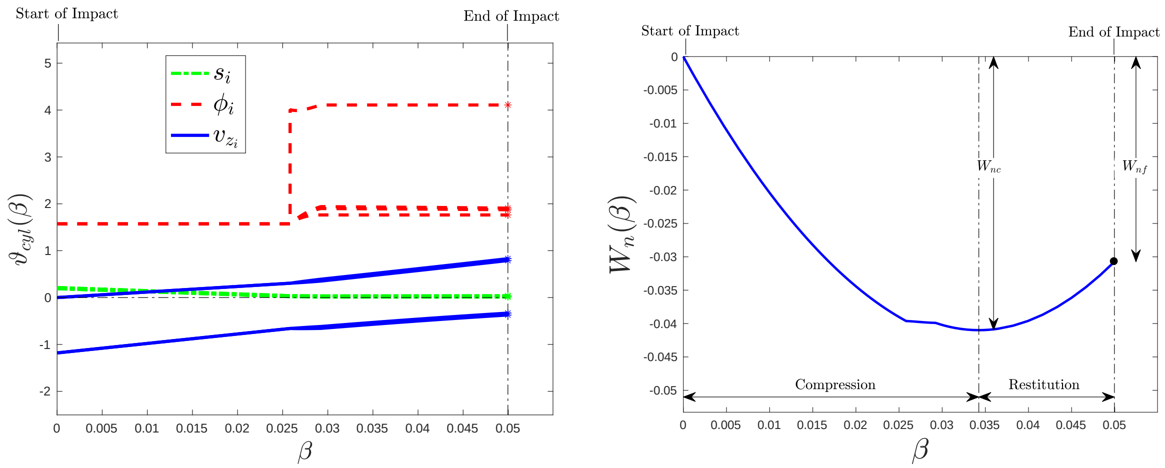

(a) (b)

Figure 8.23: (a) Evolution of the cylindrical velocities and (b) Normal work done during the 1st impact event for the 3D rocking block example with four corner impact points.

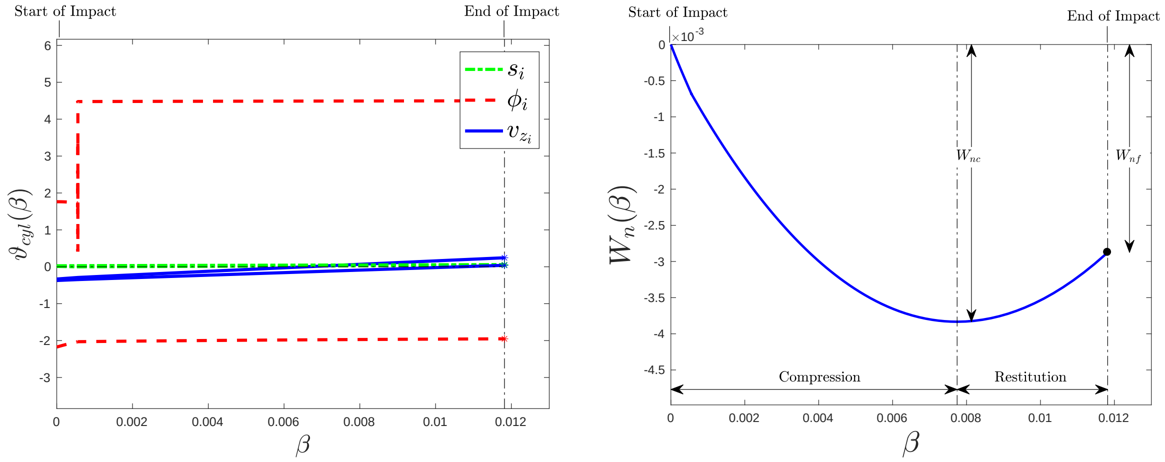

(a) (b)

Figure 8.24: (a) Evolution of cylindrical velocities and (b) Normal work done during the 2nd impact event for the 3D rocking block example with four corner impact points.

The augmented impact model also gives the deformation histories and elapsed time during the 1st and 2nd impact events. The deformation histories of all contact points are used to calculate the force-history throughout the collision. Fig. 8.25 shows the normal force - deformation curves for all four contact points throughout the collision (inclusive of both 1st and 2nd impact event). Since, points 1 an 2 have negative initial normal velocities, the points undergo a local compression phase followed by a local restitution phase. Note that normal forces of points 1 and 2 increases with increase in the deformation during their local compression phases. Although it may not be easily visible from Fig. 8.25a and Fig. 8.25b, the deformations of points 1 and 2 decrease with the decreasing restitution force during their local restitution phases. The restitution force curves for points 1 and 2 are very steep in Fig. 8.25a and Fig. 8.25b because the local restitution for these points take place during the 2nd impact event which involves only two points. Also, from Fig. 8.24 it can be seen that the normal velocity changes by a small amount during the 2nd impact event. Points 3 and 4, on the other hand, has zero initial normal velocities and only participates in the 1st impact event. Fig. 8.25c and Fig. 8.25 shows the force-deformation curve for the points 3 and 4. Since, points 3 and 4 start with zero initial normal velocities, these points do not have local compression phases. Instead these points have local restitution phase at the beginning of the 1st impact event. Points 3 and 4 unloads the contact constraint force to zero during their local restitution phase. Since, points 3 and 4 begins with local restitution and initially the deformations are assumed to be zero. Hence, in Fig. 8.25c and Fig. 8.25d the deformations start at zero and ends at small negative values.

The overall elapsed time of impact obtained from augmented impact model is very small, and in the order of 10^{-5}. Fig. 8.26a and Fig. 8.26b shows how the impulses on the system varies with respect to time during the 1st and the 2nd impact event. Fig. 8.27 shows how the forces at all contact points change through out the collision (which includes the 1st and 2nd impact events). Since, the normal force at points 3 and 4 starts with a relatively small values due to contact and then unloads to zero during the 1st impact event, the forces on points 3 and 4 are barely visible in the plot shown in Fig. 8.27, due to the scale of the forces at points 1 and 2. Note the discontinuities in the tangential forces, which demonstrate the effects of stick-slip transition on the forces, as seen earlier in case of the velocities in Fig. 8.23a and Fig. 8.24a.

Figure 8.28a shows the forces at all contact points throughout the simulation. The large spike at approximately time $t = 0.08$s indicate forces on the block due to the 4-point collision. Notice that the elapsed time of impact is not discernible in the Fig. 8.28a, which agree with the assumption that impact occurs over negligibly small time-periods for rigid bodies. In Fig. 8.28a, it is hard to see a number of significantly smaller spikes of forces associated several 2-point collisions that takes place before the block undergoes the 4-point collision. These 2-point collisions can be clearly observed in the log-magnitude plot of these forces in Fig. 8.28b.

Lastly, the forces on the block during the 4-point collision can visualized using Fig. 8.20. Fig. 8.20 shows scaled magnitude of the forces at different collision points. The forces at contact points 1 and 2 can be clearly seen, but the forces at points 3 and 4 cannot be seen as their magnitudes are significantly smaller.

8.2.4 Example-4: 3D Block Surface-Surface Contact and Impact

In [42], it was shown that the rigidity based impact model can be used to analyze surface-surface impacts. It was also shown that impacts between flat surfaces is independent of the number of points used to analyze impacts, if the rigid hypothesis is maintained in analyzing these collisions. This was shown by considering rigid block model and analyzing it for four different cases: (a) 4-point, (b) 8-point (c) 16-point and (d) 25-point grid model of the bottom surface of the block. It was found that given the same initial condition, simulation results are identical for all of these cases. In this section, the same example is repeated. As seen from earlier results, the augmented impact model proposed in this work, yields the same results as the purely rigid impact model presented in [42]. This fact is true here as well, however the main goal of redoing this example using the augmented impact model is to get an approximate estimate of the force distribution over an impacting surface. However, one hindrance towards this is to find appropriate radii for each contact point. In this work, the force model used to augment the rigid impact model only works for objects with spherical geometry. In the previous example of the block the collision was assumed to be taking place at the four corner points, therefore an assumption could be made regarding the roundness of the corners of the block, such that a radius of curvature could be selected. In this example, some of the cases involve analyzing impacts within the flat plane of contact, where the radii are infinite. Hence, some approximations are necessary here in order to use the same model of impact for all cases in this problem. The approximation used here is to consider that the rigid block is composed of a number of spheres, such that each contact point on the bottom face of the block could be associated with a sphere. The maximum number of points used to model the bottom face of the block in this example is 25 points, as shown in Fig. 8.30a. Hence, the bottom face of the block must be composed of 25 spheres. Thus, the entire block can be modeled as a lattice structure composed of 75 spheres, as shown in Fig. 8.30b. Of course, this type of a block model would not yield exact forces. Nevertheless, this approach can yield a decent approximation of the forces with a relatively simple model of contact force.

Hence, in this example the block model analyzed for contact and impact with variable number of contact points. Fig. 8.31 shows the block model with various number of contact points, positioned and oriented according to the constant initial conditions used in these simulations. The block model has a mass of 2.5 kg and has the dimensions $1.5\mathrm{m} \times 1.5\mathrm{m} \times 1\mathrm{m}$. The block is dropped from a height of $1.5m$ (the distance between the center of mass and the ground), with a roll angle of $-0.2\mathrm{rad}$. The radii of each contact point is chosen as the radii of the spheres shown in Fig. 8.30, which is $R_1 = 0.1875$m. Again the block is assumed to be made out of `SUJ2 Steel` with a Young's modulus of $E_1 = 206$ GPa, Poisson's Ratio of $\nu_1 = 0.3$ and a Yield's strength of $\sigma_{y_1} = 350$ MPa. The ground is assumed to be composed of a material whose Young's modulus is $E_2 = 102$ GPa, Poisson's Ratio is $\nu_2 = 0.4$ and Yield's strength is $\sigma_{y_2} = 120$ MPa. The ground is considered to have radius of $R_2 = \infty$. The hardness values for both the block and the ground is selected to be $\bar{H} = 290 \text{ kgf}/\text{mm}^2$. The damping coefficient used in this impact is $b = 10 \text{ kg} \cdot \text{m}^{-\frac{1}{2}} \cdot \text{s}^{-\frac{1}{2}}$. The values for static and dynamic coefficients of friction are selected to be $\mu_s = 0.5$ and $\mu_d = 0.4$, respectively. The global ECOR value is chosen to be $e_* = 0.5$. All parameters used in these simulations are listed in Tab. 8.4. The bottom face of the block interacts with the ground throughout the simulation. Simulation results. over a 2 seconds period, are generated for each of the four different cases, using the proposed augmented impact model along with the contact constraints, as proposed in [42].

Parameters	**Block**	**Ground**
Mass	$m = 2.5$ kg	-
Radius	$R_1 = 0.1875$ m	$R_2 = \infty$ m
Young's Modulus	$E_1 = 206$ GPa	$E_2 = 102$ GPa
Poisson's Ratio	$\nu_1 = 0.3$	$\nu_2 = 0.4$
Yield Strength	$\sigma_{y_1} = 350$ MPa	$\sigma_{y_2} = 120$ MPa
Hardness	$\bar{H}_1 = 290 \ \text{kgf}/\text{mm}^2$	$\bar{H}_1 = 290 \ \text{kgf}/\text{mm}^2$
Damping Coefficient	$b = 10 \ \text{kg} \cdot \text{m}^{-\frac{1}{2}} \cdot \text{s}^{-\frac{1}{2}}$	
Coefficient of friction	$\mu_s = 0.5$, $\mu_d = 0.4$	
ECOR	$e_* = 0.50$	

Table 8.4: Parameters used to simulate 3-point sphere impact

Figure 8.32 shows the evolution of the generalized coordinates for the 1) Four Point, 2) Eight Point, 3) Sixteen Point, and 4) Twenty-Five Point cases for the 2 second simulation.

It is clear from these plots, that the trajectories of the generalized coordinates for these cases remains very close to one another throughout the simulation period. Note that, again these results here obtained using the proposed augmented impact model is identical to the ones generated using purely rigid impact model in [42]. The augmented impact model used here also gave the deformation history of the contact points and the elapsed time for each impact event. These deformation histories, along with the velocity histories of the contact points were used to generate the force histories at each contact point. During the contact phases, the forces were calculated based on the rigid contact model shown in [42]. Finally, these forces at all contact points are plotted with respect to time for each of the four cases i.e. (a) 4-point, (b) 8-point, (c) 16-point, and (d) 25-point grid bottom surface model in Fig. 8.33. Notice, that the force-time plots in Fig. 8.33a-8.33d, the magnitude of the forces decreases as the number of contact points to the block model is increased. Also, note that in Fig. 8.33, the force-histories obtained for different number of points have a very similar pattern of evolution. This is due to the fact that the block impacts with the same configuration regardless of the number of points used to model its bottom surface. This pattern is more clearly visible in the log-magnitude plots in Fig. 8.34. All force-histories obtained in this experiment are visualized in Figs. 8.35, 8.36, Fig. 8.37 and Fig. 8.38. The magnitude of the forces in these plots are scaled down. Notice, that the forces on the block for (a) 4-point, (b) 8-point, (c) 16-point, and (d) 25-point grid bottom surface model mostly takes place at the edges of the block. In Fig. 8.37 and Fig. 8.38, specific instances are shown where the forces on the contact points are within the bottom face, such that a force distribution can be observed over the entire surface of impact. The energy dissipation exhibited by the system during all these simulations are shown in Fig. 8.39. Again the energy dissipation plots reaffirm that the overall behavior of the simulation is not affected due to the redundant number of points used for the contact and impact analysis. The steps on the total energy plot reflect the energy dissipation due to impact.

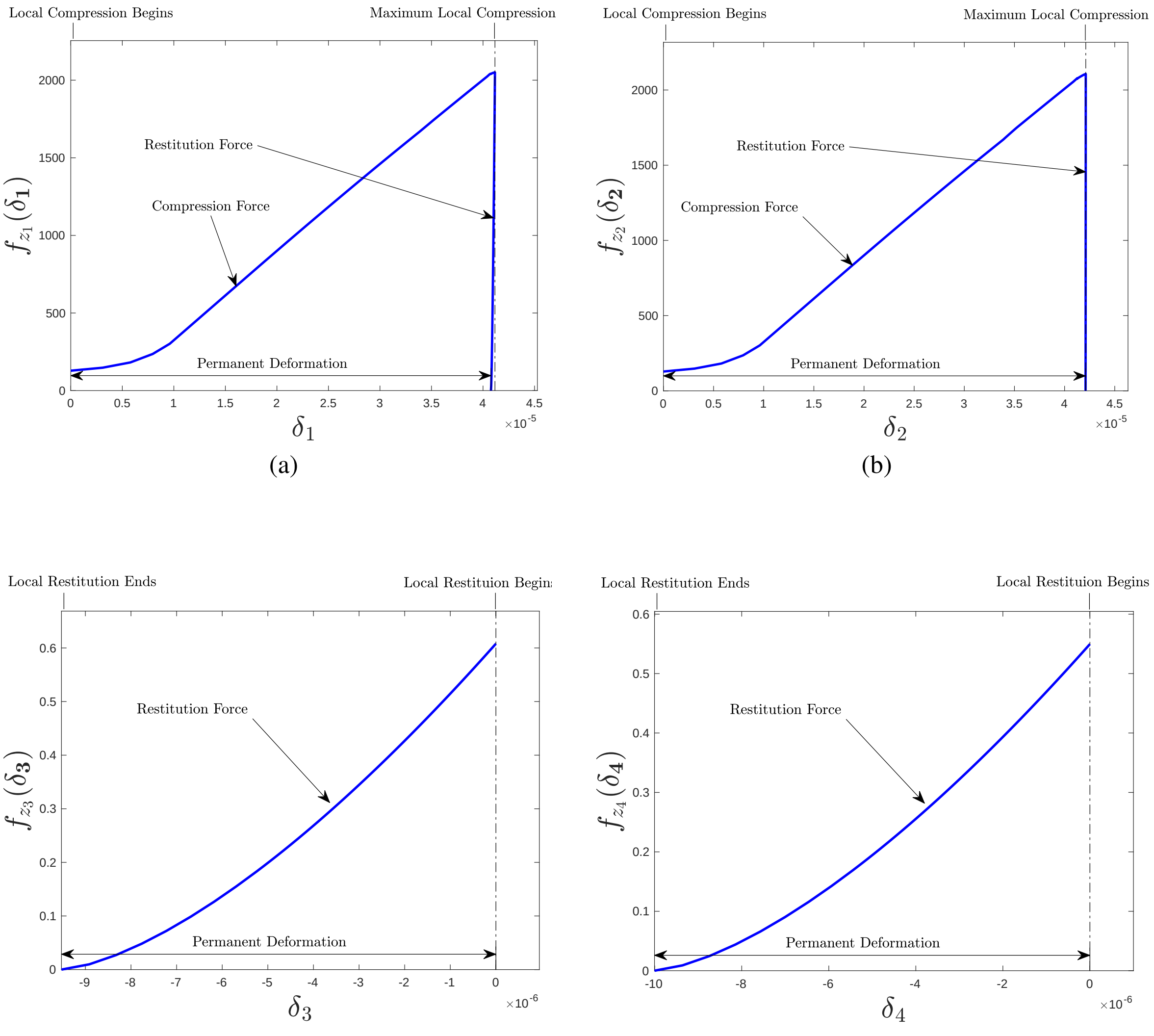

(a)

(b)

(c)

(d)

Figure 8.25: Normal Forces-Deformation curve for (a) point 1, (b) point 2, (c) point 3 and (d) point 4 during the collision

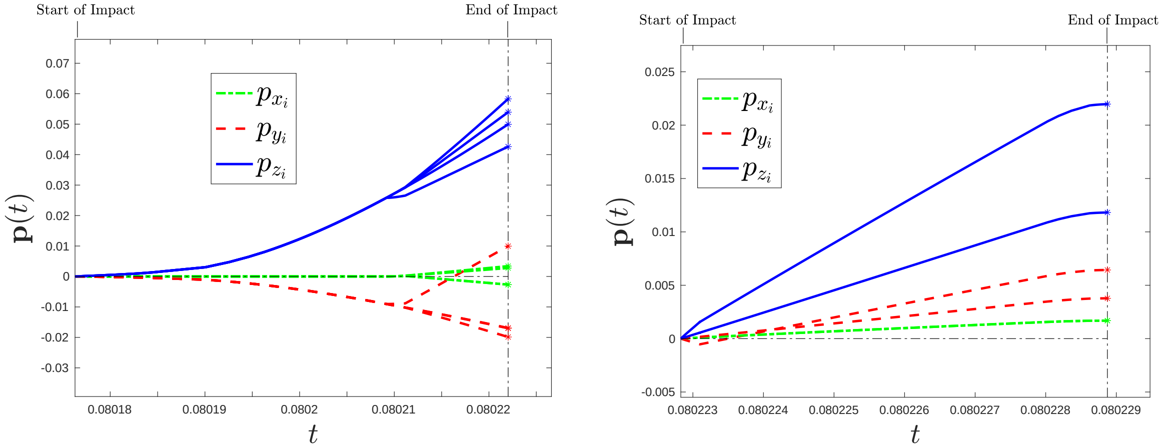

(a) (b)

Figure 8.26: Change in the impulses on the block with respect to time during (a) 1st and (2) 2nd impact events

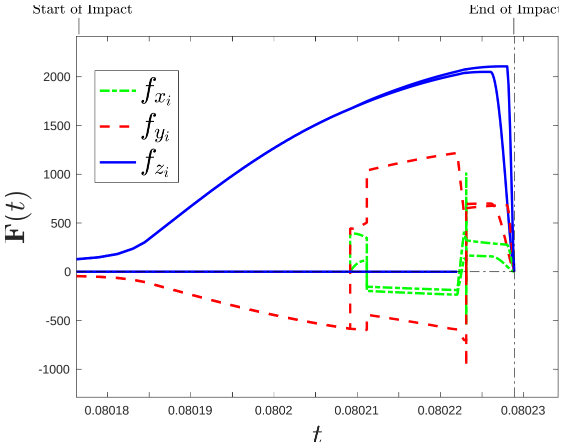

Figure 8.27: Evolution of forces with respect to time throughout the collision (1st and 2nd impact events combined)

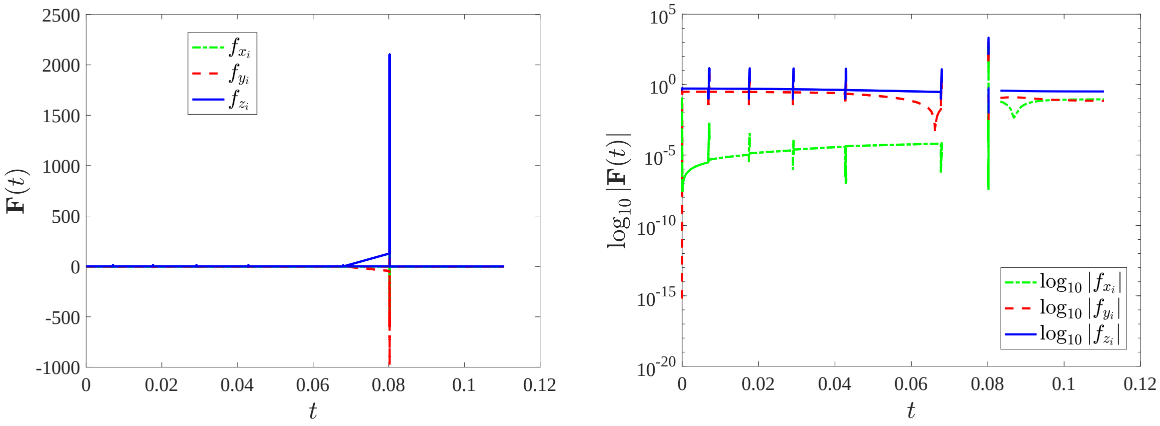

(a) (b)

Figure 8.28: (a) Forces and (b) log-magnitude of the forces at all points throughout the simulation

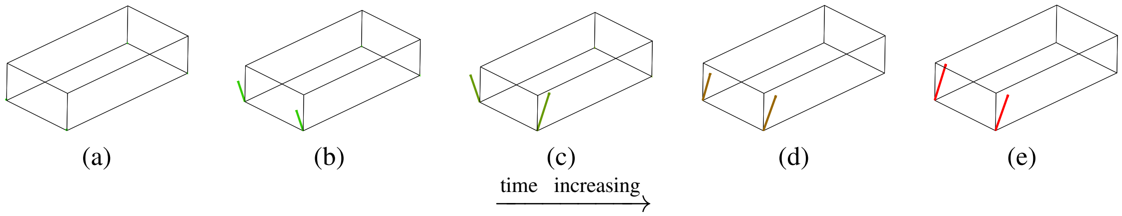

(a) (b) (c) (d) (e)

Figure 8.29: Visualization of the contact forces on the block at different times block during the first impact event (time increases from left (a) to right (e))

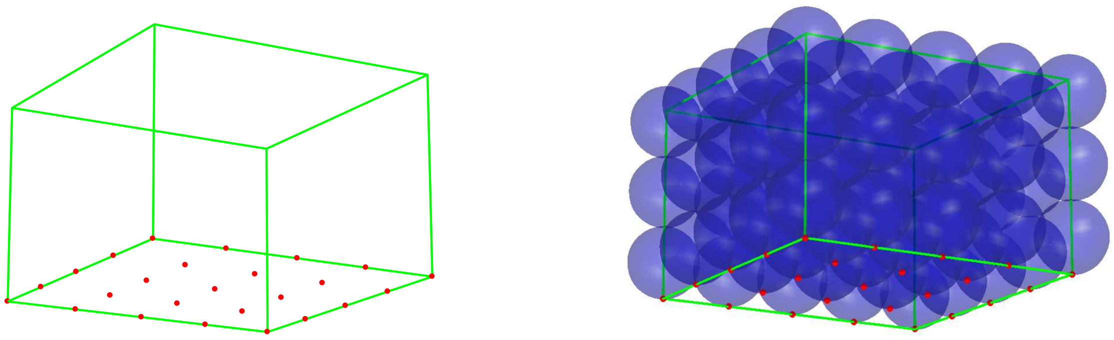

(a) (b)

Figure 8.30: (a) 3D rigid block model with 25 contact points and (b) Approximated block model as a lattice structure composed of 75 spheres

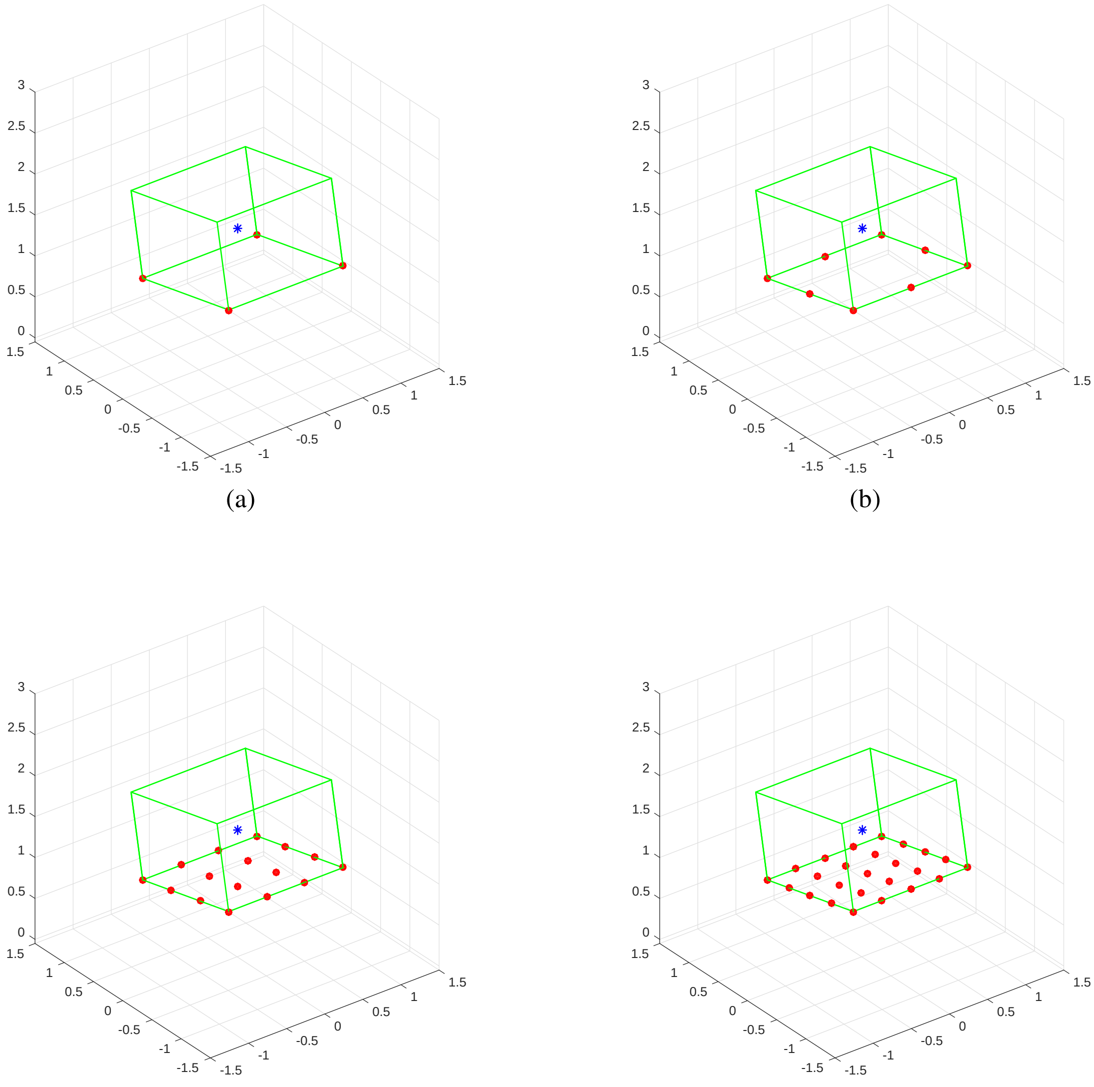

(a) (b) (c) (d)

Figure 8.31: Block with (a) four points (b) eight points (c) sixteen points (d) twenty-five points

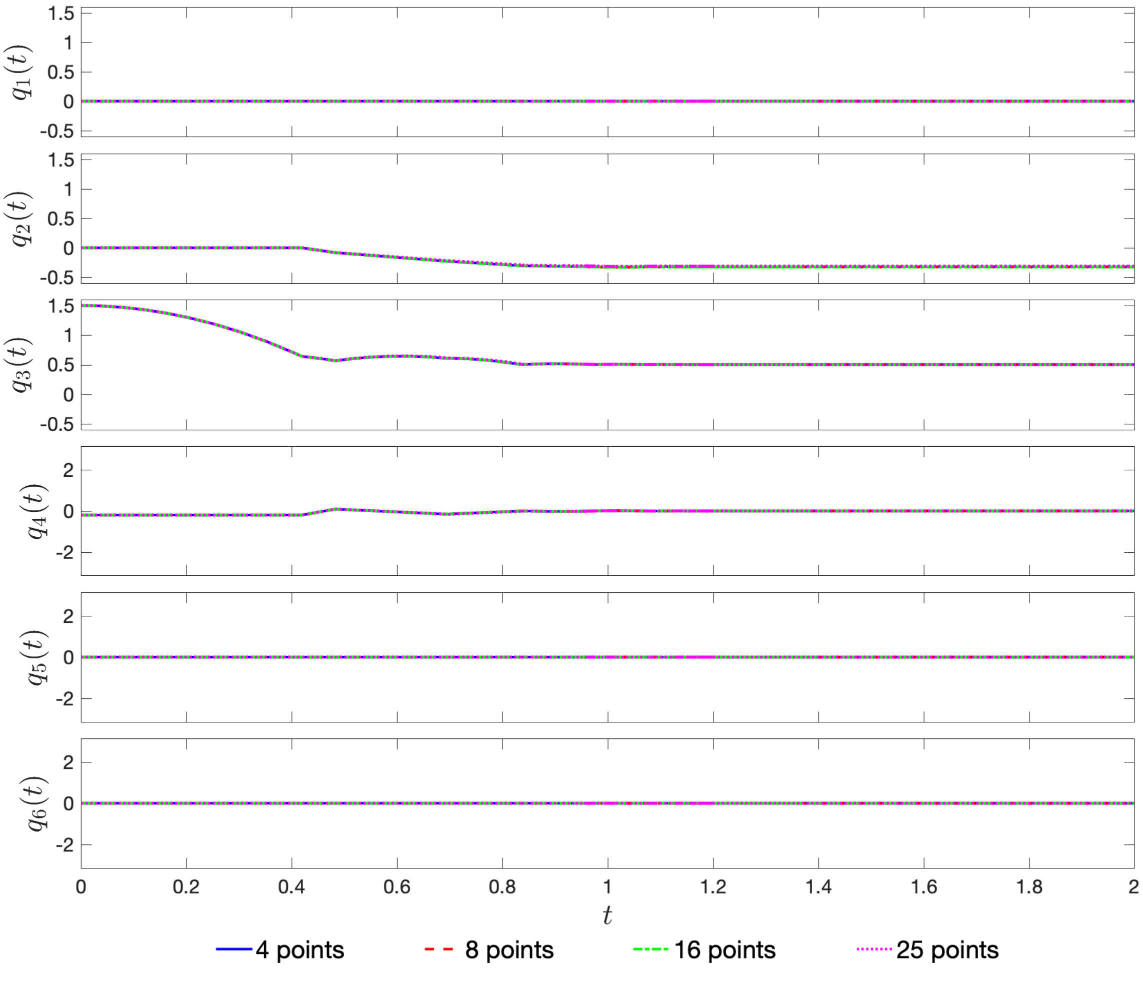

Figure 8.32: Comparison of the generalized coordinates of the block

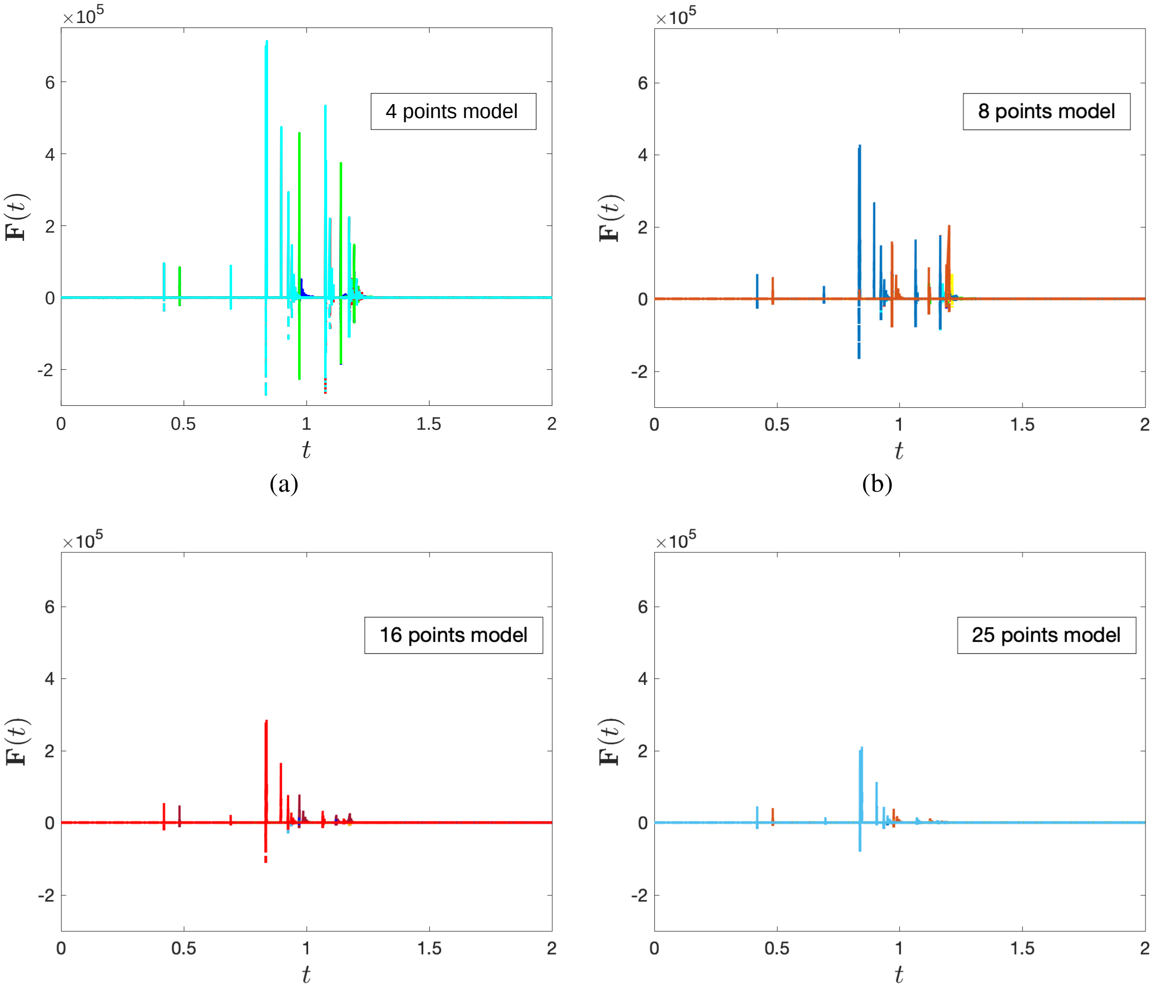

(a) (b) (c) (d)

Figure 8.33: Forces on (a) 4 points, (b) 8 points, (c) 16 points, and (d) 25 points block model with respect to time

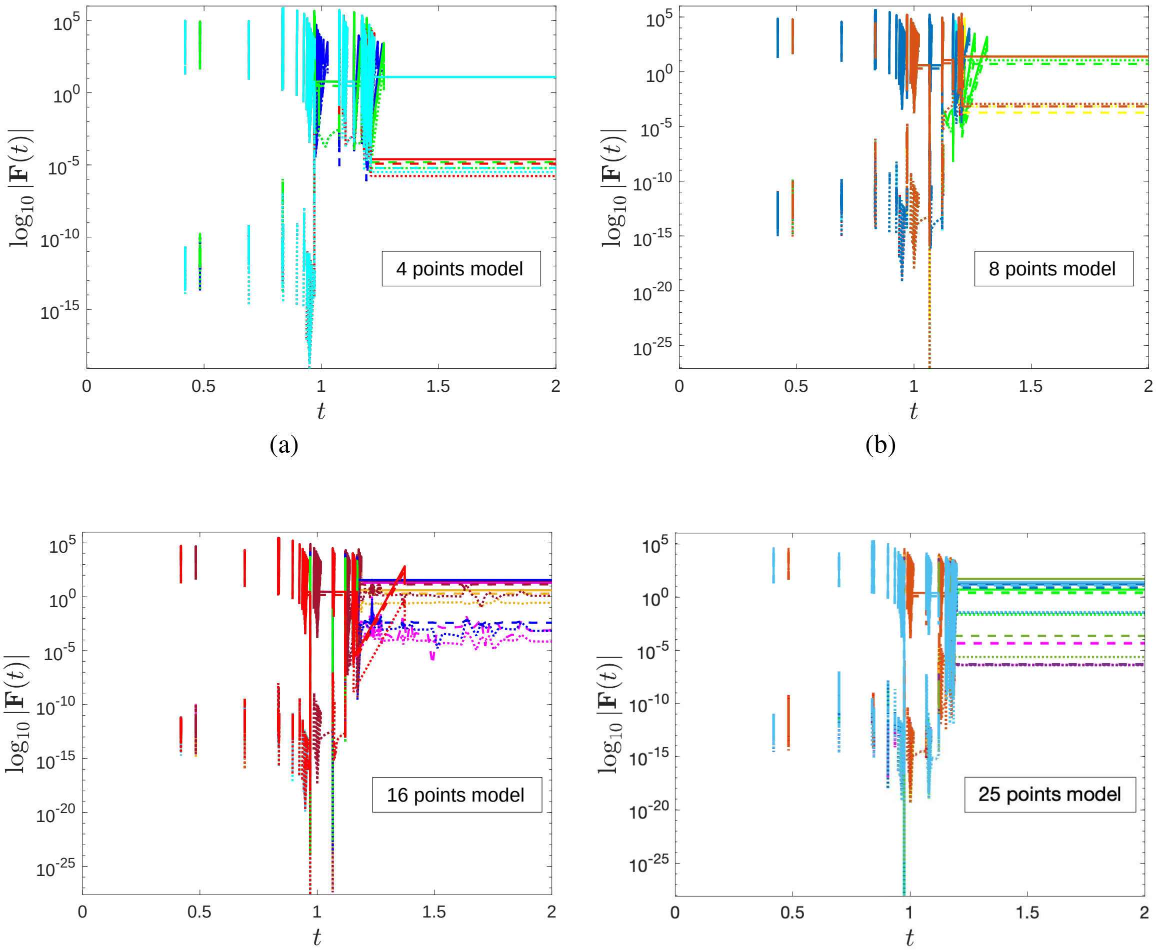

(a) (b)

(c) (d)

Figure 8.34: Log-magnitude of forces on (a) 4 points, (b) 8 points, (c) 16 points, and (d) 25 points block model with respect to time

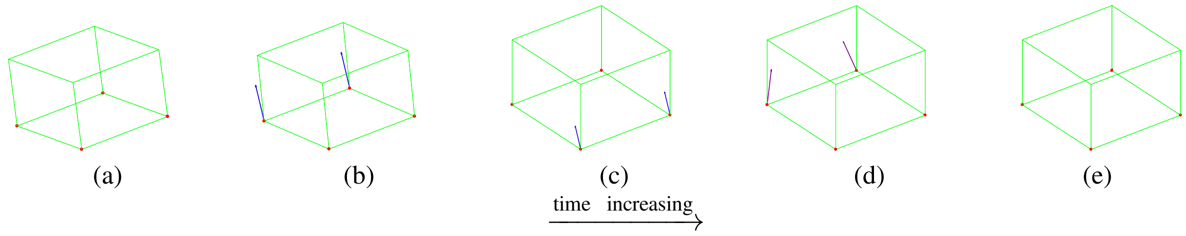

Figure 8.35: Visualization of the contact forces on the block at different times block during the first impact event (time increases from left (a) to right (e))

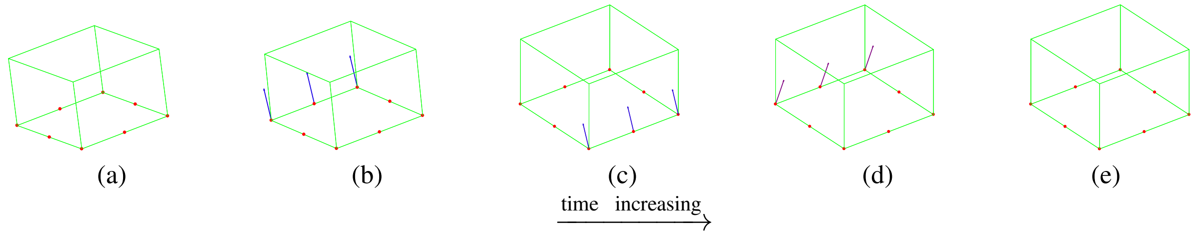

Figure 8.36: Visualization of the contact forces on the block at different times block during the first impact event (time increases from left (a) to right (e))

8.2.5 Example-5: 3D Rocking Block Angular Response

In [38, 42], the angular response of various specimens of 3D rocking block are analyzed. The rocking block problem has been an important benchmark problem related to earthquake engineering, and has been studied extensively over the years [34, 54, 103, 109–115]. Unlike various other studies which modeled the rocking block problem with some stiffness properties, [38, 42] showed that the dynamics of the rocking block problem can be modeled reasonably well using a purely rigidity based impact model. [38, 42] showed this by first matching experimental data from [113, 114], while using a rigid impact model. At first this data was matched using a planar impact model in [38] by appropriately selecting the global ECOR values. Then a 3D model of impact was used to match theses results in [42], while using the same values of global ECOR. Since, the present work is an extension of the work in [42], it is expected that the experimental data from [113, 114] could be

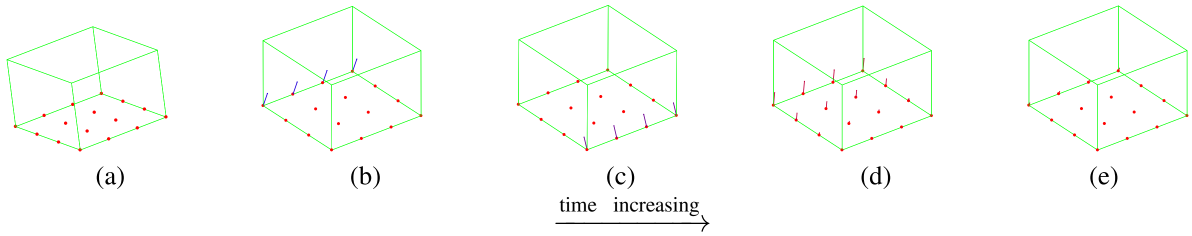

Figure 8.37: Visualization of the contact forces on the block at different times block during the first impact event (time increases from left (a) to right (e))

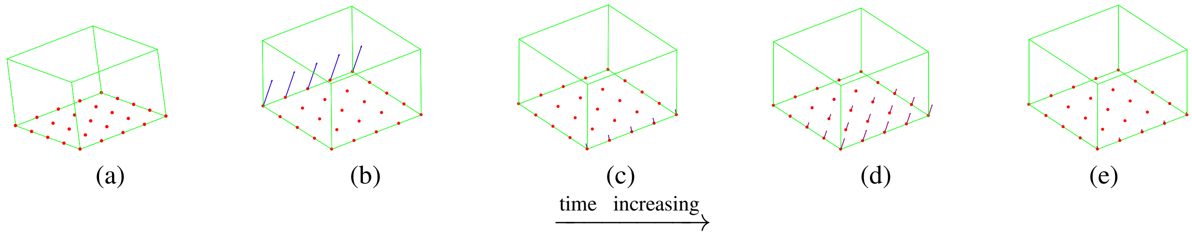

Figure 8.38: Visualization of the contact forces on the block at different times block during the first impact event (time increases from left (a) to right (e))

matched using the proposed augmented impact model, with the same parameters as in [42]. However, the main goal here is to redo the examples of angular rocking block response as in [42], while using the augmented impact model to simultaneously calculate deformation and force histories throughout these simulations.

Three different specimens were used for the free-rocking block experiments in [114]: 1) *Specimen 1* with a width of 0.25 m, height of 1 m and mass of 503 kg, 2) *Specimen 2* with width and height 0.17 m and 1 m respectively and a mass of 228 kg, and 3) *Specimen 4* of width 0.16 m, height 0.457 m and mass 245 kg. The width of the block needs to be calibrated, since the angular response to a rocking block problem is highly sensitive to variations in width [116]. A detailed discussion on this presented in [103, 116]. The *effective width* selected herein for all of the specimens are the same as in [38,42,103,116], which are 0.23m for *Specimen 1*, 0.155m for *Specimen 2*, and 0.115m for *Specimen 4*.

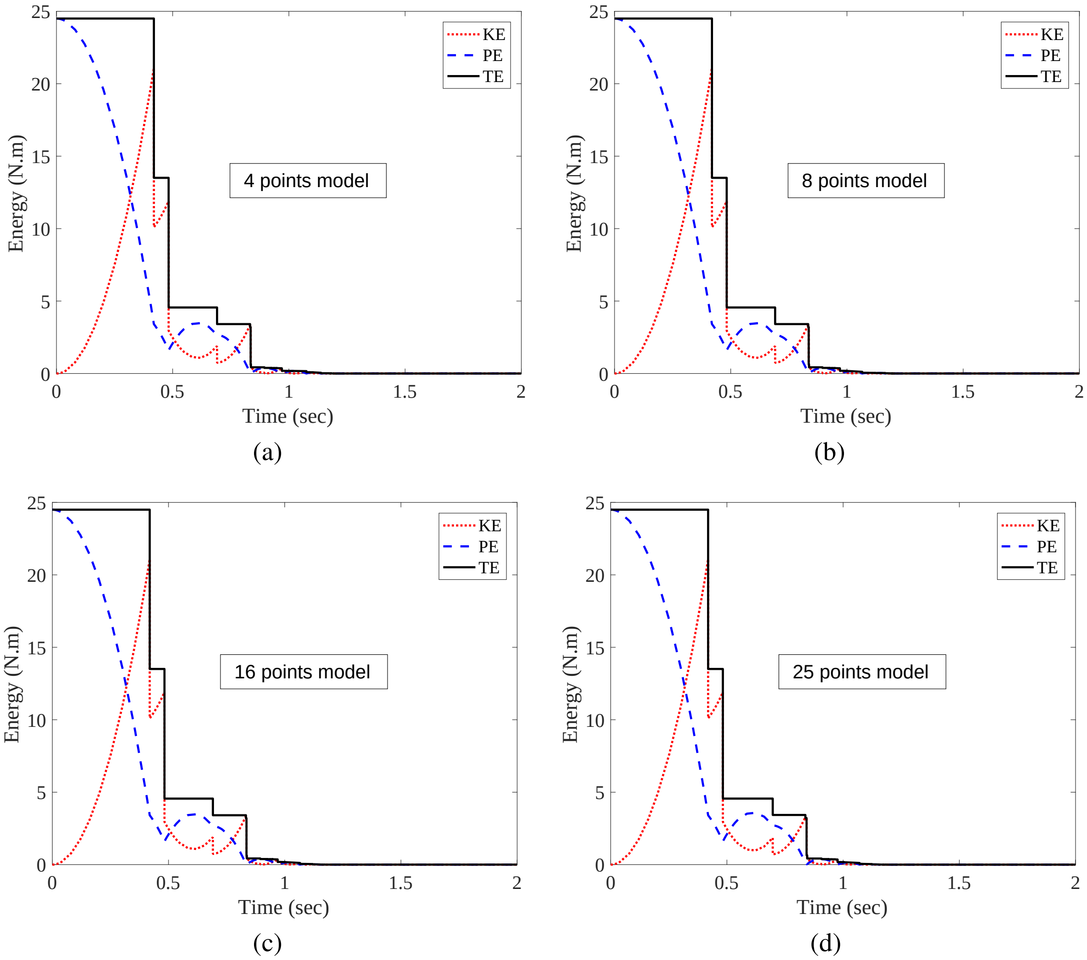

(a) (b) (c) (d)

Figure 8.39: Energy Dissipation for (a) Four Point, (b) Eight Point, (c) Sixteen Point and, (d) Twenty-Five Point Cases

The length of the three specimens were selected to be the same as in [114]: 0.7594m, 0.502m and 0.705m for *Specimen 1*, *Specimen 2* and *Specimen 4* respectively. According to [114], the specimens used in this experiment are composed of granite which has a Young's Modulus of $E_1 = 70$ GPa. Unfortunately some of the other material properties required for the force model used in this work does not exist for a non-metallic brittle material such as granite. Hence, all the other material property values used in this example are assumed. The Poisson's Ratio for the specimens are assumed to be $\nu_1 = 0.3$ and the Yield's strength is assumed to be $\sigma_{y_1} = 2200$ MPa. Similar to the 3D Block example, here the corners of the specimen are assumed to be rounded with a radius of $R_1 = 0.005$m. The ground is assumed to be composed of a material whose Young's modulus is $E_2 = 102$ GPa, Poisson's Ratio is $\nu_2 = 0.4$ and Yield's strength is $\sigma_{y_2} = 120$ MPa. The ground is considered to have radius of $R_2 = \infty$. The hardness values for both the block and the ground is selected to be $\bar{H} = 290$ $\mathrm{kgf/mm^2}$. The damping coefficient used in this impact is $b = 10^4\ \mathrm{kg \cdot m^{-\frac{1}{2}} \cdot s^{-\frac{1}{2}}}$. Lastly the values for static and dynamic coefficients of friction are selected to be $\mu_s = 0.577$ and $\mu_d = 0.3$, respectively. Using these parameters the simulations were performed for the three specimens. The global ECOR, e_* values were selected to be same as [38, 42]. These were $e_* = -0.73, 0.8$ for *Specimen 1*, $e_* = -0.95, 0.8$ for *Specimen 2*, and $e_* = -0.96, 0.8$ for *Specimen 4*, where all the negative values of ECORs were used for 4-point or 3-point impact events and all positive values of ECORs were used for 2-point and 1-point impacts. The list of all parameters for the three specimens is summarized in Tab. 8.5

Parameters	**Specimen 1**	**Specimen 2**	**Specimen 4**	**Ground**
Mass	$m = 0.7594$ kg	$m = 0.502$ kg	$m = 0.705$ kg	-
Radius	$R_1 = 0.005$ m	$R_1 = 0.005$ m	$R_1 = 0.005$ m	$R_2 = \infty$ m
Young's Modulus	$E_1 = 70$ GPa	$E_1 = 70$ GPa	$E_1 = 70$ GPa	$E_2 = 102$ GPa
Poisson's Ratio	$\nu_1 = 0.3$	$\nu_1 = 0.3$	$\nu_1 = 0.3$	$\nu_2 = 0.4$
Yield Strength	$\sigma_{y_1} = 2200$ MPa	$\sigma_{y_1} = 2200$ MPa	$\sigma_{y_1} = 2200$ MPa	$\sigma_{y_2} = 120$ MPa
Hardness	$\bar{H}_1 = 290\ \ \mathrm{kgf/mm^2}$	$\bar{H}_1 = 290\ \ \mathrm{kgf/mm^2}$	$\bar{H}_1 = 290\ \ \mathrm{kgf/mm^2}$	$\bar{H}_2 = 290\ \ \mathrm{kgf/mm^2}$
ECOR	$e_* = -0.73, 0.8$	$e_* = -0.95, 0.8$	$e_* = -0.96, 0.8$	-
Damping Coefficient	$b = 10^4\ \ \mathrm{kg \cdot m^{-\frac{1}{2}} \cdot s^{-\frac{1}{2}}}$			
Coefficient of friction	$\mu_s = 0.6$, $\mu_d = 0.35$			

Table 8.5: Parameters used to simulate 3-point sphere impact

Fig. 8.40 compares the simulated and experimental angular response of the three specimens. Here, Pena refers to the measured angular response from the experiments done by Pena et.al [114], LZB refers to the simulated response using the LZB model [103], and CBGB refers to the response obtained using the proposed augmented impact model, and

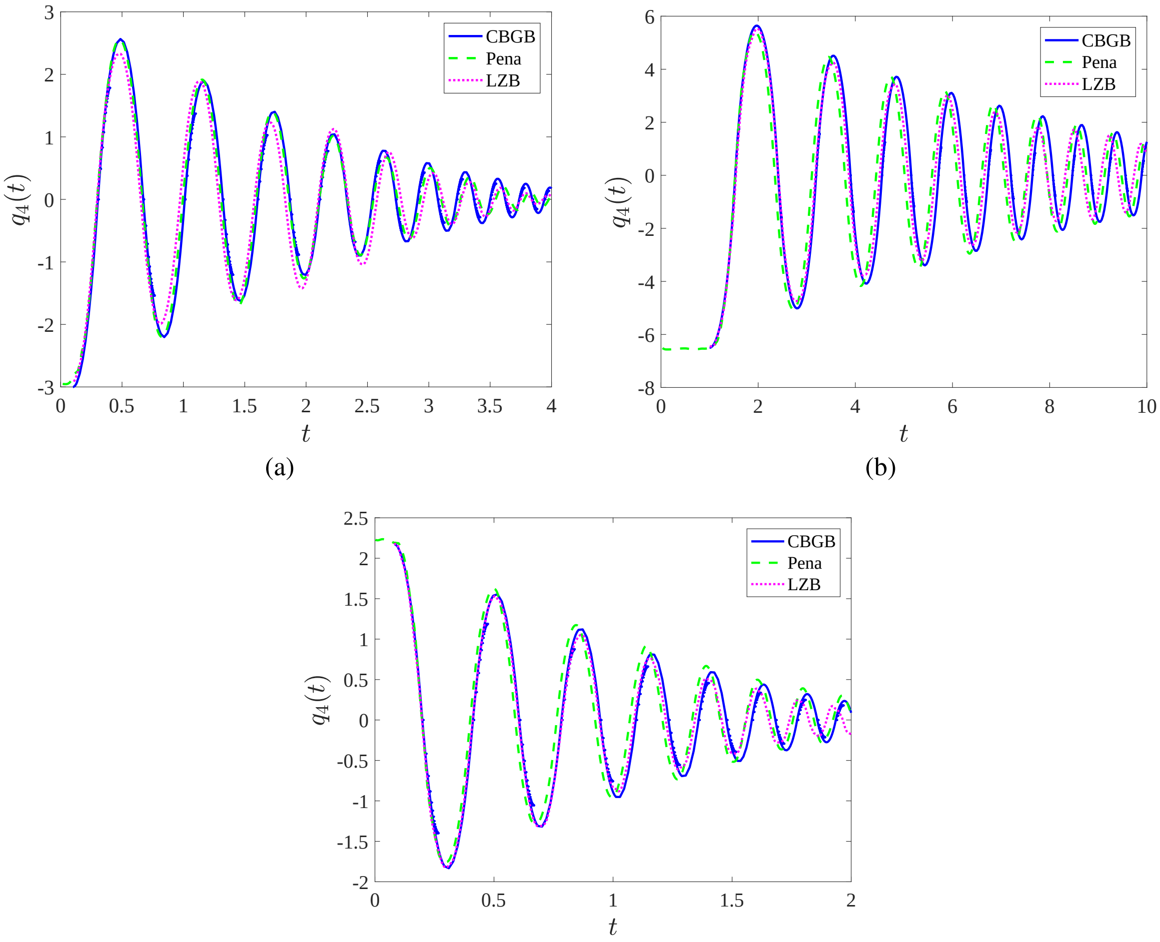

(a) (b)

(c)

Figure 8.40: Angular Response for (a) Specimen 1 (b) Specimen 2 (c) Specimen 4. The angular response data for Pena and LZB, were obtained from plots shown in Fig.5 of [103].

is identical to the results obtained using the purely rigid models in [38, 42]. Based on the deformation histories obtained using the augmented impact model the forces associated with all collisions were calculated. Fig. 8.41, shows the forces at the four contact points for (a) *Specimen 1*, (b) *Specimen 2* and (c) *Specimen 4*. Note that in Fig. 8.41, a pattern can be observed where several collisions (represented by the force spikes) take place in quick succession before some points enter contact and rocking is resumed. Fig. 8.42 shows the energy dissipation of the block throughout the simulation. Notice, the steps in

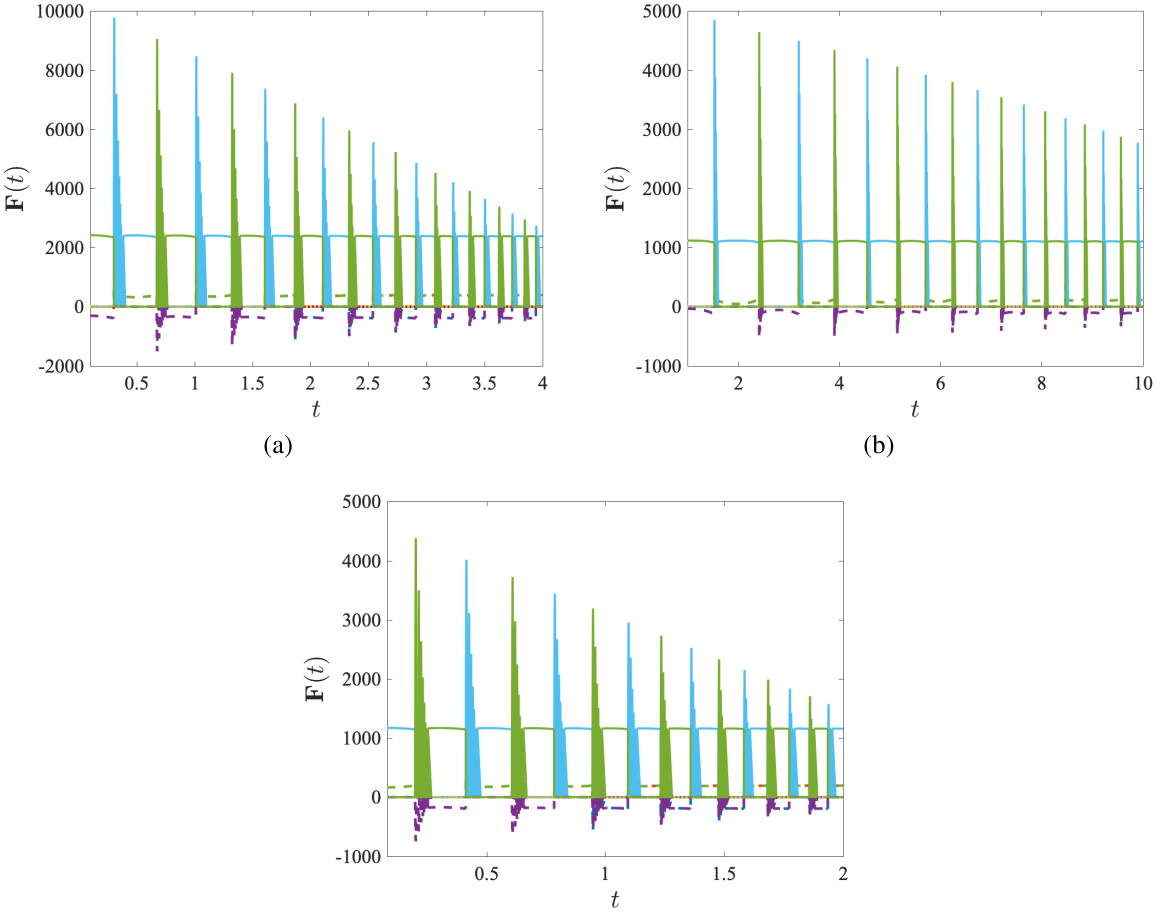

(a) (b)

(c)

Figure 8.41: Forces at the four contact points during the rocking response

the total energy plot, which indicate energy losses due to every collision. The total energy of the system always decreases in this simulation, this shows that these simulation results are energetically consistent.

8.3 Discussion

The purpose of the augmented impact model developed in this work is to obtain an approximation of the forces experienced by rigid objects during collision. The forces during collisions are always related to the induced deformations using a variant of the Hertzian contact model. Yet for hard objects (which can be assumed to be rigid) the deformations are negligibly small. Hence it is more convenient to use an approximate model for the collision forces based on rigidity, compared to developing an exact model based on the tiny deformations. The proposed method uses an indirect approach for solving the collision forces based on an existing analytic contact force model. The contact force model used in this work is ideally used to model contact between spherical surfaces. However, as shown in some of the examples, rigid non-spherical objects can be approximated as a collection of rigidly-attached spheres.

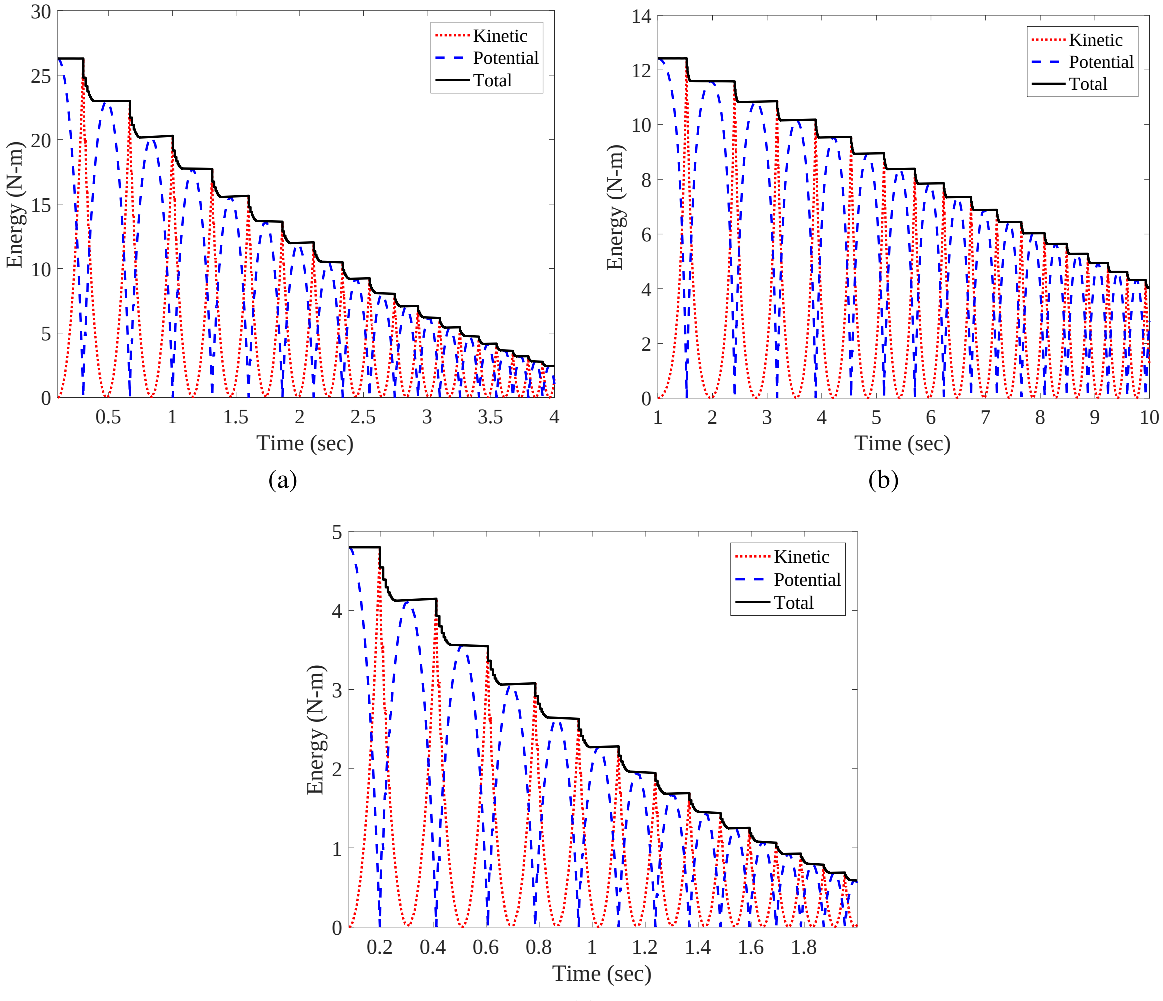

(a)

(b)

(c)

Figure 8.42: Energy consistency throughout the simulation for (a) Specimen 1 (b) Specimen 2 (c) Specimen 4

APPENDIX A

PROJECTION OF VELOCITY-CONSTRAINTS AS FORCE-CONSTRAINTS

In order to demonstrate, how a rigid body constraint expressed in terms of velocity can be projected in terms of impulses. Lets consider a two-point contact involving the points i and j. Let the velocity-level rigid body constraints between the two points be expressed as,

$$\mathbf{w}\boldsymbol{\vartheta} = (v_{x_i} - v_{x_j})\eta_x + (v_{y_i} - v_{y_j})\eta_y + (v_{z_i} - v_{z_j})\eta_z = 0 \tag{A.1}$$

Then the velocity vector may be rewritten as,

$$\boldsymbol{\vartheta} = \begin{bmatrix} v_{x_j} - (v_{y_i} - v_{y_j})\frac{\eta_y}{\eta_x} - (v_{z_i} - v_{z_j})\frac{\eta_z}{\eta_x} \\ v_{y_i} \\ v_{z_i} \\ v_{x_j} \\ v_{y_j} \\ v_{z_j} \end{bmatrix} = \underbrace{\begin{bmatrix} -\alpha & -\beta & 1 & \alpha & \beta \\ 1 & 0 & 0 & 0 & 0 \\ 0 & 1 & 0 & 0 & 0 \\ 0 & 0 & 1 & 0 & 0 \\ 0 & 0 & 0 & 1 & 0 \\ 0 & 0 & 0 & 0 & 1 \end{bmatrix}}_{P} \boldsymbol{\vartheta}_s \tag{A.2}$$

where $\boldsymbol{\vartheta}_s$ are independent velocities, P is a matrix representing the rigid body constraint, and $\alpha = \frac{\eta_y}{\eta_x}$ and $\beta = \frac{\eta_z}{\eta_x}$. This may be also expressed as,

$$\boldsymbol{\vartheta} = J\dot{\mathbf{q}} = P\boldsymbol{\vartheta}_s \tag{A.3}$$

This yields,

$$\boldsymbol{\vartheta}_s = P^{+}J\dot{\mathbf{q}} \tag{A.4}$$

where $P^{+} = (P^T P)^{-1} P^T$ is the generalized inverse of the matrix P. As shown in [128], the virtual work due to the contact forces yields the relation,

$$\mathbf{F}^T\boldsymbol{\vartheta} = \boldsymbol{\Gamma}^T\dot{\mathbf{q}} \tag{A.5}$$

Let $\mathbf{F}_s$ be a vector containing the constrained force terms corresponding to the independent velocities $\boldsymbol{\vartheta}_s$. Enforcement of the velocity level rigid body constraints shouldn't cause any change in the virtual work of the system. Hence,

$$\mathbf{F}_s{}^T \boldsymbol{\vartheta}_s = \boldsymbol{\Gamma}^T \dot{\mathbf{q}} \tag{A.6}$$

Now substituting the relation $\boldsymbol{\Gamma} = J^T \mathbf{F}$ and (A.4) into (A.6) yields,

$$\mathbf{F}_s{}^T P^+ J \dot{\mathbf{q}} = \left(J^T \mathbf{F}\right)^T \dot{\mathbf{q}} \tag{A.7}$$

This yields the constrained force relationships,

$$\mathbf{F} = (P^+)^T \mathbf{F}_s \qquad \mathbf{F}_s = P^T \mathbf{F} \tag{A.8}$$

Therefore, from (A.8), a projection of rigid body constraints onto the force space can be obtained as,

$$\left(I - \left(P^+\right)^T P^T\right) \mathbf{F} = \mathbf{0} \tag{A.9}$$

Note that in (A.9), $\left(P^+\right)^T P^T \neq I$. The matrix $\left(P^+\right)^T P^T$ projects the forces $\mathbf{F}$ to a space orthogonal to the velocity-level constraint such that it is equal to $\mathbf{F}$. Now using the coefficients of P from (A.2), the matrix $I - \left(P^+\right)^T P^T$ can be symbolically obtained as,

$$I - \left(P^+\right)^T P^T = \frac{1}{2\left(\alpha^2 + \beta^2 + 1\right)} \begin{bmatrix} 1 & \alpha & \beta & -1 & -\alpha & -\beta \\ \alpha & \alpha^2 & \alpha\beta & -\alpha & -\alpha^2 & -\alpha\beta \\ \beta & \alpha\beta & \beta^2 & -\beta & -\alpha\beta & -\beta^2 \\ -1 & -\alpha & -\beta & 1 & \alpha & \beta \\ -\alpha & -\alpha^2 & -\alpha\beta & \alpha & \alpha^2 & \alpha\beta \\ -\beta & -\alpha\beta & -\beta^2 & \beta & \alpha\beta & \beta^2 \end{bmatrix} \tag{A.10}$$

It can be seen that all equations obtained by substituting (A.10) into (A.9), yields the same force constraint:

$$f_{x_i} + \alpha f_{y_i} + \beta f_{z_i} - f_{x_j} - \alpha f_{y_j} - \beta f_{z_j} = 0 \tag{A.11}$$

Now substituting back $\alpha = \frac{\eta_y}{\eta_x}$ and $\beta = \frac{\eta_z}{\eta_x}$, and rearranging gives the rigid body constraint,

$$(f_{x_i} - f_{x_j})\eta_x + (f_{y_i} - f_{y_j})\eta_y + (f_{z_i} - f_{z_j})\eta_z = \mathbf{wF} = 0 \tag{A.12}$$

or in terms of differential impulses as,

$$\mathbf{w}d\mathbf{p} = 0 \tag{A.13}$$

APPENDIX B

SOLVING MULTI-POLYNOMIAL ROOTS USING MACAULAY MATRIX

In the literature, one can find two main approaches for solving multipolynomial system of equations. These are either homotopy-continuation based approaches [129–133] or elimination-theory based approaches [134–137]. The homotopy-continuation based methods essential transform the the multipolynomial root problem into an ordinary differential equation initial value problem, by harnessing some topological properties. The initial values here are some known roots of a polynomial system of the same degree. The idea is to perform numerical integration to reach the solution set for the desired multipolynomial system The elimination based approaches on the other hand make use of the algebraic structure of the multipolynomial system to simplify the problem in terms of an independent variable. These approaches may be further classified in to two categories which either use 1) Gröbner Basis [134–136, 138] or use 2) Resultants [135, 137, 139–142]. The Gröbner basis of a multipolynomial system is analogous to the row-reduced echelon obtained for linear systems after performing the Gaussian elimination process. If there exists finitely many solutions to any given system, then the Gröbner basis for this system would yield a unique set of equations (known as ideals) such that it contains atleast one univariate equation. Thus, the root-finding methods which use Gröbner basis first find the roots in terms of a single variable and perform repeated substitution to obtain all roots [134, 136, 138]. One of the drawbacks of Gröbner basis based approaches is that it requires a great deal of symbolic manipulation, which makes this process computationally expensive [140].

Another class of elimination based root-finding methods use resultants for simultaneously calculating all possible roots for a given system of polynomials. Resultants were originally proposed for two univariate polynomial systems, and was defined as the determinant of what is known as the Sylvester matrix. The Sylvester matrix contains the coefficients of the two polynomials. If there exist a common root for any two univariate polynomial system, the resultant of these polynomial must be zero [140, 142]. Resultants for two polynomial systems can be also formulated as the determinant of Bezout-Cayley matrix [142]. In addition to determining the existence of a common root for univariate bi-polynomial systems, resultants may be also used calculating the common roots of two multivariate polynomials. This is usually done by forming a Sylvester matrix while treating one of the two variables (known as the hidden variable) to be part of the coefficients of the polynomial. This yields the resultant to be a function of the hidden variable included as coefficient. The value(s) of this hidden variable at the common roots are then calculated by setting the resultant to zero, and solving for the unknown. Subsequently, the other variables may be treated as the hidden variable to find their values at the common roots. This method of calculating the common roots of two polynomial system may be extended for more general multivariate polynomial system by repeated resultant computation by selecting any two polynomials at a time. However, such a method yields misleading roots, since any two polynomials picked from a set of polynomials may not necessarily have a common root. A more standard way of extending the resultant formulation for multipolynomial system is expressed as the ratio of the determinant of two matrices, which are known as the Macaulay matrices. Similar to the Sylvester resultants, the Macaulay resultants can be used to determine the existence of any common roots in the multipolynomial system. The Macaulay matrix may be also used to calculate the roots of a multipolynomial system. This can be done by calculating what is known as the U-resultant of the multipolynomial system. The U-resultant can be calculated by augmenting the given polynomial system with a symbolic coefficient linear equation, and taking the determinant of its Macaulay matrix. The symbolic expression given by the U-resultant can then be used to calculate all roots of the system. Despite the simplicity of the U-resultant technique, the symbolic computation involved makes this method computationally expensive.

This work uses a more popular and comparatively inexpensive method for solving the multipolynomial system in (5.45). This method extends the idea of hiding variable using the Macaulay matrix form, to transform the root-finding problem to a polynomial eigenvalue problem (PEP). However, this transformation can only be performed for a system with same number of variables as equations. Note the system in (5.45) is a over-determined system of polynomials with the same degree. Hence, before transforming (5.45) into a PEP, one needs to find the minimal basis set of equations. This can be done by simply performing a Gauss-Jordan elimination on the coefficients of the system. Let the reduced set of equations, after performing the G-J elimination on the coefficients of (5.45) be,

$$\bar{f}_1(u_1, u_2, u_3) = \quad \dots \quad = \bar{f}_3(u_1, u_2, u_3) \quad = \quad 0 \tag{B.1}$$

The reduced system of polynomials (B.1) has 3 equations and 3 unknowns, and have roots identical to (5.45). Now the first step in transformation of (B.1) to PEP is to formulate the macaulay matrix by hiding one of the variables into the coefficient field, or in other words, treating one of the variables to be part of the coefficient of the system. Let us choose u_1 as the hidden variable. Then the multipolynomial system in (B.1) is given by,

$$\bar{f}_1(u_2, u_3) = \quad \dots \quad = \bar{f}_4(u_2, u_3) \quad = \quad 0 \tag{B.2}$$

The equations (B.2) are defined using the variables u_2, and u_3. Let the degrees of the polynomials $\bar{f}_1$, $\bar{f}_2$, and, $\bar{f}_3$ be d_1,d_2 and d_3. These degrees are counted while disregarding u_1 as a variable. The method of hidden variable only works for homogeneous polynomials so (B.2) needs to be homogenized by adding an extra variable u_4. The homogenized set of equations are given by,

$$\mathcal{F}_i(u_2, u_3, u_4) = \quad \dots \quad = \mathcal{F}_i(u_2, u_3, u_4) \quad = \quad 0 \tag{B.3}$$

where,

$$\mathcal{F}_i = {u_4}^{d_i} \bar{f}_i \left(\frac{u_2}{u_4}, \frac{u_3}{u_4} \right) \qquad\qquad i = 1, \dots, 3$$

Note, that the polynomial system given in (5.45) is already homogenous, so the homogenization has not effect on the original polynomial system. The total degree d of the multipolynomial system is calculated using the degrees of each polynomial d_i in the system as,

$$d = \sum_{i=1}^{n=3} (d_i - 1) + 1 \tag{B.4}$$

The next step is to take the set of all monomials of degree d using the variables u_2, u_3, and u_4 and partition them into $n = 3$ subsets. Let the set of all monomials of degree d be represented as $\mathbf{u}^\alpha = {u_2}^{\alpha_2} {u_3}^{\alpha_3} {u_4}^{\alpha_4}$, such that $|\alpha| = \sum_{i=2}^{n+1=4} \alpha_i = d$. The set of monomials $\mathbf{u}^\alpha$ is then partitioned into $n = 3$ subsets as,

$$\begin{aligned} S_1 &= \left\{ \mathbf{u}^\alpha : {u_2}^{d_1} \text{ divides } \mathbf{u}^\alpha \right\} \\ S_2 &= \left\{ \mathbf{u}^\alpha : {u_2}^{d_1} \text{ doesn't divide } \mathbf{u}^\alpha, \text{ but } {u_3}^{d_2} \text{ does } \right\} \\ S_3 &= \left\{ \mathbf{u}^\alpha : {u_2}^{d_1}, {u_3}^{d_2} \text{ doesn't divide } \mathbf{u}^\alpha, \text{ but } {u_4}^{d_3} \text{ does } \right\} \end{aligned} \tag{B.5}$$

Now a new set of polynomials equivalent to (B.3) can be created using these partitions,

$$\begin{aligned} \frac{\mathbf{u}^\alpha}{{u_2}^{d_1}} \mathcal{F}_1 = 0 \quad &\text{for all} \quad \mathbf{u}^\alpha \in S_1 \\ \frac{\mathbf{u}^\alpha}{{u_3}^{d_2}} \mathcal{F}_2 = 0 \quad &\text{for all} \quad \mathbf{u}^\alpha \in S_2 \\ \frac{\mathbf{u}^\alpha}{{u_4}^{d_3}} \mathcal{F}_3 = 0 \quad &\text{for all} \quad \mathbf{u}^\alpha \in S_3 \end{aligned} \tag{B.6}$$

Note that the functions $\mathcal{F}_i$ have the hidden variable u_1 included in its coefficient field. Hence, the homogeneous system of polynomials in (B.6) also contains the hidden variable u_1. Now, the polynomials in (B.6) can be dehomogenized by setting the additional variable $u_4 = 1$. Thus after dehomogenization (B.6) may be represented as,

$$\mathcal{M}(u_1) \boldsymbol{\nu} = \mathbf{0} \tag{B.7}$$

where $\mathcal{M}(u_1)$ is the Macaulay matrix for the multipolynomial system (5.45) with the variable u_1 hidden in the coefficient field, such that the elements of $\mathcal{M}(u_1)$ are univariate functions of u_1. $\boldsymbol{\nu}$ is a vector containing all possible monomials in variables u_2 and u_3. Since, the elements of $\mathcal{M}(u_1)$ contains powers of u_1, it may be also represented as a matrix polynomial. Thus, (B.7) can be posed as a polynomial eigenvalue problem (PEP),

$$\left(\lambda^k \mathcal{M}_k + \lambda^{k-1} \mathcal{M}_{k-1} + \ldots + \lambda \mathcal{M}_1 + \mathcal{M}_0\right) \boldsymbol{\nu} = 0 \tag{B.8}$$

where k is the highest power of u_1 in $\mathcal{M}(u_1)$. Note, that $\mathcal{M}_k$ are matrices with numeric elements. PEPs such as (B.8) can be easily solved by transforming the problem into a generalized eigenvalue problem. However, this work uses a built in command in MATLAB called `polyeig()` to obtain the solutions of PEPs. Solving the PEP in (B.8) yields the eigenvalues λ and eigenvectors $\boldsymbol{\nu}$. The eigenvalues λ take the values of the hidden variable u_1 at the roots of the multipolynomial system (5.45). The eigenvectors $\boldsymbol{\nu}$ would contain the variables u_2 and u_3, which can be selected for corresponding values of $u_1 = \lambda$.

Now it is noteworthy, that solution of PEPs such as (B.8) by transformation to generalized eigenvalue problem, generates matrices of very large dimensions for large values of n and d. The eigenvalue problems for very large matrices are usually difficult to compute and can be numerically unstable. However, in the context of this work the eigenvalue problem encountered involve only moderately large dimensioned matrices, (since $n = 3$ and $d = \sum_{i=1}^{n=3}(d_i - 1) + 1 = 4$) that are typically easy to compute. The accuracy of the solution can usually be improved by a method known as “Root Polishing”, which involve using the solutions from the eigenvalue problem as initial guesses and performing Newton-Raphson iterations [139]. However, in this work, this wasn’t necessary due to the relatively low dimension of the PEP.

REFERENCES

[1] G. Darboux, “Etude géométrique sur les percussions et le choc des corps,” *In Bulletin des Sciences Mathématiques et Astronomiques, deuxiéme série*, vol. 4, no. 1, pp. 126–160, 1880.

[2] S. Djerassi, “Stronge’s hypothesis-based solution to the planar collision-with-friction problem,” *Multibody System Dynamics*, vol. 24, no. 4, pp. 493–515, Dec. 2010.

[3] ——, “Collision with friction; Part A: Newton’s hypothesis,” *Multibody System Dynamics*, vol. 21, no. 1, pp. 37–54, Feb. 2009.

[4] ——, “Three-dimensional, one-point collision with friction,” *Multibody System Dynamics*, vol. 27, no. 2, pp. 173–195, 2012.

[5] Y.-T. Wang, V. Kumar, and J. Abel, “Dynamics of rigid bodies undergoing multiple frictional contacts,” in *Robotics and Automation, 1992. Proceedings., 1992 IEEE International Conference on*. IEEE, 1992, pp. 2764–2769.

[6] P. R. Kraus and V. Kumar, “Compliant contact models for rigid body collisions,” in *Robotics and Automation, 1997. Proceedings., 1997 IEEE International Conference on*, vol. 2. IEEE, 1997, pp. 1382–1387.

[7] Y.-B. Jia, “Energy-based modeling of tangential compliance in 3-dimensional impact,” in *Algorithmic Foundations of Robotics IX*. Springer, 2011, pp. 267–284.

[8] Y. Gonthier, J. McPhee, C. Lange, and J.-C. Piedboeuf, “A regularized contact model with asymmetric damping and dwell-time dependent friction,” *Multibody System Dynamics*, vol. 11, no. 3, pp. 209–233, Apr. 2004.

[9] I. Sharf and Y. Zhang, "A contact force solution for non-colliding contact dynamics simulation," *Multibody System Dynamics*, vol. 16, no. 3, pp. 263–290, Oct. 2006.

[10] H. Lankarani, "Contact force model with hysteresis damping for impact analysis of multibody systems," *Journal of Mechanics and Design*, vol. 112, no. 3, pp. 369–376, Sep. 1990.

[11] G. Gilardi and I. Sharf, "Literature survey of contact dynamics modeling," *Mechanism and Machine Theory*, vol. 37, no. 10, pp. 1213–1239, Oct. 2002.

[12] P. Wriggers and G. Zavarise, "Computational contact mechanics," *Encyclopedia of computational mechanics*, 2004.

[13] K. L. Johnson and K. L. Johnson, *Contact mechanics*. Cambridge university press, 1987.

[14] J. Jaeger, *New solutions in contact mechanics*. Wit Pr/Computational Mechanics, 2005.

[15] I. Huněk, "On a penalty formulation for contact-impact problems," *Computers & structures*, vol. 48, no. 2, pp. 193–203, 1993.

[16] J. C. Simo and T. Laursen, "An augmented lagrangian treatment of contact problems involving friction," *Computers & Structures*, vol. 42, no. 1, pp. 97–116, 1992.

[17] P. Papadopoulos and J. Solberg, "A lagrange multiplier method for the finite element solution of frictionless contact problems," *Mathematical and computer modelling*, vol. 28, no. 4, pp. 373–384, 1998.

[18] T. Kane and D. Levinson, *Dynamics: Theory and Applications*. McGraw-Hill, New York, 1985.

[19] D. Marghitu and E. Stoenescu, "Rigid body impact with moment of rolling friction," *Nonlinear Dynamics*, vol. 50, no. 3, pp. 597–608, Nov. 2007.

[20] E. Whittaker, *A Treatise on the Analytical Dynamics of Particles and Rigid Bodies*. Cambridge University Press, 2nd ed., 1917.

[21] J. Keller, "Impact with friction," *Journal of Applied Mechanics, Transactions ASME*, vol. 53, no. 1, pp. 1–4, Mar. 1986.

[22] W. Stronge, *Impact Mechanics*. Cambridge Univ Press, 2000.

[23] I. Han and B. Gilmore, "Multi-body impact motion with friction-analysis, simulation, and experimental validation," *Journal of Mechanical Design, Transactions of the ASME*, vol. 115, no. 3, pp. 412–422, Sep. 1993.

[24] F. Pfeiffer and C. Glocker, *Multibody dynamics with unilateral contacts*. John Wiley & Sons, 1996, vol. 9.

[25] F. Pfeiffer, *Mechanical system dynamics*. Springer Science & Business Media, 2008, vol. 40.

[26] B. Brogliato, *Nonsmooth Mechanics: Models, Dynamics and Control*. Springer-Verlag London Ltd., 2nd ed., 1999.

[27] B. Brogliato, A. Ten Dam, and et al., "Numerical simulation of finite dimensional multibody nonsmooth mechanical systems," *Applied Mechanics Reviews*, vol. 55, no. 2, pp. 107–149, Mar. 2002.

[28] S. Djerassi, "Collision with friction; Part B: Poisson's and Stronge's hypotheses," *Multibody System Dynamics*, vol. 21, no. 1, pp. 55–70, Feb. 2009.

[29] Y. Wang, V. Kumar, and J. Abel, "Dynamics of rigid bodies undergoing multiple frictional contacts," *Proc-IEEE Int'l Conference on Robotics and Automation*, vol. 3, pp. 2764–2769, May 1992.

[30] G. Boulanger, "Sur le choc avec frottement des corps non parfaitement élastiques," *Revue Scientifique*, vol. 77, pp. 325–327, 1939.

[31] E. J. Routh *et al.*, *Dynamics of a system of rigid bodies*. Dover New York, 1960.

[32] W. Stronge, "Smooth dynamics of oblique impact with friction," *International Journal of Impact Engineering*, vol. 51, pp. 36–49, Jan. 2013.

[33] P. Bergés and A. Bowling, "Rebound, slip, and compliance in the modeling and analysis of discrete impacts in legged locomotion," *Journal of Vibration and Control*, vol. 17, no. 12, pp. 1407–1430, Dec. 2006.

[34] C. Liu, Z. Zhao, and B. Brogliato, "Frictionless multiple impacts in multibody systems. i. Theoretical framework," *Proc. R. Soc. A Math. Phys. Eng. Sci.*, vol. 464, no. 2100, pp. 3193–3211, Dec. 2008.

[35] Z. Zhao, C. Liu, and B. Brogliato, "Planar dynamics of a rigid body system with frictional impacts. ii. Qualitative analysis and numerical simulations," *Proceedings of the Royal Society A: Mathematical, Physical and Engineering Sciences*, vol. 465, no. 2107, pp. 2267–2292, Jul. 2009.

[36] A. Rodriguez and A. Bowling, "Solution to indeterminate multi-point impact with frictional contact using constraints," *Multibody System Dynamics*, vol. 28, no. 4, pp. 313–330, Nov. 2012.

[37] ——, "Study of newton's cradle using a new discrete approach," *Multibody System Dynamics*, vol. 33, no. 1, pp. 61–92, Jan. 2015.

[38] A. Chatterjee, A. Rodriguez, and A. Bowling, "Analytic solution for planar indeterminate impact problems using an energy constraint," *Multibody System Dynamics*, vol. 42, no. 3, pp. 347–379, 2018.

[39] A. Rodriguez, "Dynamic simulation of multibody systems in simultaneous, indeterminate contact and impact with friction," Ph.D. dissertation, UTA, 2014.

[40] A. Rodriguez, A. Chatterjee, and A. Bowling, "Solution to three-dimensional indeterminate contact and impact with friction using rigid body constraints," in *ASME 2015 International Design Engineering Technical Conferences and Computers and Information in Engineering Conference*. American Society of Mechanical Engineers, 2015, pp. V006T10A037–V006T10A037.

[41] A. Chatterjee and A. Bowling, “Resolving the unique invariant slip-direction in rigid three-dimensional multi-point impacts at stick-slip transitions,” in *ASME 2018 International Design Engineering Technical Conferences and Computers and Information in Engineering Conference*. American Society of Mechanical Engineers, 2018, pp. V006T09A008–V006T09A008.

[42] ——, “Modeling three-dimensional surface-to-surface rigid contact and impact,” *Multibody System Dynamics*, pp. 1–40, 2019.

[43] D. Flickinger and A. Bowling, “Simultaneous oblique impacts and contacts in multibody systems with friction,” *Multibody System Dynamics*, vol. 23, no. 3, pp. 249–261, Mar. 2010.

[44] B. Brogliato, “Kinetic quasi-velocities in unilaterally constrained lagrangian mechanics with impacts and friction,” *Multibody System Dynamics*, vol. 32, no. 2, pp. 175–216, 2014.

[45] C. Liu, Z. Zhao, and B. Brogliato, “Frictionless multiple impacts in multibody systems. i. theoretical framework,” in *Proceedings of the Royal Society of London A: Mathematical, Physical and Engineering Sciences*, vol. 464. The Royal Society, 2008, pp. 3193–3211.

[46] D. Stewart, “Rigid-body dynamics with friction and impact,” *SIAM Review*, vol. 42, no. 1, pp. 3–39, Mar. 2000.

[47] N. Chakraborty, S. Berard, S. Akella, and J. C. Trinkle, “An implicit time-stepping method for multibody systems with intermittent contact.” in *Robotics: Science and Systems*, 2007.

[48] M. Anitescu, F. A. Potra, and D. E. Stewart, “Time-stepping for three-dimensional rigid body dynamics,” *Computer methods in applied mechanics and engineering*, vol. 177, no. 3, pp. 183–197, 1999.

[49] D. E. Stewart and J. C. Trinkle, "An implicit time-stepping scheme for rigid body dynamics with inelastic collisions and coulomb friction," *International Journal for Numerical Methods in Engineering*, vol. 39, no. 15, pp. 2673–2691, 1996.

[50] T. Liu and M. Y. Wang, "Computation of three-dimensional rigid-body dynamics with multiple unilateral contacts using time-stepping and gauss-seidel methods," *Automation Science and Engineering, IEEE Transactions on*, vol. 2, no. 1, pp. 19–31, 2005.

[51] J. Moreau, "Numerical aspects of the sweeping process," *Computer Methods in Applied Mechanics and Engineering*, vol. 177, no. 3, pp. 329–349, May 1999.

[52] S. Najafabadi, J. Kovecses, and J. Angeles, "Generalization of the energetic coefficient of restitution for contacts in multibody systems," *Journal of Computational Nonlinear Dynamics*, vol. 3, no. 4, pp. 70–84, Oct. 2008.

[53] C. Yilmaz, M. Gharib, and Y. Hurmuzlu, "Solving frictionless rocking block problem with multiple impacts," *Proceedings of the Royal Society A: Mathematical, Physical and Engineering Sciences*, vol. 465, no. 2111, pp. 3323–3339, Nov. 2009.

[54] Z. Zhao, C. Liu, and B. Brogliato, "Planar dynamics of a rigid body system with frictional impacts. ii. qualitative analysis and numerical simulations," in *Proceedings of the Royal Society of London A: Mathematical, Physical and Engineering Sciences*, vol. 465. The Royal Society, 2009, pp. 2267–2292.

[55] M. Brake, "An analytical elastic-perfectly plastic contact model," *International Journal of Solids and Structures*, vol. 49, no. 22, pp. 3129–3141, Nov. 2012.

[56] R. L. Jackson, I. Green, and D. B. Marghitu, "Predicting the coefficient of restitution of impacting elastic-perfectly plastic spheres," *Nonlinear Dynamics*, vol. 60, no. 3, pp. 217–229, 2010.

[57] Y. Zait, V. Zolotarevsky, Y. Kligerman, and I. Etsion, "Multiple normal loading-unloading cycles of a spherical contact under stick contact condition," *ASME Journal of Tribology*, vol. 132, no. 4, pp. 041 401–1–7, Sep. 2010.

[58] H. Hertz, "Über die berührung fester elastischer körper. on the contact of elastic solids, reine und angewandte mathematik. london:(instruction anglaise dans miscellaneous papers by h. hertz) eds jones et schaott," 1896.

[59] H. Ghaednia, O. Cermik, and D. B. Marghitu, "Experimental and theoretical study of the oblique impact of a tennis ball with a racket," *Proceedings of the Institution of Mechanical Engineers, Part P: Journal of Sports Engineering and Technology*, vol. 229, no. 3, pp. 149–158, 2015.

[60] L. Skrinjar, J. Slavič, and M. Boltežar, "A review of continuous contact-force models in multibody dynamics," *International Journal of Mechanical Sciences*, vol. 145, pp. 171–187, 2018.

[61] W. Goldsmith, *Impact*. Courier Corporation, 2001.

[62] K. Hunt and F. R. E. Crossley, "Coefficient of restitution interpreted as damping in vibroimpact," *Journal of applied mechanics*, vol. 42, no. 2, pp. 440–445, 1975.

[63] D. W. Marhefka and D. E. Orin, "A compliant contact model with nonlinear damping for simulation of robotic systems," *IEEE Transactions on Systems, Man, and Cybernetics-Part A: Systems and Humans*, vol. 29, no. 6, pp. 566–572, 1999.

[64] W. Stronge, "Chain reaction from impact on aggregate of elasto-plastic ?rigid?bodies," *International journal of impact engineering*, vol. 28, no. 3, pp. 291–302, 2003.

[65] H. Gheadnia, O. Cermik, and D. B. Marghitu, "Experimental and theoretical analysis of the elasto-plastic oblique impact of a rod with a flat," *International Journal of Impact Engineering*, vol. 86, pp. 307–317, 2015.

[66] A. S. Yigit, A. P. Christoforou, and M. A. Majeed, “A nonlinear visco-elastoplastic impact model and the coefficient of restitution,” *Nonlinear Dynamics*, vol. 66, no. 4, pp. 509–521, 2011.

[67] K. Kardel, H. Ghaednia, A. L. Carrano, and D. B. Marghitu, “Experimental and theoretical modeling of behavior of 3d-printed polymers under collision with a rigid rod,” *Additive Manufacturing*, vol. 14, pp. 87–94, 2017.

[68] F. Zhang, M. Yeddanapudi, and P. J. Mosterman, “Zero-crossing location and detection algorithms for hybrid system simulation,” *IFAC Proceedings Volumes*, vol. 41, no. 2, pp. 7967–7972, 2008.

[69] P. J. Mosterman, “An overview of hybrid simulation phenomena and their support by simulation packages,” in *International Workshop on Hybrid Systems: Computation and Control*. Springer, 1999, pp. 165–177.

[70] V. Utkin, “Chattering problem,” *IFAC Proceedings Volumes*, vol. 44, no. 1, pp. 13 374–13 379, 2011.

[71] A. Aljarbouh and B. Caillaud, “Chattering-free simulation of hybrid dynamical systems with the functional mock-up interface 2.0,” in *The First Japanese Modelica Conferences*, vol. 124, 2016, pp. 95–105.

[72] V. P. Pennestrı and P. Valentini, “Coordinate reduction strategies in multibody dynamics: A review,” in *Proceedings of the Conference on Multibody System Dynamics*, 2007.

[73] O. A. Bauchau and A. Laulusa, “Review of contemporary approaches for constraint enforcement in multibody systems,” *Journal of Computational and Nonlinear Dynamics*, vol. 3, no. 1, p. 011005, 2008.

[74] J. Baumgarte, “Stabilization of constraints and integrals of motion in dynamical systems,” *Computer methods in applied mechanics and engineering*, vol. 1, no. 1, pp. 1–16, 1972.

[75] G.-P. Ostermeyer, “On baumgarte stabilization for differential algebraic equations,” in *Real-Time Integration Methods for Mechanical System Simulation*. Springer, 1990, pp. 193–207.

[76] C. Nikravesh and P. Nikravesh, “An adaptive constraint violation stabilization method for dynamic analysis of mechanical systems,” *J. Mech. Trans. Auto. Des*, vol. 107, pp. 488–492, 1985.

[77] K. Park and J. Chiou, “Stabilization of computational procedures for constrained dynamical systems,” *Journal of Guidance, Control, and Dynamics*, vol. 11, no. 4, pp. 365–370, 1988.

[78] E. Bayo, J. G. De Jalon, and M. A. Serna, “A modified lagrangian formulation for the dynamic analysis of constrained mechanical systems,” *Computer methods in applied mechanics and engineering*, vol. 71, no. 2, pp. 183–195, 1988.

[79] R. Wehage and E. Haug, “Generalized coordinate partitioning for dimension reduction in analysis of constrained dynamic systems,” *Journal of mechanical design*, vol. 104, no. 1, pp. 247–255, 1982.

[80] J. García de Jalón, J. Unda, A. Avello, and J. Jiménez, “Dynamic analysis of three-dimensional mechanisms in «natural» coordinates,” *Journal of mechanisms, transmissions, and automation in design*, vol. 109, no. 4, pp. 460–465, 1987.

[81] C. G. Liang and G. M. Lance, “A differentiable null space method for constrained dynamic analysis1,” *Journal of Mechanisms, Transmissions, and Automation in Design*, vol. 109, no. 3, pp. 405–411, November 1987.

[82] S. Kim and M. Vanderploeg, “Qr decomposition for state space representation of constrained mechanical dynamic systems,” *ASME J. Mech. Trans*, vol. 108, no. 2, pp. 183–188, 1986.

[83] F. Amirouche and S. Ider, “Coordinate reduction in the dynamics of constrained multibody system a new approach,” *Journal of Applied Mechanics*, vol. 55, p. 899, 1988.

[84] L. Righetti, J. Buchli, M. Mistry, and S. Schaal, “Inverse dynamics control of floating-base robots with external constraints: A unified view,” in *Robotics and Automation (ICRA), 2011 IEEE International Conference on*. IEEE, 2011, pp. 1085–1090.

[85] M. Mistry, J. Buchli, and S. Schaal, “Inverse dynamics control of floating base systems using orthogonal decomposition,” in *Robotics and Automation (ICRA), 2010 IEEE International Conference on*. IEEE, 2010, pp. 3406–3412.

[86] M. Haghshenas-Jaryani and A. Bowling, “A new switching strategy for addressing euler parameters in dynamic modeling and simulation of rigid multibody systems,” *Multibody System Dynamics*, vol. 30, no. 2, pp. 185–197, 2013.

[87] P. Song, P. Krauss, and P. Dupont, “Analysis of rigid-body dynamic models for simulation of systems with frictional contacts,” *ASME Journal of Applied Mechanics*, vol. 68, no. 1, pp. 118–128, Jun. 2000.

[88] M. Anitescu and F. Potra, “Formulating dynamic multi-rigid-body contact problems with friction as solvable linear complementarity problems,” *Nonlinear Dynamics*, vol. 14, no. 3, pp. 231–247, Nov. 1997.

[89] A. Chatterjee, “On the realism of complementarity conditions in rigid body collisions,” *Nonlinear Dynamics*, vol. 20, no. 2, pp. 159–168, Oct. 1999.

[90] R. Leine and N. Van de Wouw, *Stability and convergence of mechanical systems with unilateral constraints*. Springer Science & Business Media, 2007, vol. 36.

[91] R. Jackson, I. Green, and D. Marghitu, “Predicting the coefficient of restitution of impacting elastic-perfectly plastic spheres,” *Nonlinear Dynamics*, vol. 60, no. 3, pp. 217–229, Mar. 2010.

[92] R. Brach, “Formulation of rigid body impact problems using generalized coefficients,” *International Journal of Engineering Science*, vol. 36, no. 1, pp. 61–71, Jan. 1998.

[93] C. Glocker and C. Studer, “Formulation and preparation for numerical evaluation of linear complentarity systems in dynamics,” *Multibody System Dynamics*, vol. 13, no. 4, pp. 447–463, May 2005.

[94] T. Mouri, T. Yamada, A. IWAI, N. Mimura, and Y. Funahashi, “Identification of contact conditions from contaminated data of contact force and moment,” *Proceedings IEEE International Conference on Robotics and Automation*, vol. 1, pp. 597–603, May 2001.

[95] A. Bowling, “Dynamic performance, mobility, and agility of multi-legged robots,” *Journal of Dynamic Systems, Measurement and Control, Transactions of the ASME*, vol. 128, no. 4, pp. 765–777, Dec. 2006.

[96] D. Karnopp, “Computer simulation of stick-slip friction in mechanical dynamic systems,” *Journal of Dynamic Systems, Measurement and Control, Transactions of the ASME*, vol. 107, no. 1, pp. 100–103, Mar. 1985.

[97] D. Haessig and B. Friedland, “On the modeling and simulation of friction,” *American Control*, vol. 113, no. 3, pp. 354–362, Sep. 1991.

[98] L. F. Shampine and M. W. Reichelt, “The matlab ode suite,” *SIAM journal on scientific computing*, vol. 18, no. 1, pp. 1–22, 1997.

[99] J. Dormand and P. Prince, “A family of embedded runge-kutta formulae,” *Journal of Computational and Applied Mathematics*, vol. 6, no. 1, pp. 19–26, Mar. 1980.

[100] P. Flores, R. Leine, and C. Glocker, “Modeling and analysis of planar rigid multibody systems with translational clearance joints based on the non-smooth dynamics approach,” *Multibody System Dynamics*, vol. 23, no. 2, pp. 165–190, Feb. 2010.

[101] J. Choi, H. Ryu, C. Kim, and J. Choi, “An efficient and robust contact algorithm for a compliant contact force model between bodies of complex geometry,” *Multibody System Dynamics*, vol. 23, no. 1, pp. 99–120, Jan. 2010.

[102] D. Lopes, M. Silva, J. Ambrosio, and P. Flores, “A mathematical framework for contact detection between quadric and superquadric surfaces,” *Multibody System Dynamics*, vol. 24, no. 3, pp. 255–280, Oct. 2010.

[103] H. Zhang, B. Brogliato, and C. Liu, “Dynamics of planar rocking-blocks with coulomb friction and unilateral constraints: comparisons between experimental and numerical data,” *Multibody System Dynamics*, vol. 32, no. 1, pp. 1–25, Jun. 2014.

[104] B. Brogliato, H. Zhang, and C. Liu, “Analysis of a generalized kinematic impact law for multibody-multicontact systems, with application to the planar rocking block and chains of balls,” *Multibody System Dynamics*, vol. 27, no. 3, pp. 351–382, Jan. 2012.

[105] Y. Hurmuzlu, F. Génot, and B. Brogliato, “Modeling, stability and control of biped robotsÃćÂĂÂŤa general framework,” *Automatica*, vol. 40, no. 10, pp. 1647–1664, 2004.

[106] J. W. Grizzle, C. Chevallereau, R. W. Sinnet, and A. D. Ames, “Models, feedback control, and open problems of 3d bipedal robotic walking,” *Automatica*, vol. 50, no. 8, pp. 1955–1988, 2014.

[107] G. W. Housner, “The behavior of inverted pendulum structures during earthquakes,” *Bulletin of the seismological society of America*, vol. 53, no. 2, pp. 403–417, 1963.

[108] C.-S. Yim, A. K. Chopra, and J. Penzien, “Rocking response of rigid blocks to earthquakes,” *Earthquake Engineering & Structural Dynamics*, vol. 8, no. 6, pp. 565–587, 1980.

[109] T. Liu, “Non-jamming conditions in multi-contact rigid-body dynamics,” *Multibody System Dynamics*, vol. 22, no. 3, pp. 269–295, Oct. 2009.

[110] Z. Zhao, C. Liu, and B. Brogliato, “Energy dissipation and dispersion effects in granular media,” *Physical Review E*, vol. 78, no. 3, p. 031307, 2008.

[111] C. Liu, Z. Zhao, and B. Brogliato, “Variable structure dynamics in a bouncing dimer,” Ph.D. dissertation, INRIA, 2008.

[112] ——, “Frictionless multiple impacts in multibody systems. ii. numerical algorithm and simulation results,” in *Proceedings of the Royal Society of London A: Mathematical, Physical and Engineering Sciences*, vol. 465. The Royal Society, 2009, pp. 1–23.

[113] F. Peña, F. Prieto, P. B. Lourenço, A. Campos Costa, and J. V. Lemos, “On the dynamics of rocking motion of single rigid-block structures,” *Earthquake Engineering & Structural Dynamics*, vol. 36, no. 15, pp. 2383–2399, 2007.

[114] F. Peña, P. B. Lourenço, and A. Campos-Costa, “Experimental dynamic behavior of free-standing multi-block structures under seismic loadings,” *Journal of Earthquake Engineering*, vol. 12, no. 6, pp. 953–979, 2008.

[115] A. Giouvanidis and I. Dimitrakopoulos, “Modelling contact in rocking structures with a nonsmooth dynamics approach,” in *ECCOMAS Congress 2016-Proceedings of the 7th European Congress on Computational Methods in Applied Sciences and Engineering*, 2016, p. 0000.

[116] H. Zhang and B. Brogliato, “The planar rocking-block: analysis of kinematic restitution laws, and a new rigid-body impact model with friction,” Ph.D. dissertation, INRIA, 2011.

[117] C. Glocker and C. Studer, “Formulation and preparation for numerical evaluation of linear complementarity systems in dynamics,” *Multibody System Dynamics*, vol. 13, no. 4, pp. 447–463, May 2005.

[118] F. Pfeiffer and C. Glocker, *Multi-body dynamics with unilateral constraints*. Wiley, New York, 1996.

[119] C. Glocker, “Energetic consistency conditions for standard impacts,” *Multibody System Dynamics*, vol. 32, no. 4, pp. 445–509, 2014.

[120] H. Lankarani and P. Nikravesh, “A contact force model with hysteresis damping for impact analysis of multibody systems,” *Journal of mechanical design*, vol. 112, no. 3, pp. 369–376, 1990.

[121] P. Flores, M. Machado, M. T. Silva, and J. M. Martins, “On the continuous contact force models for soft materials in multibody dynamics,” *Multibody system dynamics*, vol. 25, no. 3, pp. 357–375, 2011.

[122] M. Gharib and Y. Hurmuzlu, “A new contact force model for low coefficient of restitution impact,” *Journal of Applied Mechanics*, vol. 79, no. 6, p. 064506, 2012.

[123] C. Putignano, L. Afferrante, G. Carbone, and G. Demelio, “A new efficient numerical method for contact mechanics of rough surfaces,” *International Journal of Solids and Structures*, vol. 49, no. 2, pp. 338–343, 2012.

[124] V. A. Yastrebov, G. Anciaux, and J.-F. Molinari, “From infinitesimal to full contact between rough surfaces: evolution of the contact area,” *International Journal of Solids and Structures*, vol. 52, pp. 83–102, 2015.

[125] R. L. Jackson and I. Green, “A finite element study of elasto-plastic hemispherical contact against a rigid flat,” *Journal of tribology*, vol. 127, no. 2, pp. 343–354, 2005.

[126] H. Ghaednia, M. R. Brake, M. Berryhill, and R. L. Jackson, “Strain hardening from elastic–perfectly plastic to perfectly elastic flattening single asperity contact,” *Journal of Tribology*, vol. 141, no. 3, p. 031402, 2019.

[127] S. M. Roberts and J. S. Shipman, “Two-point boundary value problems: shooting methods,” 1972.

[128] J. Craig, *Introduction to Robotics: Mechanics and Control*. Addison-Wesley Publishing Company, Inc., 1989.

[129] T.-Y. Li, “Numerical solution of multivariate polynomial systems by homotopy continuation methods,” *Acta numerica*, vol. 6, pp. 399–436, 1997.

[130] A. Morgan and A. Sommese, “Computing all solutions to polynomial systems using homotopy continuation,” *Applied Mathematics and Computation*, vol. 24, no. 2, pp. 115–138, 1987.

[131] E. Lee and C. Mavroidis, “Solving the geometric design problem of spatial 3r robot manipulators using polynomial homotopy continuation,” *Journal of Mechanical Design*, vol. 124, no. 4, pp. 652–661, 2002.

[132] A. Morgan and A. Sommese, “A homotopy for solving general polynomial systems that respects m-homogeneous structures,” *Applied Mathematics and Computation*, vol. 24, no. 2, pp. 101–113, 1987.

[133] C. W. Wampler, A. Morgan, and A. Sommese, “Numerical continuation methods for solving polynomial systems arising in kinematics,” *Journal of mechanical design*, vol. 112, no. 1, pp. 59–68, 1990.

[134] D. Cox, J. Little, and D. O’shea, *Ideals, varieties, and algorithms*. Springer, 1992, vol. 3.

[135] D. A. Cox, J. Little, and D. O’shea, *Using algebraic geometry*. Springer Science & Business Media, 2006, vol. 185.

[136] B. Sturmfels, *Solving systems of polynomial equations*. American Mathematical Soc., 2002, no. 97.

[137] D. Kapur and Y. N. Lakshman, “Elimination methods: an introduction. symbolic and numerical computation for artificial intelligence b. donald et. al,” 1992.

[138] D. Kapur, “Using gröbner bases to reason about geometry problems,” *Journal of Symbolic Computation*, vol. 2, no. 4, pp. 399–408, 1986.

[139] D. Manocha, “Solving systems of polynomial equations,” *IEEE Computer Graphics and Applications*, vol. 14, no. 2, pp. 46–55, 1994.

[140] Z. Kukelova, M. Bujnak, and T. Pajdla, “Polynomial eigenvalue solutions to minimal problems in computer vision,” *IEEE Transactions on Pattern Analysis and Machine Intelligence*, vol. 34, no. 7, pp. 1381–1393, 2012.

[141] G. Jónsson and S. Vavasis, “Accurate solution of polynomial equations using macaulay resultant matrices,” *Mathematics of computation*, vol. 74, no. 249, pp. 221–262, 2005.

[142] P. Stiller, “An introduction to the theory of resultants,” *Mathematics and Computer Science, T&M University, Texas, College Station, TX*, 1996.

BIOGRAPHICAL STATEMENT

Abhishek Chatterjee was born in Calcutta (now Kolkata), India, in 1990. He came to the United States in 2009 to pursue college education. He received his B.S. degree from Midwestern State University in 2013, before joining The University of Texas at Arlington for graduate studies in Mechanical Engineering. At the University of Texas at Arlington, he first earned his Master's degree in 2015, and later a PhD in 2019. His research interest is in the area of robotic manipulation and controls, and wishes to continue working on these areas after the completion of his doctoral program.